


# The Development of a Fast Response Measurement System for use in Turbomachinery Applications

**Shamal Mena Crowther, MSc. BEng.**

University of Nottingham

Department of Chemical and Environmental Engineering

Supervised by: Dr David Hann & Dr Buddhika Hewakandamby

Sponsored by: GE Power, UK




Thesis submitted to the University of Nottingham in partial fulfilment for the Degree of Doctor of Engineering,

April 2018

## Abstract

Improvements in the efficiency of power generation via turbomachinery are essential in order to reduce greenhouse gas emissions throughout the world. Advancements in measurement techniques are therefore crucial to understanding the main areas of energy loss in turbines and compressors. This thesis presents a novel system which allows that loss to be characterised using fast response, 3-D measurements of the pressure field within industrial scale rigs.

Turbulent energy dissipation rates give an insight into where useable energy is lost from. To gain an insight into such rates, measurement techniques must be able to take data in all three dimensions simultaneously at high sampling rates, usually over 50 kHz. Traditional methods of flow characterisation such as optical techniques and pneumatic pressure probes are unable to capture the rapid fluctuations in pressure and velocity which lead to energy loss from the turbomachine. A new system was therefore designed and implemented into a 6-stage compressor rig to take fast response measurements at sampling frequencies up to 100 kHz behind the last stage stator.

A fast-response 5-sensor pressure head, acquired from Kulite Semiconductor Products Inc, has been embedded into a bespoke stem to allow turbulence measurements in a range of turbomachinery applications. The five-sensor (5S) probe was calibrated for pressure sensitivity as well as aerodynamically to give total and static pressure along with velocity magnitude and direction. Individual sensors were calibrated and characterised at temperatures within a range of $20^0$C and $50^0$C, which corresponds to the conditions found within the final application. The probe was also used in a vortex shedding experiment where alternative eddies were detected from the 5S probe measurements in both the time and frequency domain.

The aerodynamic calibration of the 5S probe consists of exposing the probe sensors to a range of flow angles in order to map their response between $\pm 20^0$ in both the yaw and pitch directions. This results in four non-dimensional coefficients, two to represent pressure and two to signify the flow angles. A linear interpolation method was written and implemented to deduce pressure and flow angles from experimental query points and the calibration data. The linear interpolation was used as an alternative to the standard surface fit method, where the calibration data is expressed as system of polynomial equations. It was found that the linear method was applicable to the interpolation of flow angles and gave a reduction in computation time of the order of $10^4$. The total and static pressure values do however require the more tried and tested polynomial interpolation method due to the need for higher order interaction terms in the surface fit equation describing the terms.

The fully calibrated 5S probe was then implemented into a 6-stage industrial scale rig where it acquired fast response pressure data from the flow field at the exit of the last stage vane. The data was processed to give time resolved, 3-D measurements of total and static pressure, flow angle and velocity. Due to the simultaneous capture of data from all 5 sensors, the resulting velocity vectors can be decomposed into their mean and periodic components to obtain values of energy loss from the turbomachine. The acquisition of such data from an industrial rig marks a novel advancement in the area of turbomachinery flow characterisation and the use of the 5S probe in a range of applications will begin to fulfil the need for a database of fast response data from chaotic and turbulent flow fields.

This thesis is dedicated to the loving memory of Patrick and Margaret Hanson.

# Acknowledgements

I would like to thank many people for their support, inspiration and most importantly, their patience over the past few years. It has been a long journey, made possible only by the team of individuals around me.

Firstly, I'd like to extend my gratitude to my academic supervisor, Dr David Hann, for his motivation and support in times of success as well as adversity. A special thank you is also required for Dr Kris Vernon who went above and beyond to give his support and guidance throughout this research project.

I'd like to thank the sponsor company, General Electric for their financial contribution as well as the wealth of knowledge which accompanied it. I am very grateful to all members of the technical and testing team within the company and would like to give special thanks to Joe Jamieson, Peter Bates, Tim Rice, Alberto D'Ovivo, Scott Barham and for their much-appreciated input throughout the years.

There are so many people on both University Park and Jubilee campus who deserve my eternal thanks for answering my many queries and helping me to succeed. These include Phil, Mick and Mel from the university workshop as well as Faycal, for his many stories and encouragements.

I am forever indebted to my fellow researchers who always helped me to progress, these include Gulcan Serdaroglu and Bilaal Hussain. You always told me that I could do it even when I thought I couldn't.

Lastly but by no means least, I'd like to thank my family and friends for their support and understanding throughout this process. Mam and dad, I hope I've made you proud. Matthew, your love and kind words (and late nights talking about our research) made this all possible.

# Contents

Chapter 1: Introduction ..... 1

1.1 Overview ..... 1

1.2 Turbomachinery Irreversabilities ..... 3

1.3 Research Objectives ..... 5

1.4 Thesis Outline ..... 6

Chapter 2: The Energy Loss Problem Within turbomachines ..... 9

2.1 Introduction ..... 9

2.2 Sources of Turbomachinery Energy Loss ..... 9

2.3 Unsteady pressure ..... 12

2.4 Energy loss via turbulence ..... 14

2.4.1 Homogeneous turbulence ..... 17

2.5 Understanding Complex Turbomachinery Flows ..... 20

2.5.1 CFD ..... 20

2.5.2 Measurement of unsteady flows ..... 24

2.6 Conclusions ..... 25

Chapter 3: Developments in Turbomachinery Measurement Techniques ..... 27

3.1 Introduction ..... 27

3.2 Measurement techniques ..... 27

3.2.1 Laser Doppler Anemometry ..... 28

3.2.2 Particle Image Velocimetry ..... 30

3.2.3 Hot wire anemometry ..... 33

3.2.4 Pressure probes ..... 35

3.2.5 Application to turbomachinery rigs ..... 36

3.3 Fast response measurement techniques ..... 40
3.3.1 Type of sensor ..... 40
3.3.2 Resolution and frequency response ..... 43
3.4 Application to turbomachinery ..... 43
3.5 The Kulite FAP-250 probe tip ..... 46
3.6 Conclusions ..... 49
Chapter 4: Probe stem design ..... 51
4.1 Introduction ..... 51
4.2 Key challenges ..... 51
4.2.1 Low Pressure steam turbine rig application ..... 52
4.2.2 Compressor Rig ..... 52
4.3 Probe attachment methods ..... 55
4.3.1 Laser welding test ..... 55
4.3.2 Other attachment methods ..... 58
4.3.3 Coupling piece ..... 59
4.4 Temperature compensation module considerations ..... 60
4.5 Stem designs ..... 63
4.5.1 Stem α design ..... 64
4.5.2 Stem β design ..... 67
4.5.3 Stem γ design ..... 69
4.6 Probe design considerations ..... 72
4.7 Conclusions ..... 73
Chapter 5: Measurement Technique Development ..... 75
5.1 Introduction ..... 75
5.2 Measurement chain set-up ..... 75

5.3 Characterisation of the 5S probe ..... 78
5.3.1 Sensor calibration ..... 79
5.3.2 Sensor calibration results ..... 82
5.3.3 Temperature dependency ..... 86
5.4 The air jet rig .....100
5.4.1 Theory of jet flow .....102
5.4.2 Characterisation of Air Jet Rig Exit .....104
5.5 Defining the 5S Probe Capabilities .....107
5.5.1 Fluid structure interaction .....108
5.5.2 Experimental design and set up .....109
5.5.3 Vortex shedding experimental results .....118
5.5.4 Vortex shedding frequency verification .....120
5.5.5 Visual inspection of the individual sensors after initial testing .....130
5.6 Conclusions .....131
Chapter 6: 5S Probe Calibration .....132
6.1 Introduction .....132
6.2 Calibration types .....132
6.2.1 Sensor calibration .....132
6.2.2 Aerodynamic calibration .....133
6.2.3 Dynamic calibration .....135
6.3 Air jet rig adaptations .....136
6.4 Aerodynamic calibration procedure .....137
6.5 Calibration results .....142
6.6 Data reduction from calibration data .....149
6.6.1 Polynomial interpolation method .....149

6.6.2 Linear interpolation method .....156
6.6.3 Interpolation method comparison: Software validation testing.....161
6.6.4 Interpolation method comparison for real test case...165
6.7 Uncertainty analysis .....169
6.7.1 Uncertainty methodology.....169
6.7.2 Errors in pressure acquisition .....172
6.7.3 Errors in the aerodynamic calibration and interpolation processes .....173
6.8 Conclusions .....176
Chapter 7: Application of 5S probe to Compressor rig .....177
7.1 Introduction .....177
7.2 Compressor rig description .....177
7.3 Rig adaptations to allow access to measurement area.....182
7.4 Probes used in compressor rig application .....188
7.4.1 Fast response probes .....188
7.4.2 Pneumatic probes .....189
7.5 Experimental set-up and design .....190
7.5.1 Measurement and analysis chain .....191
7.5.2 Measurement of nozzle exit angle .....192
7.6 Compressor flow characterisation .....193
7.7 Time-averaged results .....195
7.8 Time-resolved measurements .....198
7.9 Statistical averaging of the results.....201
7.10 Time resolved 5S probe measurements .....203
7.11 Blade passing cycle results .....204

7.12 Presentation of unsteady data .....207
7.13 Wake analysis .....214
7.14 Vector component trace results .....218
7.15 Conclusions .....220
Chapter 8: Conclusions and future outlook .....222
8.1 Research overview .....222
8.1.1 Probe design summary .....222
8.1.2 5S probe characterisation summary .....223
8.1.3 Aerodynamic calibration and validation summary .....224
8.1.4 Compressor rig testing summary .....226
8.2 Limitations .....226
8.3 Future work .....228
8.3.1 Improving calibration accuracy .....228
8.3.2 Taking measurements in the turbine rig .....228
References .....230
Appendices .....241
Appendix 1: Resistor diagrams for temperature compensation modules .....241
Appendix 2: Intermediate drawings of Stem β .....246
Appendix 3: Vortex shedding experimental measurement points .....247
Appendix 4: CAD drawings of flow extension tube for Air Jet Rig .....248
Appendix 5: Yaw–Pitch manipulator design .....249
Appendix 6: Unit vector relations for the aerodynamic calibration .....250

Appendix 7: Data flow overview .....251

Appendix 8: Error propagation rules.....252

Appendix 9: Deadweight tester calibration certificate .....254

Appendix 10: Kulite FAP-250 probe head specification.....255

# List of Figures

Figure 1.1: Brayton power generation gas cycle layout..... 4

Figure 1.2: Brayton power generation gas cycle, depicted as a T-s diagram ..... 4

Figure 2.1: Turbulent boundary layer regions..... 11

Figure 2.2: Classification of flow types based on how deterministic they are in nature ..... 12

Figure 2.3: Energy cascade, Sourced from Davidson (2004) ..... 15

Figure 2.4: Identified regions of TKE dissipation with the distribution of eddy sizes identified for each zone. Adapted from Davidson (2004). ..... 18

Figure 2.5: High level view of the computational modelling process ..... 20

Figure 3.1: Typical Laser Doppler Anemometry system, adapted from Dantec Dynamics, (2017)..... 29

Figure 3.2: PIV setup (Dantec, 2017)..... 31

Figure 3.3: Hot wire sensor types (JØrgensen, 2002)..... 33

Figure 3.4: Axisymmetric layout for a five-hole pressure probe .... 35

Figure 3.5: Wheatstone bridge circuitry..... 42

Figure 3.6: Capabilities of fast response probes based on their number of sensors ..... 45

Figure 3.7: Kulite leadless pressure transducer technology (Kulite, 2017) ..... 47

Figure 3.8: CAD drawing of the Kulite FAP 250 transducer with birds eye view. The transducer is to be embedded into a probe stem to be used as a 5 Sensor pressure probe. ..... 48

Figure: 3.9: Schematic drawing of a slice through the centreline of the FAP 250 probe head with actual dimensions measured upon delivery of the sensor tip ..... 48

Figure 3.10: Back of FAP-250 probe head with silicone sealant securing 20 sensor leads, with table denoting the role of each coloured wire in the probes circuitry ..... 49

Figure 4.1: Step-wise procedure followed to assess the laser welding method in its applicability to attaching the probe tip to a designed stem ..... 56

Figure 4.2: Results of the first laser welding test. Two stainless steel plates of thickness 1mm were used ..... 57

Figure 4.3: Cylindrical test pieces used in the second phase of the laser weld testing. The pieces were not successfully welded and they were damaged during the trial ..... 57

Figure 4.4: Probe coupling concept demonstrated using a straight stem ..... 60

Figure 4.5: Potential configurations for the placement of the temperature compensation modules inside of probe stem ..... 61

Figure 4.6: Expanded diagram showing the assembly of probe α .. 62

Figure 4.7: Photograph of air jet rig nozzle, through which air is exhausted to produce an axisymmetric jet ..... 65

Figure 4.8: Swan neck probe design used in the calibration of the sensor head and the development of the measurement technique used throughout the final stage of testing ..... 65

Figure 4.9: Swan neck probe fixed into the 2DOF traverse motor via the pitch table, allowing adjustments in the pitch angle during probe balancing ..... 66

Figure 4.10: CAD drawing of LP rig and traverse ..... 67

Figure 4.11: Final probe stem design. The stem is first bent upwards by $10^0$ then the probe tip is to be attached at the designated $20^0$. This gives an overall bend of $10^0$ ..... 69

Figure 4.12: Compressor rig used in the final stage of testing the 5S probe ..... 70

Figure 4.13: CAD drawing showing a 2D slice through the compressor rig. The area in which measurements were taken is shown relative to the last stage blades ..... 70

Figure 4.14: Probe design for use in the compressor rig. The compression fitting used to lock the probe in the rig as well as the security fitting are shown ..... 71

Figure 4.15: Conceptual drawing of proposed traverse extension piece to allow one probe to be used for calibration and testing ..... 73

Figure 5.1: Data acquisition system with labels expanded in table 5.1 ..... 76

Figure 5.2: Deadweight tester used in the calibration of pressure sensors ..... 81

Figure 5.3: Centre sensor calibration ..... 83

Figure 5.4: Left sensor calibration ..... 83

Figure 5.5: Right sensor calibration ..... 84

Figure 5.6: Top sensor calibration ..... 84

Figure 5.7: Bottom sensor calibration ..... 85

Figure 5.8: Resistor network for the broken right sensor ..... 88

Figure 5.9: Calibration of the 5S probe carried out in a sealed oven. Temperature range was $25^0$C to $50^0$C. ..... 90

Figure 5.10: Right sensor calibration results with no temperature compensation module in circuit. Calibration carried out over a temperature range of $25^0$ to $50^0$ ..... 92

Figure 5.11: Centre sensor calibration results with no temperature compensation module in circuit. Calibration carried out over a temperature range of $25^0$ to $50^0$ ..... 92

Figure 5.12: Left sensor calibration results with Kulite temperature compensation module in circuit. Calibration carried out over a temperature range of $25^0$ to $50^0$ ..... 93

Figure 5.13: Bottom sensor calibration results with Kulite temperature compensation module in circuit. Calibration carried out over a temperature range of $25^0$ to $50^0$ ..... 93

Figure 5.14: Centre sensor calibration results with in-house temperature compensation module in circuit. Calibration carried out over a temperature range of 250 to 500 ..... 94

Figure 5.15: Right sensor calibration results with in-house temperature compensation module in circuit. Calibration carried out over a temperature range of 250 to 500 ..... 94

Figure 5.16: Temperature recorded on the surface of the 5S probe tip during the excitation ..... 97

Figure 5.17: Thermal camera image of the 5S probe head after 10 minutes of warm up ..... 98

Figure 5.18: Thermal camera image of the 5S probe head, with the measurement point located as close to the sensor ..... 99

Figure 5.19: Single sensor probes used to investigate the axisymmetric jet used in the calibration of the 5S probe .....102

Figure 5.20: Jet flow theory drawing, showing the change in velocity profile at increasing distances from the nozzle exit .....103

Figure 5.21: Air jet rig Mach number calibration with motor speed in the range of 200 rpm to 1300 rpm .....105

Figure 5.22: Air jet rig nozzle traverse results .....106

Figure 5.23: Air jet rig nozzle traverse results .....106

Figure 5.24: FFT result from the top sensor, taken during vortex shedding at a motor speed of 1000 rpm .....125

Figure 5.25: Vortex shedding time series, taken at a motor speed of 800 rpm. Alternative vortices reflected in the pressure traces acquired by the top and bottom sensors of the 5S probe .....128

Figure 6.1: Yaw and pitch planes defined in relation to the five pressure sensors at the tip .....134

Figure 6.2: Combined manual pitch and automatic yaw manipulation device .....137

Figure 6.3: Flow chart showing the steps carried out to complete the aerodynamic calibration of the 5S probe.....141

Figure 6.4: Yaw angle sensitivity of the 5S probe .....142

Figure 6.5: Yaw sensitivity of FAP-250 sensor attached to a straight stem. Sourced from Guenettee and Castner, (2011) .....143

Figure 6.6: Full 3D calibration of 5S probe at an extended calibration range of $\pm 30^0$ .....144

Figure 6.7: Calibration grid showing the yaw and pitch calibration constants plotted for each designated calibration angle .....145

Figure 6.8: Pitch coefficient plotted over calibration range .....146

Figure 6.9: Yaw coefficient plotted over calibration range .....146

Figure 6.10: Total pressure coefficient plotted over calibration range .....147

Figure 6.11: Static pressure coefficient plotted over calibration range .....147

Figure 6.12: 4th Order polynomial surface fit of yaw coefficient calibration data .....152

Figure 6.13: 4th Order polynomial surface fit of pitch coefficient calibration data .....152

Figure 6.14: 4th Order polynomial surface fit of total pressure coefficient calibration data .....153

Figure 6.15: 4th Order polynomial surface fit of static pressure coefficient calibration data .....153

Figure 6.16: Goodness of fit statistics for calibration data fitted to polynomial surface fits of increasing orders.....154

Figure 6.17: Flow chart depicting the first pass linear interpolation process .....157

Figure 6.18: Local Square around query point in first pass calibration data interpolation .....158

Figure 6.19: Second pass method representation of the local structure around the query point.....160

Figure 6.20: Calibration grid showing variations in Kα and Kβ values with changing α and β angles. A grid of simulted test points has been plotted over the calibration data.....162

Figure 6.21: Pitch angles resulting from simulated data points test .....164

Figure 6.22: Yaw angles resulting from simulated data points test .....164

Figure 6.23: Pitch angle results for both interpolation methods. Set pitch angle:-50 .....166

Figure 6.24: Yaw angle results for both interpolation methods. Set yaw angle: 130 .....166

Figure 6.25: Elapsed computation time comparison for each of the interpolation methods .....168

Figure 6.26: Overview of the errors found within the processes of calibration and measurement using the 5P probe .....171

Figure 7.1: Rig circuit overview .....179

Figure 7.2: Final stator stage blade dimensions.....180

Figure 7.3: Dimensions of the 5S probe tip used in the compressor rig .....181

Figure 7.4: Horizontal slice through rig diagram, showing cavity length between final blade row and the rig exhausts.....182

Figure 7.5: Removal of compressor rig outer casing.....184

Figure 7.6: LHS: Probe stem inserted though 10mm dimeter hole in compressor casing. Middle: Stem $90^0$ bend manoeuvred through access hole. RHS: Stem turned to align with blade passage .....185

Figure 7.7: Design of measurement access points .....186

Figure 7.8: Last stage stator exit angle, as measured from exposed compressor casing.....186

Figure 7.9: 5S probe secured through the compressor rig casing.187

Figure 7.10: Stem γ probe with main features designed for use with compressor rig.....188

Figure 7.11:Pitot total pressure probe used to characterise the flow field found within the compressor rig .....190

Figure 7.12: Flowchart showing software data analysis chain .....191

Figure 7.13: 5S probe stem angular measurement system, set-up to assess the last stage exit angle.....192

Figure 7.14: Pressure data from each sensor during angular sensitivity test. Sensors aligned at an angle of $22^0$ .....193

Figure 7.15: Mach number deduced from the Kiel probe.....197

Figure 7.16: Mach number deduced from a single sensor on the FAP-250(1) probe tip.....197

Figure 7.17: Blade passing frequencies deduced from a single sensor on the fap-250(1) probe. Results are given for each compressor speed .....200

Figure 7.18: Mach number statistical convergence.....202

Figure 7.19: BPFs calculated from the calibrated Mach numbers obtained from the 5S probe .....205

Figure 7.20: 300rpm at position 1 at vane exit, time interval: 0.499 ms.....208

Figure 7.21:500rpm at position 1 at vane exit, time interval: 0.29 ms .....209

Figure 7.22: 700rpm at position 1 at vane exit, time interval: 0.21 ms.....210

Figure 7.23: 900rpm at position 1 at vane exit, time interval: 0.166 ms.....211

Figure 7.24: Mach number trace with corresponding individual pressure traces from each of the sensors in the 5S probe.....212

Figure 7.25: Reconstructed Mach number time trace at a motor speed of 900rpm .....215

Figure 7.26: Reconstructed Mach number time trace at a motor speed of 700rpm .....215

Figure 7.27: Reconstructed Mach number time trace at a motor speed of 500rpm .....215

# List of Tables

Table 3.1: Overview of hot wire sensor arrangements and their main uses ..... 34

Table 4.1: Summary of challenges faced during the design of the 5S probe..... 54

Table 4.2: Summary of each probe stem and the rig in which it was designed for use..... 64

Table 5.1: Explanation of each step in the data acquisition chain shown in figure 5.1..... 77

Table 5.2: Atmospheric conditions measured at the time of each sensor calibration ..... 82

Table 5.3: Experimental runs carried out during the temperature dependency calibration investigation..... 91

Table 5.4: Summary of probes used in the development of the measurement technique.....101

Table 5.5: Table of vortex shedding experimental conditions with corresponding non-dimensional parameters and predicted Strouhal frequencies.....119

Table 6.1: Summary of flow quantities calculated from the 5S probe data.....148

Table 6.2: Observed corner values from simulated test grid.....162

Table 6.3: Summary of first and second statistical modes of each of the time series' resulting from the test case.....167

Table 6.4: Uncertainties calculated for pressure readings and calculated calibration coefficients.....173

Table 6.5: Uncertainties calculated for experimental parameters found through the calibration and interpolation process.....174

Table 6.6: Uncertainties calculated through the propagation of errors through calculated quantities .....175

Table 6.7: Comparison of uncertainty values from the 5S probe and two probes from the ETH lab.....175

Table 7.1: Summary of compressor operating conditions as measured during initial investigation of the flow field.....194

Table 7.2: Number of aerofoils present in each compressor stage195

Table 7.3: Calculation of blade passaging cycles until statistical convergence of the data.....203

Table 7.4: Blade passing frequencies and subsequent time data for the blade passing cycles for each set motor speed.....206

# List of Equations

Equation 2.1: Reynolds decomposition for pressure ..... 13

Equation 2.2: Rate of turbulent energy dissipation..... 16

Equation 2.3: Navier-Stokes equation used to define the fluid motion of a system ..... 21

Equation 2.4: Reynolds stress tensor ..... 22

Equation 3.1: Wheatstone bridge output relationship ..... 42

Equation 5.1: Deadweight tester pressure-mass relationship ..... 79

Equation 5.2: Span resistor network equation ..... 87

Equation 5.3: Cantilever beam fundamental frequency.....111

Equation 5.4: Strouhal number calculated from the shedding frequency .....112

Equation 5.5: Strouhal number calculated from the Reynolds number .....112

Equation 5.6: Number of samples per vortex shedding period .....121

Equation 6.1: Pitch angle pressure coefficient .....138

Equation 6.2: Yaw angle pressure coefficient .....139

Equation 6.3: Total pressure coefficient.....139

Equation 6.4: Static pressure coefficient.....139

Equation 6.5: Pseudo-static pressure .....139

Equation 6.6: Polynomial regression model equation for the experimental pitch angle .....150

Equation 6.7: Polynomial regression model equation for the experimental yaw angle .....150

Equation 6.8: Polynomial regression model for the experimental total pressure.....150

Equation 6.9: Polynomial regression model for the experimental static pressure.....151

Equation 6.10: Linear interpolation first pass method –fraction in pitch direction.....158

Equation 6.11: Linear interpolation first pass method –fraction in yaw direction.....159

Equation 6.12: Linear interpolation first pass method - experimental pitch angle .....159

Equation 6.13: Linear interpolation first pass method - experimental pitch angle .....159

Equation 6.14: Expanded uncertainty relationship .....172

Equation 7.1: Blade passing frequency equation.....198

Equation 7.2: Calculation of samples per period .....206

Equation 7.3: General Reynolds Decomposition equation.....217

## Nomenclature

| Symbol | Subscripts | Description | Notes |
|---|---|---|---|
| $Q$ | in, out | Heat (in,out) | |
| P | (1,2,3,4,5) | Pressure; | primed value denotes experimentally derived value. ($P_S'$ and $P_T'$) |
| | s,t | Pressure sensor (1,2,3,4,5) | |
| | | Static and Total pressure | |
| $\overline{\boldsymbol{P}}$ | | Mean pressure | |
| $\widetilde{\boldsymbol{P}}$ | | Periodic pressure | |
| $\boldsymbol{P}'$ | | Fluctuating pressure | |
| $\boldsymbol{\Pi}$ | | Energy dissipation (large eddies) | |
| $\boldsymbol{l}$ | | Length; Length scale | |
| $\boldsymbol{u}, \boldsymbol{V}$ | | flow velocity | |
| $\boldsymbol{\varepsilon}$ | | Energy dissipation (smallest scale) | |
| $\boldsymbol{\rho}$ | | Density | |
| $\boldsymbol{\mu}$ | | Viscosity; | |
| h | | mass of tube per unit length | |
| Re | i,j | Reynolds Stress Tensor | |
| R | Bridge,Span | Resistance | |

| Symbol | Subscripts | Description | Notes |
|---|---|---|---|
| x | 0, axial | Spatial position | |
| d,D | nozzle | Diameter | |
| U | ∞, e | Mainstream velocity, expanded uncertainty | |
| $f$ | 0, | frequency | |
| E | | Youngs modulus | |
| $I$ | | Moment of intertia | |
| α | | Pitch angle;<br>Probe stem α | primed value denotes experimentally derived value. (α′) |
| β | | Yaw angle;<br>Probe stem β | primed value denotes experimentally derived value. (β′) |
| γ | | heat capacity ratio;<br>Probe stem γ | |
| K | α, β, S, T | Calibration coefficient | |
| k | α, β,s,T,<br>f | polynomial coefficient; | |
| Ma | u,v,w | Mach number | |

| Symbol | Subscripts | Description | Notes |
|---|---|---|---|
| | | convergence factor | |
| A | | constant | |
| a | | speed of sound | |
| $\boldsymbol{V}$ | R,x,θ,r | velocity (radial/ axial, circumferential and rotational) | |
| $\overline{\boldsymbol{V}}$ | | Absolute velocity | |
| m | | gradient | |
| c | | axis intercept | |
| $n_b$ | | number of blades | |
| $\boldsymbol{\sigma_f}$ | | standard uncertainty | |

# Chapter 1: Introduction

## 1.1 Overview

The modern world is faced with the escalating problem of climate change, making the mitigation of greenhouse gas (GHG) emissions a worldwide priority. Although renewable energy technologies are becoming more mature and cost effective, reliance on fossil energy is still high and in order to improve fuel efficiency the focus must be on improving power production processes.

Overall performances of steam and gas turbine systems have been greatly enhanced through their design to well over 90%, (Denton, 1993) making further improvements difficult without a greater understanding of the small scale dynamic flow fields found within modern turbomachinery systems. Advancements in fluid measurement techniques and flow simulation software have enabled the mapping of the bulk flow path through even the most complicated turbomachines, however difficulty is still faced when deducing fluctuating quantities which contribute to the overall energy loss found within the system. Nevertheless, even a 1% increase in overall power plant performance can greatly reduce GHG emissions and such an efficiency increase within the UK alone has the potential to prevent up to 1000t of $CO_2$ from entering the environment every year, (IEA, 2008).

As stated by Denton (1993) and Tucker (2013), the reliable deduction of turbulent quantities can be essential for turbomachinery design. As further knowledge of dynamic fluid structures is often required in areas of high complexity and turbulence such as in tip jets, exhaust wakes and boundary layers, computational fluid dynamics (CFD) is often used to alleviate the cost in designing and maintaining a turbomachinery test rig. The computational cost of running such

models however, increases with their ability to resolve the smallest turbulent length scales, making the more effective methods such as Direct Numerical Simulation and Large-Eddy Simulations impractically expensive for industrial use (ANSYS, 2006). As a result, measurements of unsteady flow properties from turbomachinery rigs are required in combination with CFD to refine and validate the models used. In their research, Tucker (2013) discuss the importance of taking such measurements in rigs which are representative of powerful, industrial turbomachinery systems. In general, however, most research facilities within the field obtain their CFD input values from cascade rigs or rigs with scaled down design conditions. The need to acquire unsteady data from industrial scale turbomachinery rigs, in order to aid turbulence treatment methods, is therefore ever increasing.

Measurement techniques currently used throughout the industry are often unable to acquire time-resolved data in turbomachinery rigs, making them unfeasible for the required unsteady measurements. Multi-hole pitot probes, used to measure Mach number via total and static pressure within turbomachines (Sieverding, 2003), dampen the fluctuations in the incoming pressure signals, resulting in time-averaged data. Hot wire probes, although able to give fast response measurements, are unable to withstand the conditions found with industrial style rigs (Sieverding, 2004). A robust method of taking fast response measurements is therefore required. Fast-response pressure probes such as those developed at the ETH lab (Leherin,2010) and (Schlienger,2002) and at the von Karman Institute (Sieverding, 2000) and (Sieverding, 2004) are used to tackle this issue, as they can acquire data at rates of up to 100 kHz. Such probes do however, acquire data from one or two fast response pressure sensors at different positions and the measurements are reconstructed to give the velocity vectors in 3 dimensions. In order to deduce unsteady flow properties, such as turbulence intensity, used as inputs to CFD modelling techniques, the time-resolved

velocity must be calculated from fast response pressure measurements acquired simultaneously. This thesis therefore investigates the design, calibration and application of a new measurement system which can take time-resolved measurements from an industrial style rig and convert them into three-dimensional velocity measurements. The Kulite Flow Angle Probe (FAP)-250 pressure transducer, to be discussed in chapter 3, is assembled into a probe designed specifically for use in the turbomachinery rigs available through the sponsor company. This probe, named the 5S probe, is then calibrated aerodynamically and tested in a 6-stage industrial compressor rig to investigate its robustness and ability to acquire time-resolved physical flow information, rendering it the first of its kind for such an application. This investigation provides an advancement in turbomachinery measurement techniques and the ability to measure the turbulent kinetic energy within the flow. This development in the field of fast response measurement techniques allows the characterisation of energy loss within power generating turbomachines, information which was previously unable to be measured in 3-dimensions simultaneously.

## 1.2 Turbomachinery Irreversabilities

The specific sources of turbomachinery energy loss are discussed in the following chapter, however an overview of the effect of such losses is given in this chapter. Rudolf Clausius, a thermodynamicist studying the work of Sadi Carnot, stated that 'It is impossible to construct a device which, when operating in a cycle, will produce no effect other than the transference of heat from a colder to a hotter body' (1850, sourced from Logan, 2003). It is therefore impossible to operate an energy generation device to be 100% efficient due to irreversible losses which cannot be recovered. When improving the efficiency of turbomachinery, the aim is therefore to reduce the irreversible effects produced during their operation. Figure 1.1 shows

a basic Brayton gas cycle layout, which represents the operation of power generating gas turbines, and figure 1.2 shows the corresponding Temperature-Entropy diagram.

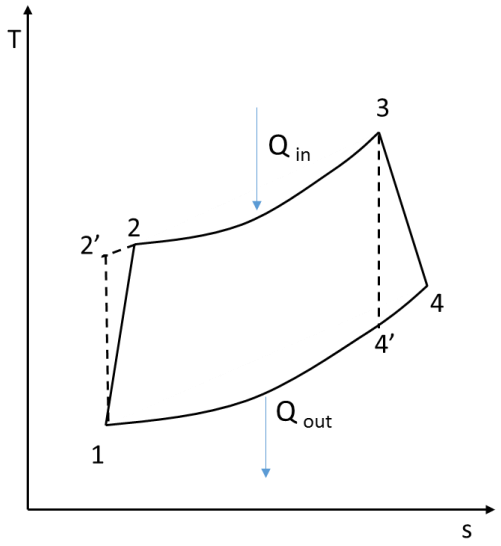



**Figure 1.1: Brayton power generation gas cycle layout**

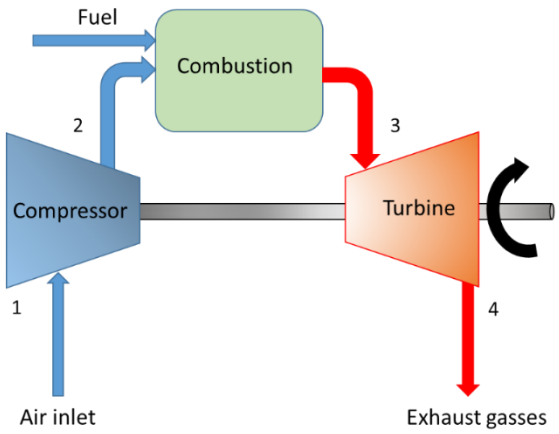



**Figure 1.2: Brayton power generation gas cycle, depicted as a T-s diagram**

The cycle steps are as follows:

- 1-2: Air pressure is increased in the compressor
- 2-3: Heat is added to the compressed gas in the combustor in a constant pressure process
- 3-4: Gas from the combustor is expanded through the turbine where energy is extracted
- 4-1: The exhaust gasses from the turbine are cooled and, in a closed system, fed back into the compressor

The steps 1-2’ and 3-4’ represent ideal compression and expansion processes which are isentropic in nature. Although the entropy generation within the compressor and turbine stages of the power generation cycle cannot be eradicated, changes in design and operation points can aid in its significant reduction. The aim of this thesis is therefore to take a step further in characterising the energy loss from these processes to aid in the understanding of how energy is lost in these regions and how the amount of unused energy can be reduced.

## 1.3 Research Objectives

The objective of this research project is to advance the method by which the sponsor company can take measurements within their turbomachinery test rigs. The scope of the project is therefore:

- To obtain a fast response pressure probe tip capable of acquiring data at a rate which allows the blade passing to be detected in the pressure field within a turbomachine
- To put together a measurement system which allows the simultaneous capture of instantaneous pressure fluctuations from all probe sensors within an industrial style rig
- To design and manufacture an interchangeable probe stem and attachment method which allows the probe tip to be used as a fully functioning measurement probe

- To investigate the capabilities of the probe after its assembly and define the best practice for taking measurements in an industrial style rig
- To design and manufacture a rig adaptation which allows the probe to be calibrated aerodynamically using the machinery available through the sponsor company
- To calibrate the probe for velocity magnitude and direction so that it can be used in any incompressible air flow application
- To use the probe in an industrial style compressor rig with the following aims:
    - To assess if the probe is able to survive a test campaign in a harsh, industrial environment,
    - To obtain, for the first time, time-resolved unsteady data from the rig to aid in the understanding of the aerodynamics present within the bulk flow at the blade exit
    - To process the test results in a way which provides statistical data which is unobtainable with the current state of the art methods used by the sponsor company

## 1.4 Thesis Outline

The chapters present in this thesis are outlined as follows:

**Chapter 1: Introduction**

An overview of the motivation of the project is given in this chapter. The need for a way of enhancing understanding of energy loss in turbomachines is introduced.

**Chapter 2: The Energy Loss Problem Within turbomachines**

The reader is introduced to the main sources of energy loss in industrial turbines and compressors. The mechanisms which lead to irreversible effects in turbomachines and the way in which these effects are currently predicted using computational fluid dynamics (CFD) is discussed. It is highlighted to the reader that an enhancement in measurement techniques is required in order to aid with CFD simulations of complex flows.

**Chapter 3: Developments in Turbomachinery Measurement Techniques**

An overview of commonly used measurement techniques is given in this chapter. It is highlighted here that time resolved measurements are essential and the current state of the art fast response techniques are presented. The FAP-250 probe tip used throughout this research project is introduced along with an overview of its working principle.

**Chapter 4: Probe Stem Design**

This chapter discusses the steps taken to design and produce a fully assembled probe, named the 5S probe, for use in turbomachinery applications. Challenges and constraints faced during the design are discussed and an optimised probe stem and method of assembly is presented.

**Chapter 5: Measurement Technique Development**

The results of the characterisation of the 5S probe are presented in this chapter. The measurement chain development and best practice methodology are also discussed. An investigation into the temperature compensation on each of the probe sensors was carried

out prior to full scale, the results of which are presented in this chapter.

**Chapter 6: 5S Probe Calibration**

Following the initial testing of the 5S probe, presented in chapter 5, the aerodynamic calibration was carried out. Chapter 6 outlines the adaptations made to allow the probe to be calibrated for direction in an air jet rig. The methodology followed is explained as well as an investigation into the interpolation processes used during the deduction of test data into flow properties such as pressure, Mach number and velocity.

**Chapter 7: The Application of the 5S probe in the Compressor Rig**

The fully calibrated probe was used to measure the flow field behind the final stage of an industrial style compressor rig. This chapter discusses the rig adaptations carried out to enable the probe to be used for the given application. The experimental design is also presented along with time resolved results obtained from the rig. Statistical results are also presented such as probability densities and velocity fluctuations, data which can only be obtained by the sponsor company, at present, using the measurement system designed and made possible throughout this research project.

**Chapter 8: Conclusions and future outlook**

This chapter gives a summary of each section of the thesis and an overall conclusion to the research. Recommendations are given on how to improve the accuracy of the measurement technique for future applications.

# Chapter 2: The Energy Loss Problem Within turbomachines

## 2.1 Introduction

This chapter gives the reader some insight into the ways in which energy is lost from turbomachines and the way that this loss is treated from an industrial point of view. The main sources of loss are presented along with the mechanisms driving the underlying unsteadiness. The role that both periodic flow fluctuations and turbulence affect turbomachinery systems is discussed along with the need for a combined approach to loss deduction, using both CFD and experimental techniques.

## 2.2 Sources of Turbomachinery Energy Loss

There are two main types of unsteadiness which can lead to energy loss within turbomachinery rigs. He (2003) introduces these as random turbulence and periodic flow effects. The former source, as discussed in more detail in section 2.4, is related to the stochastic component of the flow which, as well as turbulence, this includes the unsteady transitions of boundary layers or even intermittent blade flutter (Kupferschmied *et al,* 2000).

The periodic changes are often attributed to the intermittent passing of the blades which lead to flow oscillations. As the rotation rate of the blades is a controlled value, the flow perturbations produced by the revolving blades are usually deterministic in nature. Undesirable periodic flow phenomena such as shock waves and tip jets can lead to large gradients within the system and subsequent energy losses from the turbomachine. Kupferschmied *et al* (2002) also discuss an

intermediate level of flow fluctuation; nearly-periodic unsteadiness. This encompasses physical flow problems such as rotating stall, surging in compressors or blade row interactions. Periodic and nearly-periodic unsteadiness are grouped together in the term unsteady pressure.

As stated in chapter 1, energy is lost via irreversible entropy generation within turbomachines. Denton (1993) describes the sources of unsteadiness found within turbomachines and highlights shock waves, boundary layers and mixing processes as problem areas. The reasons that these areas are identified as problematic are described in this section.

Shock waves are unpredictable in nature and can cause a lot of unsteadiness in turbomachinery flows. Shapiro (1953) shows how, even for weak shocks, the generation of entropy is proportional to the property $(M^2-1)^3$, showing the magnitude of energy loss experienced in high Mach number flows. The measurement or computation of energy loss in such regions is extremely impractical and control volume analysis is generally applied, whereby specified input and output planes are induced and assumptions are made regarding the flow within the volume (Denton, 1993). This can lead to inaccuracies and uncertainty in derived quantities of total energy loss, enforcing the need for robust, time resolved measurements in these types of flows.

Boundary layers are inherently difficult when it comes to taking measurements of energy loss due to their widths and proximity to the surface wall. Turbulent boundary layers are of particular interest regarding energy loss from turbomachines as they are the major entropy generating components of many endwall flows such as tip

jets in blade rows. Figure 2.1 shows the regions in a turbulent boundary layer.

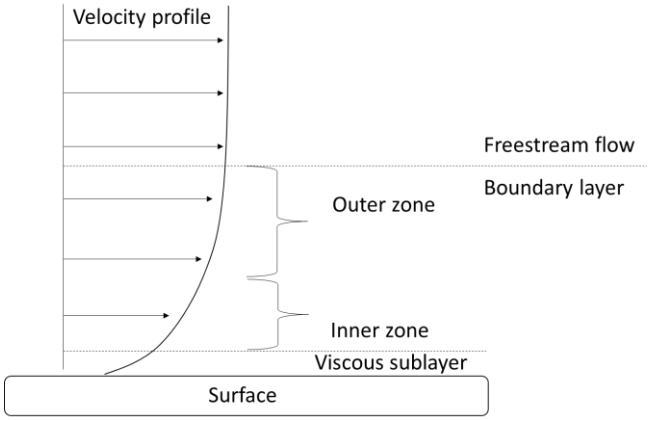



**Figure 2.1: Turbulent boundary layer regions**

The physical thickness of the layer itself can range from inches to micrometres, making measurements difficult due to the area of interest being of a similar length scale magnitude as the technique used. Adrian (2005) for example measured the flow in the outer layer of a turbulent boundary layer in a planar wall system using the optical technique Particle Image Velocimetry (PIV). Up to 90% of the energy loss via entropy generation however, occurs in the innermost part of the layer, the viscous sublayer, which is close to the surface wall (Denton, 1993). Therefore in order to acquire data regarding the dissipation of energy, measurements must be taken in the inner zone of the boundary layer. Issues such as the size of the measurement instrumentation or optical imaging area and proximity to the wall make measurements in this region very impractical. As a result, correlations are used to estimate the flow parameters in this region. More research is needed into miniaturising measurement techniques before this inner region can be thoroughly characterised.

The third troublesome flow area identified is the blade wake region, which can either lead to losses via blade row interactions or mixing losses, whereby the flow unsteadiness is mixed out after the last turbine or compressor stage. Entropy is generated in shearing flows

found in wake regions. When the flow separates from the blade edges it leads to viscous energy generation via a Von Karman vortex street. This is a repeating pattern of shed vortices through which kinetic energy is dissipated. When these wakes impinge on downstream blade rows, the interaction leads to an increase in unsteadiness and subsequent energy loss. Blades are designed to reduce these interactions however, time-resolved measurements of flow parameters around existing blades are required to give baseline values of loss coefficients.

Having discussed the main sources of energy loss within turbine and compressor rigs, a more in-depth look into how energy is lost via unsteady pressure is given in section 2.3, followed by an overview of loss from more stochastic flow unsteadiness in section 2.4.

## 2.3 Unsteady pressure

The difference between unsteady and turbulent flow properties is best described by the way that they are analysed. Figure 2.2 shows the classification of unsteady data, as sourced from Bendant and Piersol (2010).

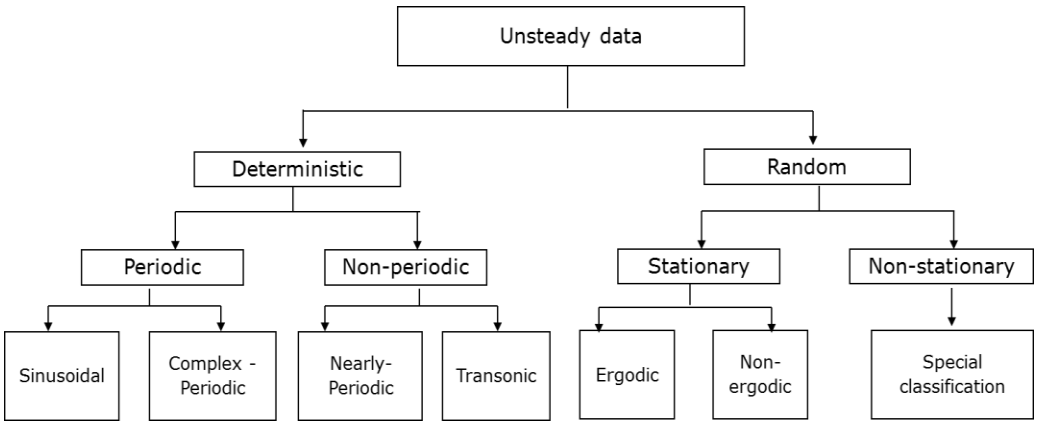



**Figure 2.2: Classification of flow types based on how deterministic they are in nature**

It is shown that turbulent data is random in nature and requires a statistical approach to its solution. Unsteady flow is deterministic because it is generally some periodic or nearly-periodic perturbation of the blade passing. It fluctuates rapidly with time due to its unsteady nature and must be solved in a time-resolved manner, either experimentally or computationally.

Unsteady flow can be described through the Reynold's Decomposition, whereby an unsteady flow quantity is separated into an averaged and a fluctuating component. Equation 2.1 shows this decomposition for unsteady pressure (Wullf, 2006).

$$P(x,t) = \bar{P}(x) + P'(x,t)$$

**Equation 2.1: Reynolds decomposition for pressure**

In non-oscillatory flows, $\bar{P}$ represents the time averaged component, calculated by taking an arithmetic mean of the measured signal. In more complex turbomachinery flows, the averaged component is represented by the periodic factor within the flow. When the mean flow field is not completely periodic, measurements taken using time-averaging techniques such as Pitot probes can lead to inaccuracies in the deduction of the mean component and subsequent estimations of the fluctuating part of the flow. Therefore, in order to take measurements in unsteady turbomachinery flows, a system with a frequency response capable of obtaining the blade passing frequency and its harmonics is essential (Kupferschmied *et al*, 2000).

The fluctuating part of the measured pressure will generally vary rapidly with time and is best described by turbulence theory. Section 2.4 gives an insight into the way in which energy is lost though this randomly fluctuating part of turbomachinery flows.

## 2.4 Energy loss via turbulence

When characterising the degree of turbulence and its affect within a particular system, it is essential to gain an understanding of the rate of kinetic energy dissipation. The reason for this is that the total loss in energy from the flow within a given system is often represented by the total energy dissipation due to turbulence (Liberzon *et al*, 2012). There are many ways by which the rate of energy dissipation can be measured experimentally, all of which involve the characterisation of turbulence in terms of its statistical properties.

Fully developed turbulence consists of a variety of time and length scales, equating to the range of eddy sizes found in complex flows. This range of scales gives an indication of how chaotic the flow can be and leads to difficulty when it comes to accurate measurement of many turbulent quantities such as instantaneous and fluctuating velocity values, vorticity and turbulence intensity.

In order to understand, measure and accurately characterise turbulent flow, it is often advantageous to look closely at a simple case such as grid generated turbulence as the flow properties are well defined and easily validated in this type of system. Due to the unpredictable nature of the flow, there are many questions which remain unanswered, meaning that specific theories and assumptions are only applicable to certain flow types. One of the most accepted theories among researchers is the cascade model describing the transport mechanism of the turbulent kinetic energy from production to dissipation. It is theorised that the largest eddies are those which contain the majority of the kinetic energy, formed through the production of turbulence, e.g. through the merging of wakes in grid generated turbulence. These large vortices fall within the integral length scale, $I$ and are the most easily measured as their size is usually within the resolution range of many commonly used techniques. The largest eddies then break up, due to instabilities within the flow, into smaller eddy structures which subsequently

continue to evolve in the same way until they reach the smallest length scale, the Kolmogorov scale, η. During the evolution of the turbulent structures, energy is passed down the cascade of eddy length scales due to the inertial forces acting within the flow. During this transfer of energy, it is thought that the viscosity has no effect upon the vortices until they get to the smallest scale. At the Kolmogorov scale, the Reynolds number tends to unity and the viscous forces begin to take effect on the smallest eddies and the energy being carried by the vortices is then dissipated as heat (Davidson, 2004). This is called viscous dissipation and is irreversible.

Figure 2.3 shows this relationship in terms of the wavenumber of the eddy structures and kinetic energy.

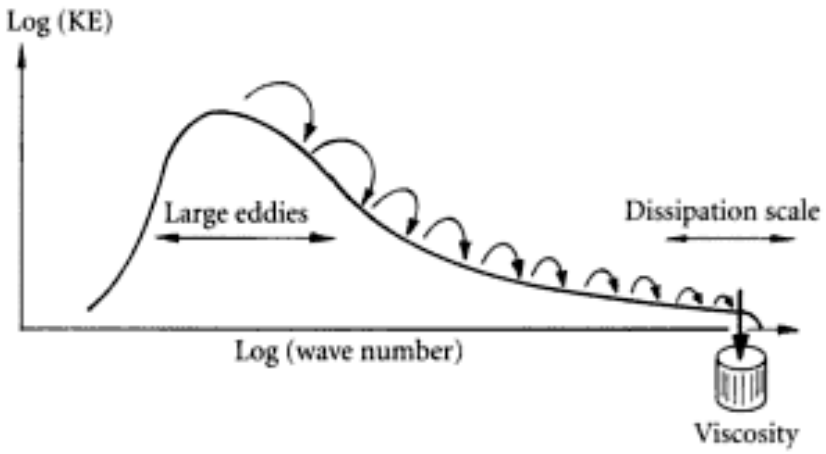



**Figure 2.3: Energy cascade, Sourced from Davidson (2004)**

In the figure, kinetic energy (KE) is the amount of kinetic energy in the vortices. It can be seen that the largest eddies contain the most energy initially and as the eddy sizes reduce, less energy is carried by individual structures until they become small enough that the viscous stresses take over and absorb the energy from any eddies within the Kolmogorov scale and causing it to be dissipated as heat. This theory highlights the difficulty in obtaining measurements at the

dissipating turbulent scales, making analysis of the energy loss within turbomachines extremely difficult.

As well as the length scales, the temporal scales found within turbulent flows are also important for deducing the total energy loss. Relationships can be assumed which link the Reynolds number and the ratios of the length and time scales of the different types of eddies within a particular flow, this give an indication of the rate at which turbulent kinetic energy is dissipated.

The rate of dissipation is very much related to the rate of production, therefore the eddy turnover times, also known as the time scales, must be known. This scale is estimated by the ratio of the length scale to the velocity of the respective eddy sizes with the Kolmogorov scale eddies having the fastest turnover time of any other scale. It may seem, therefore that the task of measuring the dissipation rate should be as simple as measuring the time and length scales of the smallest eddies, however it is often impossible to resolve down to the Kolmogorov scale. For this reason, many measurement techniques can only obtain data from the largest scale eddies and relate it to the dissipative scale.

The main assumption to be made when estimating the dissipation is that the rate at which energy is passed down the cascade, Π is approximately equal to the rate at which the large eddies evolve. This in turn is approximately equal to the rate of dissipation from the smallest eddies, ε. This is shown in the expression given in equation 2.2 (Davidson, 2004):

$$\Pi \approx \frac{u^2}{l/u} = \frac{u^3}{l} \approx \varepsilon$$

**Equation 2.2: Rate of turbulent energy dissipation**

As the approach to analysing turbulence must be a statistical one, the problem of closure arises when trying to find absolute solutions to sets of flow describing equations. The main problem with many turbulence closure models is that they are generalised for certain types of flow, however every turbulent flow has its own specific characterises which are difficult to globalise (Tropea *et al,* 2007). Section 2.4.1 discusses the theory of homogenous turbulence. The assumptions used when deducing the flow properties of homogeneous isotropic turbulence (HIT) are often used as a base to characterise more complicated regimes found within tubomachinery rigs.

### 2.4.1 Homogeneous turbulence

Although the types of flow regimes found in reality are often not consistently homogeneous, it is advantageous to look at the simplest turbulent shear flows to fully understand its fundamental concepts and theories. It is also essential to gain confidence in such theories such as the cascade model described above, in order to assess if they can be applied to more complex flows. In order to characterise the fluid dynamics of complex degrees of turbulence, the small scale physics of the most homogeneous turbulence need to first be understood.

Although it can be desirable to begin research in more complex shear flows, such as jets, channels, and boundary layers, the dynamics of these flow regimes can be specific to the rig itself. This means that not every case is the same and there is a need to study simple grid generated turbulence initially (Rose, 1966). When setting up HIT, a flow obstruction of uniform dimensions is often used, the most common devices being mesh grids and cube array turbulence generators. These allow the formation and subsequent merging of wakes behind the flow modification which is where the turbulence,

and associated kinetic energy, is generated. The measurement of the decay of turbulent kinetic energy has been a popular area of scientific research, with Taylor (1935) being one of the first to investigate turbulence in terms of its statistical properties with his four part research paper.

In order to measure the turbulence and dissipation rate correctly, the correct flow region, as presented by Taylor (1935), must be identified. Within grid turbulence there are three main regions which need to be assessed before carrying out a measurement (Mohamed and LaRue,1990).Figure 2.4 shows an overview of each region after the flow obstruction. The location of each region is dependent upon the geometry of the obstruction itself.

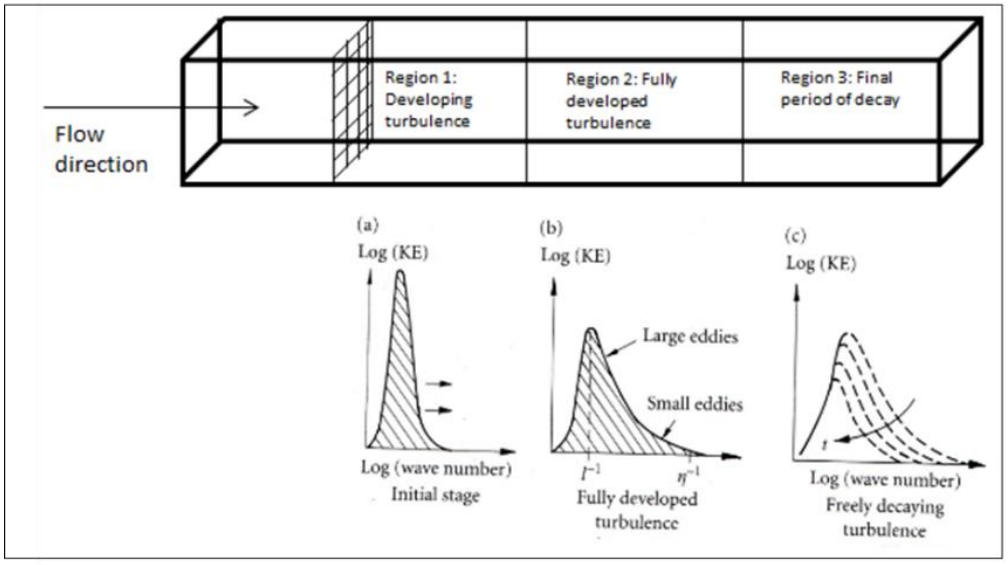



**Figure 2.4: Identified regions of TKE dissipation with the distribution of eddy sizes identified for each zone. Adapted from Davidson (2004).**

The first region identified in figure 2.4 is known as the developing zone which consists of vortices formed by shedding from the bars of the grid. The next stage is known as fully developed turbulence. Relatively slowly moving vortices from the developing zone tend to increase in speed and form turbulent motion by merging together until the turbulence is in a fully developed state.

At this stage, the flow contains a range of length scales ranging from the smallest Kolmogorov scale to the integral scale size. The third zone is known as the final period of decay, where the Reynolds number approaches unity and the turbulence begins to decay away so the flow becomes laminar.

The reason being that within the fully developed region, the smallest eddies tend to release kinetic energy first, which is dissipated as heat into the system, so the turnover rate for the large integral scale vortices is much longer than those of the Kolmogorov scale. This means that the motion begins to be dominated by the largest eddies which move at the slowest rate until a point whereby the flow becomes laminar (Davidson, 2004). The graphs (a) to (c) in figure 2.4 represent the distribution of the kinetic energy over the various length scales at each stage of the turbulence development.

It can be seen that fully developed turbulence is complicated in nature due to the range of eddy sizes present. The theory of HIT allows for some of the flow characteristics to be predicted. In oscillating flows however, the degree of turbulence is higher and the true flow regime begins to detach from the theory presented in this section. Difficulty is faced in the running of turbines and compressors when the degree of turbulence is unknown at the design stage. To account for the increase in complexity, different techniques exist to measure and model the small-scale fluctuations and their effect on the rest of the flow field.

As homogeneous turbulence is often generated by placing an organised grid or honeycomb into the flow path to cause flow separation and subsequent merging of the wakes, there is no further flow disturbance after this stage and the fully developed turbulence decays in an almost linear fashion. Due to this predictable trend, many researchers have used decaying grid turbulence to test the feasibility of various measurement techniques and estimate the applicability of such techniques to more complicated flow regimes.

## 2.5 Understanding Complex Turbomachinery Flows

The way in which unsteady flow is treated depends on the definition of unsteadiness used to describe the flow. For the majority of turbomachinery flows, the unsteadiness will be largely due to both periodic and turbulent properties. Looking particularly at turbulence, the way in which the results will be analysed must be known before a treatment method is chosen. The problem lies with the fact thorough understanding of the flow physics is then required to make such a decision. Hybrid treatment methods, whereby experimental data is obtained to support the development of computational models, are therefore common practice (Tropea *et al*, 2007). Measured data can be used to develop computational models by providing a database against which the model can be cross-referenced. It can also be used to verify specific test cases modelled by methods such as CFD and DNS.

### 2.5.1 CFD

In order to understand the way in which turbulence is treated using mathematical modelling, a high level overview of the modelling cycle is given in figure 2.5.

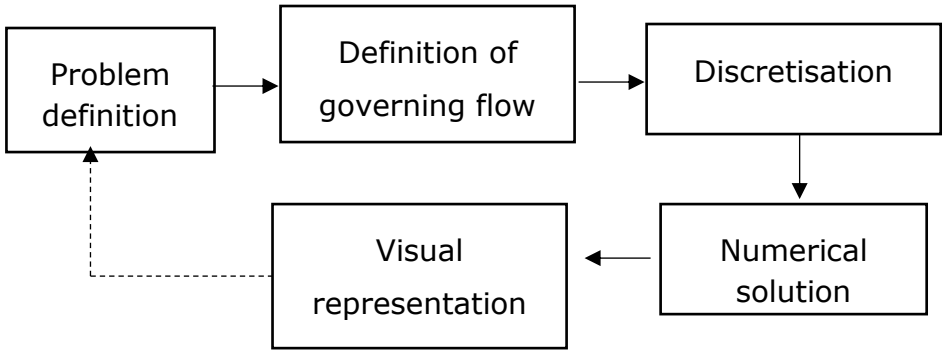



**Figure 2.5: High level view of the computational modelling process**

Following the problem definition, the steps taken to arrive at a flow solution can vary in their difficulty and assumptions are generally made during the definition of flow equations which are carried through the whole process. The results are often fed back into the definition for comparison purposes, making the modelling process an iterative one.

Once the problem has been defined, the flow is represented as a system of equations, namely the conservations of mass, momentum and energy. For a purely deterministic flow, such a system is said to fully define the flow in question. For a turbulent system however, the fluctuating component of the flow needs to be taken into account. Throughout this chapter the author has made reference to turbulent quantities which need to be measured or simulated in order to gain some understanding of the physical flow properties within a system. These quantities are all properties of the flow resulting from the 3D, time varying nature of the velocity field, $\mathbf{u}(x,t)$. The steady Navier Stokes equation, as shown in equation 2.3, governs the flow field of a system of constant properties.

$$\underbrace{\rho\left(\frac{\partial \boldsymbol{u}}{\partial t}+\boldsymbol{u}\cdot\nabla\boldsymbol{u}\right)}_{A}=\underbrace{-\nabla p}_{B}+\underbrace{\nabla\cdot\left(\mu(\nabla\boldsymbol{u}+(\nabla\boldsymbol{u})^{T})-\frac{2}{3}\mu(\nabla\cdot\mathbf{u})\boldsymbol{I}\right)}_{C}+\underbrace{\boldsymbol{F}}_{D}$$

**Equation 2.3: Navier-Stokes equation used to define the fluid motion of a system**

The terms in equation 2.3 are grouped to represent the following:

- A = Inertial forces
- B = Pressure forces

- C = Viscous forces
- D = External forces applied to the flow

To incorporate the turbulent perturbations into the equation, the Reynold's decomposition must be used (Ecke, 2005). The concept was first introduced in equation 2.1 for pressure, however it is used to decompose the velocity also. Using the Decomposition, a system of equations called the Reynolds Averaged Navier Stokes (RANS) equations is then used to give solutions to the flow definition formulas. The generation of the RANS equation leads to the formation of a component called the Reynolds Stress Tensor being added to the system. Equation 2.4 shows that the Reynolds stress is a time average of the product of both parts of the fluctuating velocity vector.

$$R_{i,j} = \overline{u_i' u_j'}$$

**Equation 2.4: Reynolds stress tensor**

The addition of this stress term results in a closure problem, whereby the number of unknown in the set of equations is greater than the number of governing equations and they cannot be solved unless extra information about the flow is provided (Pope, 2000). In order to obtain a solution to the flow describing RANS equations, the Reynolds stresses need to be determined in order to close the mathematical system. Turbulence models therefore contain a range of assumptions to allow the closure of the flow equations.

At present, the only way to provide a full flow solution is through Direct Numerical Simulation (DNS) (Ecke, 2005), however the computational power required to run such in depth calculations is not feasible on an industrial scale. Referring back to figure 2.5, following the flow describing equations, the problem of discretisation is faced.

The reason that DNS is so successful is that the size of the cells over which the RANS equations are solved is of the order of the smallest turbulent scale, the Kolmogorov scale. As a result, the computational power required is larger than any other method, and it increases rapidly with Reynolds number (Pope, 2000).

Computational models are often employed as an alternative to DNS to drive down the cost of simulation. The two main classes of model are turbulent-viscosity models, such as the k-ε model, and Reynolds-stress related models. When solving the former, transport equations for the turbulent quantities k and ε are used to derive values for the length and time scales based on the cascade theory of turbulent energy dissipation. The latter method provides solutions for individual Reynolds stresses found from RANS equation derivatives.

Both types of turbulence model require boundary conditions as inputs as well as validation data to support the flow assumptions made. As a result, hybrid CFD treatment methods are used to solve for turbulent quantities which can give variable results, often lacking in robustness (Tucker, 2013). The trend in turbomachinery CFD is tending towards a more modular system, whereby specific modes, relating to physical flow phenomena, can be activated and included in the model to give more realistic, bespoke solutions on a case-by case basis. In order for this method to be robust, improved measurement techniques for unsteady flow properties are essential so that the required activation modes can be applied based on experimentally derived physical flow properties. The measured time-resolved quantities such a Mach number and yaw and pitch angle can then be used as inputs to refine and validate the resulting model.

To improve computational estimates of turbulent flows, it can be seen that either the methods like DNS need to be employed or that 3D measurements of the fluctuating flow field need to be implemented to support existing CFD methods. As implementing more costly

simulation methods in an industrial setting is unfeasible, a much more robust method is to push for advancements in turbulence techniques.

### 2.5.2 Measurement of unsteady flows

The main requirements of a measurement system used for turbomachinery applications are given in this section. It is essential to understand these properties before individual measurement techniques are discussed in chapter 3.

Firstly, the frequency bandwidth and spatial resolution are two of the most important features of a measurement system for complex flows. In turbomachinery flows, the required bandwidth is specified by the blade passing frequency (BPF).

As Kupferschmied *et al* (2000) stated, the measurement system must have the capability to acquire the BPF and its first 3-5 blade passing frequencies in order to deduce small turbulent length scales and unsteady pressure fluctuations. This means that for an average BPF of 5 kHz, the technique would have to have a bandwidth of at least 10 kHz, according to the Nyquist theorem. In practice however, this would result in only 2 measurements in the blade passage per blade passing, therefore bandwidths of at least 50 kHz are usually desirable to improve measurement resolution. The presence of any measurement probe in the flow will lead to blockage effects, however with many techniques this intrusion is unavoidable. In order to reduce its effects, it is desirable to reduce the size of any physical probes to be present in the path of the flow.

In order to measure the rate of turbulent energy dissipation directly, it is required that the technique be able to resolve down to the Kolmogorov length scale in order to characterise the smallest turbulent eddies, from which the energy is dissipated. This is, at present, an impossible task even with current state of the art

techniques. Correction factors are therefore generally used to compensate for the lack of spatial resolution in most cases.

Other factors specific to turbomachinery applications are related to the access to the flow itself. For intrusive techniques this involves placing and then positioning a probe into the flow. For optical techniques this involves creating an optical window to view the flow as well as the seeding of the flow field itself (Kupferschmied *et al,* 2000).

The most popular methods have been constant temperature anemometry (CTA), multi-hole probes and laser Doppler velocimetry (LDV) as single point methods, where the velocity field is reconstructed from arrays of velocity values. Particle image velocimetry (PIV), a full field method, is used to visualise turbulent structures within complicated flow regimes. The potential issues that each of these methods face when used in a turbomachine is to be discussed in chapter 3.

## 2.6 Conclusions

It is essential to gain knowledge of the total dissipation of turbulent kinetic energy from most industrial processes as it counts for a significant amount of the total energy loss from the given system. It is often the norm to rely on computational fluid dynamics simulations to estimate this value, but these models generally over or underestimate the rate of energy loss, especially in particularly chaotic environments such as the wake of the last stage blade in turbomachinery rigs. For that reason, more robust and accurate experimental measurement techniques are required to bridge this gap in knowledge.

This chapter has outlined the way in which energy is lost from the most chaotic of turbomachinery flows via turbulence. The role that unsteady pressure plays in this dissipation of energy was also

discussed. The theory behind many CFD simulation techniques was introduced and the reasons for a combination of experimentation and computation being used in industry are given here. Chapter 3 gives more detail around the measurement techniques introduced in the previous section.

# Chapter 3: Developments in Turbomachinery Measurement Techniques

## 3.1 Introduction

The need for advancements in turbomachinery measurement techniques has been expressed in detail the previous chapter. The aim of this chapter is therefore to discuss the methods which have been used most commonly in industrial settings. Both optical and non-optical techniques are presented along with a discussion on their feasibility in being applied to chaotic turbomachinery flows. The emphasis of this chapter is on the trend towards fast response measurements to allow turbulent quantities to be deduced from the acquisition of long time series data taken at high sample rates.

## 3.2 Measurement techniques

The measurement of flow velocity was traditionally carried out using non-optical measurement tools such as hot-wire probes and pitot-static tubes. The intrusive nature of such techniques lead onto the development of optical measurement systems which do not disturb the flow field during their use. Intrusive methods are still much preferred in industry due to their high accuracy, ease of use and low cost, when compared with full scale optical systems. Such systems are usually employed in research settings as an aid to the advancement of industrial process. There are a vast number of optical measurement techniques which can yield velocity data from turbomachinery rigs including but not limited to Laser Doppler Anemometry (LDA) and Particle Image Velocimetry (PIV).

### 3.2.1 Laser Doppler Anemometry

Most optical techniques are particle-based (Tropea *et al, 2007*), which uses the presence of particles within a flow to scatter light from an external source. This light is then detected and processed in order to give accurate velocity data. There are certain conditions which need to be met in order to obtain reliable results, namely the size and dispersion of the particles. They need to be adequately small to ensure that they are entrained and follow the bulk flow of the system; although larger particles are able to scatter more laser light, giving a better quality signal. Therefore, one of the main issues with the design of optical experiments is ensuring a good compromise on particle size (Tropea *et al, 2007*).

Laser Doppler Anemometry (LDA), is a single point method for the measurement of velocity and turbulent quantities in up to three dimensions. A full velocity field can be reconstructed after all point measurements have been taken within a given volume. The operating principle is based on the Doppler Effect, which is used to measure the instantaneous velocities of the moving seeding particles. This velocity is measured by utilising the Doppler shift phenomenon, whereby the magnitude of the change in light frequency between the incident and the reflected light beams is directly related, to the seeding particle velocity.

A solid state laser beam is used for most optical techniques due to its temporal and spatial coherence which makes it ideal for the measurement of mechanical properties of fluids (Jensen, 2004). It is first split into two incident beams which, when crossed, form the measurement volume. The tracer particles then scatter light as they move through this this area, which is detected on a receiver such as a photodetector. When the two beams intersect, a fringe pattern with regular interval spacing is obtained by the interference of the beam wave fronts. This then leads to parallel lines which are alternatively

light and dark (Jensen, 2004). The experimental set up of such an LDA system is shown in figure 3.1. In most sophisticated systems, such as those used in industry and for research purposes, the transmitting optics consist of a Bragg cell which essentially splits the laser beam into two, and focusing lenses which ensure that the beams cross to form the measurement volume. The intensity of the light is modulated by the fringe pattern, and the light detected by the receiver contains information such as the Doppler shift in frequency which can be processed to give the velocity perpendicular to the crossed beams in the measurement volume (Dantec dynamics, 2017).

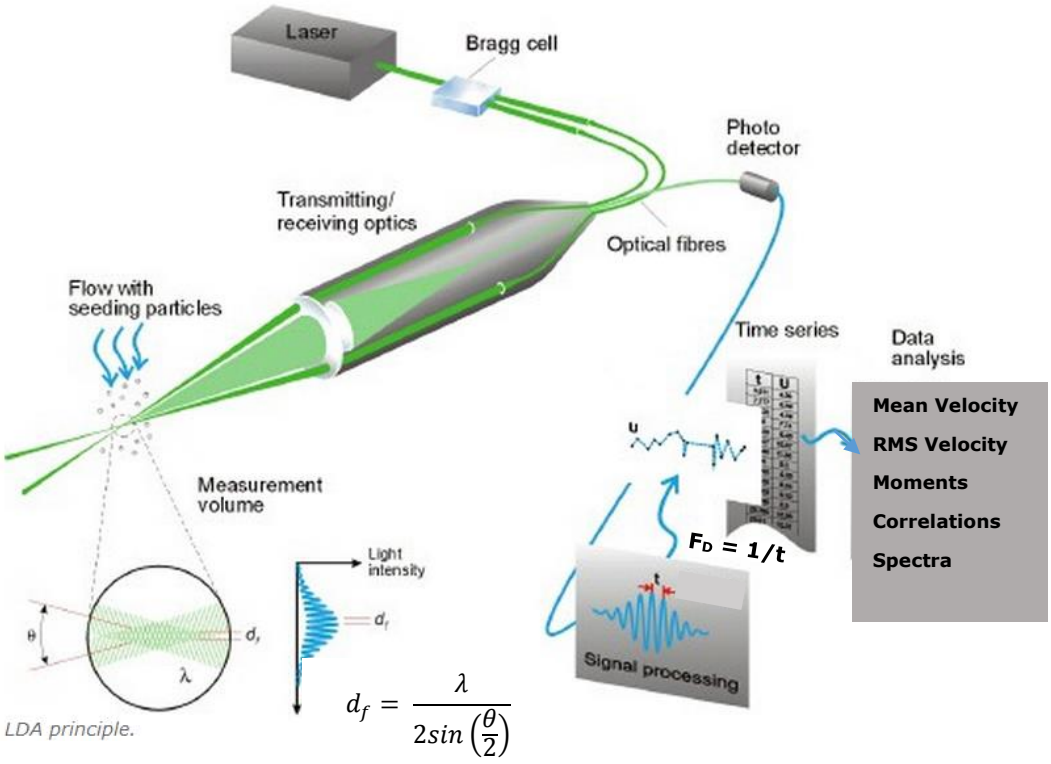



**Figure 3.1: Typical Laser Doppler Anemometry system, adapted from Dantec Dynamics, (2017)**

LDA is a good method of flow measurement, and it can be as accurate as the more intrusive method of hot wire anemometry. As with all optical methods, there is the inherent drawback that optical access and adequate seeding is required to obtain accurate results.

### 3.2.2 Particle Image Velocimetry

Particle Image Velocimetry (PIV) is an optical technique with the major advantage over LDA that it is a full-field technique and can visualise larger scale measurement areas in 2 and 3 dimensions at one point in time.

PIV has been used in the past to measure turbulence and TKE dissipation as a standalone method as well as for validation of hot wire and LDA measurement results (Saarenrinne and Piirto, 2000), (Saarenirinne *et al*, 2001). The principle of PIV is that the displacement of tracer particles with time gives the velocity of the flow. PIV can capture the full flow characteristics instantaneously, meaning that the coherent turbulent structures can be visualised at one point in time and analysed so that the full field turbulent effects can be viewed (Husted *et al*, 2009).

Figure 3.2 shows the typical set-up for a PIV system, with a double pulsed laser which allows a time delay of Δt between illuminations. Experimental PIV is not limited to the hardware shown in figure 3.2 and advances in this technique usually involve the improvement of individual subsystems. For example, stereoscopic PIV systems are used to obtain 3D flow visualisations using a similar setup to that shown but with two high speed cameras to capture the out of plane particle displacement (Sakakibara, 2007).

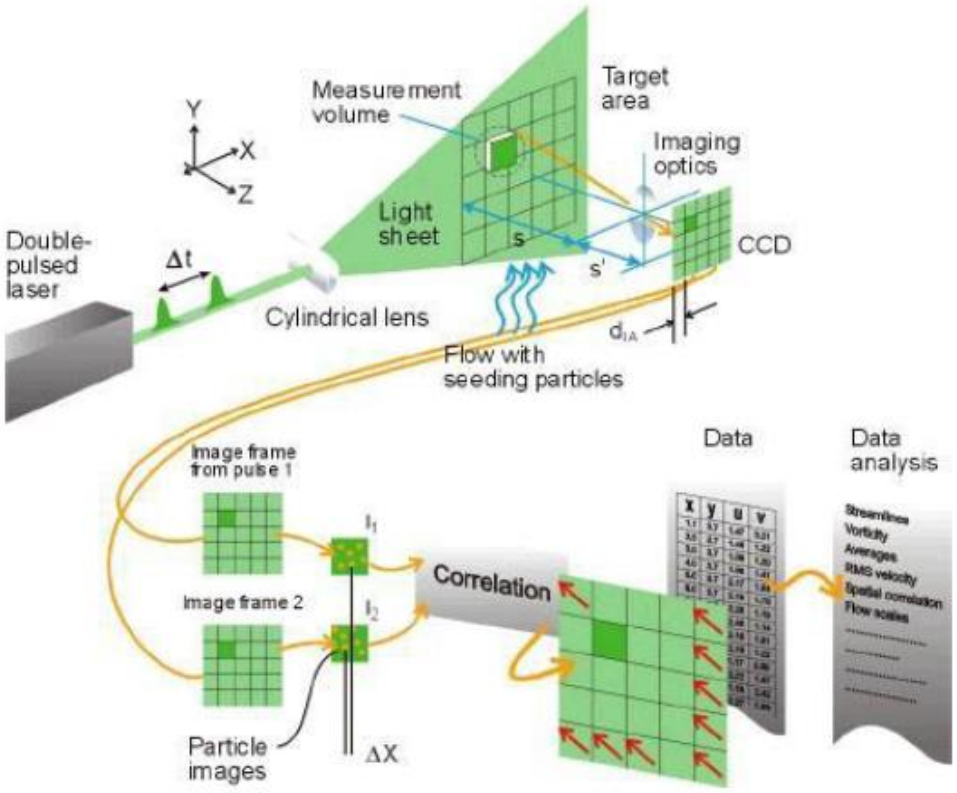



**Figure 3.2: PIV setup (Dantec, 2017)**

The main principle of PIV is the measurement of the degree of displacement of seeding particles which are used for flow visualisation. These markers usually consist of small particles, smoke or coloured dye and the distance which they are carried by the flow is measured over a time period and is used to determine the velocity. Particles in the flow are illuminated by pulses of light which are focused into a thin light sheet by a series of lenses. These then scatter the light which is detected by a high speed camera. Once the images have been taken, they are transferred to a computer for analysis. This is the most important and subsequently time consuming step in PIV, as it comprises the image-acquisition process which plays a role in the measurement accuracy and the spatial resolution of the images (Adrian, 1991). The cost incurred in obtaining high speed computers for this purpose, along with the double pulsed laser system often

limits this technique to research companies and universities as opposed to industrial use.

Another prevailing issue with PIV is the ability to seed the flow in an homogeneous and effective manner. At the high rotational speeds found within turbomachines, the flow rate at which the seeding material needs to be introduced into the rig is often too fast for the delivery system. This leads to inaccurate results due to clustering in the dispersion of seeding material. The problem lies with how to physically supply the tracer to the flow in question, allowing for homogeneous distribution as well as not causing any alteration in the flow characteristics. This process can be relatively simple for liquid flows as the tracer is usually chosen to be a solid particle which is easily mixed with the fluid to ensure homogeneity. It can be more difficult when it comes to gaseous flows however, as higher differences in densities between the observed flow and the seeding material can lead to varying degrees of velocity lag. It is therefore essential, as with the LDA system,that the particle to fluid density ratio is optimised (Jahanmiri, 2011). This process is often done practically by injecting the seeding particles into the gaseous flow before the test section, as solids can often form aggregates while travelling through the system and liquids can sometimes evaporate before reaching the measurement area, both of which can make it difficult to obtain accurate results.

Optical access can be another major issue when applying PIV to certain system, as the flow needs to be accessed from at least two directions; one to introduce the laser light and one to detect the scattered light. For 3D measurement systems, there needs to be two access points for light detection. This can be difficult in a closed system such as a turbomachine, which is why such optical methods have been best suited to purpose built turbine and compressor rigs with bespoke transparent viewing panels. The retrofitting of an optical measurement system such as PIV and LDA can often be too costly and impractical for industrial use.

### 3.2.3 Hot wire anemometry

Following on from optical techniques, more intrusive but cost-effective methods are discussed in the following sections. Hot wire anemometry has been used for decades to give accurate measurement of velocity fluctuations within a variety of different flow regimes and conditions. The most common mode of operation is constant temperature anemometry (CTA), which operates by keeping the probe temperature constant. As a fluid flows over the heated probe, usually a wire or thin film, it induces the probe to cool via forced convection, at a rate which is related to the velocity of the flow. The probe works via a Wheatstone bridge circuit, whereby the cooling rate is detected as a change in resistance across one half of the bridge. The bridge is then balanced by the compensating half of the resistor network and a proportional voltage is outputted from the probe as a measurable quantity relating directly to the velocity of the fluid. Four main types of hot wire sensors are shown in figure 3.3.

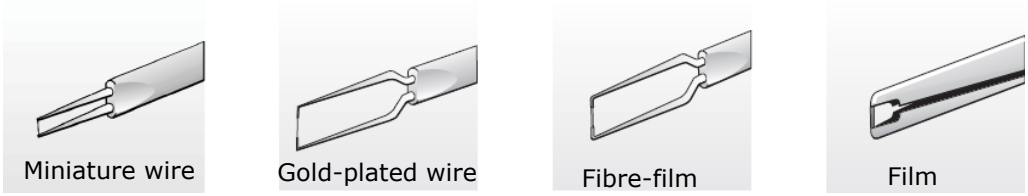



**Figure 3.3: Hot wire sensor types (JØrgensen, 2002)**

The probe sensor is made of a material whose electrical resistivity is sensitive to changes in temperature and usually consists of a thin wire around 0.5 – 5 μm in diameter and up to 2 mm in length, or a thin film deposited onto varying sizes of quartz cores (Tropea *et al, 2007*). Due to advances in electron microscopy and miniature printing techniques, more accurate sensors can be made with larger resistance ranges for use in a variety of applications.

There are many ways to arrange individual sensors which allow their use in many different types of flow. Table 3.1 shows the main features of some of these arrangements (Tropea *et al, 2007*).

| **Sensor arrangement** | **Main features** |
|---|---|
| Single wire or film | • Mainly used for small magnitudes of velocity fluctuations<br>• Can be used to measure the instantaneous velocity in one direction, which is made up of the mean and fluctuating velocity, if placed normal to the direction of the mean flow |
| Cross (x) wire | • Two sensors inclined to form an X<br>• The incline is often symmetrical relative to the U velocity direction with the angles formed by each wire being θ and −θ<br>• X wires used in 2D flows to obtain $u'_1$ and $u'_2$, but it can also be rotated to obtain $u'_3$ if required |
| Triple sensor | • This type of probe can measure the instantaneous velocity in three directions, from which the fluctuating and mean velocities can be deduced |

**Table 3.1: Overview of hot wire sensor arrangements and their main uses**

In order to take the required instantaneous 3D measurements of turbulence from a turbomachine, it can be seen from table 3.1 that at least three sensors are required. Due to the fragile nature of the hot wire probes, they are often unsuitable for harsh and chaotic turbomachinery environments. There are however some more advanced thermal anemometry techniques which can be used to overcome some of the issues relating to the fragile nature of standard hot wires. For example fibre film probes can be used to ensure that the measurements can be taken in contaminated or particularly harsh conditions. Such probes are much larger in thickness which leads to a decrease in its frequency response and most often, when film probes are manufactured to be large enough to withstand the chaotic

flow field, they are incapable of capturing the high frequency flow fluctuations which lead to turbulence measurements.

### 3.2.4 Pressure probes

Pressure probes can also be used for velocity measurements as an alternative to optical techniques. For the measurement of flow fields in turbomachinery, multi-hole probes are generally used with five or seven pneumatic holes (Gerner *et al,* 1984), (Ziliac, 1993), (Gonsalez and Arlington, 1996), (Crawford, 2011), although up to eighteen hole probes have been manufactured and used for some applications. As the flow in a rotating system such as a turbine can often include large variations and turbulent fluctuations, multi-hole pressure probes can be used to determine the flow direction as well as the static pressure and dynamic head (Tropea *et al,* 2007). Figure 3.4 shows the most common design of a five hole probe sliced longitudinally down the y-axis. There is one central stagnation pressure hole with the other 4 holes arranged around it in an axisymmetric fashion.

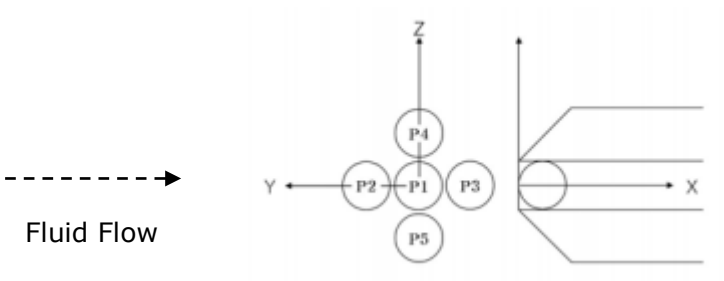



**Figure 3.4: Axisymmetric layout for a five-hole pressure probe**

The pressure probes are usually calibrated in a steady flow in relation to the yaw and pitch axis to ensure that the flow direction can be detected. This is known as an aerodynamic calibration, the principle of which is explained further in chapter 5. The pneumatic holes are extended to the end of the outer probe casing and are connected to

a manometer or digital pressure reader via rubber tubes to record the pressure from each tapping, P1 – P5. Although these types of probes have been used previously to measure the bulk velocity in turbulent flows within rotating machinery, there are some limitations on the accuracy of the recorded data in unsteady flows (Sieverding, 2000).

Rapid fluctuations in yaw angle and turbulence intensity can lead to serious limitations on the probe measurement accuracy. The long pneumatic tubing used with multi-hole probes acts as a dampener to the turbulent fluctuations, meaning that they are only able to give time averaged quantities with no turbulent information. More information the development of pneumatic pressure probes is given by Telionis (2009).

### 3.2.5 Application to turbomachinery rigs

The measurement of homogeneous turbulence has traditionally been carried out by hot wire anemometry, as a time series of velocity vector data can be obtained in up to 3 dimensions (Mohamed and LaRue, 1990). The hot wire technique has been well tried and tested and can be extremely accurate and easy to implement. It has therefore been used as validation for other measurement techniques such as multi-hole probes and optical methods such as Laser Doppler Anemometry and most recently, Particle Image Velocimetry.

There have been numerous investigations into the decay rate of turbulent kinetic energy within grid turbulence which use hot wire anemometry. There are many well established researchers with in the field including, Uberoni (1967), Tsinober (1992), George and Hussain (1991), Mohammed and LaRue (1990), Browne *et* al (1968) and Antonia *et* al (2003). In their paper, Mohamed and LaRue (1990) investigated the effect of initial conditions on the unknown decay exponent and coefficient in the decay power-law which describes the change in the variance in turbulent velocity values. They looked at grid turbulence, generated by aluminium mesh structures of different

rod diameters placed before the test section of a wind tunnel. The stream-wise turbulent velocity fluctuations were measured using a single hot wire orientated perpendicular to the main flow (Mohamed and LaRue, 1990).

Saarenrnne and Piirto (2000) investigated the reliability of PIV as a method for measuring the rate of energy dissipation within a given system. Their particle image velocimetry results compared well with those calculated using direct numerical solutions (DNS), showing that this computational method is a possibility for the future deduction of turbulent flow dynamics. Their experimental results suggest that certain parameters can greatly affect the accuracy of the turbulence measurements from the PIV method. These considerations include the spatial resolution which is controlled by the size of the area to be imaged during the experiments and the interrogation area during results analysis. In their paper, it was concluded that to obtain the most accurate results for the energy dissipation rate using PIV, the spatial resolution must be as close to the Kolmogorov length scale and the velocity measurement error must be as low as possible (Sarrenrinne and Piirto, 2000). It is however extremely difficult to take PIV measurements with spatial measurement resolutions as small as this scale. It is also just as challenging to create a hot wire probe with wire length comparable to the Kolmogorov scale in any type of flow. This notion is echoed by Elsner and Elsner (1996) in their paper on the topic of kinetic energy dissipation, where they express that there is a need for a wider experimental database comprising data for the finite spatial resolution of hot wire measurements in various flows, as well as for hot wire probes which can be described as sub miniature. Such probes have been used to measure the small scale turbulent motions in the inner boundary layer with typical length scales between 50μm and 3mm (Ligrani and Bradshaw, 1987).

Liberzon *et al* (2012) also investigated the use of PIV for the measurement of turbulent flows, within a boundary layer wind tunnel, by addressing the different assumptions which can be made about the

dissipation term in the turbulent kinetic energy budget. They came to the same conclusions as Saarenrnne and Piirto (2000) with regard to the factors affecting the accuracy of the dissipation rate estimate. They stated that these estimates were limited by the number of components measured during the experiments as more variables lead to a more reliable analysis of the dissipation rate. Although the PIV technique could potentially help to overcome some of the limitations due to its characteristic full field measurements and ability to alter the measurement volume within the flow, it is still not possible to measure directly the smallest scale velocity derivatives which would give the most accurate estimate of the dissipation rate. PIV measurements can resolve down to the smallest eddy length scale in theory, but practically this would lead to so much noise contamination that the results may not be easily deciphered. Saarenrnne and Piirto (2000) estimated the Kolvogorov length scale, which corresponds to the smallest eddy size, as being between 20 and 65 μm. The particle size used was 5 μm, meaning that the smallest scale could theoretically be resolved. The PIV system however has a resolution of around 100 μm due to the size of the viewing area and the computational procedure used to analyse the images.

Dissipation rate surrogates are used for estimation purposes, no matter which technique is used for the raw velocity measurements. The majority of measurement errors occur around low turbulence flows where the effect of viscous stresses is often not estimated properly and also when the anisotropy of the flow system is disregarded. The latter issue is a common error when the flow is not tested for characteristics such as local and global isotropy as well as homogeneity. These testing procedures are described by Mohammed and LaRue in their 1990 paper. As these errors are likely to occur, corrections must be made in shear flows which are generally non-isotropic and inhomogeneous (Liberzon *et al*, 2012).

Liberzon *et* al (2012) describe the three main approaches which have been identified as ways of estimating the dissipation rate from the

measurement of velocity vectors within the flow. The first two, which are most suited to non-optical methods such as thermal anemometry, are the time series analysis, whereby a high data sampling rate is employed in order to relate the time series results to a power spectrum of turbulent kinetic energy, and the spatial correction approach. The latter method consists of using two probes placed with known distances between them a correlation function is evaluated between the two probes for each distance used. This correlation is then translated to a power spectrum, from which the spectrum of the dissipation rate is found. The third and most commonly used approach in hot wire measurements is the spatial velocity derivative method. This technique was prominently used by Bowne *et al* (1987) where two or more probes were used to calculate the required spatial velocity derivatives directly which can be related to the rate of energy dissipation. Liberzon (2012) found that the decay rate method and direct measurement of the velocity derivatives gave similar results in their grid turbulence measurement and they found the main source of error in their analysis methods was not correcting for inhomogeneity in the flow.

Elsner and Elsner (1996) suggest that developments in the measurement of turbulence need to come from two sources. The first being the need to develop more advanced techniques which will allow for the smallest scales to be resolved effectively in chaotic, turbulent flows where hot wire anemometry is not robust enough and the latter being the need for a fundamental increase in understanding of turbulence by widening the experimental database concerning the measurement of complex flow velocity.

It can be concluded that the most tried and tested methods of turbulence deduction, PIV and Hot Wire Anemometry, are unsuitable for use in a turbomachine. Optical access is the biggest problem when it comes to retrofitting optical measurement systems into turbomachinery. The more intrusive hot wire anemometry is much cheaper to implement and has a fast enough frequency response to

allow the taking of instantaneous velocity measurements. They are, however, too fragile for use in the chaotic flows found in turbomachines. Multi-hole pitot pressure probes are implemented to characterise the velocity field as a compromise between frequency response and robustness. Due to the attenuation of the pressure signal through the pneumatic tubing connecting the flow field to the transducers, only time averaged information can be measured using pitot probes. Fast response pressure probes are therefore in demand across the industry which can combine robustness with the ability to take long time series' measurements with a high frequency response.

## 3.3 Fast response measurement techniques

The rapid advancement of fast response pressure transducers in the 1960's is often associated with the increase in development of silicon semi-conductor technology (Ainsworth, 2000). Since then, development has continued and the sensors have evolved into miniature pressure transducers of the order of 1mm. The ability to measure unsteady flow quantities with these miniature fast response sensors prompted the design of fast response aerodynamic probes (FRAP). Sieverding *et al,* (2000) reviewed the methods of measuring unsteadiness within turbomachines and found that designs have advanced since the review in 2000, even the most recent research has been based upon the ideas put forward in the paper 'Measurement techniques for unsteady flows in turbomachines'.

### 3.3.1 Type of sensor

A system which can measure unsteady quantities such as pressure in a dynamic manner has many requirements. The probe must have pressure transducers which are suitable for the type of flow environment to which they are being exposed. They must also have a fast enough response time to be able to capture the frequencies of

interest within the flow. Traditional pressure transducers, which contain metal strain gauges are not suitable for acquiring unsteady data as they are often too large and have relatively low frequency responses (Kulite, 2017).

Fast response pressure sensors are therefore currently used for the capture of unsteady flow phenomena as they are quite small and can easily be mounted into blades, onto turbine casings and into measurement probes for increased temporal resolution.

There are two types of fast response pressure sensors commercially available, those being piezoresistive and piezoelectric transducers. The latter is preferred due to its ability to be miniaturised, its sensitivity and accurate measurement of the DC component of the pressure. A piezoresistive sensor is a full bridge sensor which consists of a diaphragm which is formed on to a silicon substrate which bends when pressure is applied to it. The resultant change in diaphragm structure leads to a change in the resistivity of the material and an output voltage, which is proportional to the initial pressure, supplied from the sensor. This change is due to the Wheatstone bridge circuit in which the stain gauges are arranged to make the full bridge sensor, as shown in figure 3.5.

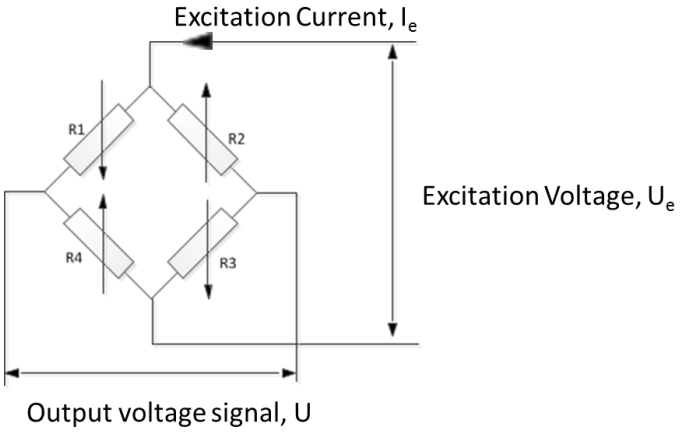



**Figure 3.5: Wheatstone bridge circuitry**

The bridge consists of four resistors which, when positioned as shown in figure 3.5 on to the membrane, will respond to the bending of the sensor diaphragm upwards or downwards due to positive or negative pressure fields respectively. As shown in the diagram, two resistors (R1 and R3) will report a decrease in resistance and two (R2 and R4) will give an increase in resistance when a positive pressure is applied to the sensor. The resistance across the bridge should be balanced as the combined increase in R2 and R4 should be of the same magnitude as that of R1 and R3. In this case, the relation between the output signal and the resistance change is given by equation 3.1.

$$\Delta U = \frac{\Delta R}{R} x\, U_e$$

**Equation 3.1: Wheatstone bridge output relationship**

Where R is the ratio between the input excitation voltage over the excitation current. This change in output voltage $(\Delta U)$ can then be related directly to pressure through calibration of the sensor.

### 3.3.2 Resolution and frequency response

The frequency response time of pressure transducers is a key consideration when taking unsteady measurements. Traditionally pneumatic pressure probes have been used within turbomachines, but they can only offer time averaged measurements. In order to gain an insight into the fast changes in flow properties, the frequency response needs to be fast enough so that little to no information is lost during transmission from the measuring point to the transducer. With traditional probes, the pneumatic coupling between the two is relatively long so when the pressure is detected by the transducer, the data reading is an averaged value. Flush mounting of a miniature sensor on to a surface or the tip of a measurement probe can therefore minimise the distance that the pressure wave has to travel, reducing any attenuation and increasing the temporal resolution of the measurement.

## 3.4 Application to turbomachinery

Many researchers have attempted to improve the frequency response of traditional pneumatic pressure probes by embedding the transducer into the probe tip. This comes at a cost to spatial resolution of the measurements as the size of the probe will inevitably be increased. Although there are many individual researchers who have successfully miniaturised fast response pressure probes (Ligrani *et al,* 1989) and (Zilliac, 1993), (Georgiou, 2014) there seem to be two main research groups looking into the topic. These are the Von Karman Institute in Belgium (Mersinligil, 2012), (Mersinligil, 2013), and the ETH lab in Switzerland (Lenherr, 2010), (Behr, 2007), (Mansour, 2008).

Many researchers including Tanaka *et al* (2002) and Schlienger *et al* (2002), have implemented a single pressure sensor into the tip of a probe to obtain dynamic information, with a very small diameters of

around 2mm. Their instrumentation, which had a 125 mV pressure sensitivity over the full scale pressure range of 34.5kPa, was used in unsteady turbomachinery flows at blade passing frequencies of up to 2kHz. Tanaka *et al* (2002) have looked at different probe geometries for yaw and pitch sensitivity when taking three dimensional measurements in a single stage compressor. The problem with single sensor probes is that they only offer measurements in one dimension at one time. They can also be used as pseudo 2D probes though a virtual measurement technique as used by Schlienger *et al* (2002), however for turbulence measurements, all dimensions must be measured at the same point in time. The main aim when miniaturising pressure probes is to obtain the most information possible with the smallest probe diameter. This is quite challenging as the smaller the measurement volume, the more difficult it usually is to obtain three dimensional flow information. The use of a single sensor which can be rotated to obtain 3D measurements is a promising technique for this task. Schlienger *et al* (2002) working at the ETH lab in Zurich have tested this type of probe and developed an adapted aerodynamic calibration procedure. They looked into different probe geometries and angles for the pressure tap to obtain the most optimised design for their application as well as the accuracy of the calibration method. They used the single sensor in 3D or ' virtual 5 sensor' mode, meaning that the probe was rotated to five positions at each measurement point to simulate the effect of acquiring data from 5 sensors at each point in space. It was found that the calibration procedure gave results comparable with other results for 5 sensor probes but when it came to detecting changes in pitch angle, the probe did not yield accurate data. This suggests that the probe used in virtual 5 sensor mode is best suited for two dimensional flows.

Virtual multi-hole probes often use averaging techniques to build up a multi-dimensional image using 1D measurements, thus missing the instantaneous nature of the fluctuating flow component. Figure 3.3 shows the capabilities and calibration requirements of pressure probes with differing numbers of sensors.

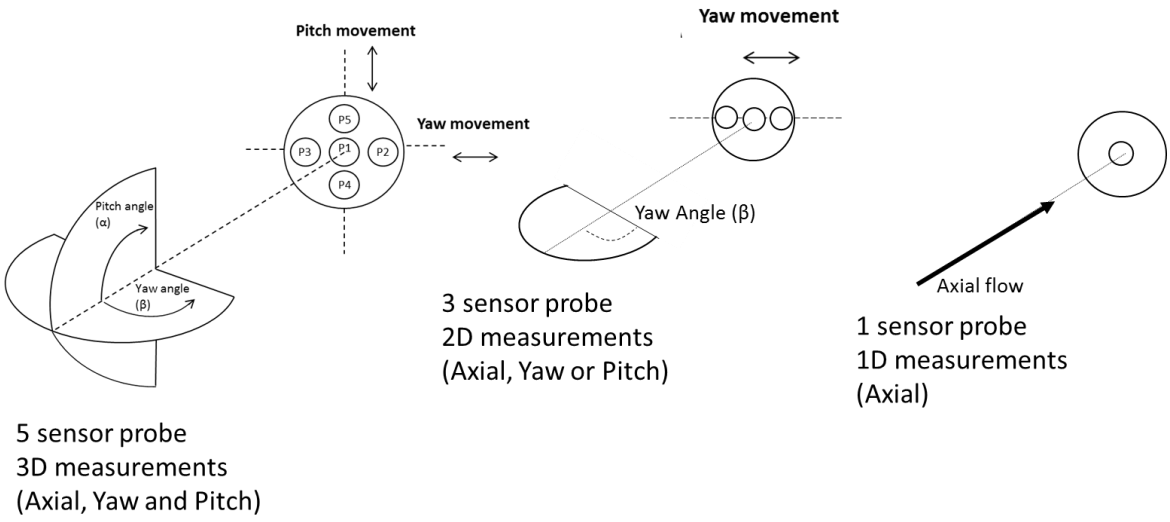



**Figure 3.6: Capabilities of fast response probes based on their number of sensors**

It can be seen that the only option for taking 3D measurements at one point in time is through the use of a probe with more than 3 sensors. Multi-hole probes with fast response pressure transducers in their tips are therefore an ideal solution for resolving 3-D velocity and pressure fluctuations in turbulent flow regimes. They do however have the disadvantage of being relatively large when compared to both pneumatic multi-hole probes and single or two-sensor fast response probes.

Sieverding *et al* (2003) from the Von Karman institute have been looking into vortex shedding from the trailing edge of turbine blades, with the flow being created using a cascade rig. They used a multi-head pressure/temperature fork probe which consisted of individual probes for the measurement of both time averaged and time resolved flow information. Their measurement system, which was used for

carrying out blade wake traverses, consisted of a Kiel head total pressure probe and a thermocouple for taking time averaged measurements as well as a fast response total pressure Kulite probe and a cold wire for measuring time resolved pressure and temperature within the flow. The total pressure probe is implemented with a Kutlie fast response sensor so that the shedding frequency of the Von Karman vortices could be captured. It was concluded that for pressure measurements, the fast response probe was able to capture dynamic changes in total pressure within in the wake, including a pressure minimum which was identified in the middle of the wake and assumed to be in the centre of the vortices being shed. It was also found that the cold wire probe, used for obtaining fast response temperature data, was too fragile for the high Reynolds number, high Mach number environment within the cascade rig. Members of the Von Karman institute have also used a cylindrical probe with a flush mounted pressure sensor to look into the entropy generation, which is one measure of energy and subsequently energy loss, between blade rows in an axial compressor. Mansour et al (2008) measured entropy generation by embedding a fast response single sensor and a pair of thin film gauges into a probe which measured pressure and temperature simultaneously. It is apparent that single and two-sensor probes are not capable of obtaining 3D measurements without phase averaging. Where 3D measurements have been taken in the literature, there has been some element of phase averaging using 'Virtual 5 sensor' techniques which can lead to data loss as time traces are superimposed onto each other. There is therefore a need for a fast response sensor which can give time resolved data in 3 dimensions simultaneously.

## 3.5 The Kulite FAP-250 probe tip

A fast response five sensor probe tip is proposed as a method of taking fast response, 3D measurements of unsteady pressure. The

probe takes the shape of a traditional 5-hole probe, as shown in figure 3.4, however the sensors are flush-mounted into the probe tip to maximise frequency response.

The sensors themselves can achieve a frequency response of up to 100 kHz which is much higher than traditional wire bonded sensors. Such sensors use Kulite's leadless technology which eliminates the problematic connection between transducer layers. The fine gold wires usually used to connect the sensor chip to the header pins are not required in the leadless sensors, meaning that faults relating to the breakage of these connectors are eliminated. This makes them more robust and more suitable for use in turbomachinery applications. The leadless pressure sensor is shown in figure 3.7.

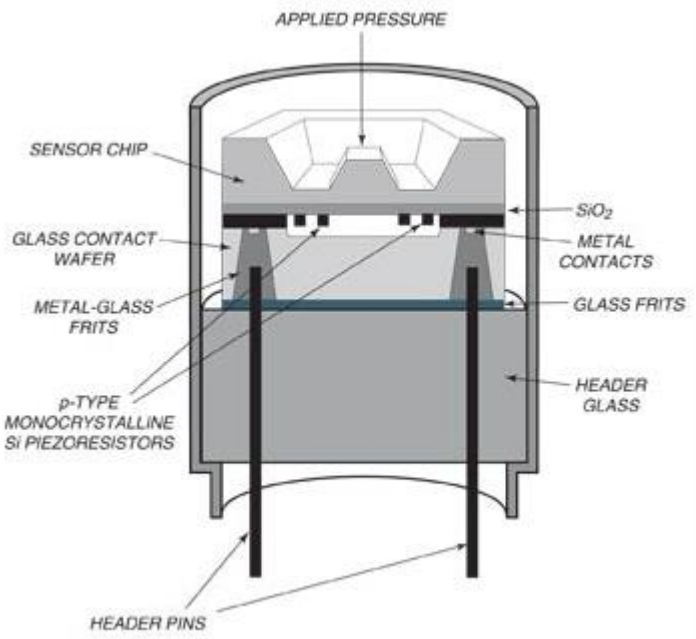



**Figure 3.7: Kulite leadless pressure transducer technology (Kulite, 2017)**

The Kulite Flow Angle Probe (FAP) 250 head contains five fast response pressure sensors surface mounted at the tip in a cross formation. The transducers themselves are 15 psi (1 bar) absolute sensors, meaning that they are full bridge sensors, with the ability to work in environments of up to twice that rating with confidence in the

static calibration. Figure 3.8 shows the orientation of the sensors in the cross formation. Each of the sensors are protected by a mesh filter and a metal screen.

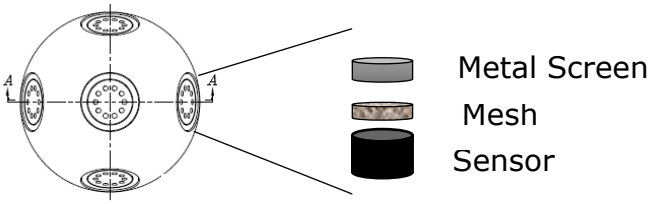



**Figure 3.8: CAD drawing of the Kulite FAP 250 transducer with birds eye view. The transducer is to be embedded into a probe stem to be used as a 5 Sensor pressure probe.**

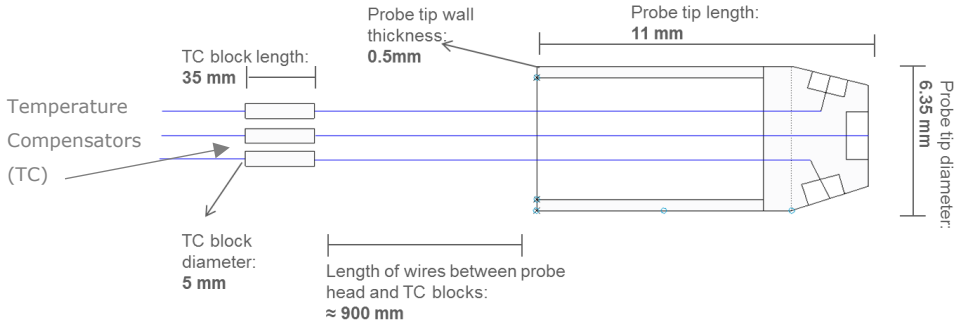
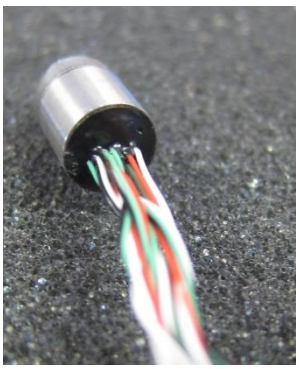



**Figure: 3.9: Schematic drawing of a slice through the centreline of the FAP 250 probe head with actual dimensions measured upon delivery of the sensor tip**

Figure 3.9 gives a schematic drawing of the FAP 250 probe head with measured dimensions taken from the delivered probe head. As shown in figure 3.9, the temperature compensation modules are included in the circuitry of the probe. Each sensor has its own compensator which acts to regulate the output voltage spike caused by changes in the temperature of the test environment. The compensating resistors are spliced into the wiring of the sensors outside of the probe head, however the resistors used in the compensation modules serve to

correct the output voltage of the sensors only and are not connected into the 4-resistor Wheatstone bridge directly. The modules contain resistors, the rating of which is chosen by the manufacturer during their calibration process for each sensor, and they are housed in cylindrical casings made of hard, inflexible plastic. Four leads were attached to each of the sensors for the inputs and outputs of the Wheatstone bride, making 20 36 AWG wires which were secured at the back of the probe using silicone, which can be seen in Figure 3.10. More information on the probe head is given in the Kulite FAP-250 specification sheet in appendix 10.



| Wire | Designation |
|---|---|
| Red | + input |
| Black | - input |
| White | + output |
| Green | - output |

**Figure 3.10: Back of FAP-250 probe head with silicone sealant securing 20 sensor leads, with table denoting the role of each coloured wire in the probes circuitry**

## 3.6 Conclusions

Tried and tested fluid measurement techniques have been presented along with an assessment of their feasibility to turbomachinery applications. It was established that the ability to acquire long time series data whilst withstanding the harsh environments found within such rig was essential. Traditional methods such as hot wire anemometry, pitot probes and PIV often fall short of such

requirements in full scale industrial test rigs. In order to obtain advanced measurements within turbomachinery rigs, instantaneous 3D data is essential and no method is currently available to deliver such results. The following chapters aim to present a new measurement system with the capabilities to withstand the chaotic flows within a compressor rig whilst delivering unsteady flow data in 3 dimensions.

# Chapter 4: Probe stem design

## 4.1 Introduction

The need for unsteady pressure measurements was presented in chapter 3 along with an introduction to the working principle of the Kutlie FAP-250 sensor head. This chapter aims to discuss the design of the assembled five sensor probe, henceforth referred to as the 5S probe, including bespoke stem body designs and the method of attachment used. The equipment supplied by the manufacturer consisted of the sensor head only with no provision for the attachment of the head to a probe for measurement or calibration. As a result, tailored solutions were designed and implemented so that the sensor head could be used as a fully functioning probe. Key challenges faced during this design phase are addressed in this chapter along with solutions to each problem faced.

Three stems were constructed corresponding to potential applications which are discussed in this chapter. Probe stem α was used initially for calibration of the five-sensor head, while the two other stems, β and γ, were designed for use in the low pressure turbine rig and compressor rig respectively.

## 4.2 Key challenges

The implementation of the Kulite-250 probe tip into a fully developed probe brought about some key challenges which are addressed throughout this chapter. The calibration process is time consuming and the opportunity was taken to design multiple probe stems so that the probe head could be calibrated initially and separately from the final application. As the probe head was also an expensive purchase, it was advantageous to allow for its initial calibration in a bespoke stem and changing the probe geometry to that specific to the final application. This means that the research cost was reduced by having

interchangeable stems as opposed to the buying of multiple sensor heads.

### 4.2.1 Low Pressure steam turbine rig application

The Low Pressure (LP) steam turbine model test rig is a 1/10$^{th}$ scale single stage model. The model uses a mixture of ~93% R134a refrigerant gas with air as a working fluid, to achieve Mach number and Reynold's number similitude. Operating purely on air, similitude is not achieved, due to the high rotational frequency required.

During the course of the research, the sponsor company underwent a critical upgrade of their facilities which included the temporary decommissioning of the transonic nozzle used for calibration in R134a. The fabrication of a dedicated facility was deemed out of the scope of the project and there was therefore no method for calibration of the probe in the refrigerant gas. It was however, a key research objective for the 5 sensor fast response head to be assembled as a functioning probe to be used for the measurement of unsteady pressure at the last stage blade of the LP turbine rig. A bespoke probe stem was therefore designed for this application which is to be used by the sponsor company on the LP model turbine rig once the calibration facility is re-commissioned, and a calibration in the refrigerant gas is performed.

### 4.2.2 Compressor Rig

The compressor also posed a challenge in that the rig required some essential adaptations before it could become a feasible application for the 5S probe. In order to take measurements at various positions after the last stage blade, the probe needed to be inserted from outside of the rig. As there was no access through the outer casing a method of inserting and moving the probe in relation to the

compressor blades was designed and implemented, to be discussed in section 5.3

Table 4.1 below outlines all of the challenges faced during the design and summarises the solutions carried out for each problem.

| Design stage | Challenges faced | Solution | Section |
|---|---|---|---|
| Attaching the sensor head to any designed stem body | Methods such as laser welding and chemical bonding were deemed too harsh and permanent for the given application | A bespoke coupling piece was designed to allow temporary attachment without putting stress onto the sensor head | 4.3 |
| Removing and re-soldering temperature compensation modules during assembly | Modules became damaged beyond repair during assembly trials | New resistor networks were manufactured in-house to account for drifting temperatures | 4.4 |
| Design of stem $\alpha$: For use with Air Jet Rig | Sensor tip needed to be calibrated using the Air jet rig. Traverse mechanism on rig imposed a 10mm OD limit on the probe. | A swan neck probe stem was fabricated | 4.5.1 |
| Design of stem $\beta$: For use with Low Pressure turbine rig | Rig was designed with a hub flare angle larger than the acceptance angle of the probe.<br>Strict access requirements for probes to be inserted into the traverse gear attached to the rig | Bespoke stem designed to allow probe to be angled towards the exiting flow while still complying with the outer diameter limit imposed by the rig access hole. | 4.5.2 |
| Design for stem $\gamma$: For use with Compressor rig | No access points for probe insertion.<br>The probe needed a $90^0$ bend to face the flow field when inserted from outside the rig casing | Rig casing was adapted to allow testing with the probe.<br>The probe stem and method of access to the flow were designed to allow testing. | 4.5.3 |

**Table 4.1: Summary of challenges faced during the design of the 5S probe**

## 4.3 Probe attachment methods

As the sensor head was acquired as a standalone piece of instrumentation, a method of attaching it to a stem was required as well as the design of the stem itself. In an attempt to avoid increasing the diameter of the probe, methods which would allow the sensor head to be attached flush with the stem were first investigated. A series of laser welding investigations was carried out on test pieces of the same wall thickness and diameter as the sensor head to assess the applicability of the technique. As the surface area for gluing was too small to guarantee safe attachment, a sleeve was also designed and demonstrated on the Stem β design as shown in section 4.4.3.To allow calibration of the sensor head independently of the final test application, a non-permanent solution was required to allow interchangeability of the stems. Therefore a coupling piece, which evolved from the sleeve design, was fabricated and used throughout the calibration and final stage testing.

### 4.3.1 Laser welding test

Laser welding, which involved creating a welded seam between the two pieces with a precision laser was first investigated. The test was carried out in several steps in order to assess the capabilities of the 2000 Watt IPG fibre laser system which was available at the University of Nottingham. The stepwise test procedure is given in figure 4.1.

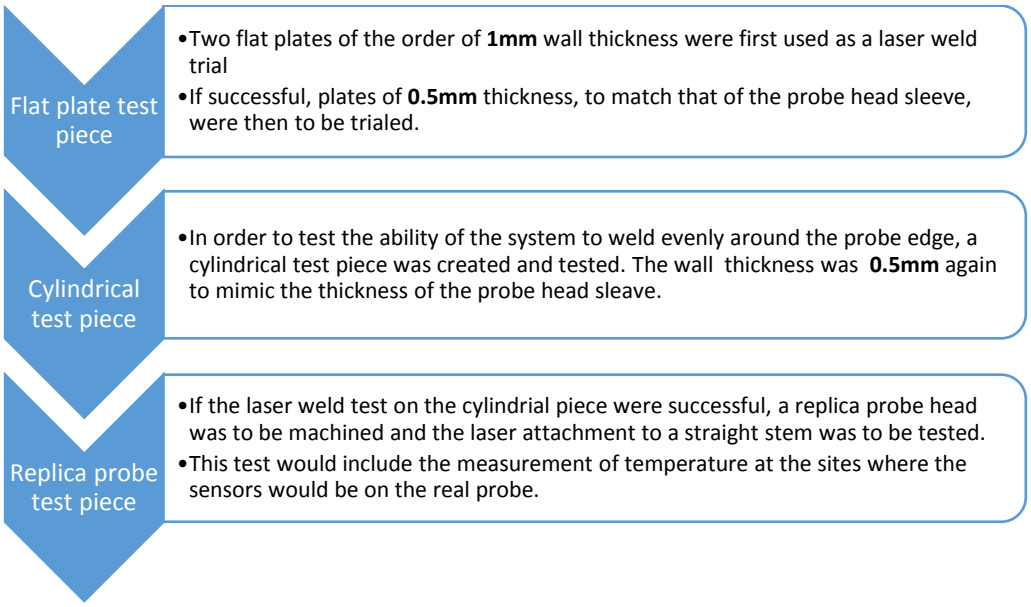



**Figure 4.1: Step-wise procedure followed to assess the laser welding method in its applicability to attaching the probe tip to a designed stem**

Figure 4.1 shows the progression of the planned testing for the laser welding trial. The commencement of many of the tests was dependant on the passing of the previous trial and the criteria by which the success of the tests was measured were purely qualitative and no experimental characterisation of the welds was carried out at this stage in the investigation. The test specimens had to be successfully attached without any damage to either piece in order to pass the visual inspection.

Figure 4.2 shows the test piece resulting from the welding of two pieces of 1mm thick flat stainless steel plate. After visual inspection it was decided that the test had failed and it would not have been useful to run the test with the smaller diameter specimen.



**Figure 4.2: Results of the first laser welding test. Two stainless steel plates of thickness 1mm were used**

It can be seen that although the pieces themselves had been joined together, both sides of the weld have become burned and buckled as the laser proved to be too powerful for the test.

Although the laser used was proven too be too powerful, a cylindrical test piece was also trialled to see how capable the system was at tackling a geometry similar to the probe head. Unfortunately, as shown in figure 4.7, the laser was unable to weld the 0.5mm thick tube and the edges of the specimen were again singed and buckled. During this test the pieces were not successfully welded together as shown below.



**Figure 4.3: Cylindrical test pieces used in the second phase of the laser weld testing. The pieces were not successfully welded and they were damaged during the trial**

Kovacs (2017) outlines the major parameters which need to be optimised for successful laser welding. The main variables, which alter the size of the heat affected zone (HAZ) were found to be laser power density, heating time and the type of laser used. Although laser welding produces a thin HAZ compared to traditional welding techniques, the control of the welding parameters is still being perfected in the industry.

Windmann et al (2017) investigated the laser welding process on a range of metals, including stainless steel and steel-aluminium hybrids. They found that in cases where the sample had failed during testing, a decrease in hardness in the HAZ was to the cause. They concluded that the size of the HAZ and the subsequent reduction in material hardness was attributed to the laser energy. The weld effectiveness is a balance between having enough heating energy from the laser power and not causing an increase in the HAZ (Bhattacharya et. al, 2018). If a less powerful laser were available during this investigation, an optimum power density and heating time compromise may have been established to allow the 5S probe to be laser welded. Further testing would need to be carried out to establish how the HAZ changes under different conditions due to the proximity of the weld to the heat-sensitive pressure sensors in the probe tip.

The purpose of the two tests with results shown in Figures 4.2 and 4.3 was to investigate how feasible it was to create a laser weld with the given geometry of the probe. The next phase of testing was to create a replica probe tip made of stainless steel and of wall thickness 0.5mm and a straight probe stem of the same criteria. As the initial laser welding testing provided negative results, it was concluded that other attachment methods needed to be explored.

### 4.3.2 Other attachment methods

Other methods of attachment were considered such as gluing and spot welding. The former was disregarded due to the relatively small surface area on which to glue the pieces together, as well as the risk of contamination of the sensors with adhesives. It was also decided that the latter method was unsuitable as an attachment method due to the high temperatures required near the sensors of the probe. All options considered which permanently attached the probe tip to the stem were

deemed too intensive for use around the sensors and therefore undesirable.

In order to calibrate and use the probe in an industrial style rig, it was decided that the probe be disassembled and the stems changed between tests. As the final application was unknown at the time of calibration, the sponsor company required a calibrated sensor head which could be applied to a range of test rigs. Due to the high cost of the FAP-250 sensor heads and the time incurred by the calibration procedure, one head was obtained and calibrated to cover a range of applications for the sponsor company. A versatile stem could have been designed which would allow for both calibration and rig testing without the need to change stems between the two, however due to rigid geometric constraints on all available test rigs, an interchangeable attachment method was to be used. A probe stem was then designed for each potential application of the 5S probe along with a coupling to allow flexibility in the probe geometry.

### 4.3.3 Coupling piece

In order to ensure that the probe head be safely and interchangeably attached to a designated stem, an attachment piece was designed. This enabled the probe tip to be fixed into the adapter using grub screws and for the respective stem to be attached and removed while reducing the risk of damage to the instrumentation. The design schematic for a straight stemmed probe is shown in figure 4.4, with the sensor head attached to a straight stem.

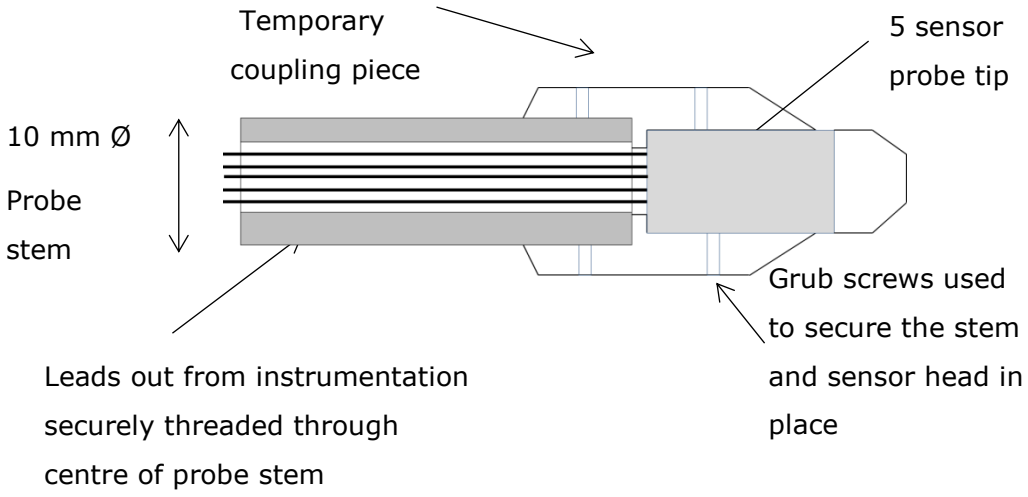



**Figure 4.4: Probe coupling concept demonstrated using a straight stem**

The coupling piece did increase the diameter of the probe tip from 6.25 to 14mm, a problem that was tackled by adding a ramp into the design to negate the effects of a sudden step in the flow around the probe. In order to assess the effect of the increased diameter on the pressure distribution around the probe head, the yaw calibration results were compared to that of an independent study from the Massachusetts Institute of Technology. This comparison is discussed along with the calibration results in chapter 6.

## 4.4 Temperature compensation module considerations

As shown in Figure 3.9, the sensors contain temperature compensation modules in their circuitry, the purpose of which was to adjust the voltage output when the probe was subject to drifts in atmospheric temperatures. More details surrounding the working principle of these compensators is given in Chapter 5, where results from experimental investigations into their operation are given. With regards to the design phase, the biggest challenge was related to the logistics involved in the

assembly of the probe with any of the designed stems. An example was made of stem α, the swan neck stem, because it was the first stem in which the sensor head was installed as well as the most complicated in terms of assembly due to its double bend. Attempts were made to assemble the probe with the compensators inside the stem to ensure their safety during testing. It was considered to bundle the compensators so that they could be slid down the inside of the stem. Schematics are shown in Figure 4.5 which address the required outer diameter for 4 or 5 compensators to be assembled in this way. In the example with 4 compensators, the first module was to be placed inside the stem before the bundle of 4, to reduce the overall diameter. In this case, the compensation module for sensor 1 is placed into the stem first and the bundle of 4 is then placed behind the first one. Figure 4.5 illustrates that the outer diameter required is 30% larger than the required 10 mm OD; a restriction imposed due to the access requirements of the yawing traverse system to be introduced in section 4.5.1.

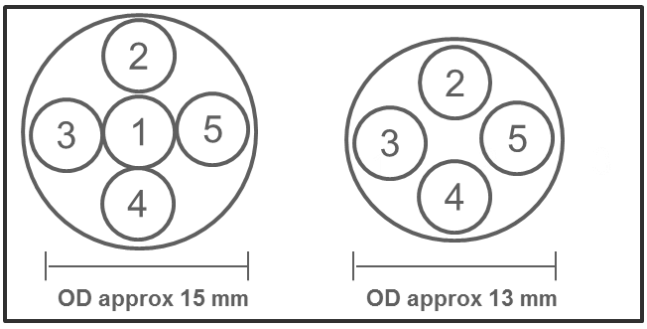
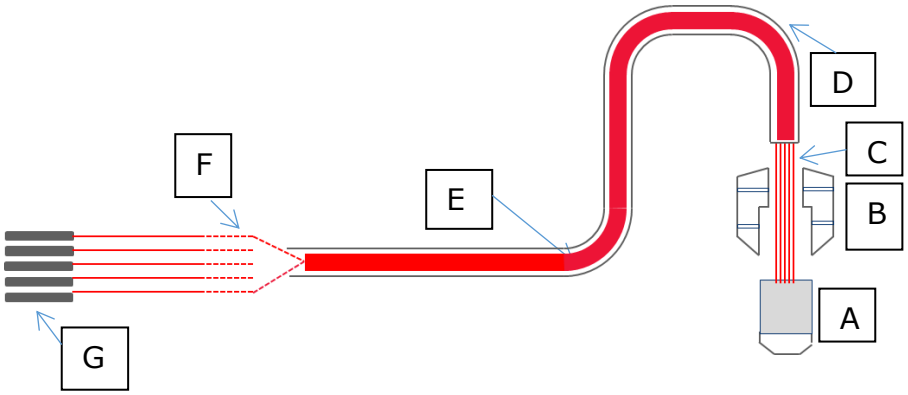



**Figure 4.5: Potential configurations for the placement of the temperature compensation modules inside of probe stem**

Housing the modules within the stem was found to be unfeasible, not only due to the larger diameter requirements which would be imposed on the stem, but also due to the length of the compensators themselves. With 35mm of solid plastic casing around the modules, it would have

been impossible to thread them through the internal geometry of any of the designed stems. They were therefore intended to be spliced from the senor head during probe assembly and soldered back into the circuitry when the tip was secured into the stem.

An expanded diagram of the probe assembly is given in figure 4.6 which shows the path of the wiring from the sensor head through to the compensation modules.




| Letter on diagram | Description |
|---|---|
| A | FAP-250 probe tip |
| B | Bespoke coupling piece |
| C | Internal wiring; 20 wires (4 per sensor) |
| D | Swan neck probe stem |
| E | Internal wiring thread through probe stem |
| F | Spliced wiring to allow detachment of temperature compensators |
| G | Temperature compensation modules |

**Figure 4.6: Expanded diagram showing the assembly of probe α**

Unfortunately, during assembly of the 5S probe with stem α, 2 of the 5 compensation modules became damaged. Four wires were threaded through the plastic casing of the module; two inputs and two outputs of

opposite polarity. The wire resistances were measured before and after the resistors were spliced from the probe tip. No continuity was found through one of the wires on two of the compensators at this stage and they were unable to be repaired by the manufacturer.

New temperature compensation modules were manufactured in-house at the sponsor company using precision resistors and circuit diagrams of the broken resistor networks. The diagrams are provided in appendix 1.

The performance of the new modules was tested in comparison with the undamaged, miniature compensators provided with the sensor head. It was decided that all five of the modules would be changed for in-house manufactured networks as they allowed less drift in output with temperature than the originals. This decision was made through an investigation into the compensator performance at a range of operating temperatures, where the manufacturer's modules did not perform as well as the in-house compensators. The full investigation results are given in the next chapter.

## 4.5 Stem designs

The design of the probe geometry as well as the method of attaching the tip to the stem was based on the requirements of:

- Aerodynamic calibration
- Testing in an industrial rig

The calibration was carried out on an open air jet rig which is described below. It was a requirement that the stem have a $90^0$ bend for use on the jet rig so that the tip was to be positioned in the jet centre whilst being held parallel to the platform around the rig. This design was however not applicable for use in either of the industrial test rigs available during the experimental investigation. For this reason, a

separate design was carried out for each application. The process of attaching the probe was fragile and time consuming, and it was decided that a coupling piece would be designed to ease the strain on the sensor head when moving from one rig to another. A summary of the probe stems designed for each rig is given in Table 4.2.

| Stem design name | Shape | Rig application |
|---|---|---|
| Stem α | Swan neck stem | Air jet rig |
| Stem β | Angled stem | Low pressure turbine rig |
| Stem γ | $90^0$ stem | Compressor rig |

**Table 4.2: Summary of each probe stem and the rig in which it was designed for use**

### 4.5.1 Stem α design

The air jet rig was utilised in the development of the measurement technique used throughout this investigation, as well as the initial testing and 3D aerodynamic calibration of the 5S probe. The rig consists of an exit nozzle through which atmospheric air is drawn by a motorised fan situated below the nozzle outlet. After flowing through an inlet valve and a mesh screen used to catch any debris being drawn into the rig, the flow is turned by $90^0$ and then exhausted through the contraction nozzle. The axisymmetric jet Mach number range produced is between 0.02 and 0.34, depending on the driving motor speed. The air jet rig, as shown in Figure 4.7, has inner and outer flange diameters of 342 mm and 440 mm respectively.



**Figure 4.7: Photograph of air jet rig nozzle, through which air is exhausted to produce an axisymmetric jet**

The stem design for this rig had to ensure that the probe could be placed into the central core of the jet and easily be traversed across the diameter of the nozzle exit. The design also ensured that the stem of the probe was in line with the sensor tip. This allowed the probe to be yawed via a rotation about the stem centreline without changing the physical position of the probe tip in space, but simply altering the angle of attack with respect to the incoming air jet. A representation of the hook neck probe is shown in Figure 4.8.

The stem diameter used was 10mm, a condition set by the access point of the available traverse system, with a wall thickness of 1.5mm which allowed the 20 instrumentation leads to be thread through the centre of the stem safely.



**Figure 4.8: Swan neck probe design used in the calibration of the sensor head and the development of the measurement technique used throughout the final stage of testing**

Figure 4.9 shows the hook necked probe fixed into the yawing traverse system. This 2 Degree-Of-Freedom (DOF) traverse was used to rotate the probe around its centreline to achieve movement of the sensor in the yaw plane as well as lateral movements of the whole probe. This allowed the central sensor firstly, to be aligned with the flow through angular movements and secondly, traversing of the probe across the axisymmetric jet. During the alignment of the probe to the highest flow vector, Nulling in pitch was achieved by adjustment on the balancing screws on the pitch table until the central sensor was reading its highest pressure and the top and bottom (nulling sensors) were reading equal values.

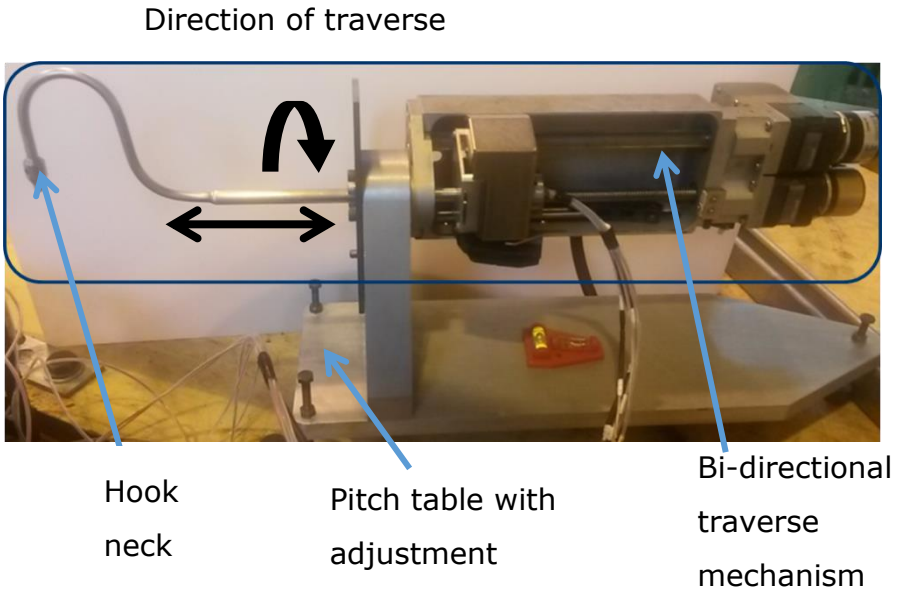



**Figure 4.9: Swan neck probe fixed into the 2DOF traverse motor via the pitch table, allowing adjustments in the pitch angle during probe balancing**

After calibration and initial testing using the air jet rig, the probe was disassembled successfully in preparation for its use in the compressor rig using stem γ.

### 4.5.2 Stem β design

The LP steam turbine model test rig is a 1/10th scale single stage model. The model uses a mixture of ~93% R134a refrigerant gas with air as a working fluid, to achieve Mach number andReynolds number similitude. The rig consists of a last stage and exhaust system able to replicate flow conditions found in full size turbomachines on site. Measurements are generally taken using a standard pneumatic five hole probe after the last stage blade, at the exit of the diffuser lip, and across the exhaust duct. Unsteady pressure measurements after the last stage are required as a high proportion of the leaving kinetic energy in the flow is dissipated in this area as it passes over the diffuser lip and is turned $90^0$ through the exhaust system (Burton, 2013). Characterisation of the flow field in this area could give an insight into the loss mechanisms which result in irreversibilities, leading to a reduction in energy efficiency.

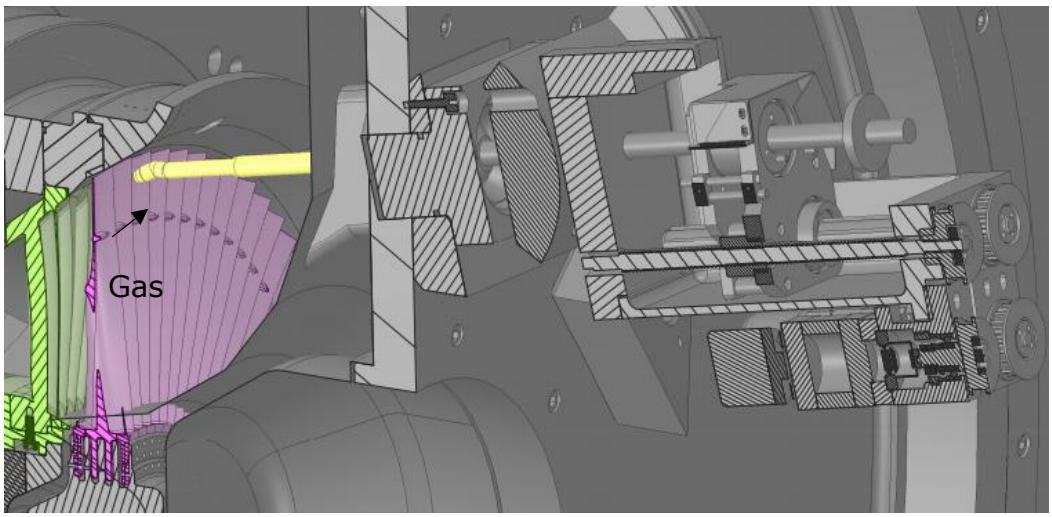



**Figure 4.10: CAD drawing of LP rig and traverse**

Figure 4.10 shows the 5S probe implemented into the traverse mechanism of the LP turbine rig. The 4DOF traverse gear allows the probe to be moved anywhere within the full volume between blade exit and exhaust.

Of the rigs considered suitable for testing the probe, the LP rig had the strictest access requirements. The reason for this was that the access point and traverse mechanism were already designed and in place for use with conventional multihole probes. The probe stem design was tailored completely for use in the low pressure rig so that no alterations had to be made to the rig itself. The mounting point in the traverse through which probes are inserted has a diameter of 9.6 mm. This posed a challenge at the design stage as the sensor tip diameter was already 2/3 the size of the access point. The probe could be inserted into the traverse with a straight stem, however the high hub flare angle of the rig required the probe to have a bend in the stem to align to the high exit pitch angle.

There is a significant pitch angle, as highlighted in Figure 4.10, at the exit from the last stage blade meaning that any probe inserted into the rig must be angled towards the incoming velocity vectors. This ensures that the probe is able to follow the flow path of the exiting fluid, which would otherwise be partially missed by a straight probe in areas where the pitch angle was greater than the acceptance angle of the probe. The rig pitch angle measured during testing was a maximum of $30^0$. This means that for the probe to be able to capture the incoming flow vector, it would have to be angled towards the exiting flow. The sensor head has an acceptance angle of $20^0$, meaning that it is able to accept incoming vector angles of up to $20^0$ from the probe axis, therefore the probe design was given a $10^0$ angle at the tip This ensured that the probe could measure the incoming flow vector.

In order for the 5S probe to fit into the traverse mechanism installed in the turbine rig without any change to the turbine itself, a strict boundary was imposed during the design stage of 9.6mm OD.

Different designs were trialled to find a compromise between the angle of the stem and the outer diameter of the entire probe. Three major design iterations were carried out, with the third being the final probe

stem application. Drawings of the intermediate iterations are given in appendix 2.

The problem was resolved in the third and final iteration of the design, shown in Figure 4.15 which includes a $10^0$ upwards bend in the probe stem before it was cut at the $20^0$ angle at which the tip was to be attached. This gives a final pitch angle of $10^0$ on the probe head. This iteration was found to be an optimised design between the maximum allowable angle and the overall probe diameter.

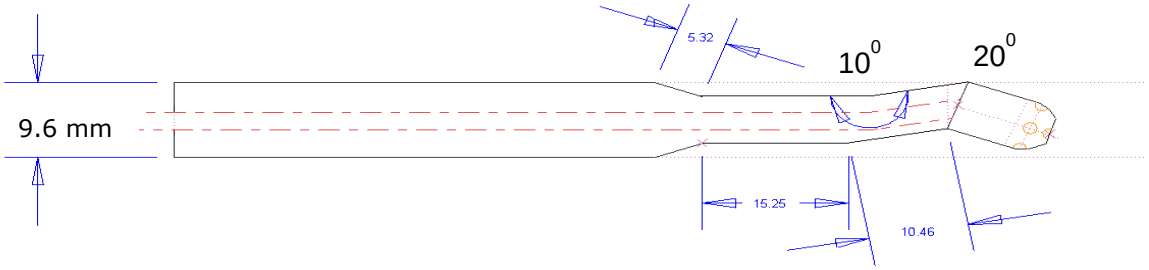



**Figure 4.11: Final probe stem design. The stem is first bent upwards by $10^0$ then the probe tip is to be attached at the designated $20^0$. This gives an overall bend of $10^0$**

This design did not include the use of the coupling piece designed for use with the other stems as it was too large to be used with the current access restrictions on the LP rig. This design was not used by the sponsor company however, if it is to be used in the future, an attachment method which does not increase the overall diameter of the probe will need to be considered.

### 4.5.3 Stem γ design

The compressor, used for the final stage of experimentation with the 5S probe, is a 6-stage air rig where measurements were taken after the last stage vane. Access to the flow path was radially through the outer casing. The probe stem therefore needed to bend through $90^0$ to face the flow, as shown in Figure 4.12. The bend radius of the swan neck

stem α was too large to fit within the compressor casing, so a new probe stem γ was required.

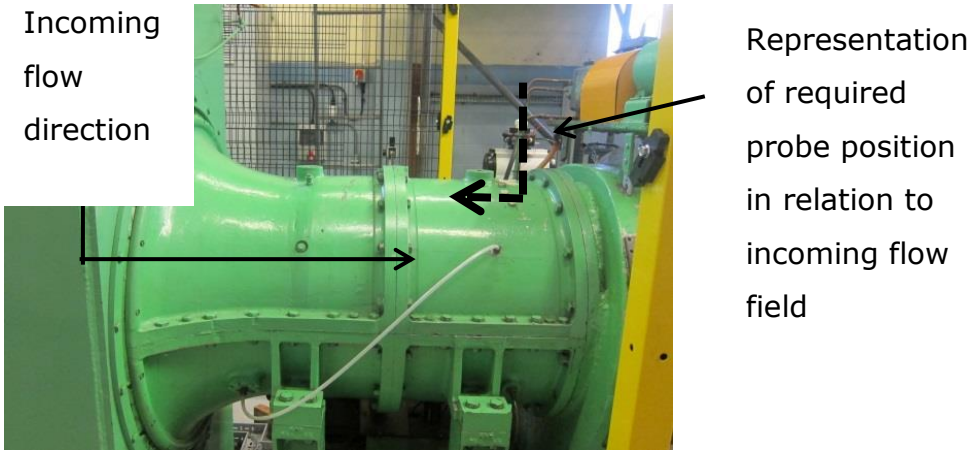



**Figure 4.12: Compressor rig used in the final stage of testing the 5S probe**

A longitudinal slice through the centreline of the rig is shown in figure 4.13 which highlights the space in which the measurements were taken after the last stage blades and the area for the probe to be traversed.

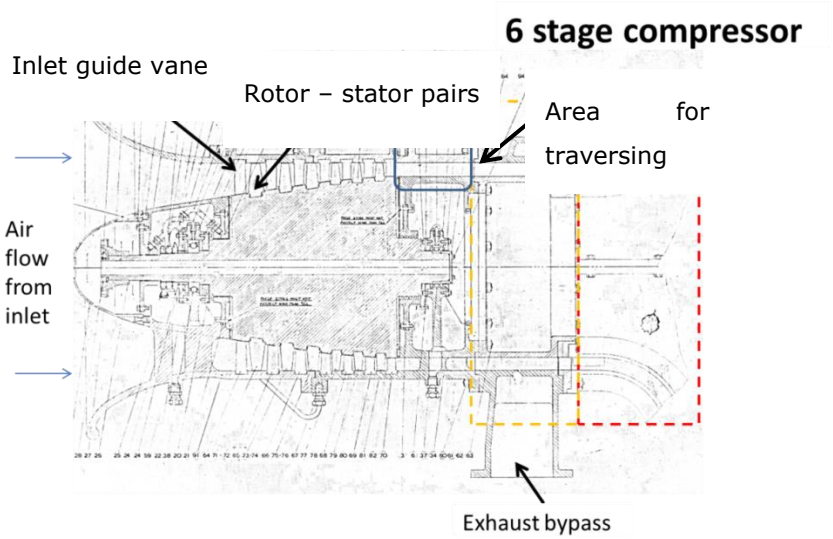



**Figure 4.13: CAD drawing showing a 2D slice through the compressor rig. The area in which measurements were taken is shown relative to the last stage blades**

The probe designed for this application is an adaptation of the swan neck probe used during calibration on the air jet rig. It combines a straight $90^0$ bend with a smaller coupling piece manufactured specifically for use in the compressor rig. The overall design of the temporary attachment piece is the same as the first iteration although the overall diameter is only 10mm enabling the probe to be inserted into the 1/2in holes in the casing of the compressor. Figure 4.18 shows the probe design used along with the fittings used to secure the stem in place.

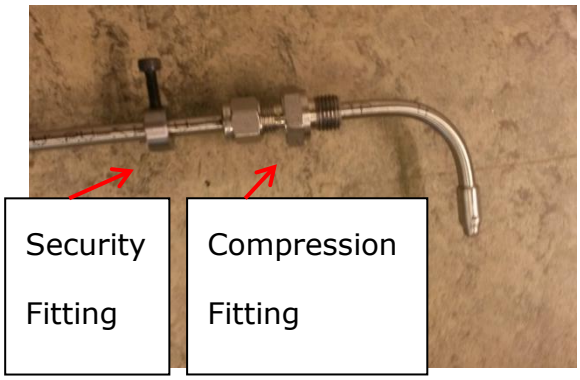



**Figure 4.14: Probe design for use in the compressor rig. The compression fitting used to lock the probe in the rig as well as the security fitting are shown**

Inside the compression fitting is a bespoke nylon olive which allows the probe to be securely fixed in place repeatedly, without permanently crimping the ferrule. In the unlikely event that the fitting would fail, an extra fitting was made to limit the probe's radial range of motion to prevent rubbing on the rotor hub.

## 4.6 Probe design considerations

When reflecting on the designs presented in this chapter, the practicalities of using each probe were considered as well as the different stem designs themselves. Thoughts were centred on stems α and γ as they were physically implemented and used with test rigs at the sponsor company. Stem α proved to be a successful design as it allowed for a repeatable aerodynamic calibration and was easily implemented into the traverse motor for accurate repositioning of the probe tip. The main advantages of having the interchangeable stems was the flexibility which was offered by calibrating the probe head independently. There was also a large cost saving benefit to being able to transfer the calibrated probe between test rigs.

Efforts were made to assess the effect of changing the probe geometry on the calibration results by comparing the yaw sensitivity graph produced from the 5S probe, implemented into stem α, with that of an independent test (Guenette and Castner, 2011) where a straight stem was used. Similarities were found in the pressure distribution around the probe head and it was concluded that changing the stem before testing was not detrimental to the calibration of the 5S probe. This is discussed in more detail in Chapter 6.

If the designs were to be altered with the intention to use the probe solely on the air jet rig for calibration and the compressor rig for testing, one permanent probe stem could have been designed to save time and reduce the risk of damage to the sensor head during change over. This would have been based on stem γ with an attachment piece used to convert the probe between calibration and testing mode. A forecast of such a design is given in figure 4.15.

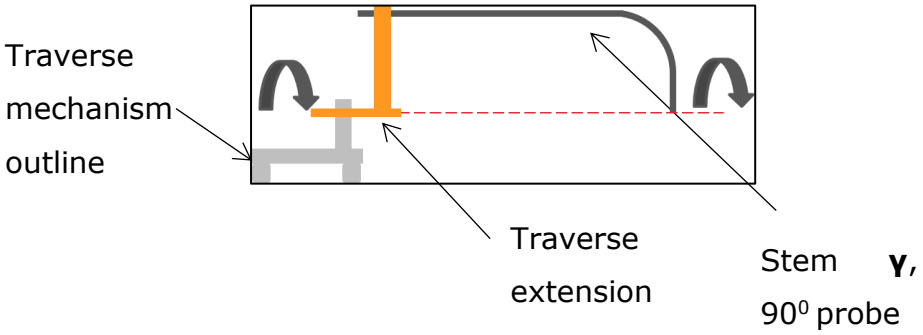



**Figure 4.15: Conceptual drawing of proposed traverse extension piece to allow one probe to be used for calibration and testing**

The concept shown in fig 4.15 would allow only one probe, with a $90^0$ bend such as stem γ, to be used for calibration on the open air jet and testing in the compressor rig. It allows the point of rotation to be centred on the probe tip, negating the need for a swan neck stem.

It was decided that the implementation of two stems, α and γ, would be more advantageous than one stem with an attachment piece. This reduced the risk of inaccuracies on the proposed attachment piece, shown in figure 4.15, being carried into the calibration measurement. The concept of using only one probe would also reduce the flexibility in the use of the calibrated probe stem. Should another application for the 5S probe arise within the sponsor company, another bespoke stem could be designed at a much lower cost than buying a new sensor head.

## 4.7 Conclusions

Three probe stem designs were considered with two being implemented into test rigs for experimentation. Considerations around the attachment of the probe head to the tailored stems were discussed and the coupling piece used to allow interchangeability between each stem was designed. Introductions to the geometries and access requirements of each of the available test rigs were also given in this chapter along with bespoke

designs for probe stems applicable to each of them. The following chapter gives an insight into the working principles and operating conditions of the 5S probe after its assembly into stem α.

# Chapter 5: Measurement Technique Development

## 5.1 Introduction

This chapter describes a series of developmental investigations which were carried out on the 5S probe, prior to its aerodynamic calibration. Sensor calibration was performed as an initial step in the characterisation of the probe. It was achieved using a deadweight tester (DWT) to determine the pressure sensitivity, in mV/Psi, of the individual sensors. The effect of temperature and acquisition time on the measurements was also taken into account during the development of the measurement technique. Initial trials to prove the probe and measurement system were performed where vortex shedding from a cylindrical rod in the free air jet was measured.

The probe was able to measure the vortex shedding frequency in the flow across a range of flow speeds. This chapter demonstrates the novelty in the 5S probe's use and its ability to acquire data at sample rates of up to 100 kHz simultaneously from all sensors on the probe tip.

## 5.2 Measurement chain set-up

The measurement chain consists of the hardware used to acquire data from the probe as well as the software used for acquisition and analysis. Figure 6.3 shows an overview of the steps used to achieve simultaneous capture of the 5 sensor outputs.

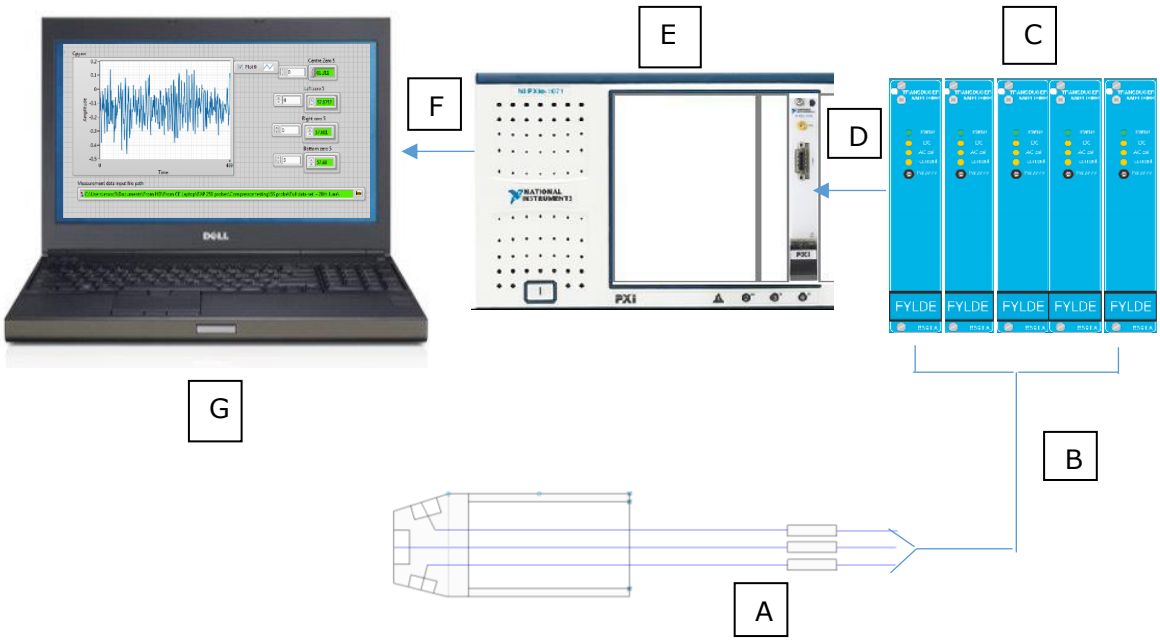



**Figure 5.1: Data acquisition system with labels expanded in table 5.1**

The equipment and data links shown in figure 5.1 are explained in more detail in table 5.1.

| Letter | Name | Description |
|---|---|---|
| **A** | 5S probe | 5 individual sensors with 2 inputs and 2 outputs each |
| **B** | Link between probe and amplifier | 5-pin out Amphenol Tuchel connectors attached to each set of sensor lead outs |
| **C** | Fylde Amplifier | 5 FE-859TA transducer amplifier modules housed in Fylde enclosure. |
| **D** | Link between Amplifier and NI PXI data acquisition system | BNC cables used to connect signal outputs from each of the 5 amplifier channels to the acquisition card in the PXI chassis |
| **E** | NI PXI chassis | A PXI-express 4492 acquisition card was used within the 4-slot PXI-e chassis. |
| **F** | NI controller | PXI remote controller module used to allow connection between the PXI chassis and the laptop via a PXI-e BUS connector |
| **G** | Laptop | A customised LabVIEW program was used as data acquisition software |

**Table 5.1: Explanation of each step in the data acquisition chain shown in figure 5.1**

The lead outs from each sensor were connected to a channel on the Fylde amplifier which acted to amplify the output signal. A gain multiplier of 10 V/V was used over each channel to amplify the resulting signals from each sensor. The Fylde output was connected to a National Instruments 8 channel PXI data acquisition card. This set up allowed simultaneous acquisition of the 5S probe sensor values at rates of up to 200 kHz, although an upper limit of 100 kHz was imposed to avoid amplitude modulation close to the natural frequency of the sensors. Acquisition from the NI PXI-e 4492 card is simultaneous on all channels, which is crucial to proper interpretation of the data from the 5S probe. The software used to acquire and store the probe data was written and saved as a Virtual Instrument (VI) using LabVIEW software.

## 5.3 Characterisation of the 5S probe

During the 5S probe measurement technique development, the FAP-250 sensor head was assembled into stem $\alpha$, as explained in Chapter 4. The first step when using the 5S is to calibrate the sensors individually to measure the V/psi sensitivity. A single sensor stagnation probe with a shrouded inlet, known as a Kiel probe, was initially calibrated to gain understanding of the process before it was applied to the 5S probe, where all 5 sensors were calibrated simultaneously. The procedure for this is discussed in Section 5.3.1. The effect of temperature, not only on the calibration process but on the sensor head itself during testing could affect the performance, so the effect of this is presented along with calibration results for each of the five sensors over a range of atmospheric conditions. During the temperature effect tests, the FAP-250 probe head was damaged. The damaged tip, hereafter named FAP-250(1) was replaced with a new head, named FAP-250(2) for parts of this investigation, prior to its full aerodynamic calibration. The new head underwent sensor calibration and these results are given in section 5.3.2. The new head was then used in validation experiments to

investigate the vortex shedding behind a cylinder. These vortex shedding experiments are shown in section 5.5.3.

### 5.3.1 Sensor calibration

Two main calibration techniques should be carried out before the probes can be applied to unknown flow fields (Kupferschmied, 2000). The first step must be a sensor calibration, whereby sensitivities for each individual transducer are deduced. The aerodynamic calibration, which is described in more detail in chapter 6, is carried out afterwards which allows the probe pressure measurements to be mapped over a range of yaw and pitch angles. This order is important since the second calibration needs correct datum points for optimal results.

The sensor calibrations of this 5S probe were carried out using a deadweight tester; a closed system which delivers a known, fixed pressure to the probe via a piston and cylinder arrangement. The method uses the basic principle of balancing a known mass against the force exerted by the fluid on a known piston area.This simple relation is shown in Equation 5.1, where P is the applied pressure in Psi, M is the known mass in pounds, and A is the area of the piston used in the deadweight tester in $in^2$.

$$P = \frac{M}{A}$$

**Equation 5.1: Deadweight tester pressure-mass relationship**

A photograph of the deadweight tester is given in Figure 5.2 and the procedure of calibrating individual sensors is as follows:

- The system is set-up by attaching the pump and piston balance table to the probe via rubber tubing

- The discharge valve is tightened to ensure a closed system between the probe and the pump
- The chosen weight, corresponding to an applied pressure, is added to the balance table
- Enough pressure is introduced to the system via the pump so that the weight table above the piston is lifted and is able to spin freely to remove friction
- At this point the pressurised system is considered to be in a steady equilibrium and voltage measurements can be taken from the transducer

The procedure is repeated for each weight corresponding to the required pressure range of calibration. The applied pressure range was from 0.2 to 2 psi for the calibration of the sensors in the single sensor probes as well as the 5 sensor fast response probe. The deadweight tester system is shown in Figure 5.2.

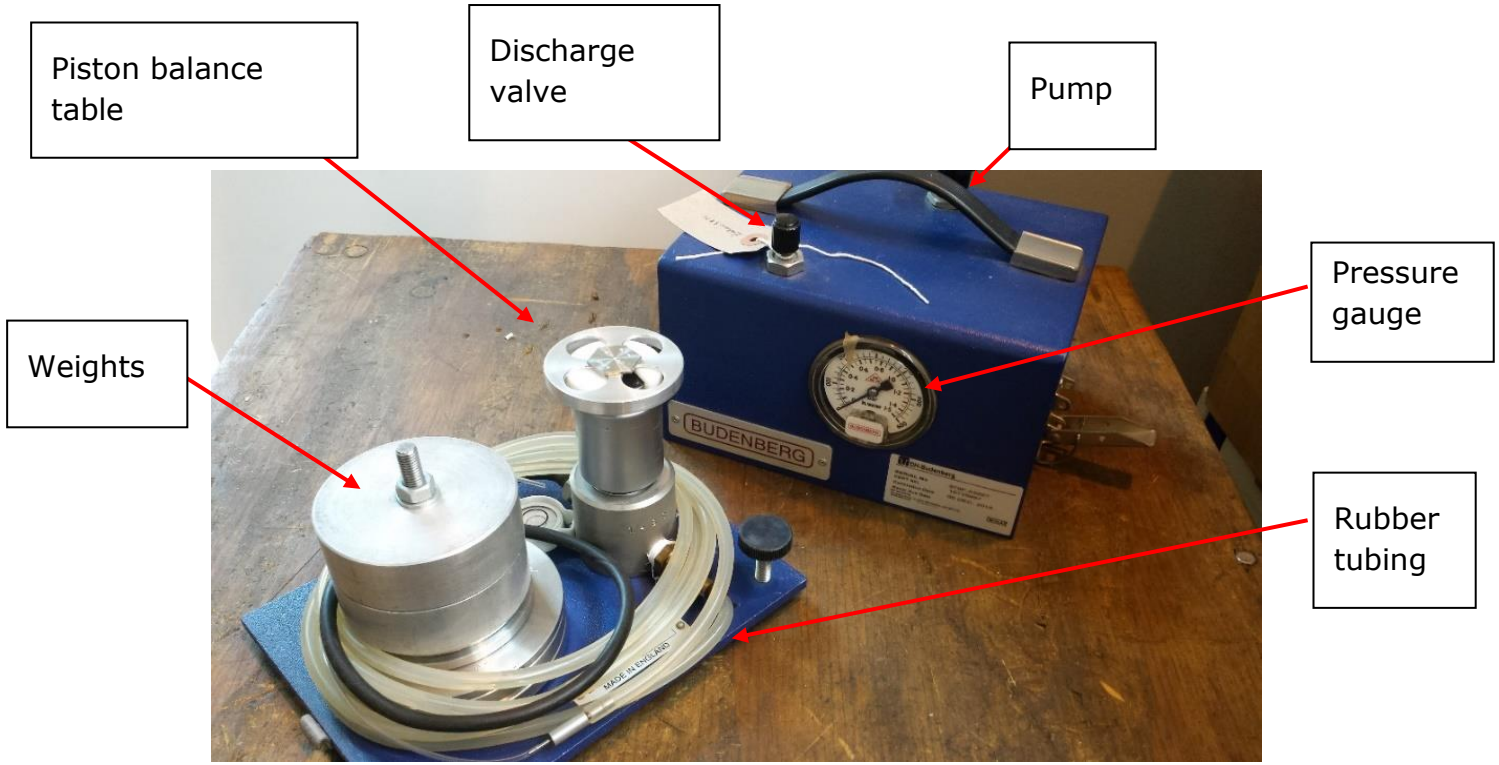



**Figure 5.2: Deadweight tester used in the calibration of pressure sensors**

### 5.3.2 Sensor calibration results

The results of the individual sensor calibrations for each of the 5 sensors on the 5S probe are presented in Figures 5.3 – 5.7. These results were taken at atmospheric temperature and pressure, with three experimental runs taken at different times of the day shown in each figure. Table 5.2 shows the atmospheric conditions at which each calibration run was taken.

| **Condition** | **Run 1** | **Run 2** | **Run 3** |
|---|---|---|---|
| Atmospheric temperature, $^0$C ($\pm 0.5^0$C) | 22 | 25 | 21 |
| Atmospheric pressure, psi ($\pm$0.0325 PSI) | 14.45 | 14.48 | 14.39 |

**Table 5.2: Atmospheric conditions measured at the time of each sensor calibration**

The calibration results are presented along with linear fits for each data set to allow the best fit line equations to be deduced and the probe sensitivity to pressure (mV/psi) derived. The sensitivity of each sensor was found to be between 4 and 5 mV/psi.

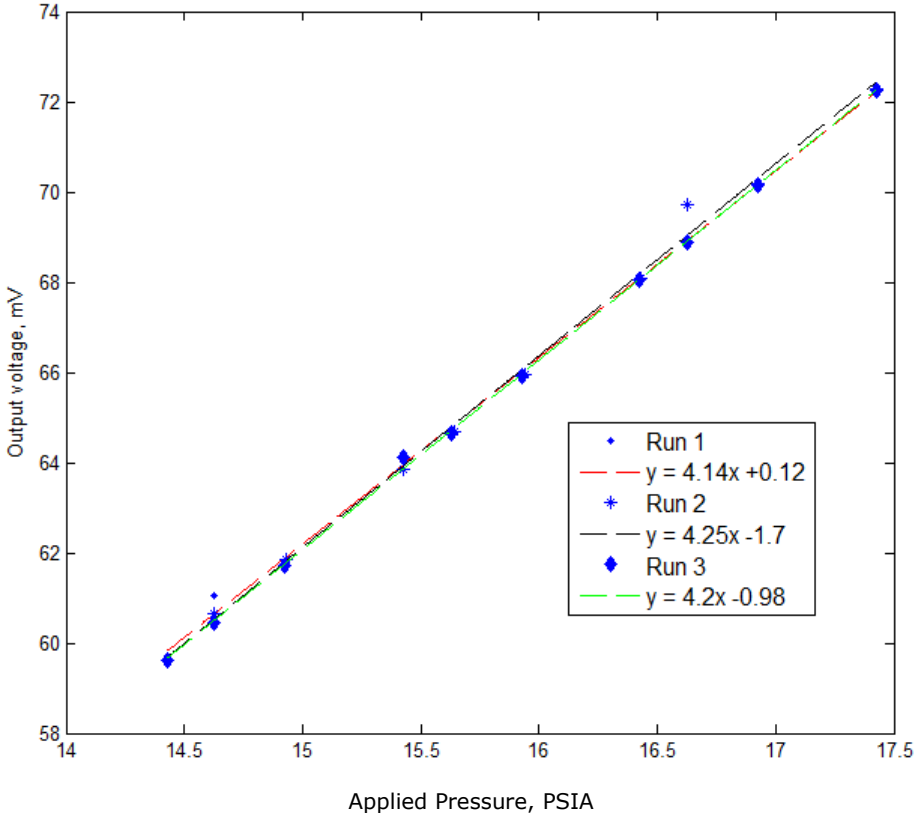



**Figure 5.4: Left sensor calibration**

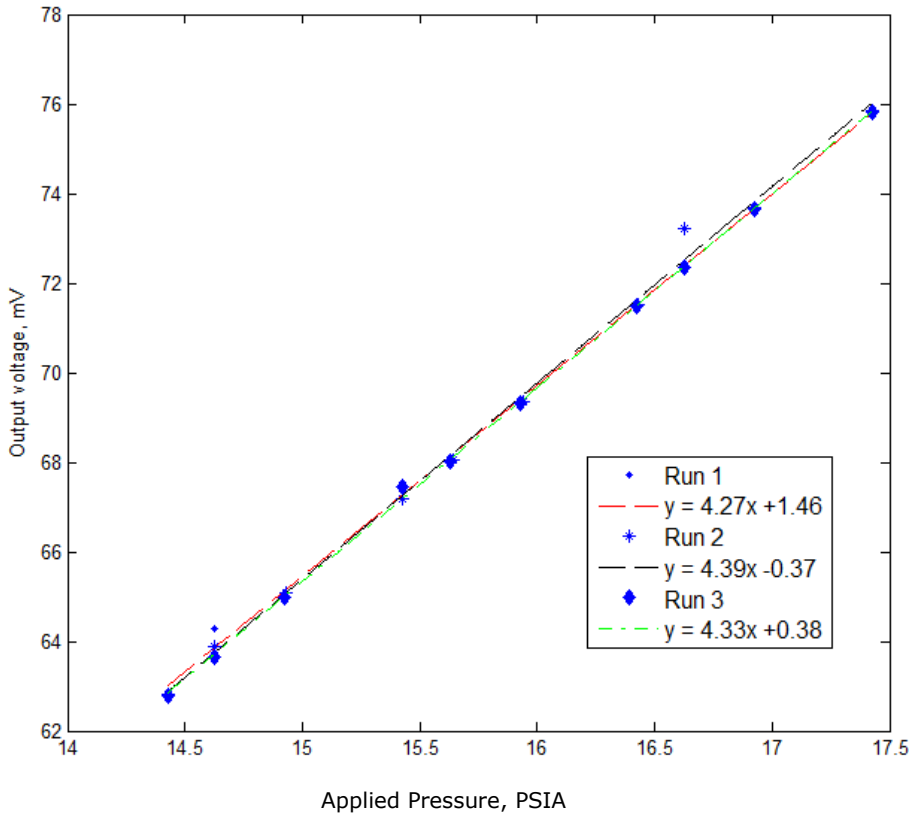



**Figure 5.3: Centre sensor calibration**

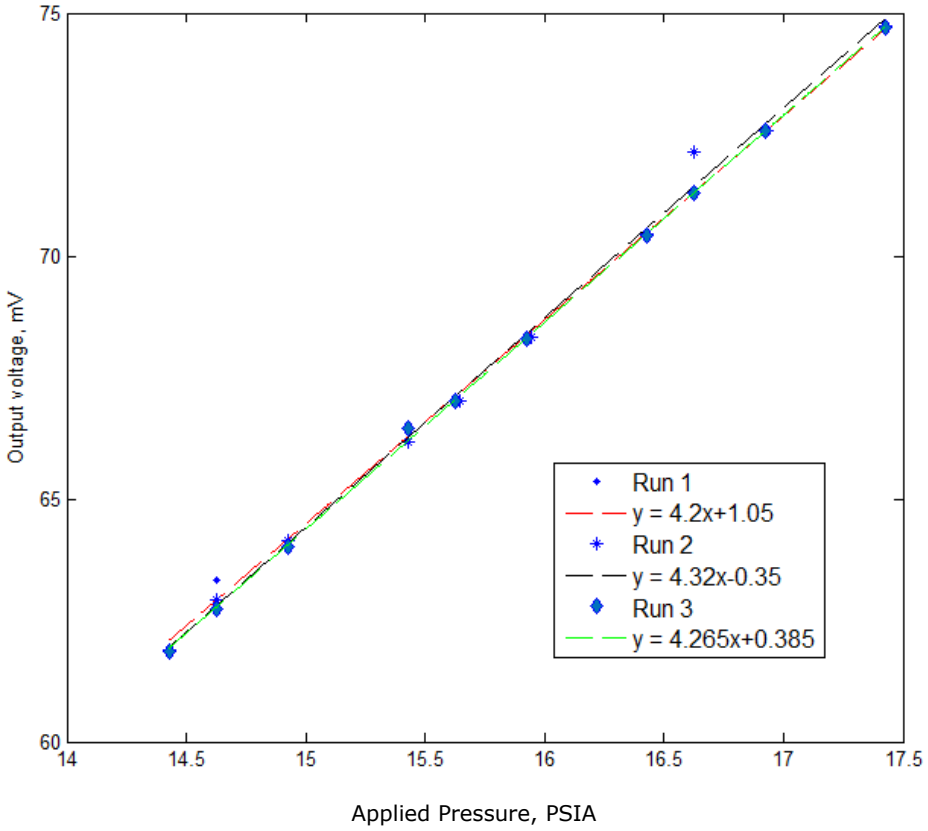



**Figure 5.6: Top sensor calibration**

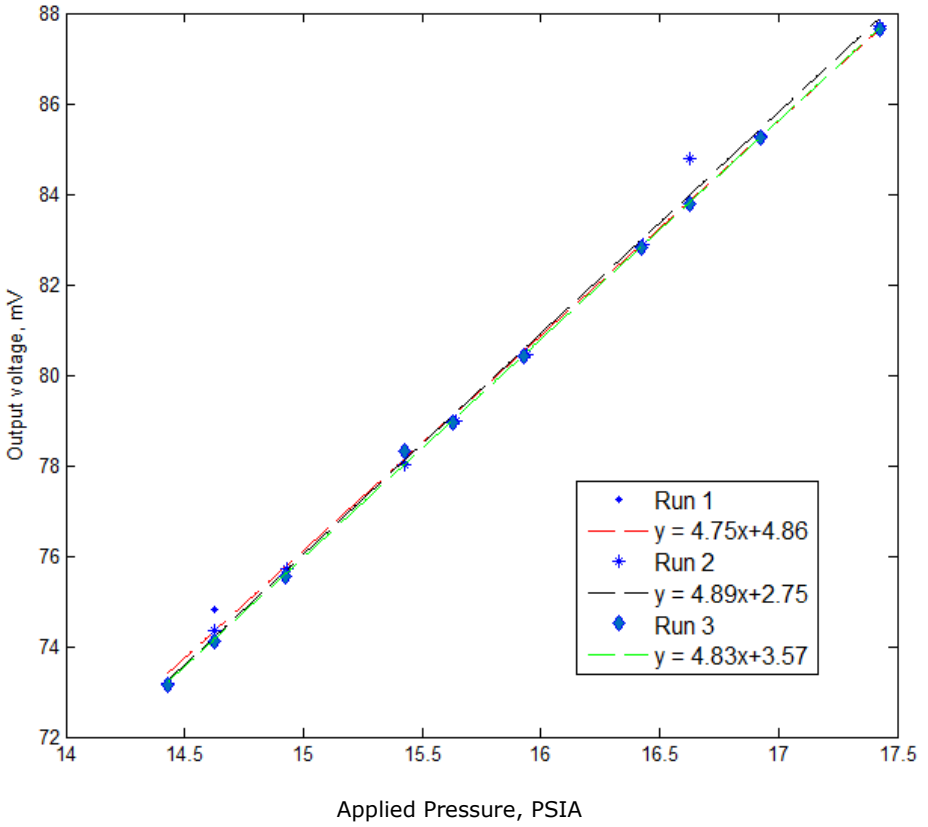



**Figure 5.5: Right sensor calibration**

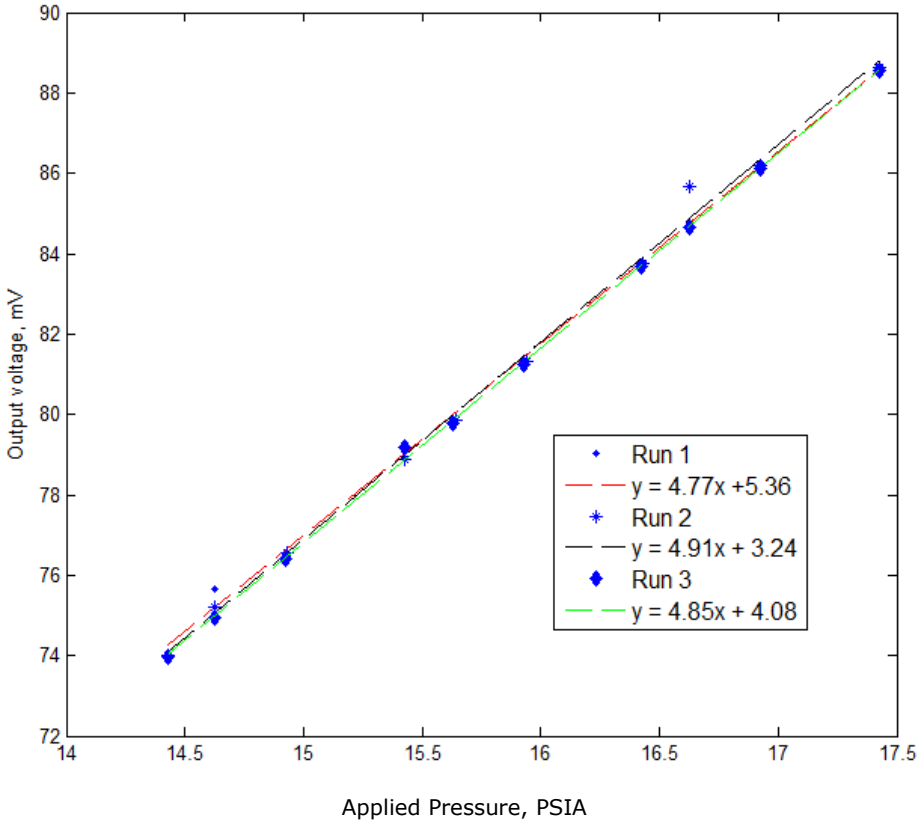



**Figure 5.7: Bottom sensor calibration**

It can be seen that, for all 5 sensor results, although the gradients are relatively steady, differences exist between the three runs. The intercept results can be seen to change a lot more dramatically over different atmospheric conditions. In order to negate the drift in the calibration intercept value over smaller changes in atmospheric condition, all measurements were taken with respect at the probe's atmospheric pressure reading.

Dynamic pressure sensors suffer from zero drift, where the DC-offset voltage can vary up to 5% of full scale as outlined in the manufacturer's datasheet. To negate the effects of zero drift, calibration and measurements are taken as a difference to atmosphere, where an atmospheric zero is taken each time prior to measurements being acquired. Voltages are then recorded as a difference to atmosphere, and converted to pressure using the calibrated sensitivity (V/Psi). The assumption is made that no change in atmospheric pressure or zero drift occurs during the period of a test.

An investigation was also carried out, whereby the probe sensors were calibrated in an oven in the range $25^0$C to $50^0$C, to assess the effect of temperature on the calibration. The way in which the pressure sensors of the 5S probe are affected by changes in temperature are discussed in the Section 5.3.3. Two main considerations are presented; the way that the sensor calibration changes with increasing temperature as well as the rise in temperature of the sensor head due to self-heating during warm up of the instrumentation.

### 5.3.3 Temperature dependency

Peizoresistive pressure sensors are temperature sensitive, meaning that a change in voltage output can be due to either pressure or temperature fluctuations. This sensitivity contributes to fluctuations in the offset of the sensor, leads to uncertainty in the pressure measurements. In order to increase the accuracy of measurements, temperature compensation

is used to balance the Wheatstone Bridge during temperature fluctuations, ensuring that any change in voltage output is a reflection of pressure only. The compensation process can either be active, whereby the change in bridge resistance is monitored simultaneously with the sensor temperature, or passive, whereby the resistance of the bridge is corrected with the addition of shunt resistors, during drifts due to temperature changes (Kulite, 2004).

Kulite Semiconductor Products Inc compensate for temperature drift by applying a passive resistor network in series to the bridge, the circuity for which is located in a separate housing as  as introduced in section 3.5 (Kulite, 2004). Equation 5.2 describes the process of compensation using the span resistor network to correct for changes in bridge resistance.

$$V_{out} = V_{in}\left(\frac{R_{Bridge}(T)}{R_{Bridge}(T) + R_{Span}}\right)\{S(T)P\}$$

**Equation 5.2: Span resistor network equation**

Where V is the bridge voltage, $R_{Bridge}$ and $R_{span}$ represent the bridge and span resistors respectively and S(T)P is the sensitivity of the bridge. As temperature increases, the bridge resistance increases and the voltage DC offset of the sensor decreases. The span resistor is therefore used to rebalance the bridge and stabilise the sensitivity of the sensor to pressure changes. This is shown diagrammatically in Figure 5.8 for the right sensor, with the rest of the resistor network drawings being shown in appendix 1.

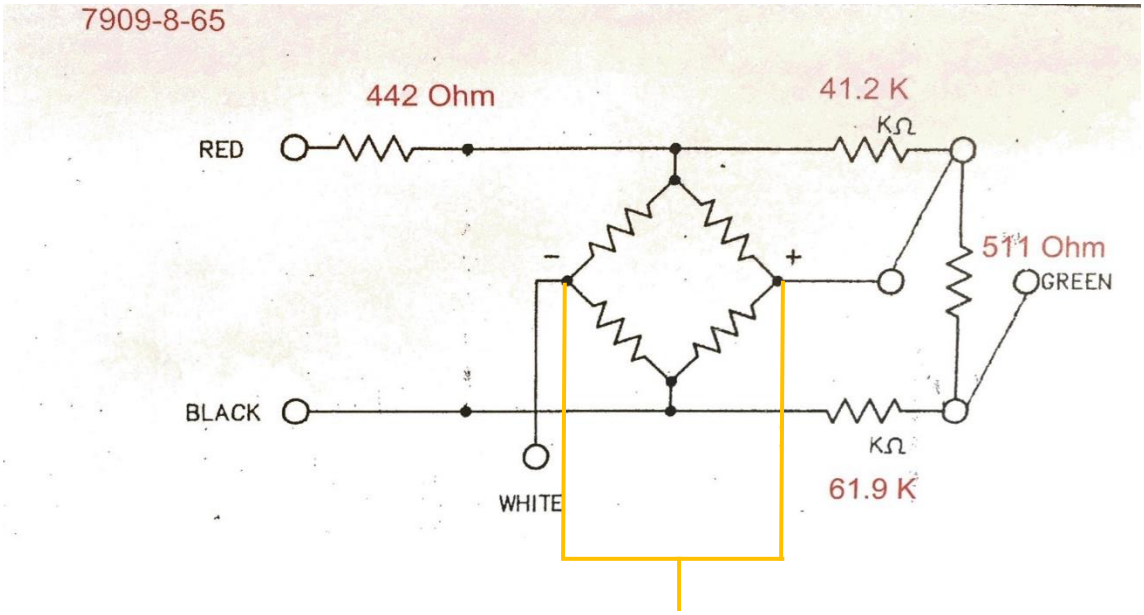



**Figure 5.8: Resistor network for the broken right sensor**

During operation, as the bridge resistance increases due to a rise in temperature, the compensating resistor does not change as it is not temperature sensitive. This results in a proportional increase in the supply voltage applied to the bridge and subsequent change in $V_{out.}$The change is then offset proportionally by the applied span resistance to reduce any step changes in pressure sensitivity. This procedure allows Kulite compensation modules to be placed externally from the sensor head itself, meaning that they do not need to be at the same temperature as the sensing bridge. The correct resistor network is chosen during manufacture for each sensor produced.

#### 5.3.3.1 Manufacture of temperature compensation modules

During the assembly of the FAP-250 probe into stem α, the five temperature compensation modules attached to the probe were cut out of the circuit so that the sensor lead outs could be threaded through the stem. Once the probe head was secured into the coupling sleeve, the compensation modules were soldered back into the circuit. The assembly method is shown in Figure 4.10 in Chapter 4. As discussed in Section 4.5, temperature compensation modules were manufactured in-house

An investigation was carried out with the following aims:

- To assess if the compensation modules need to be placed at the same temperature as the sensor
- To assess the difference in performance of the sensors working with the compensation modules from Kulite semiconductors, with those manufactured in house and without any compensators attached

#### 5.3.3.2 Oven testing

Temperature variation tests were performed in a high accuracy/stability oven. Fixed temperatures were set over a range of 25-50degC, and at each temperature a sensor calibration was performed.

The experimental set up for the oven testing, with the compensation modules located outside of the oven itself, is shown in figure 5.9.

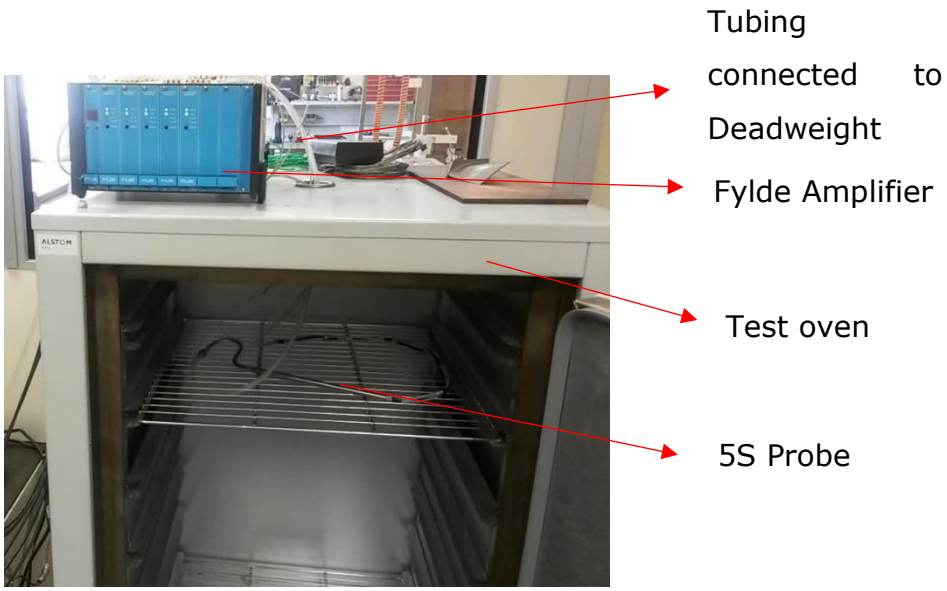



**Figure 5.9: Calibration of the 5S probe carried out in a sealed oven. Temperature range was 25$^0$C to 50$^0$C.**

Table 5.3 shows the range of test conditions carried out during the temperature dependence investigation. The sensor calibration was carried out under each set of conditions. Firstly, a comparison was carried out to highlight any differences in the calibration when the compensation modules were placed inside and then outside of a test oven.

The comparison showed that the temperature of the modules did not make any difference in the sensor calibration results due to the compensation method being passive. The new resistor networks were then manufactured and imbedded into the circuitry for the centre, right and top sensor circuits. The in house modules were then tested against the Kulite temperature compensators, with all modules at room temperature.

| Sensor to be tested | State of temperature compensation module during testing | | |
|---|---|---|---|
| | No compensation | Kulite | In-house |
| Centre | x | | x |
| Left | | x | |
| Right | x | | x |
| Top | | x | |
| Bottom | x | | x |

**Table 5.3: Experimental runs carried out during the temperature dependency calibration investigation**

### 5.3.3.3 Temperature compensation investigation results

The results of the temperature dependency investigation are shown in Figures 5.10 to 5.15. Figures 5.10 and 5.11 give two examples of sensor calibrations taken over a temperature range of $25^0$C to $50^0$C with no temperature compensation modules in the circuit. Figures 5.12 and 5.13 show results of the same investigation with the manufacturer's compensation modules connected to the sensors. The final two figures, 5.14 and 5.15, show the results with the modules manufactured in house during the project.

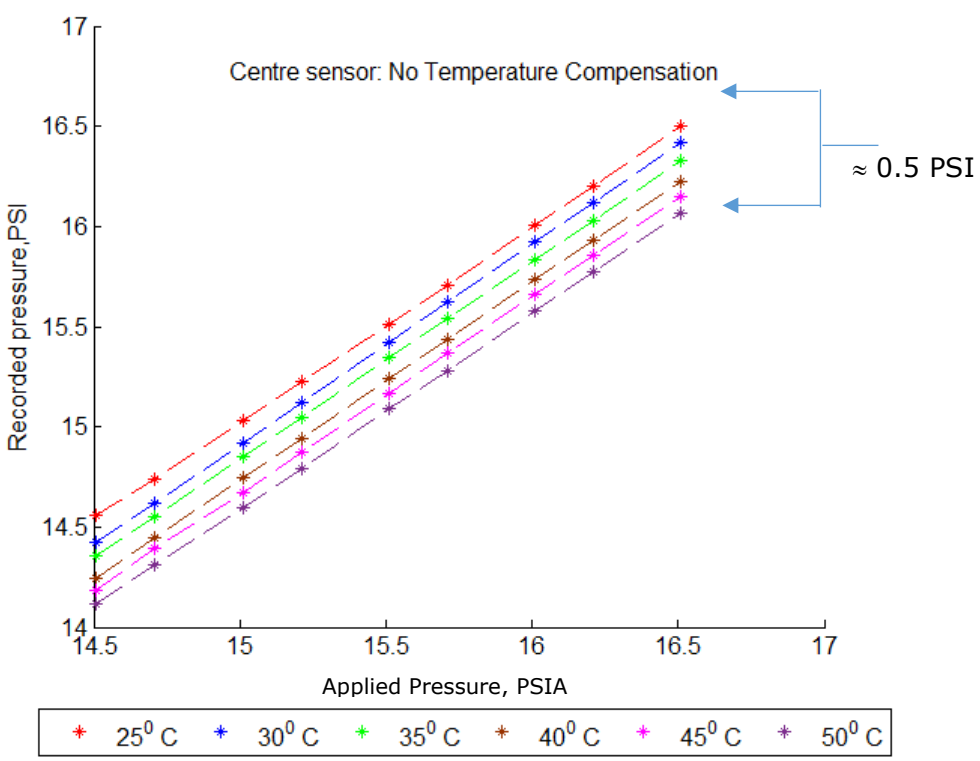



**Figure 5.11: Centre sensor calibration results with no temperature compensation module in circuit. Calibration carried out over a temperature range of 25⁰ to 50⁰**

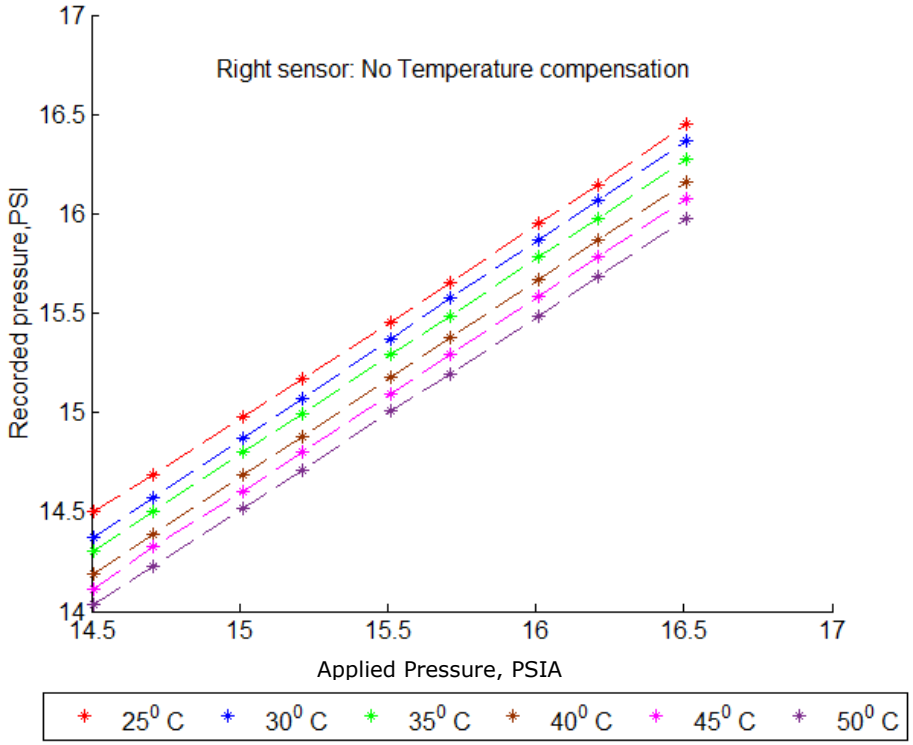



**Figure 5.10: Right sensor calibration results with no temperature compensation module in circuit. Calibration carried out over a temperature range of 25⁰ to 50⁰**

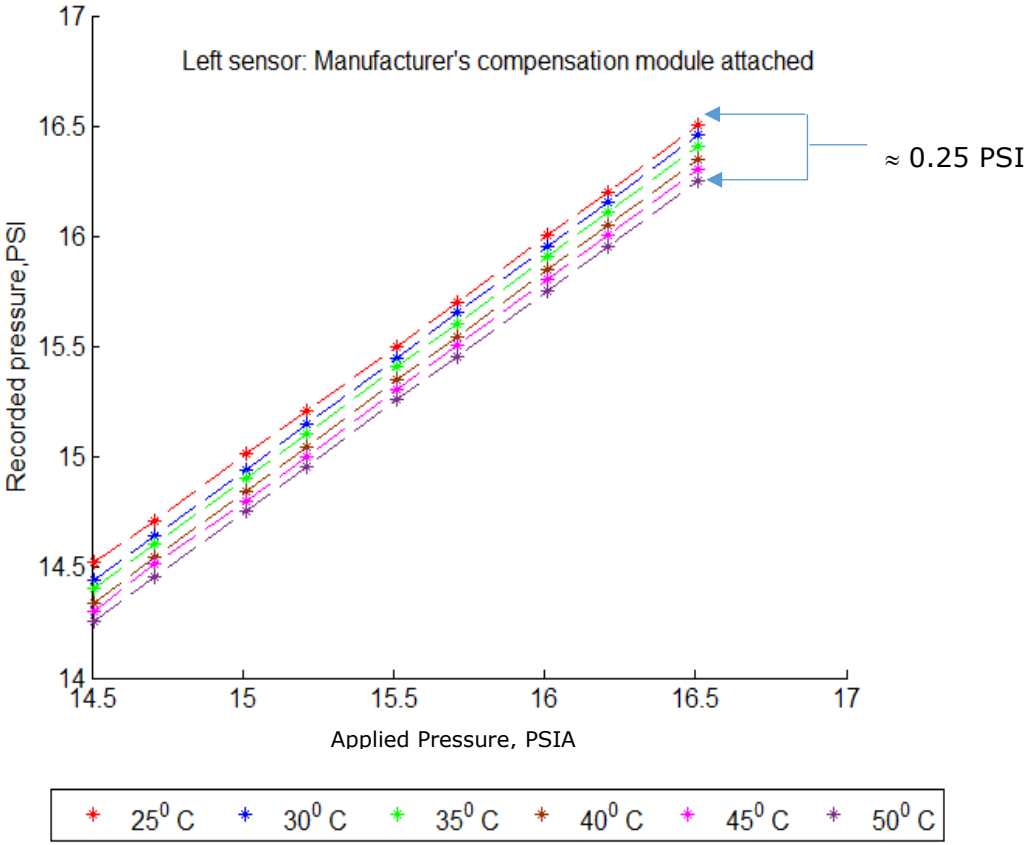



**Figure 5.12: Left sensor calibration results with Kulite temperature compensation module in circuit. Calibration carried out over a temperature range of 25⁰ to 50⁰**

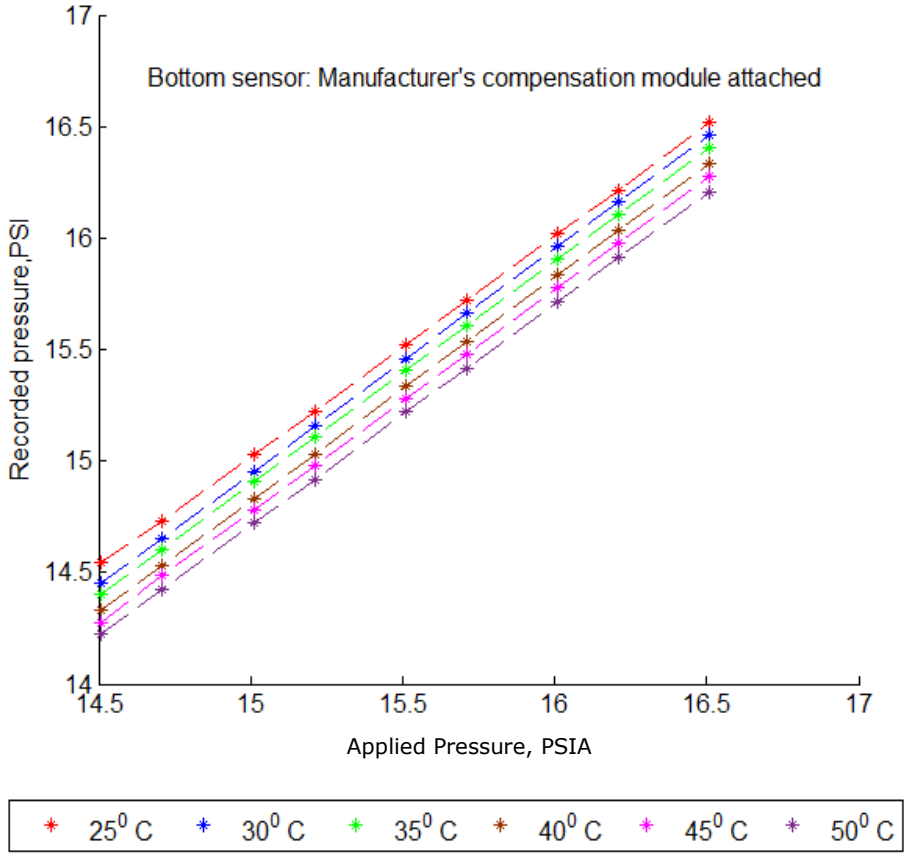



**Figure 5.13: Bottom sensor calibration results with Kulite temperature compensation module in circuit. Calibration carried out over a temperature range of 25⁰ to 50⁰**

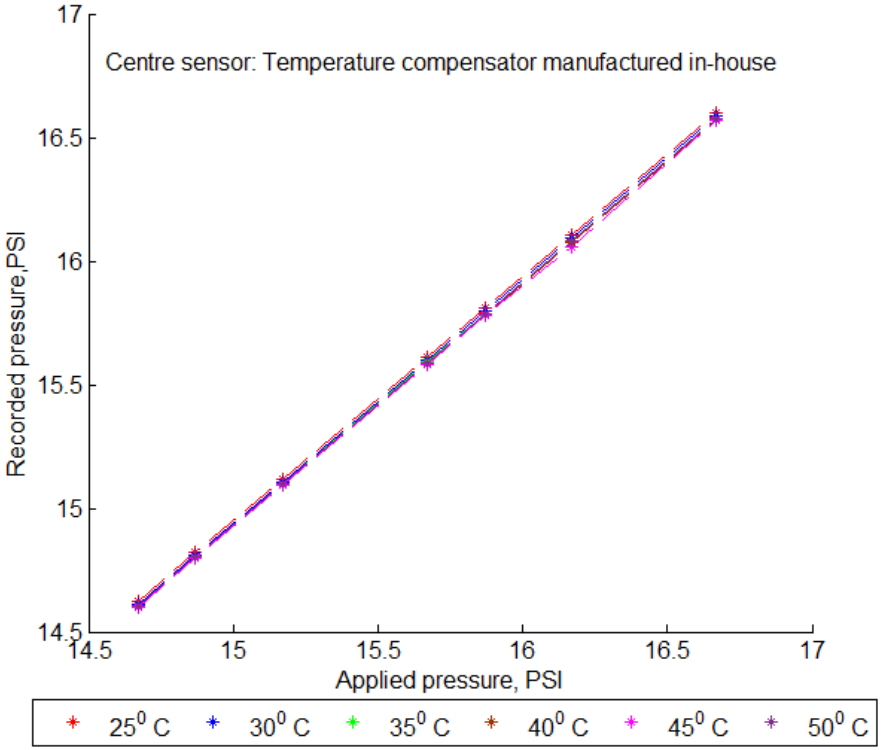



**Figure 5.14: Centre sensor calibration results with in-house temperature compensation module in circuit. Calibration carried out over a temperature range of 250 to 500**

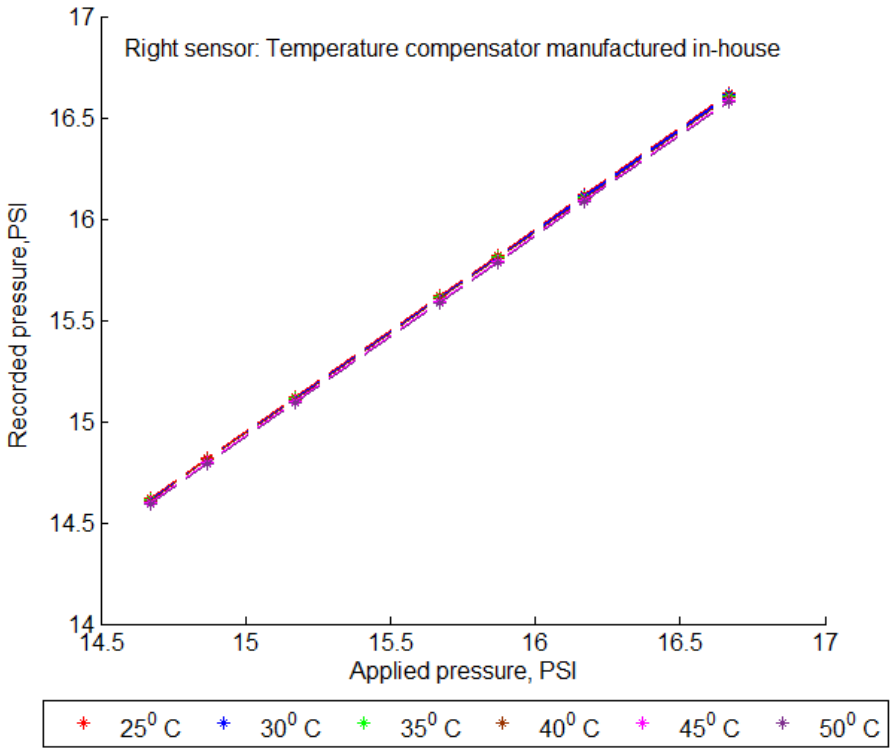



**Figure 5.15: Right sensor calibration results with in-house temperature compensation module in circuit. Calibration carried out over a temperature range of 250 to 500**

The results in Figures 5.10 to 5.15 show a gradual improvement in the spread of the y-intercept values between the cases with no compensation modules, to the addition of the Kulite modules and then in the change to the modules manufactured internally. With the addition of the Kulite modules it can be seen that the change in the spread of the y-intercept values reduced from 0.5 psi to 0.25 psi, giving up to a 50% reduction in the spread in the measurements taken over the temperature range. A similar reduction of 45% in spread is seen between the manufacturer's modules and those made internally at the sponsor company. The reason for this noticeable improvement, despite the same resistor network being used for both types of modules, has been attributed to the lack of size restriction in the in-house modules. It was determined at the beginning of this investigation that the placement of the modules with respect to the sensor head did not make a difference to the results due to the compensation being of a passive nature. For the in-house compensators, the size of the resistor networks therefore did not have any restrictions, meaning that high precision resistors could be used throughout, resulting in the housing being 50x80x50mm, as opposed to the Kulite rod-like housings of 35x5mm.

This testing was carried out using the FAP-250(1) sensor head prior to its damage. When the FAP-250(2) head was assembled into the 5S probe, it was decided that the original compensation modules could be used as no damage was sustained to them when the probe was put together. The FAP-250(2) compensation modules were therefore not calibrated in the oven because the manufacturer provided a guarantee of ±1%/38$^0$C output change over a temperature range of 25$^0$C to 80$^0$C. This is shown in the FAP-250 specification sheet in appendix 10. Also, the 0.25 psi difference shown in figures 5.12 and 5.13 shows a difference in y-intercept value, but no change in gradient was seen. It was decided in section 5.3.2 that all measurements would be taken with respect to atmosphere. Practically atmospheric zeros recorded at the time of

testing were subtracted from the final results. This ensured that the effect of zero drift was reduced.

The offsets measured in this section highlight the effect on the probe output of the temperature drifting during experimental testing. Such drift cannot be accounted for by atmospheric zeroing of the probe before testing.

#### 5.3.3.4 Change in temperature of probe head during operation

During the initial stages of testing, it was noticed that the sensor outputs would drift initially due to heating of the probe tip upon start up. An investigation was therefore carried out to assess the temperatures that the sensor head reaches when it is first excited by the completion of the Wheatstone bridge. A type E thermocouple was used to assess the temperature of the sensor head, while an FLIR thermal camera was used to verify its readings. Measurements were taken at two locations on the probe head; in the space between sensors and on top of the protective mesh to be as close to the sensor as possible. A National Instruments C series temperature input module was used to acquire and convert measurements from the thermocouple into temperature data.

The probe head temperature measurement was taken during the warm up period of the probe, the results of which are shown in Figure 5.16 over a period of 250 seconds.

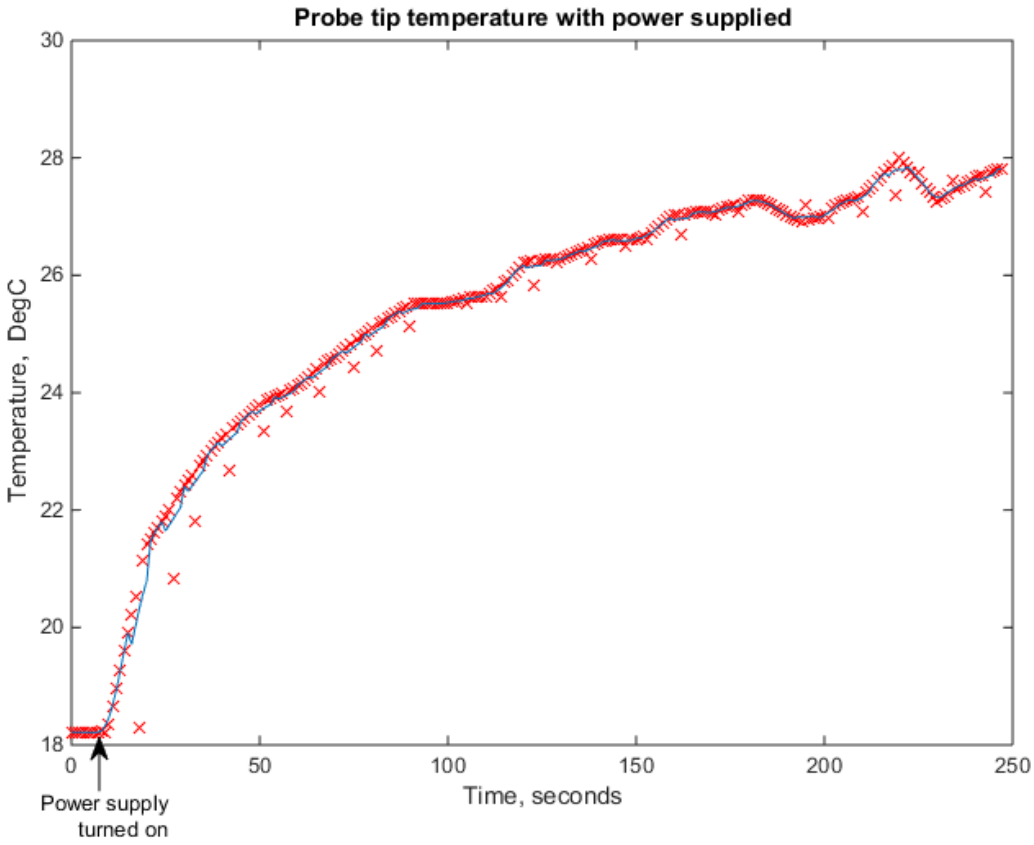



**Figure 5.16: Temperature recorded on the surface of the 5S probe tip during the excitation**

Figure 5.16 shows the point at which the power supply to the sensors was turned on and the steady increase in the probe head temperature from $18^0$C to approximately $28^0$C over a time period of 200 seconds. During the set-up of the second phase of thermocouple testing, where the measurements were to be taken on the mesh covering the sensors themselves, the thermocouple was broken and a piece of the wiring punctured the sensor, eliminating its sensitivity to pressure change.

Following the damage to the sensor head and thermocouple, the thermal camera was used to verify the originally discovered temperature increase of $10^0$C over the measurement time.

Figure 5.17 shows an image obtained from the thermal camera taken after the probe amplifier was turned on and allowed to warm up for 10 seconds until the sensor head reached a steady temperature.

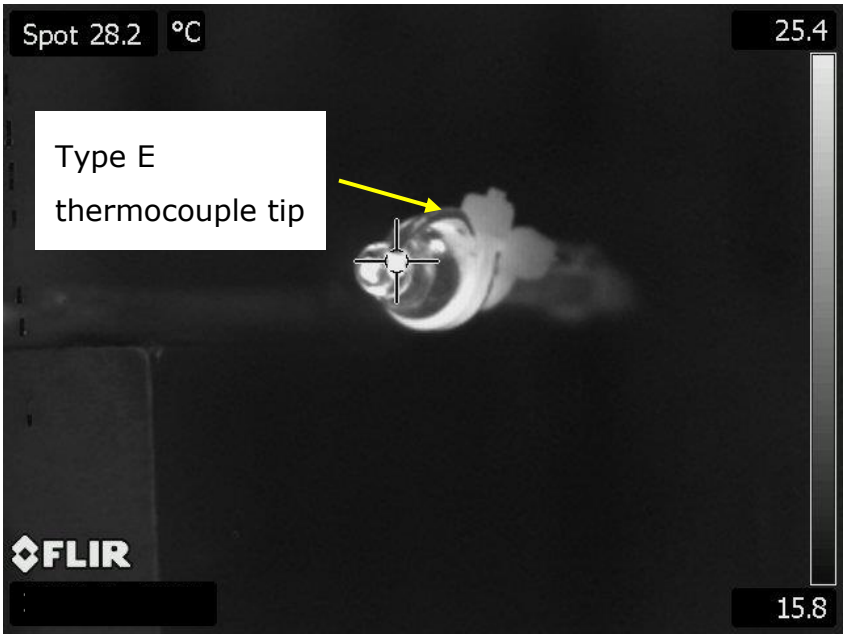



**Figure 5.17: Thermal camera image of the 5S probe head after 10 minutes of warm up**

It can be seen from Figure 5.18 that the measurement point, located at the thermocouple measurement point between two sensors, shows a temperature of 28.2$^0$C. This thermal camera image was used to verify the thermocouple measurement in figure 5.17. Following the puncture of one of the sensors, the thermal camera was used to assess the increase in heat during operation on the sensors themselves. Figure 5.19 shows the temperature, measured by the thermal camera, of the surface of the probe which is closest to the centre pressure sensor. The measurement spot shows a temperature of 32.2$^0$C, confirming an increase of more than 10$^0$C of the sensors after warm up.

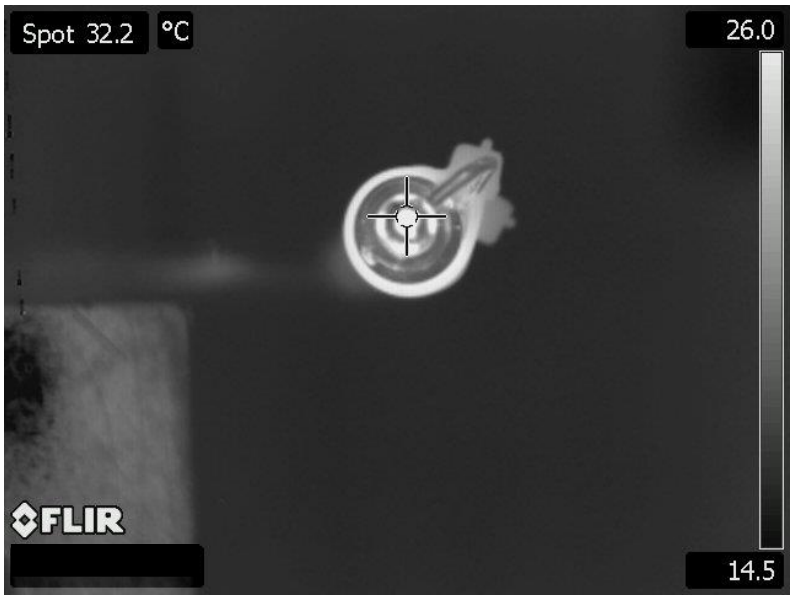



**Figure 5.18: Thermal camera image of the 5S probe head, with the measurement point located as close to the sensor**

During operation of the probe in a working fluid, the sensor temperature and that of its surrounding flow will come to an equilibrium over time. For this reason, it was decided that the probe should be allowed to reach a steady mean value before measurements were taken during any fluid application.

This conclusion, when coupled with the measurements being taken with reference to the atmospheric value, resulted in a best practice methodology for taking measurements with the 5S probe. A summary of such practice is given:

- Measurement chain set up as described in section 5.2
- Ensure that connections to and from all equipment are made and power is supplied to the PXI kit before starting laptop
- Turn on power to amplifier
- Take a zero reading from the probe after it has time to heat up to $28^0$C. Between 30 and 60 seconds was found to be, on average, the time interval in which the probe was at room temperature
- Secure the probe in place for the chosen experiment

- Take measurements after the probe has had sufficient time to equalise with the fluid temperature
- Take the raw voltage data with reference to the zero values before processing the data to pressure and beyond

## 5.4 The air jet rig

The air jet rig, which was first introduced in Chapter 4, was used throughout this investigation to assess the capabilities and frequency range of the 5S probe. The flow produced by the rig was first characterised using a single sensor probe and then the ability of the 5S probe to acquire physical flow information was established. Testing of the probe in the jet flow took place using the FAP-250(2) probe head following damage to the FAP-250(1) during the temperature testing. As well as the fast response 5S probe, a single sensor Kiel probe was used throughout this investigation. Table 5.4 gives a summary of each probe used along with its stem geometry.

| Probe name | Probe type and stem orientation | Sensor calibration | Application |
|---|---|---|---|
| **One sensor total Kiel probe - 1S(T)** | Single sensor, $90^0$ to the flow with a shroud around opening to the sensor | Deadweight tester | Used to characterise air jet rig exit flow |
| **One sensor probe – 1S** | Single sensor, straight stem with tapped opening to the sensor | Deadweight tester | Used to characterise air jet rig flow |
| **5S 1bar probe** | 5 sensor 1 bar absolute probe, swan neck stem | Deadweight tester | Used to characterise air jet rig flow and vortex shedding around metal rod |

**Table 5.4: Summary of probes used in the development of the measurement technique**

In order to understand the fundamentals of the multi sensor fast response probe, a single sensor Kiel head total pressure probe was first used to characterise the air jet rig chosen for the calibration of the 5 sensor probe. This allowed for the data acquisition process to be trialled before applying it to the 5S probe. Both total pressure instruments, the Kiel probe and the tapped sensor probe, are shown in figure 5.19.

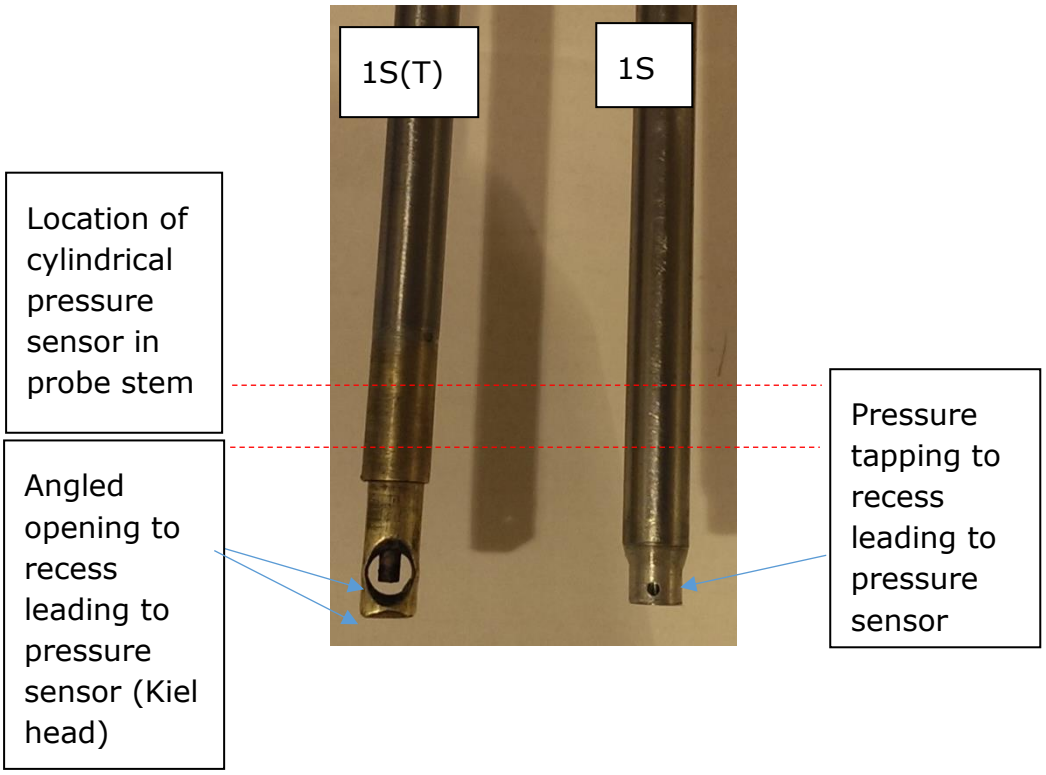



**Figure 5.19: Single sensor probes used to investigate the axisymmetric jet used in the calibration of the 5S probe**

## 5.4.1 Theory of jet flow

Tests were performed to characterise the jet flow rig. In order for the 3D calibration to be accurate and repeatable, all measurements are to be taken in the central of the jet to ensure measurement continuity.

Figure 5.21 gives an overview of the theory of axial jet flow and the way in which it interacts with the surrounding air when it's exhausted through the nozzle. In the diagram, x corresponds to the axial distance from the nozzle exit and d is the diameter of the air jet nozzle itself.

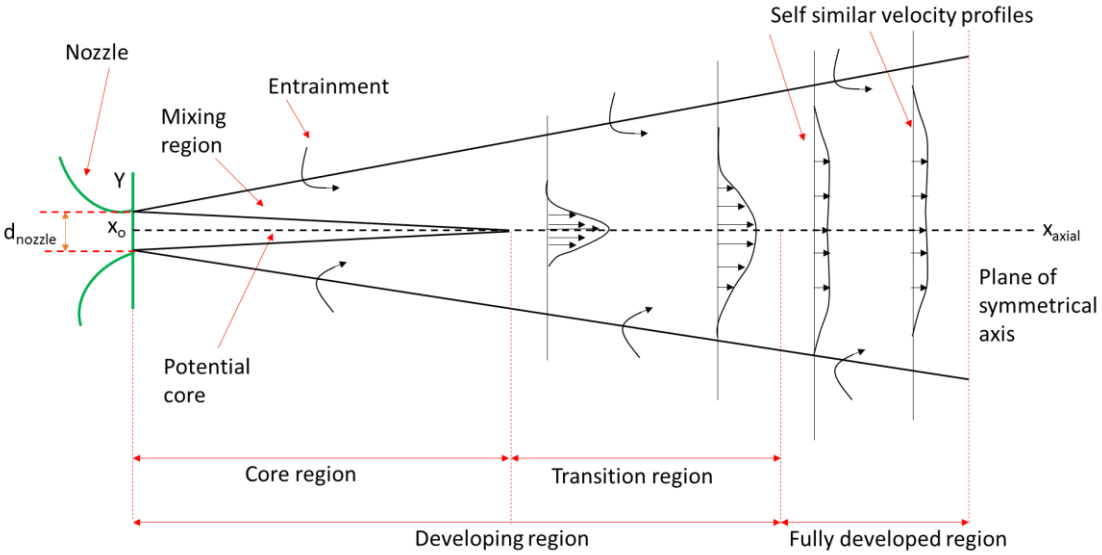



**Figure 5.20: Jet flow theory drawing, showing the change in velocity profile at increasing distances from the nozzle exit**

The flow profile of a free jet has been studied by many researchers such as Bradbury (1965) and 4 distinct regions have been identified. There is a core jet region which holds the jet exit velocity at the centre-line until the length defined as $X_{axial}/d_{nozzle} \leq 5$, where it starts to dissipate. It is preferential to take measurements at the centre of this region to ensure steady flow velocities. It can be seen that the velocity profile narrows around the centreline, reducing the width of the maximum velocity, which is accompanied by an expansion at the edges of the jet. This is due to the turbulent mixing of the jet with the surrounding air. As the jet core dissipates, a turbulent mixing region at the edges of the core forms. It is the aim of this investigation to assess where this region begins to form to ensure that measurements are taken in the core of the jet.

In the transition region, the centreline velocity starts to decay at a faster rate and atmospheric air begins to be entrained into the mixing area. This region can extend up to 20 diameters axially and is where the shear layers from the sides of the jet start to interact and merge together, causing the decay in centreline velocity and the broadening of the velocity profile across the jet radius. Finally, an area of fully developed

jet flow is seen where the velocity decays more rapidly until the jet is totally mixed out into the surrounding fluid.

This theory was tested on the low speed blower nozzle by carrying out radial pressure probe traverses across the flow exhaust at varying heights from the blower exit. The core was identified by the pressure distribution across radial traverses of the nozzle at increasing distance from the $X_0$ position. The results were used to characterise the jet to assess the point at which the measurement area could be compromised by mixing effects at the jet edges.

### 5.4.2 Characterisation of Air Jet Rig Exit

Characterisation of the nozzle jet was first carried out using the Kiel probe. Figure 5.21 shows the maximum velocity measured at the centreline of the nozzle at increasing speeds. It can be seen that the maximum Mach number measured at a motor speed was 0.22, however during the aerodynamic calibration discussed in the next chapter, the testing was carried out at higher speeds of 1900 rpm. This top motor speed corresponded to a Mach number of 0.28. This initial characterisation of the jet was carried out to gauge the correct speed for each desired Mach number and the testing in this section highlighted that the 5S probe gave more consistent results at Mach numbers of 0.2 and above, , hence the move to higher Mach numbers in latter stages of the research project.

In order to confirm the theory described in Section 5.4.1, a one dimensional traverse of the nozzle exit was carried out using the 1S(T) probe. The traverse was carried out by yawing the probe into the highest flow vector before each measurement was taken. This was carried out across the nozzle diameter at varying heights from the rig exit. The traverse was carried out at three separate distances from the nozzle

exit; 0.2 nozzle diameters from the exit, 0.5 diameters and at 1.5 diameters. Figure 5.22 shows the results from each set of measurements.

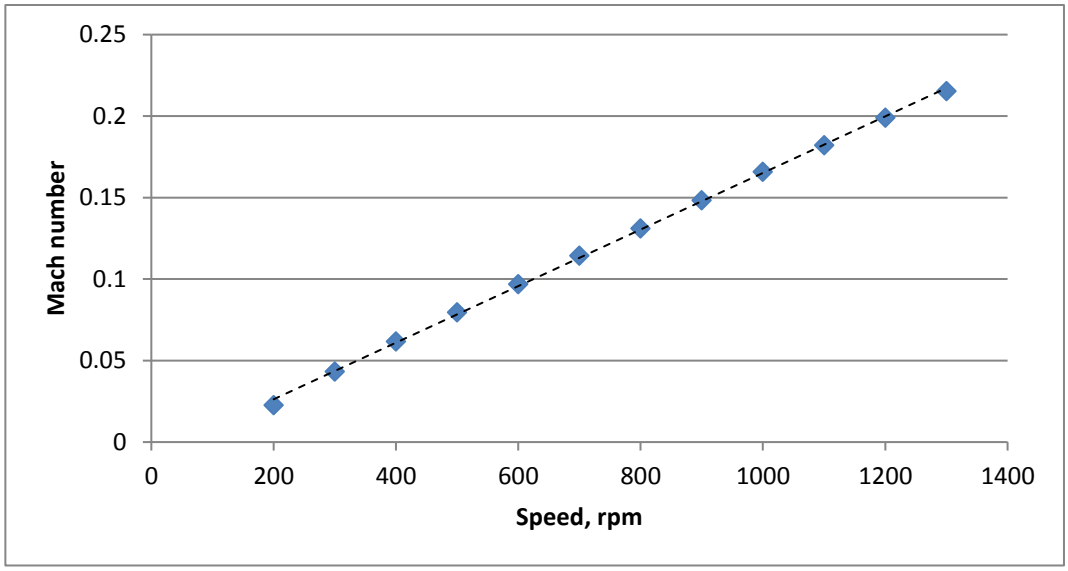



**Figure 5.21: Air jet rig Mach number calibration with motor speed in the range of 200 rpm to 1300 rpm**

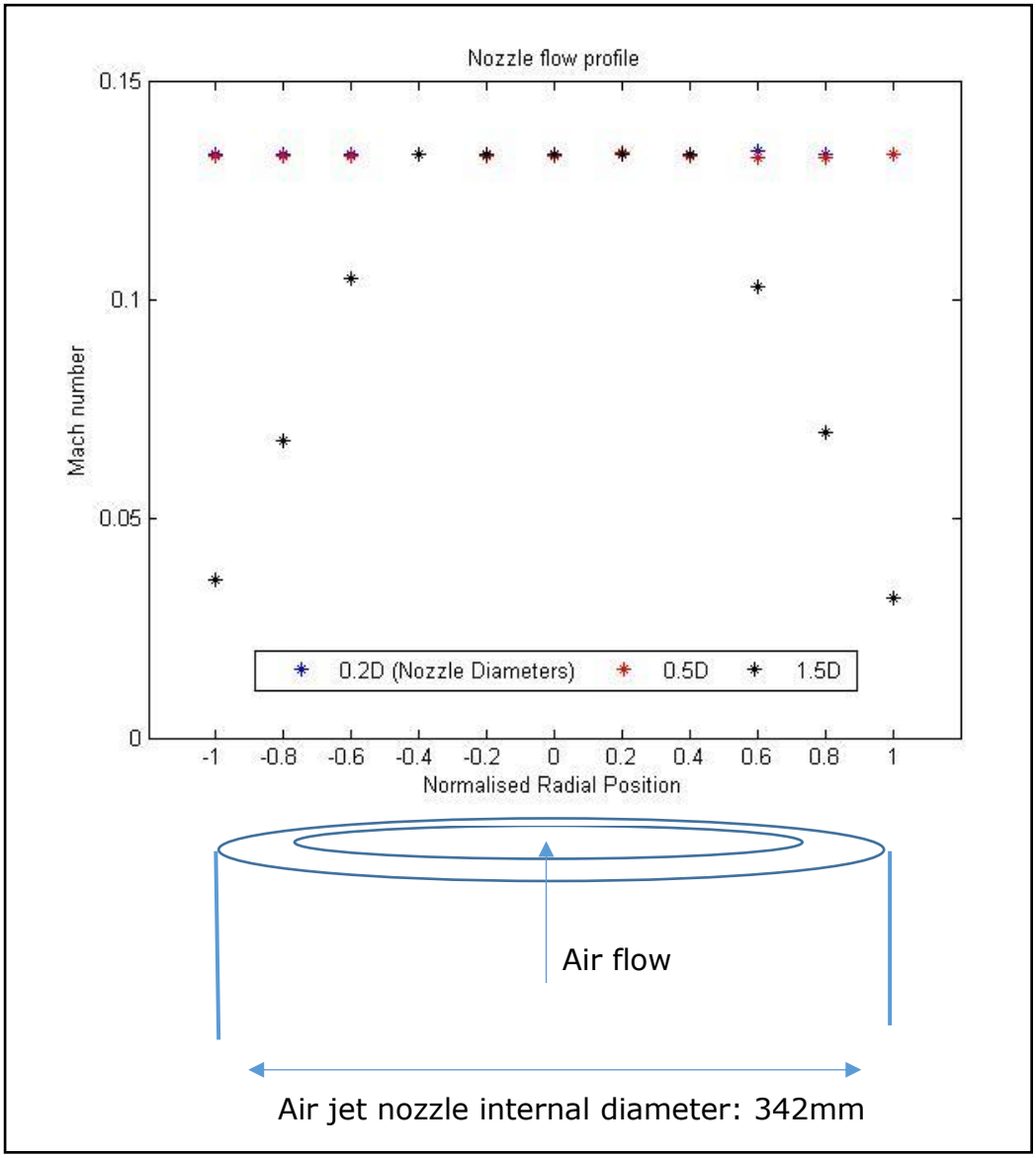



**Figure 5.22: Air jet rig nozzle traverse results**

It can be observed that at heights 0.2D and 0.5D, the velocity profile is well preserved, as shown by the measurements close to the edges of the nozzle being preserved at the maximum Mach number. The measurement at a height of 1.5D highlighted the effect of turbulent mixing at the edges of the jet by a drop in Mach number at points close to the nozzle edge. For this reason, it was decided to design and retrofit a flow extension piece to the nozzle to allow the jet velocity to be preserved throughout the measurement area. The design of this extension is explained in Section 5.5.2, where the planning of the vortex shedding experimental investigation is also discussed.

## 5.5 Defining the 5S Probe Capabilities

Having calibrated the 5S probe sensors individually, testing was carried out to assess the ability of the probe to acquire unsteady flow characteristics as well as its mechanical robustness in a relatively steady flow situation. The aim of the following investigation was to assess whether the sensor hardware in the 5S probe was capable of obtaining clear frequency information in a relatively low Mach number flow, before it was exposed to more harsh working conditions in the compressor rig. An experiment was performed to measure vortex shedding from a cylindrical tube. This experiment generated a controlled frequency to which the probe was exposed and its response measured directly against the set point. The test was designed as a fluid-structure interaction investigation, which would allow the probe to be tested in an unsteady situation, with the ability to be used in a steady vortex shedding experiment too.

### 5.5.1 Fluid structure interaction

Fluid structure interaction (FSI), whereby a structure becomes deformed due to the forces exerted on it by a surrounding fluid, and the energy separation in a Vortex street are of current interest to many researchers and designers in the field of aerodynamics. If the structure deformations are relatively slow in terms of time variation, the effect of the fluid forces can be stresses on the solid structure. If the deformations are faster, the effect on the solid structure can be much more dramatic and can lead to vibrations in the structure itself. It is particularly important to be able to predict the effect that different fluid frequencies have on a particular structure, otherwise the structure itself can easily be broken without prior warning. A famous case of this occurrence is the Tacoma bridge disaster, in which vortex induced vibrations – structural vibrations caused by the transference of energy from fluid vortices shed around the solid assembly - caused the bridge to mechanically fail and collapse. This phenomenon, known as 'lock in' occurs when one of the fluid frequencies matches a resonant frequency within the structure, resulting in oscillations which can cause damage and material failure.

There are many ways to counteract such unplanned oscillations, the most common methods being the addition of dampeners to the structure, or the periodic movement of the assembly, both of which act to alter the natural frequency of the solid so that it is not so easily matched with a fluid oscillation frequency (Kurosakat, 1987) and (Westphal, 1987). The first step in tackling vortex induced interactions is to identify the key frequencies present, which will cause a problem during operation. The aim of this experiment was to test the capabilities of the 5S probe. Throughout this investigation, the 5S probe proved that it was able to clearly identify the dominant vortex shedding frequencies.

### 5.5.2 Experimental design and set up

A flow situation was set up using a retrofit flow extension on to the air jet rig nozzle, which was used to secure a metal tube, which was to act as the body form which vortex shedding would take place. The design of the tube dimensions and the experimental parameters is discussed below. The experiment was planned to be flexible enough to give a constant vortex shedding as well as an unsteady oscillating system with the correct conditions, whereby the natural frequency of the metal tube is equal to the Strouhal frequency of the air jet. The design procedure was carried out by optimising the two frequencies based on flow speeds achievable using the air jet rig.

A nozzle expansion piece was designed due to the need to keep the flow velocity profile constant, as well as the need to define repeatable measurement positions with set distances from the tube itself. A flange was first created to match the profile of the nozzle of the air jet rig and a Perspex cylinder was attached to the flange. The duct was tailored to the experimental parameters by setting the measurement points at varying heights. The proposed measurement points are explained in appendix 4. A CAD drawing of the flow extension duct with respect to the air jet rig nozzle is shown in Figure 5.23. The tube itself was secured using a 28mm diameter compression fitting.

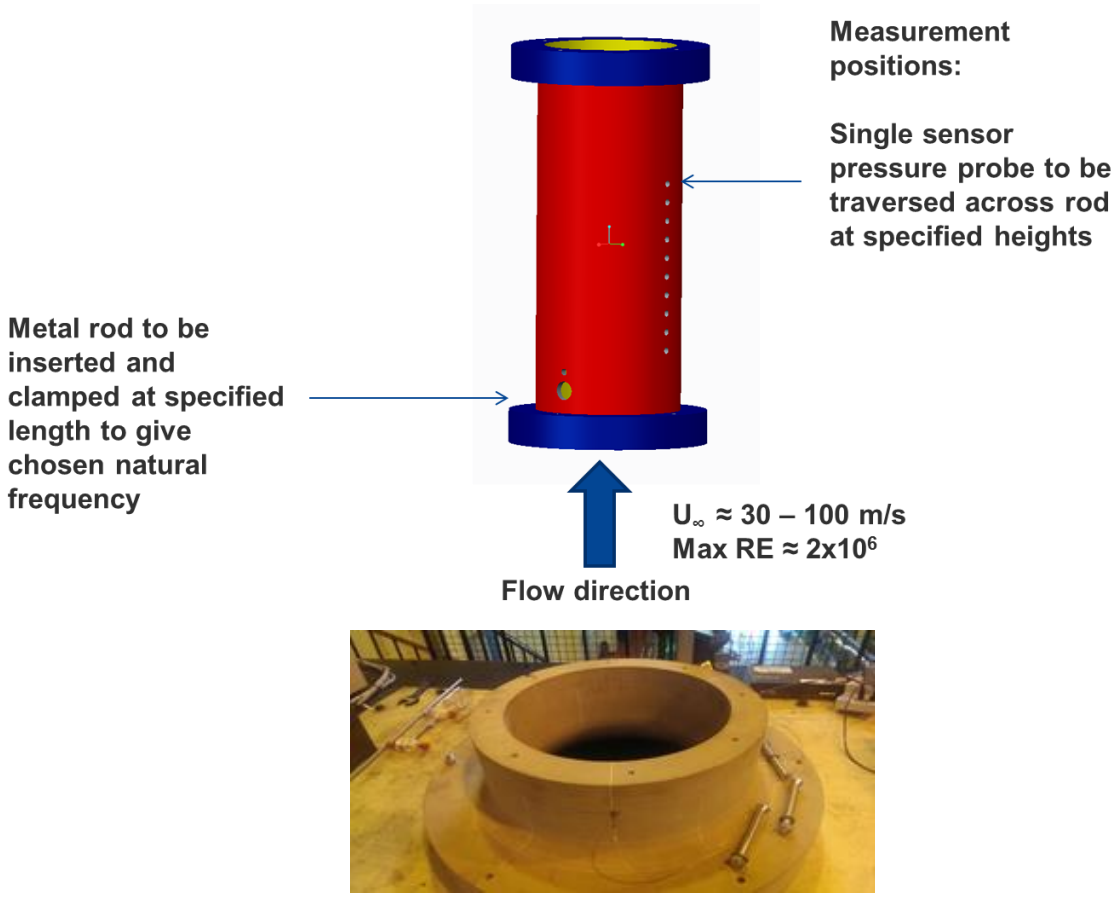



**Figure 5.23: Flow extension duct designed to be retrofitted to the existing Air Jet Rig nozzle**

The 28mm diameter tube was set at 0.5 nozzle diameters (170mm) from the edge of the nozzle to eliminate the effect of any misalignment of the flange onto the nozzle. A 10 mm diameter measurement hole was then placed at 1 tube diameter above it to measure any axial changes in pressure along the length of the tube. The measurement ports, at $90^0$ to the tube, are then also spaced one tube diameter from each other. A photograph of the experimental set-up is shown in Figure 5.24. A more detailed CAD drawing with exact dimensions is also given in appendix 4.



**Figure 5.24: The flow extension duct secured in place on the Air Jet Rig. The 28mm diameter tube can be seen as well as the probe measurement access points**

The basis of the design was around the point at which the natural frequency of the tube corresponded with the frequency at which vortices were to be shed from the tube. The lock in point was estimated using Equations 5.3 to 5.5.

Fundamental frequency of a fixed-free cantilever beam:

$$f_0 = \frac{A}{2\pi\, l^2}\sqrt{\frac{E\, I}{h^4}}$$

**Equation 5.3: Cantilever beam fundamental frequency**

Where $f_0$, fundamental frequency of interest, is a function of A, is a constant corresponding to the first node pattern of oscillation of a cantilever beam which is fixed at one end. Other parameters include:

- $I$ is the tube length, m
- $E$ is the Young's modulus, Pa
- $h$ is the mass of the tube per unit length
- $I$ is the moment of intertia, defined as $\frac{\pi}{64}\left(d_0^2 - d_i^2\right)$ for a hollow cylinder

The vortex shedding frequency is calculated from the Strouhaul number which is defined as:

$$St = \frac{fD}{V}$$

**Equation 5.4: Strouhal number calculated from the shedding frequency**

Where f is the vortex shedding frequency of interest, D is the tube diameter in meters and V is the velocity of the flow in m/s.

The Strouhal number, often taken as 0.2 for a large range of Reynolds numbers, was found by the following relation:

$$St = 0.198\left(1 - \frac{19.7}{Re}\right)$$

**Equation 5.5: Strouhal number calculated from the Reynolds number**

Equation 5.5 is valid for Reynolds numbers below $2x10^5$, making it applicable to this investigation (Blevins, 1990). It was found that the Strouhal number calculated by equation 5.5 was always within 2% of the predicted literature value of 0.2.

Matlab software was used to simulate a series of combinations of tube length, diameter, material type and Reynolds numbers until the frequencies in question were matched. This allowed the design variables such as mass per length, Youngs modulus and moment of inertia to be altered until the natural frequency of the metal tube matched the vortex shedding frequency in the air jet rig flow. Two metals were investigated, aluminium and copper. The calculations gave the trend in tube natural frequency and shedding frequency with changing velocities and tube dimensions. Logistically, the least flexible parameter was the tube length. As the probe was positioned perpendicular to the tube, the tube itself had to reach the centre of the nozzle itself, but not protrude longer than the nozzle diameter due to the presence of the flow duct. Therefore the length had to be between 190mm (20mm longer than the midpoint of the jet) to 330mm. The most sensible tube diameter was then chosen based on available standard fittings. This was chosen by fixing the Mach number to one of the highest available on the rig, 0.25 and varying the tube diameter until the frequencies matched. The results used to deduce the dimensions of the tube are shown below. It can be seen that the diameter of 28mm was chosen because the frequencies match at this dimension. Copper was chosen as the material due to the availability of the material in the designed outer diameter. The length was then determined at the same Mach number by fixing the diameter and

varying the length until a match between the frequencies was found. The test case results are shown in figures 5.25 and 5.26.

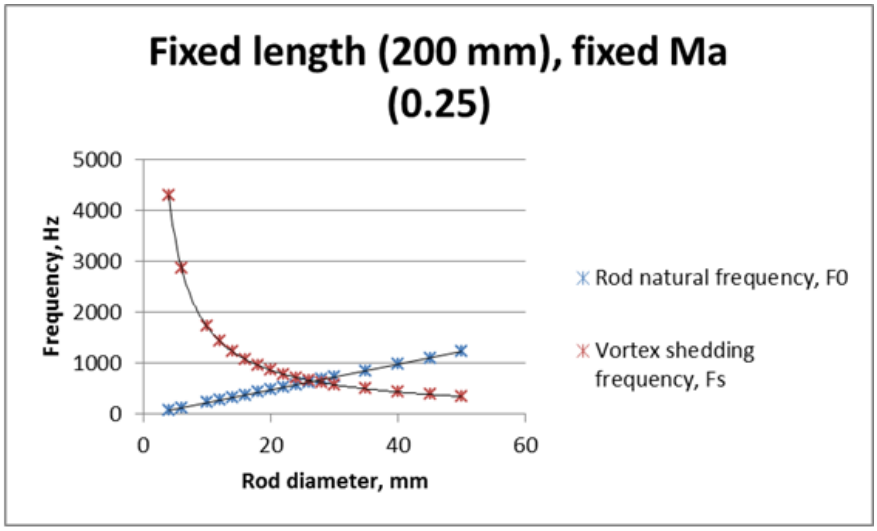



**Figure 5.25: Finding a length value where Fs=F0 at fixed diameter**

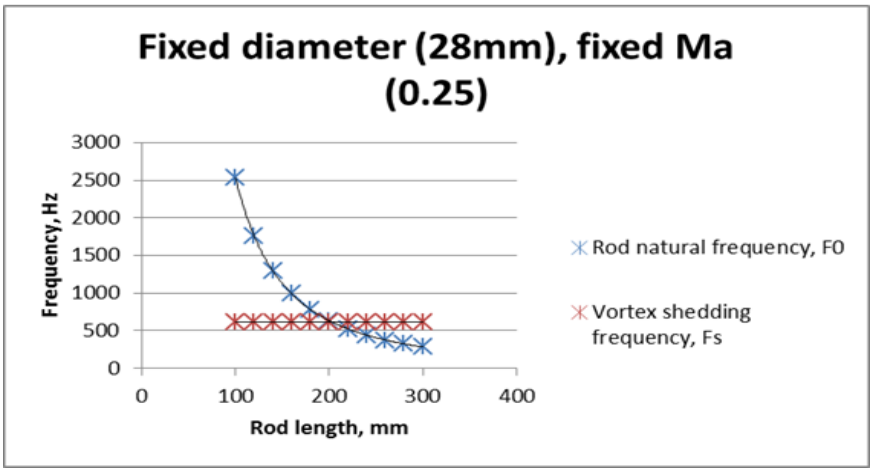



**Figure 5.26: Finding a diameter where Fs=F0 for fixed rod length**

Figure 5.25 shows the change in both $f_o$ and f when the length of the metal tube was fixed at 200 mm and its diameter was altered incrementally up to 50mm. It shows that the point at which the frequencies overlap is around 28mm. When the tube diameter was then

fixed at this value of 28mm and the tube clamping length was changed between 100 and 300 mm, the lengths set by the diameter of the jet nozzle, the frequencies met at around 200mm as shown in Figure 5.26. These results were used to verify the design of the FSI system.

Before manufacturing with the flow exhaust with the tube dimensions discussed above, the accuracy of the numerical calculations was checked using a specific test case. The natural frequency of a tube was measured using a tap test and the vortex shedding frequency was calculated by measuring the pressure field around the same tube within the nozzle flow.The natural frequency was measured using a proximity probe. The verification was carried out by tap testing the tube at varying clamp lengths. Figure 5.27 shows the predicted tube natural frequencies when a 14mm diameter copper tube was clamped at the variety of distances as shown in the legend. It can be seen that the computationally predicted values of the natural frequency for the three lengths were 1,7%, 3% and 2%, in increasing clamp lengths, away from those measured during the tap testing.

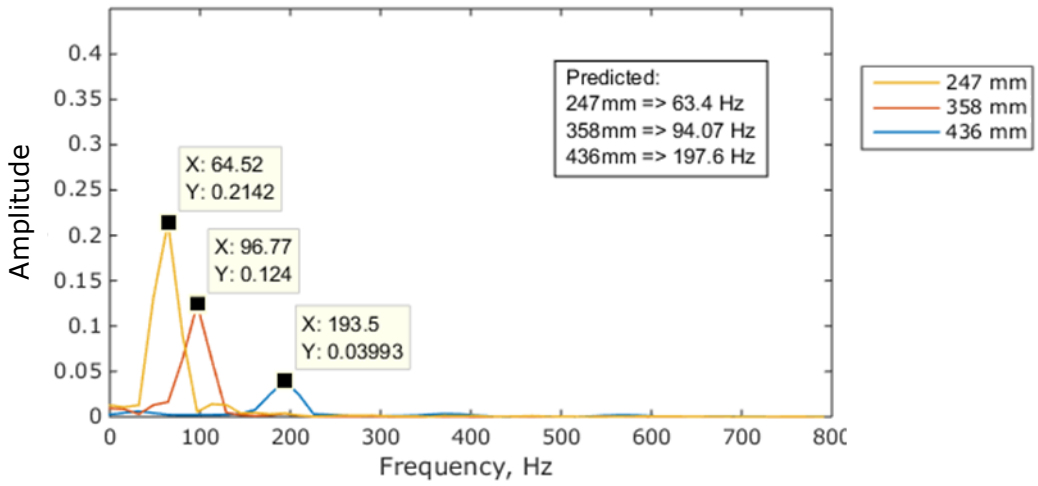



**Figure 5.27: Validation of the natural frequency calculations using a physical tap test**

Having verified the calculation of the tube natural frequency, the accuracy in the calculation of the vortex shedding frequency was

considered. The tube was clamped at a given distance at the edge of the nozzle and the vortex shedding frequency at a Mach number of 0.2 was predicted to be 799Hz. The shedding frequency was measured at increasing distances, non-dimensionalised by the tube diameter, from the tube and the results are shown in Figure 5.28. The results shown are for distance of 0 tube diameters (D) up to 9D.

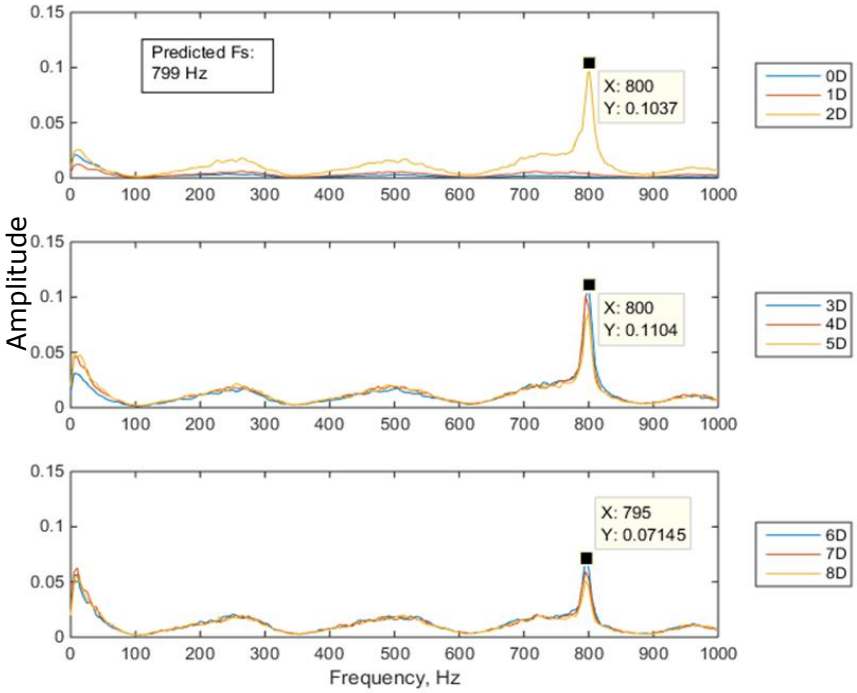



**Figure 5.28: Comparison between measured and predicted vortex shedding frequencies**

Again, good agreement can be seen between the predicted and measured results, with the maximum difference being 5Hz which was less than 1% different from the computed frequency. These results gave confidence in the tube dimensions predicted previously and the flow exhaust duct was designed around a tube diameter of 28mm.

Preliminary results for measurement of the shedding frequency at increasing Mach number, taken at 3 diameters from the tube are shown

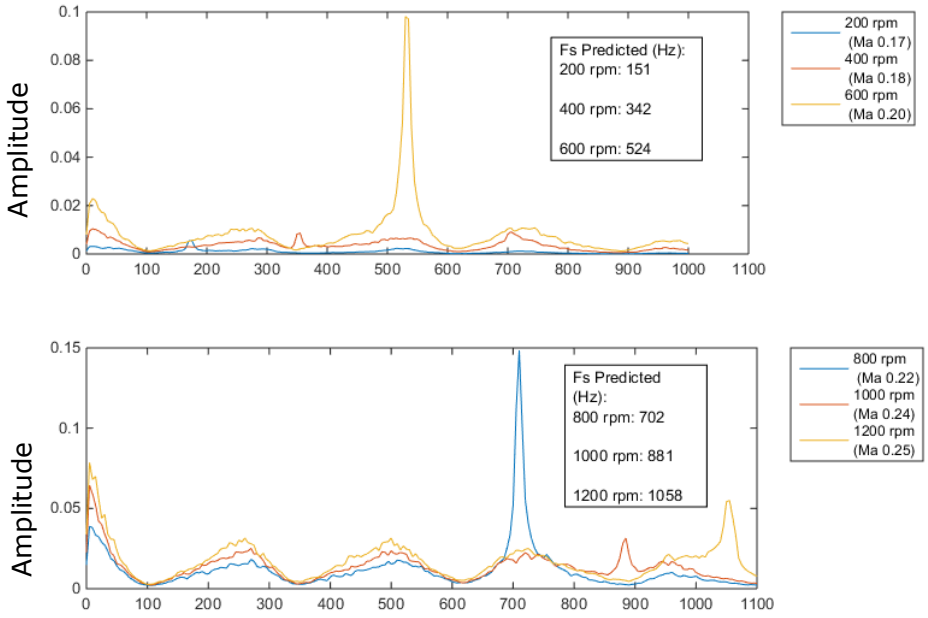



**Figure 5.29: Variation of measured vortex shedding frequency with increasing Mach number**

It can be seen that at increasing Mach numbers the shedding frequency can be seen between Ma 0.2 – 0.25. The reason that the peak did not appear below 0.2 Ma is that the velocity of the air flow was too low to produce vortex shedding. The frequency peak is then measured after Mach number 0.2. Its intensity does however decrease after Ma = 0.22. This could mean that at this distance of 3 tube diameters away, the probe was still in the wake of the cylinder, and the frequency seems to be washed out in the noise of the system at the lower speeds.

During the initial stages of the investigation, a strain gauge was attached to the tube to measure the oscillations found at the lock in point. The tube was found to be too large in diameter to be affected by the oscilating drag and lift forces exerted on it during the experiment. A much smaller diameter tube would have been capable of producing visible tube vibrations, however the Air Jet rig was not capable of producing jet speeds fast enough to achieve a lock in point. The stiffness

of the tube was also considered. The Youngs modulus of the chosen material was almost double that of aluminium, meaning that the experiment may have been more successful in terms of producing Vortex Induced Vibration in the tube if a material with lower stiffness was used. As a result, the designed experiment was used as a vortex shedding set-up, as opposed to a Fluid Structure Interaction experiment, which allowed the capabilities of the probe to be assessed in a steady environment. This will allow the 5S probe to be tested in terms of its ability to pick up rapid periodic changes in the flow.

### 5.5.3 Vortex shedding experimental results

The vortex shedding rig was run with the conditions shown in Table 5.5. It shows the various motor speeds that the air jet rig was set at and their corresponding velocities, non-dimensional parameters and predicted vortex shedding frequencies.

| Nozzle motor speed [rpm] | Velocity [ms-1] | Mach number | Reynolds number | Predicted vortex shedding frequency [Hz] |
|---|---|---|---|---|
| 500 | 29 | 0.08 | $5 \times 10^4$ | 204 |
| 600 | 35 | 0.10 | $6 \times 10^4$ | 248 |
| 700 | 41 | 0.11 | $7 \times 10^4$ | 289 |
| 800 | 48 | 0.13 | $8 \times 10^4$ | 332 |
| 900 | 51 | 0.15 | $9 \times 10^4$ | 360 |
| 1000 | 57 | 0.165 | $1 \times 10^5$ | 391 |
| 1100 | 63 | 0.18 | $11 \times 10^5$ | 446 |
| 1200 | 68 | 0.192 | $12 \times 10^5$ | 487 |

**Table 5.5: Table of vortex shedding experimental conditions with corresponding non-dimensional parameters and predicted Strouhal frequencies**

The main aim of this investigation was to assess the ability of the probe to capture the Strouhal frequency with a sampling rate of up to 100 kHz. The simultaneous acquisition of data, sampled at rate of over 50 kHz, was deemed essential in the assessment of turbulent quantities in turbomachines. The final application for the probe is in a compressor rig; with blade passing frequencies of 6 kHz and sample rates of over 60 kHz, a minimum of 10 samples per blade passing can be achieved. This investigation was therefore carried out to ensure that the 5S probe could acquire fluctuating data at high sample rates, to give confidence in its novelty when applied to the compressor rig.

Data has been taken behind the tube in the air jet rig using sampling frequencies between 10kHz and 100kHz to show the capabilities of the probe across its bandwidth specified by the manufacturer.

### 5.5.4 Vortex shedding frequency verification

The ability of the 5S probe to acquire the predicted vortex shedding frequencies was investigated. The results for 500rpm motor speed, sampled at a rate of 10 kHz are shown in figure 5.30. The frequency analysis was carried out using both a standard FFT function as well as the predefined pwelsch function in Matlab, which uses Welch's overlapped segment averaging to arrive at a much smoother estimate of the power density spectrum (PDS).

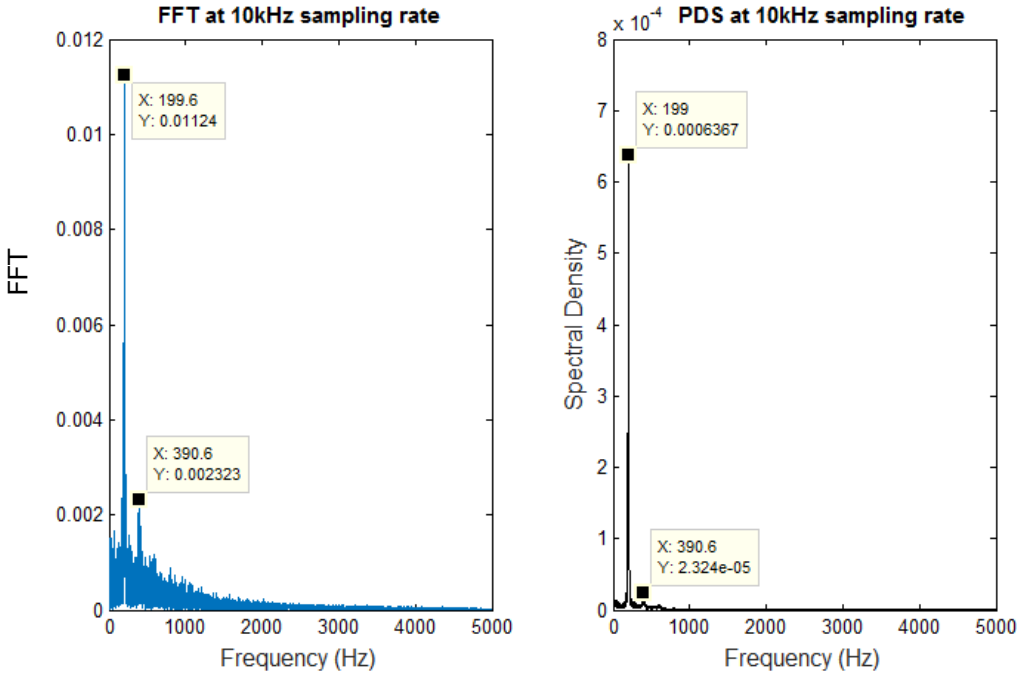



**Figure 5.30: FFT and PDS results at a motor speed of 500rpm**

It can be seen from the FFT and PDS analysis that the dominant frequency in the flow is 199.6Hz with an error of ±0.34 hz. This is within 5% of the predicted Strouhal frequency as shown in Table 5.4.

The actual frequency calculated was 199 Hz which was used to calculate the number of samples required per period. The number of samples per period was calculated as in Equation 5.6.

$$Samples\ per\ period = \frac{f_{sample}}{f_{blade\ passing}}$$

**Equation 5.6: Number of samples per vortex shedding period**

The pressure was sampled for 3 seconds at 10 kHz, making the total length of the signal equal to 30,000 samples. The first 1000 samples of the signal were used to obtain the FFT results in figure 5.31. This corresponded to a time of 0 to 0.1 seconds. If the signal was truly sampled at 10 kHz and there were 50 samples per period, then there should be 10 periods in a 5 millisecond signal. The result shown in figure 5.32 shows the number of samples taken per period, with the same data displayed in fig 5.33 with respect to time.

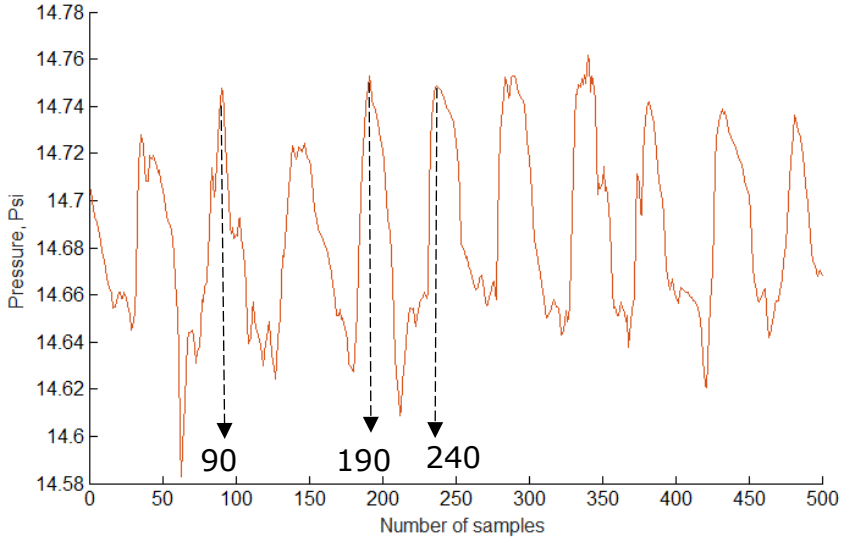



**Figure 5.31: Vortex shedding at motor speed of 500rpm, acquisition rate of 10 kHz. Number of samples per period shown on the x axis.**

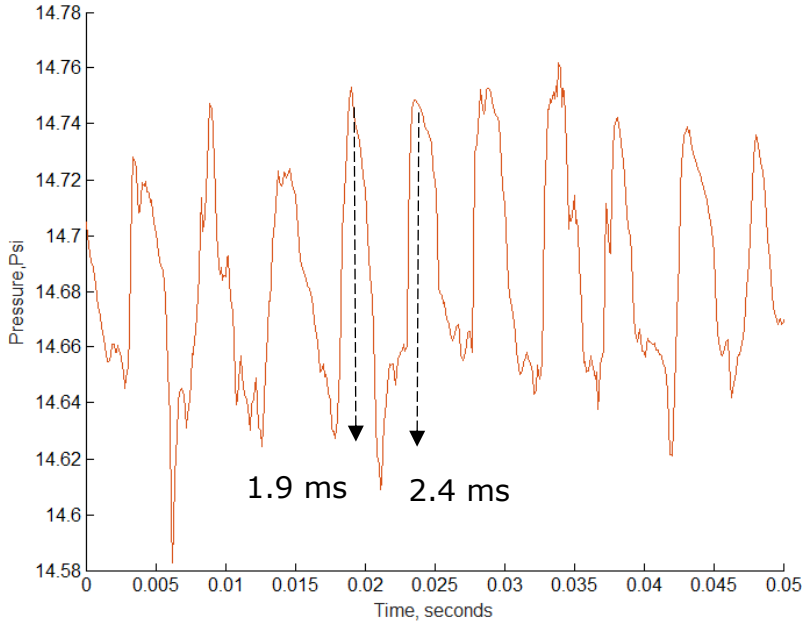



**Figure 5.32 : Vortex shedding at motor speed of 500rpm, acquisition rate of 10 kHz. Time interval of 5ms shown between each period.**

Data was taken at a range of sample rates as well as motor speeds to show the ability of the probe to maintain the integrity of the results over the proposed acquisition bandwidth. A clear peak at 311 Hz is shown in Figure 5.33 when a sampling rate of 100 kHz was used at a motor speed of 800rpm.

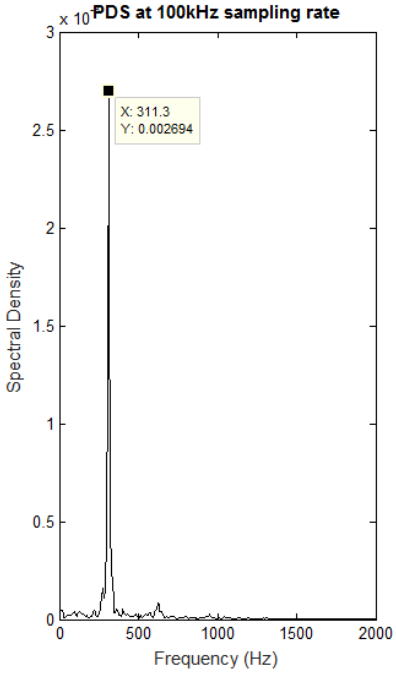



**Figure 5.33 : Frequency analysis showing the vortex shedding frequency of 311 Hz using a sample rate of 100 kHz**

Pressure signals were obtained simultaneously from all 5 sensors on the probe to show where the vortex shedding was occurring during the experiment. The probe sensor positions have been superimposed on to the tube which is obscuring the flow. Figure 5.35 shows the positioning of the sensors in the wake of the tube.

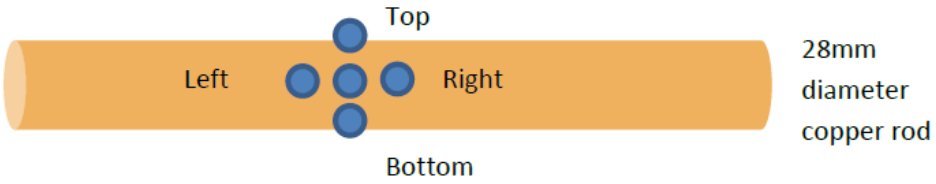
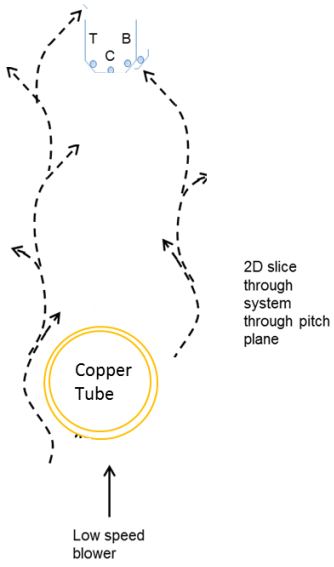



**Figure 5.34: Approximate positioning of the 5S probe sensors with respect to the copper tube. Not to scale**

Figure 5.35 shows the author's interpretation of the vortex shedding experiment with respect to the metal tube.The prediction shows that the top and bottom sensors should be recording pressure oscillations which are 180degrees out of phase with each other. This expectation is assessed by looking at the time series signals obtained from the sensors in question.




Air jet rig

**Figure 5.35: Author's interpretation of vortex shedding around experimental set-up. Not to scale**

It was predicted that the top and bottom sensors would record a clearer Strouhal frequency than the other three sensors as they'd be seeing the shedding of either side of the rod, whereas the other sensors would be picking up the frequency content of the merging wake. The results for the top sensor taken at a motor speed of 1000 rpm and for the bottom sensor at a motor speed of 800 rpm are shown in Figures 5.36 and 5.37 respectively.

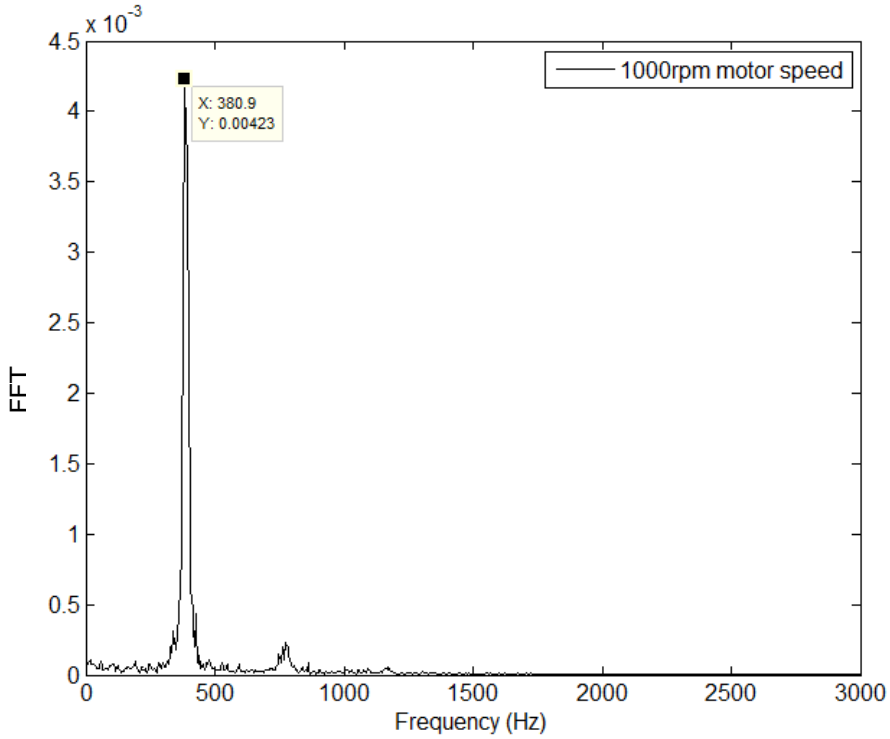



**Figure 5.24: FFT result from the top sensor, taken during vortex shedding at a motor speed of 1000 rpm**

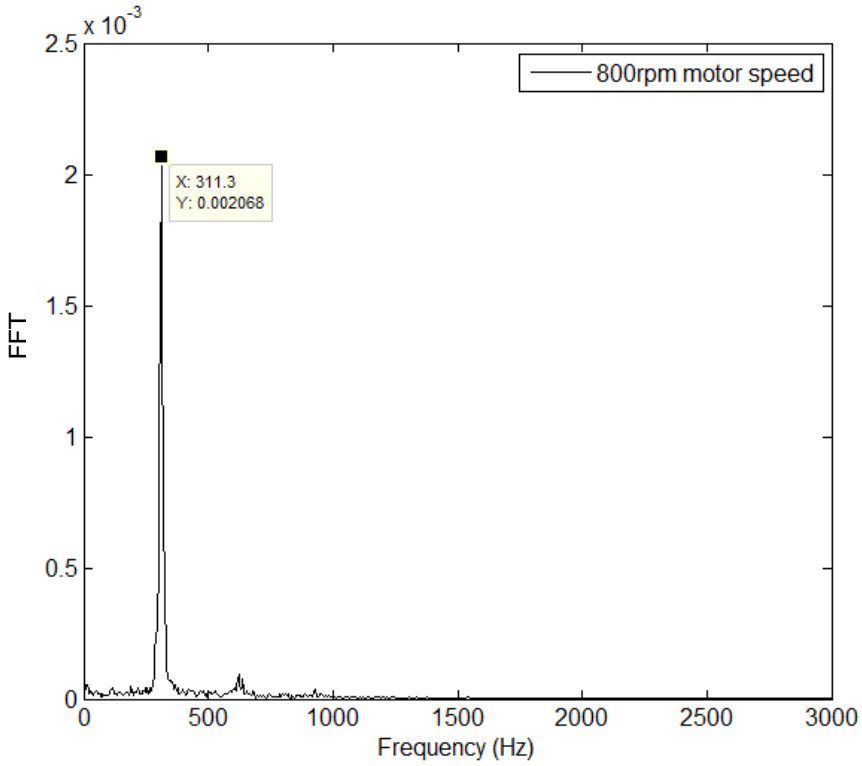



**Figure 5.37: FFT result from the bottom sensor, taken during vortex shedding at a motor speed of 800 rpm**

The frequency results in Figures 5.36 and 5.37 highlight the fact that the sensors can obtain dominant flow frequencies clearly. The time series results are also shown to see if the probe is able to not only acquire the correct frequencies from individual sensors, but also if it is able to simultaneously acquire the pressure fluctuations caused by the alternative shedding of vortices around the copper tube.

Two test cases were used to demonstrate this ability to acquire simultaneous vortices in both sensors exposed to the rod edges. The results of the first are shown in Figure 5.39, and are from data taken at the 1000rpm case and at a sample rate of 30 kHz. The vortex shedding frequency, as shown in Figure 5.37, was found to be 380 Hz. The time interval between shed vortices was therefore calculated to be 2.6ms, as shown in the time series data. Similarly, Figure 5.38 shows the time

series data from the 800rpm case which was proven to have a dominant shedding frequency of 331 Hz. The calculated time interval between vortices being shed of 3.2 ms is shown clearly in figure 5.39.

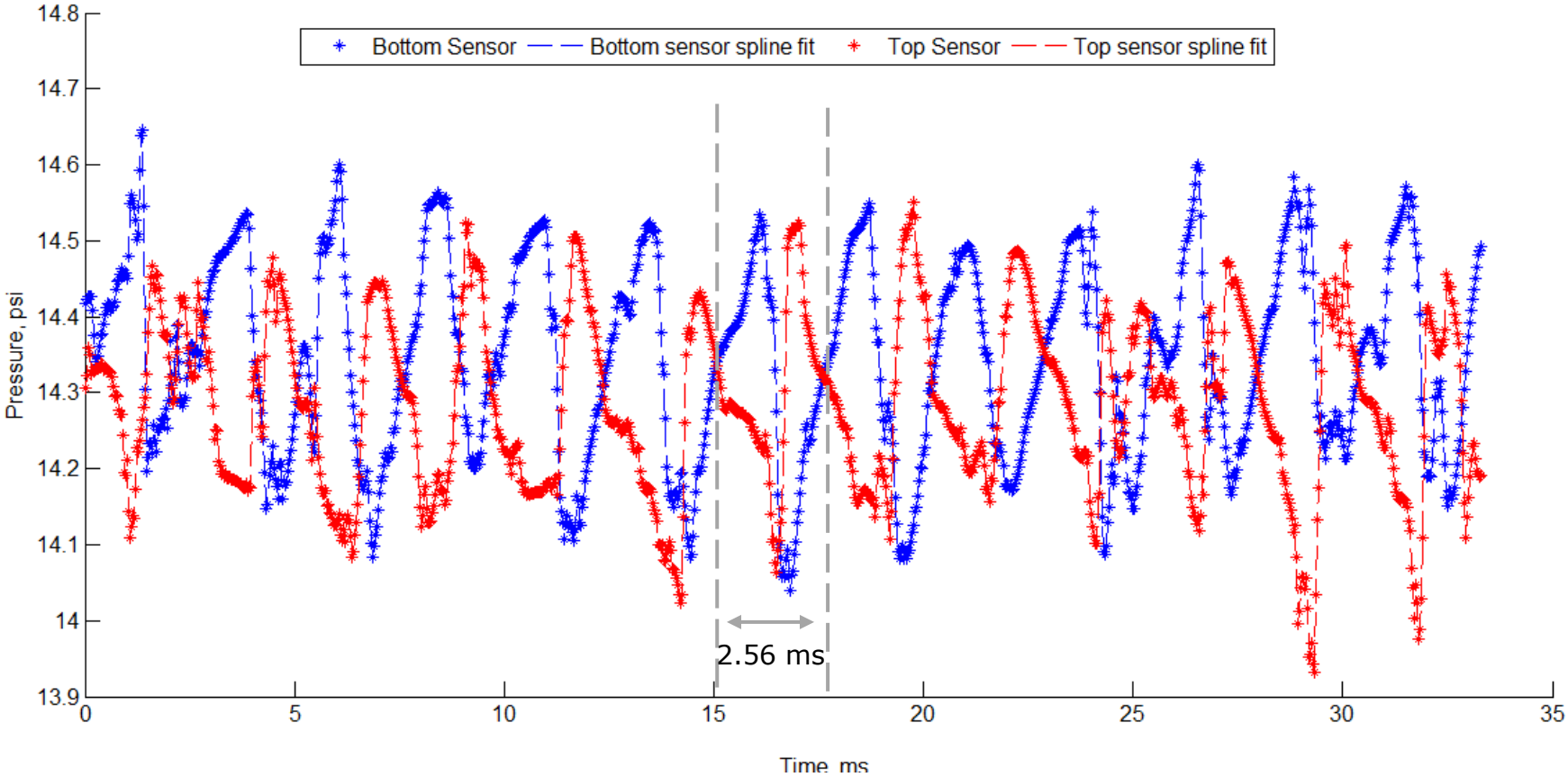



**Figure 5.38: Vortex shedding time series, taken at a motor speed of 1000 rpm. Alternative vortices reflected in the pressure traces acquired by the top and bottom sensors of the 5S probe**

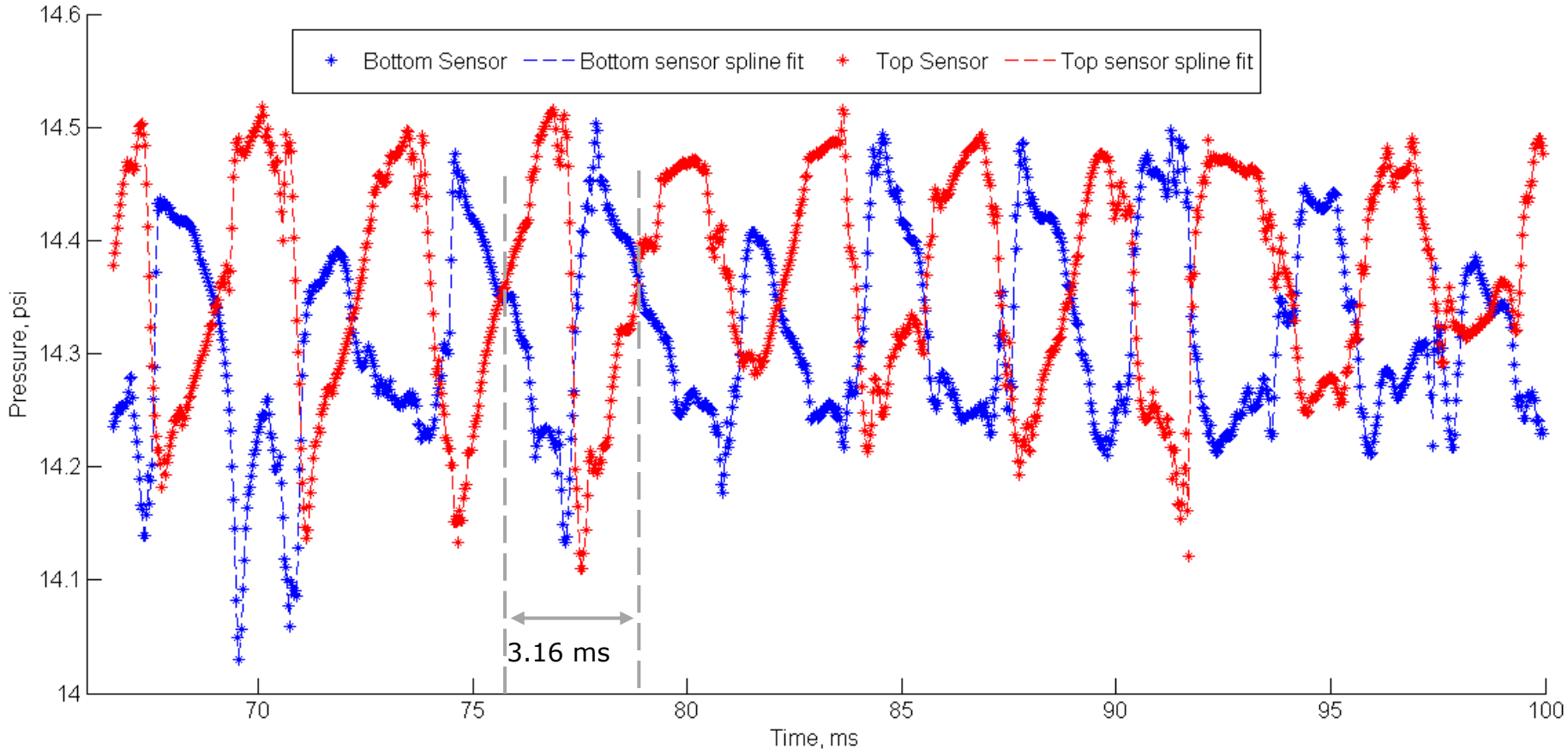



**Figure 5.39: Vortex shedding time series, taken at a motor speed of 800 rpm. Alternative vortices reflected in the pressure traces acquired by the top and bottom sensors of the 5S probe**

### 5.5.5 Visual inspection of the individual sensors after initial testing

Following the sensor calibration and initial characterisation of the 5S probe, a visual inspection was carried out after approximately 250 hours of use. Although this probe was not used for the full 3D calibration and compressor testing due to the damage to one of the sensors during testing, it was useful to see the effect of this initial testing on the probe itself. Figure 5.40 shows microscope images of the sensors at a 4 times magnification. These images were taken prior to the damage caused during temperature dependency testing so all sensors are working correctly at this stage.

It can be seen that, other than a small amount of surface damage to the protecting screens, at this stage the probe sensors were in reasonably good condition. The damage was most likely caused by small dust and debris particles in the flow as the air was drawn from outside of the building which housed the air jet rig. The fact that the screens themselves are still in good condition despite the unfiltered air gives confidence that the sensors are well protected.

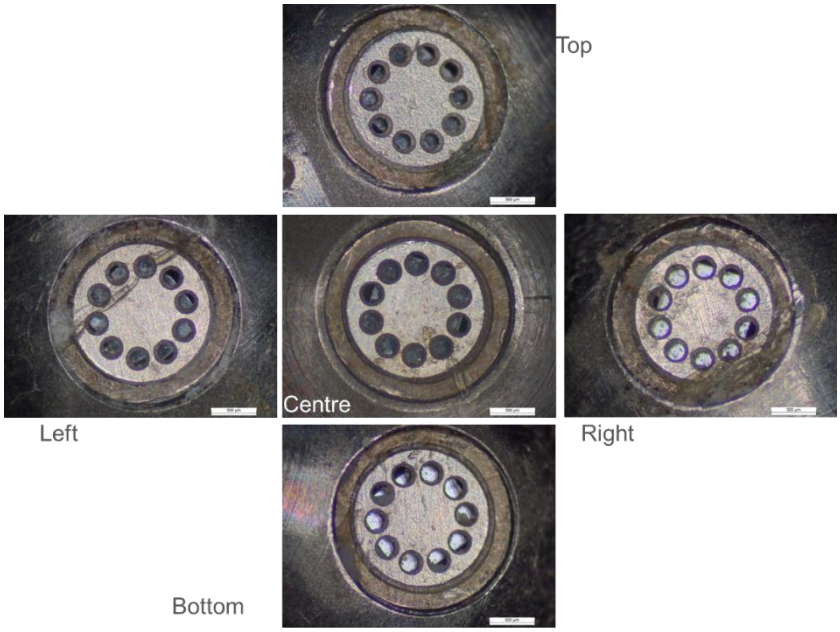



**Figure 5.40 : Microscope images of the FAP-250(1) sensor**

## 5.6 Conclusions

This chapter highlights the capabilities of the 5S probe when used as a set of standalone sensors as well as a working probe where sensor measurements are taken simultaneously. A best practice method of taking measurements was defined and thereafter all data was taken with respect to ambient conditions. It was decided that, although compensation modules manufactured at the sponsor company gave a smaller drift in the sensor calibrations over the temperature range of $25^0$ to $50^0$ than the Kulite modules, the original compensators would be used during testing in the compressor rig. The measurement chain was also presented and both the hardware and bespoke data acquisition software were proven to work effectively in this chapter. Following the successful vortex shedding investigation, whereby the effect of the alternating vortices can be clearly seen in both the frequency analysis as well as the raw time data, it was determined that the 5S probe was ready to undergo aerodynamic calibration. This chapter begins to highlight the novelty in the measurement technique when going forward through directional calibration and testing in an industrial style.

# Chapter 6: 5S Probe Calibration

## 6.1 Introduction

Following the sensor calibration and initial testing as discussed in Chapter 5, this chapter aims to discuss the methodology behind its full 3D aerodynamic calibration in preparation for rig testing. A general discussion on the different methods of aerodynamic calibration is given. The selected aerodynamic calibration technique is presented along with the results obtained when applied to the 5S probe. Two interpolation methods are discussed; a linear method which allows unknown flow angles to be deduced through spline fits of the calibration data and a polynomial method which plots the data as polynomial surfaces of varying orders. This chapter also includes an analysis of the uncertainty found within the 5S probe measurement technique to give an estimate of the boundaries within which experimentally derived quantities lie.

## 6.2 Calibration types

There are various calibration techniques which can be applied to multi sensor pressure probes. The necessity for the application of each method to the 5S probe is discussed in the following sections. The three methods are as follows:

- Sensor calibration
- Aerodynamic calibration
- Unsteady calibration

### 6.2.1 Sensor calibration

During the sensor calibration, the raw voltages obtained from the probe sensors are mapped against a range of known applied pressures, in order to obtain the sensitivity (mV/psi). In order to

calculate experimental flow quantities, the sensor calibration must first be carried out. The procedure, as described in more detail in Chapter 5, consists of exposing the sensors to a range of steady and repeatable pressures using a deadweight tester, with the output voltage being recorded at each pressure interval. The accuracy of this calibration is an essential first step for carrying out the aerodynamic calibration.

### 6.2.2 Aerodynamic calibration

An aerodynamic calibration was carried out by exposing the 5S probe to a series of angles of attack in a steady air jet, with the aim of viewing the pressure distribution around the probe tip over a range of flow positions. This then allows the flow angles to be deduced when the instrument is inserted into an unknown flow.

There are two potential methods which can be used during the aerodynamic calibration of multi hole probes; the nulling or the non-nulling method. In the nulling method, 3-hole calibration is performed for pitch angle only. Fixed angles of pitch are set relative to a straight jet of known velocity and the sensor pressures in the pitch angle plane are recorded. This procedure is repeated at a range of Mach numbers, such that the relationship between sensor pressures, pitch angle and flow velocity can be derived. For the measurement of yaw angle, the probe is rotated in yaw until the sensors either side of centre in plane of rotation are balanced. This is done for each measurement point during testing. This method does not require a full 3D calibration, however it is only suited to steady 5-hole probes measuring average flow conditions.

The non-nulling technique performs a full 3D, 5-hole calibration for both yaw and pitch. This is the aerodynamic calibration technique applied to the 5S probe, and the technique discussed in this chapter. Figure 6.1 shows the yaw and pitch planes within the probe's frame of reference. The key at the bottom of the figure shows the naming of each of the sensors numbered in the schematic.

| **Sensor** | P1 | P2 | P3 | P4 | P5 |
|---|---|---|---|---|---|
| **Orientation** | Centre | Left | Right | Bottom | Top |

It should be noted that the left sensor, P2 is in the left most position when viewing the oncoming flow from the probes frame of reference.

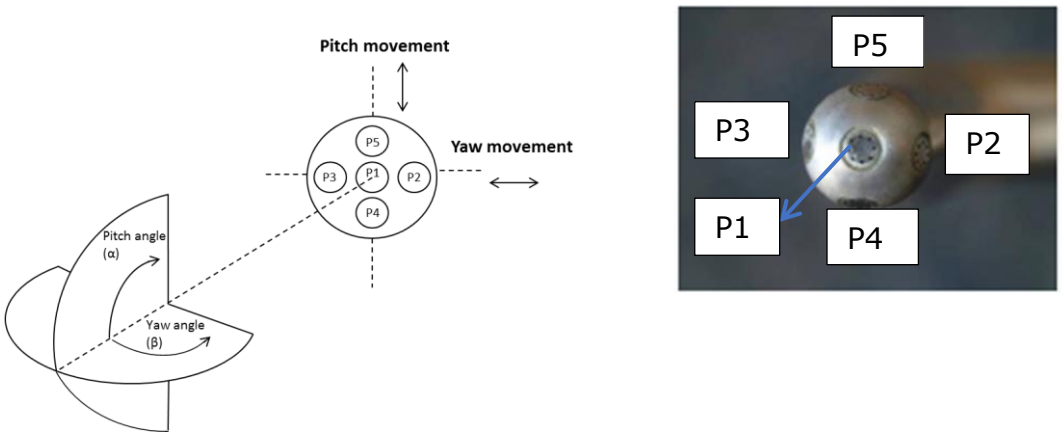



**Figure 6.1: Yaw and pitch planes defined in relation to the five pressure sensors at the tip**

The working principle of the 5S probe is similar to that of a standard 5-hole probe, however the pressure transducers are located in the tip of the probe as opposed to at the end of long flexible tubes, thus significantly improving the frequency response of the probe. The well-known aerodynamic calibration methodology has been applied to the probe, as discussed in Section 6.5.

### 6.2.3 Dynamic calibration

Knowledge on the dynamic behaviour of fast response probes is essential due to the high frequency response of the piezoresistive sensors. There are two main factors affecting the dynamics within fast response probes; the cavity behind the pressure tapping and the diaphragm within the sensor itself (Lenherr, 2010). Firstly, the pneumatic cavity often formed between the sensor and the tapping leads to signal attenuation and uncertainty in the true frequency response of the probe. The effect is extremely difficult to investigate analytically and an experimental approach is often taken usingturbulence generating mesh (Lenherr, 2010) or a shock tube (Johansen et al, 2001). As the sensors in the 5S probe tip are flush mounted within the head only the cavity between the diaphragm and protective screen needs to be be considered in a dynamic calibration

A shock tube calibration is often used to define the natural frequency of piezoresistive sensors, which is used as an upper limit when determining the frequencies which can be obtained using the transducer**.** During this procedure, the probe sensor is exposed to an impulse pressure wave to deduce the natural frequency of the sensor. Awareness of the resonance frequency is essential because the sensor diaphragm starts to vibrate at this level and the reliability in the resulting amplitude reading is reduced. Too much excitement of the transducer at its natural frequency can also cause it to become damaged and unusable. As the natural frequency of the FAP-250 probe sensors had already been deduced by the manufacturer and the transducers themselves were flush mounted to the probe tip, it was deemed unnecessary to design and commission a shock tube for unsteady calibration. If such a rig were readily available, any changes to the natural frequency during assembly of the 5S probe could have been determined. It was therefore decided that the frequency limit in which the 5S probe could be used was to be set at 50% of the natural frequency quoted by the manufacturer as 200 kHz. This allowed the

probe to be used safely in both the compressor rig as well as the low-pressure turbine rig.

## 6.3 Air jet rig adaptations

The air jet rig, as first introduced in Chapter 4, was used in the aerodynamic calibration of the 5S probe, the procedure for which required the probe to be moved in both the pitch and yaw direction. The traverse motor was used to alter the yaw position of the probe through the designated angles and, when mounted onto the pitch table, to adjust the pitch angle between ± $5^0$. To set the designated angles in both planes, a pitch manipulator was designed and mounted to the air jet rig.

The range of pitch angles required was out of the scope of the readily available pitch table, therefore a combined automatic yaw and manual pitch manipulator was implemented by adapting the existing yaw traverse motor. The traverse gear allowed the probe to be rotated about the central axis of the stem, where the tip could be kept in the same spatial position but simply rotated with respect to the incoming jet flow. This effectively simulated graded changes in the angle of attack between the jet and the probe tip without having to physically move the air jet rig. The same rotation was demonstrated in the pitch plane by the combined pitch-yaw manipulator shown in figure 6.2.

The probe manipulation plate was designed as an extension to the air jet rig nozzle as shown above. A CAD drawing of the dimensions used to ensure that the probe tip be kept in the same position at every designated pitch angle is given in Appendix 5. At each pitch angle the yaw traverse motor was secured to the plate loosely using an M12 bolt and a digital inclinometer was then used to set the angle more precisely before it was tightened up.

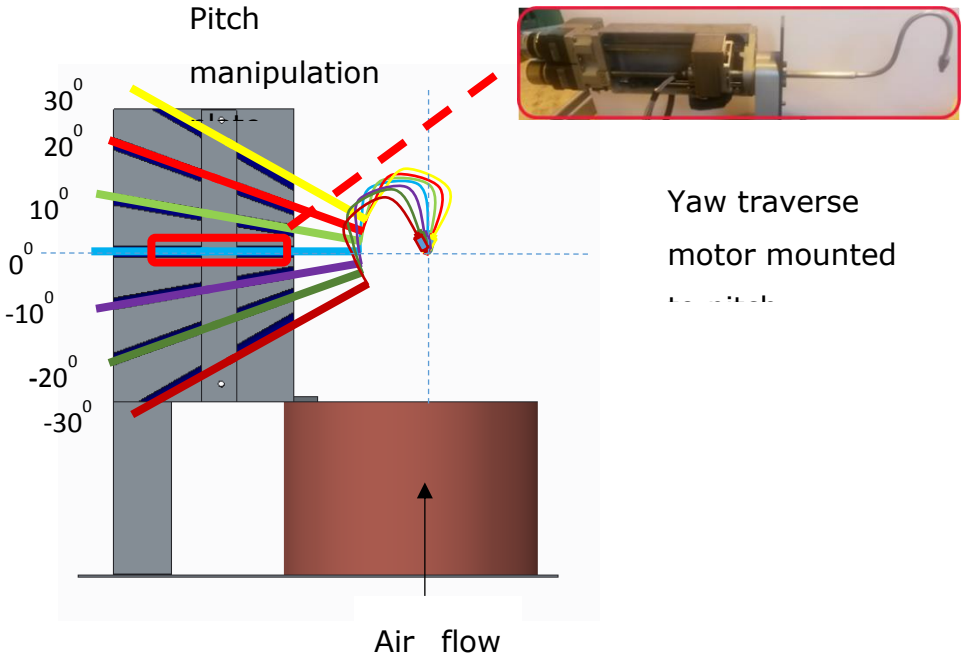



**Figure 6.2: Combined manual pitch and automatic yaw manipulation device**

## 6.4 Aerodynamic calibration procedure

The non-nulling method for obtaining calibration data for the 5S probe is presented in this section. Averaged pressure readings acquired from all 5 sensors are non-dimesionalised to give four pressure coefficients for each angular position that the probe is calibrated at. Of the four coefficients, two represent the probe angles in the yaw

and pitch directions and two signify the total and static pressures measured by the 5S probe. This method has been tried and tested, as presented throughout the literature. Dudinski and Krause (1969) non-dimensionalised the pressure readings from pneumatic 5-hole probes at a NASA research centre to arrive at a semi-regular grid of angular pressure coefficients within a yaw and pitch calibration range of $\pm 30^0$. The method has been used throughout the industry more recently by Gonsalez and Arlington (1990), Babinsky *et al* (2002), Lenherr (2010) and Georgiou and Milidonis (2014). The method was traditionally used for pneumatic probes and it has been applied in this investigation to the fast response 5S probe.

Differences in the way that other researchers have deduced experimental data, via the interpolation of the calibration data, have been observed. Many researchers (Treaster and Yacum, 1979, Reichert and Wendt, 1994 and Lenherr, 2010) have represented their pressure coefficient data as a series of surface fit equations, and then used polynomial interpolation techniques to arrive at experimental values of pressure, yaw and pitch. Section 6.6 presented this methodology along with a new, less timely method of deducing experimental values from the valibration data. The validity of this method is also presented for all non-dimensional coefficients used throughout this investigation.

The four pressure coefficients were used throughout the calibration and data reduction process to non-dimensionalise the five pressures obtained during both. The pressure coefficients, shown below in Equations 6.1 – 6.4, were used to relate the flow direction to the pressure values recorded from the probe head sensors.

$$K_\beta = \frac{(P_2 - P_3)}{(P_1 - \bar{P})}$$

**Equation 6.1: Pitch angle pressure coefficient**

$$K_{\alpha} = \frac{(P_4 - P_5)}{(P_1 - \bar{P})}$$

**Equation 6.2: Yaw angle pressure coefficient**

$$K_T = \frac{(P_1 - P_{total})}{(P_1 - \bar{P})}$$

**Equation 6.3: Total pressure coefficient**

$$K_S = \frac{(\bar{P} - P_{static})}{(P_1 - \bar{P})}$$

**Equation 6.4: Static pressure coefficient**

$$\text{Where } \bar{P} = \frac{P_2 + P_3 + P_4 + P_5}{4}$$

**Equation 6.5: Pseudo-static pressure**

The values $P_{static}$ and $P_{total}$ were taken during the calibration at each designated angle set. The flow chart in Figure 6.3 gives an overview of the methodology used to carry out the calibration.

The probe was secured at its datum of $0^0$ in the pitch and yaw directions using the pitch manipulator plate and the yaw traverse motor respectively. The yaw angle was set using the 2DOF traverse mechanism and the pitch angle was however set using a digital inclinometer. The air jet rig was set to run at 1700rpm, which translated to a Mach number of 0.28. The fan speed was set to a higher value than that used for the testing in Chapter 5 because the final application for the probe had been decided before the calibration procedure was carried out. This allowed the probe to be calibrated at

a Mach number which was more representative of the flow found within the compressor rig.

The pressure recorded within the nozzle plenum chamber was taken as the total pressure at nozzle exit. This measurement was taken using a pneumatic tapping in the plenum and was viewed using a Druck DPI 140. An atmospheric pressure measurement was taken with no flow using the same measurement block to provide the static pressure at nozzle exit, as the jet diffused into the open air during the calibration.

The probe was then yawed into the flow using the traverse motor until P1 was at a maximum and P2 to P4 were equal. This signifies the point at which the probe is facing the highest velocity vector in the air jet. At the datum point the outputs from the five pressure sensors were recorded. The probe was then set to all combinations of pitch and yaw angles with the outputs being recorded each time. This resulted in five output pressure time series', P1 to P5, for each pair of angles. Equations 6.1 – 6.5 were then used to non-dimensionalise the 5 pressure series' resulting in 4 matrices of pressure coefficients.

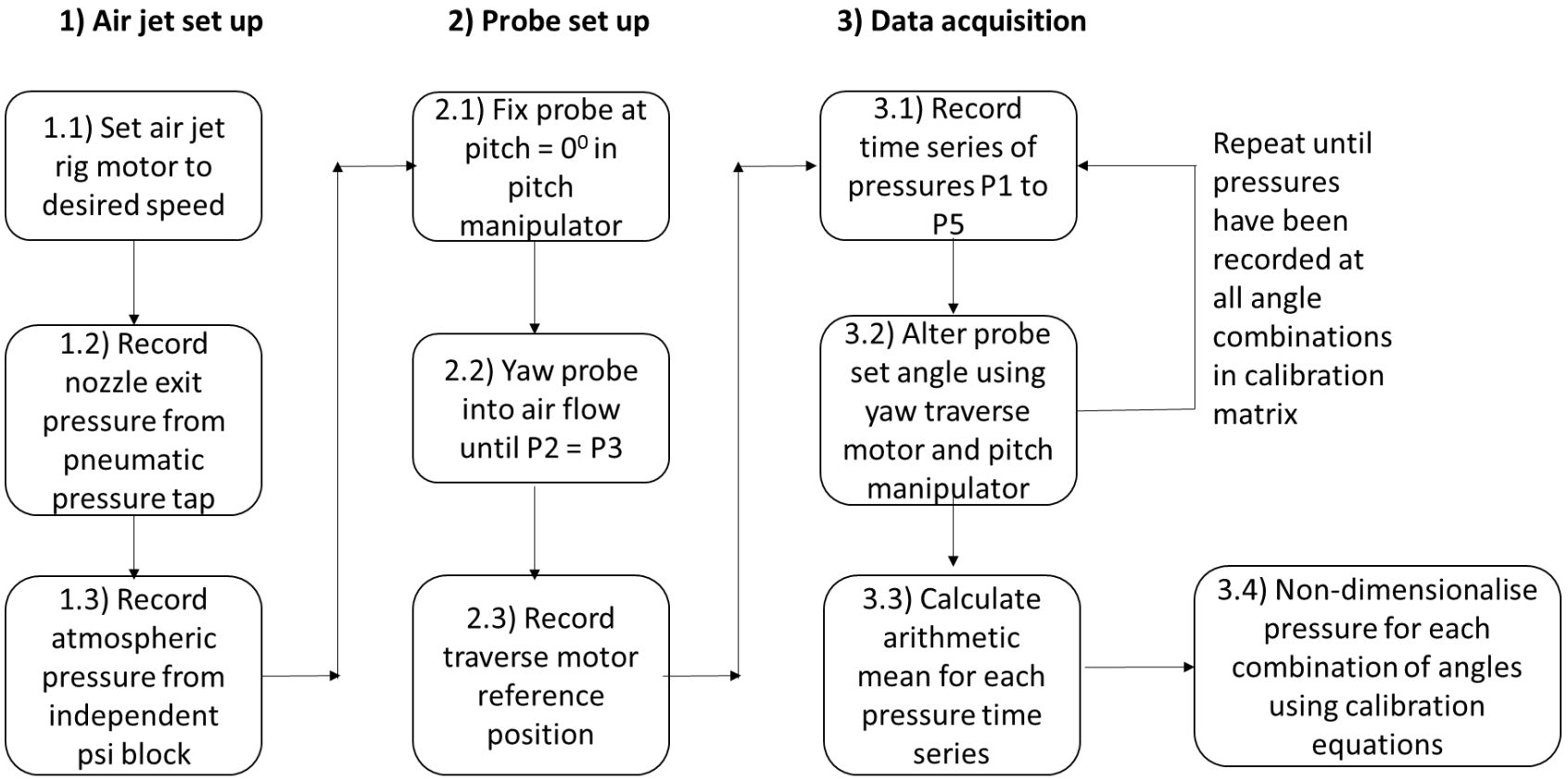



**Figure 6.3: Flow chart showing the steps carried out to complete the aerodynamic calibration of the 5S probe**

## 6.5 Calibration results

Initially, a simple 2D yaw calibration of the 5S probe was carried out, with the pitch angle set to its datum value of $0^0$. Figure 6.4 shows the pressure readings from each of the sensors when the 5S probe is exposed to calibration angles of $\pm 30^0$.

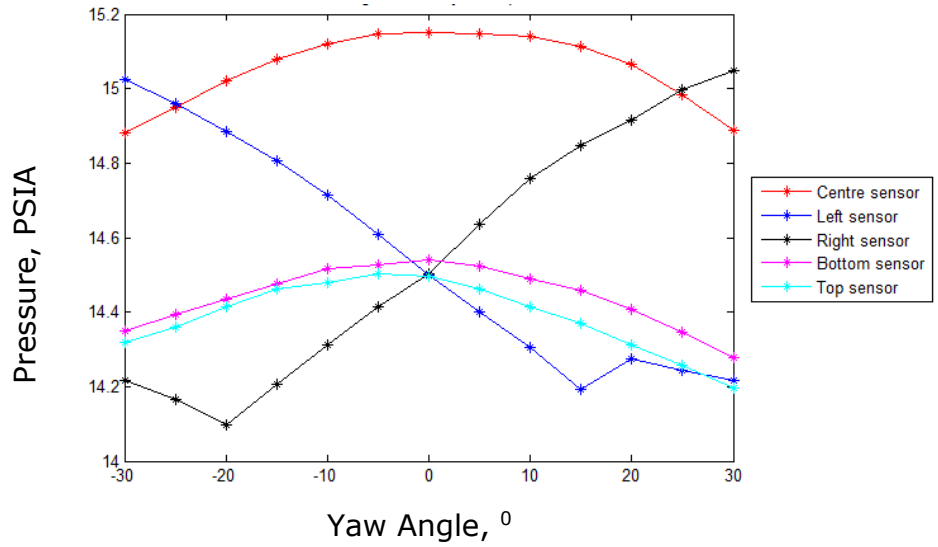



**Figure 6.4: Yaw angle sensitivity of the 5S probe**

It can be observed that at a yaw angle of $0^0$, all the side sensors are reading the same pressure and the centre sensor (P1) is giving a maximum value. This is the point at which the probe is aligned to the main flow vector within the air jet.

The result in Figure 6.4 was also compared with a graph of yaw sensitivity for the FAP-250 sensor head mounted onto a straight stem presented by Guenettee and Castner (2011) in their research paper. Their result for comparison is shown in Figure 6.5.

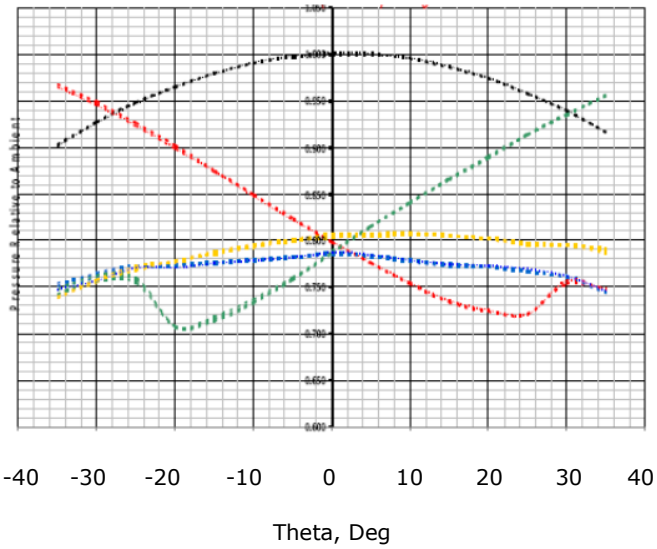



**Figure 6.5: Yaw sensitivity of FAP-250 sensor attached to a straight stem. Sourced from Guenettee and Castner, (2011)**

It is seen from this comparison that some defining features are present in both graphs, such as the increase in output pressures in the left and right sensors when they reach $\pm 20^0$. The increase in the difference between the top and bottom sensors at positive yaw angles is also highlighted during the comparison. These similarities between the results indicate that altering the stem, in this case between the straight stem used by the Kulite, MIT, NASA collaboration, and the stem α probe used in this investigation does not significantly alter the calibration characteristics of the probe. This gives confidence that the calibration data is correct when the probe stem was changed from Stem α to Stem γ.

It can however be seen that flow separation around the 5S probe at positive yaw angles causes a sharp increase in the reading of the left pressure sensor at $16^0$, whereas Figure 6.6 shows a much more symmetrical separation in the straight stemmed probe. It was assumed that this early flow separation was a result of either the

sensor head manufacture or the probe assembly into the stem. Although yaw angle variation in both potential rig applications for the 5S probe was expected to be less than $16^0$, it was decided that the probe would be yawed into the flow during experimentation to increase the effective acceptance angle of the sensor head.

To confirm the calibration range of $\pm 20^0$, an initial 3D calibration was carried out on the 5S probe at an extended range of $\pm 30^0$ in both the yaw and pitch directions. Figure 6.6 shows the results plotted as non-dimensionalsed pressure coefficients.

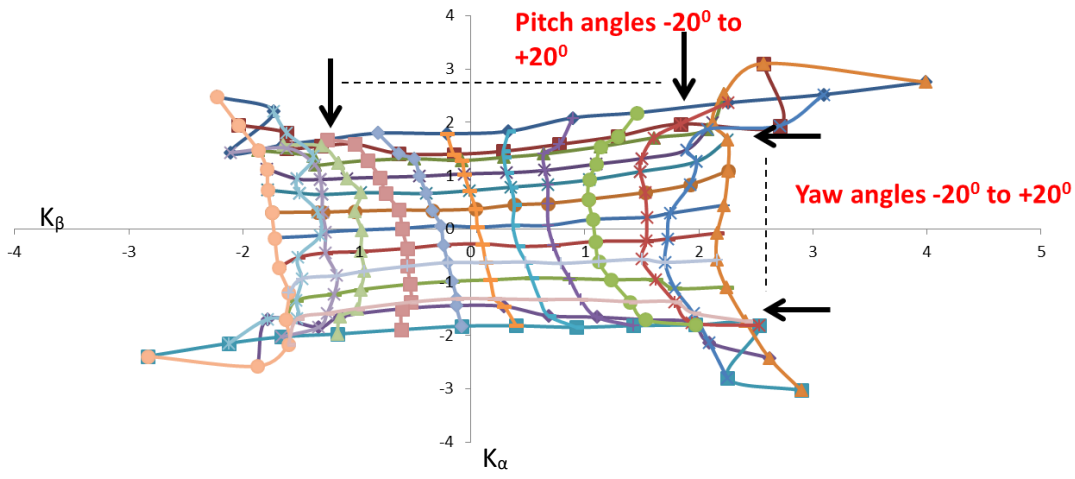



**Figure 6.6: Full 3D calibration of 5S probe at an extended calibration range of $\pm 30^0$**

It can be seen in Figure 6.6 that non-regular results were found when the calibration range was extended past $\pm 20^0$ in both directions. As flow separation was clearly observed at the corners of the calibration grid, the calibration range was limited to $\pm 20^0$.

The final 3D calibration results used throughout this investigation are given in Figure 6.7, where a grid of $K_\alpha$ Vs $K_\beta$ for each of the calibration angle is presented.

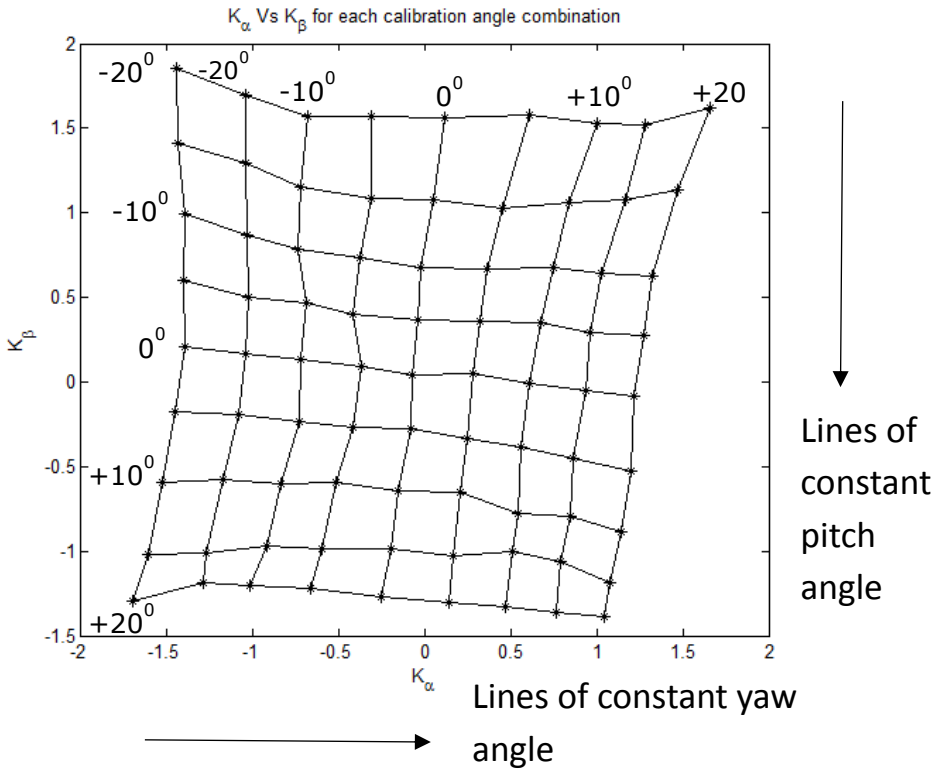



**Figure 6.7: Calibration grid showing the yaw and pitch calibration constants plotted for each designated calibration angle**

On the grid shown in Figure 6.7 each combination of yaw and pitch angles used in the calibration is represented by a single point. It can be seen however that the grid itself is not completely regular indicating that the probe head may not be completely symmetrical. This indicates the necessity of carrying out a rigorous calibration before testing the probe in an unknown flow as a purely empirical approach can only be applied to a perfect hemisphere (Johansen, 2005). All four of the pressure coefficients resulting from the aerodynamic calibration are given in Figures 6.8-6.11.

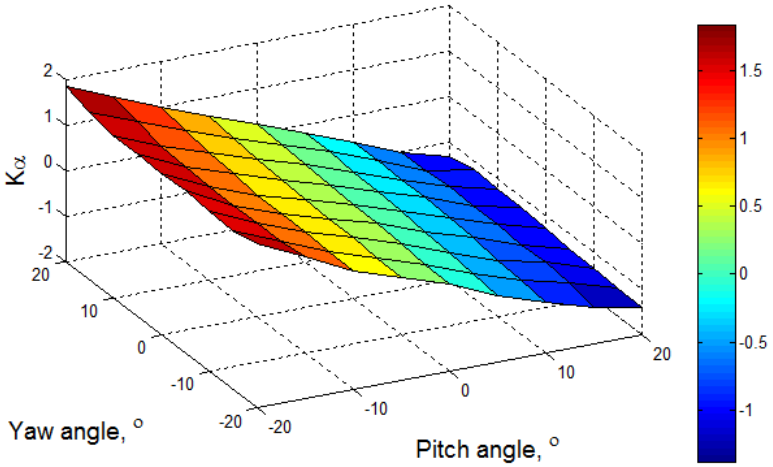



**Figure 6.8: Pitch coefficient plotted over calibration range**

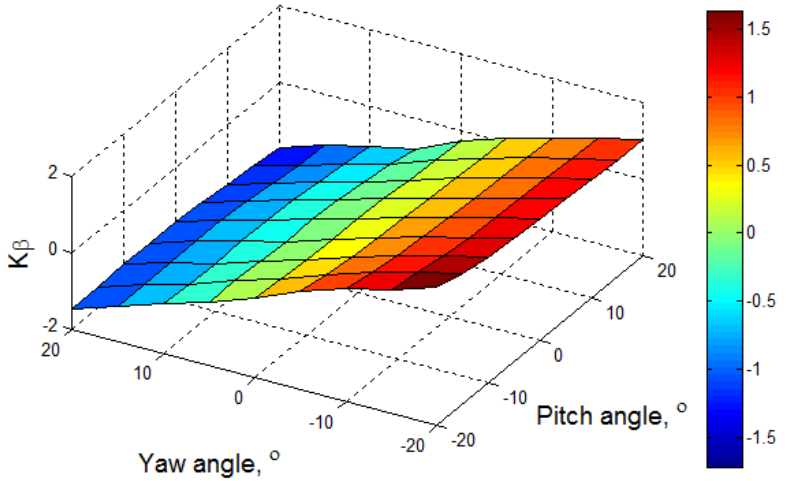



**Figure 6.9: Yaw coefficient plotted over calibration range**

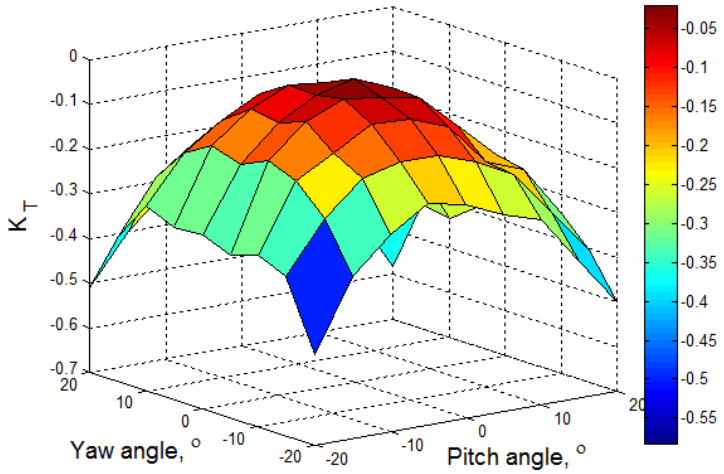



**Figure 6.10: Total pressure coefficient plotted over calibration range**

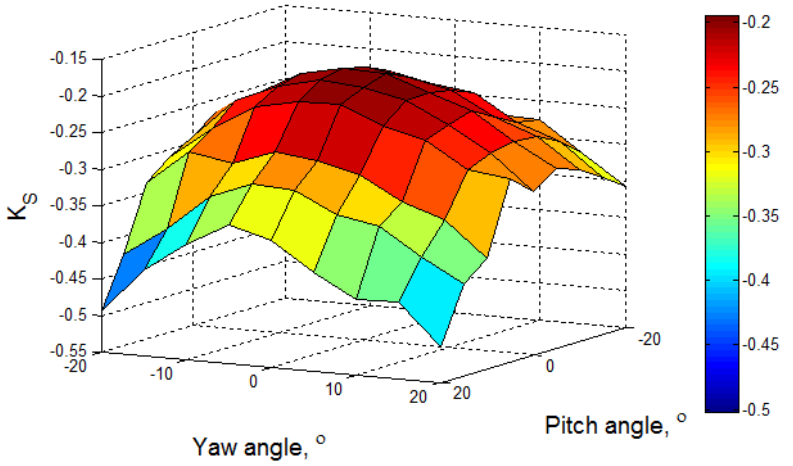



**Figure 6.11: Static pressure coefficient plotted over calibration range**

When the probe is used in a rig application, the calibration data in Figures 6.9-6.12 can be used to derive desired flow properties. Hereafter, experimentally derived quantities are displayed as primed variables such as α′ and β′.

Experimental yaw and pitch coefficients are calculated using Equations 6.1 and 6.2 then used as query points in the interpolation of the calibration data to arrive at α′ and β′ values. The interpolation procedures are discussed in Section 6.6. The deduced flow angles are then used in the interpolation of the total and static pressure coefficient calibration results, so that $K_T'$ and $K_S'$ can be found. Equations 6.3 and 6.4 are then rearranged so that $P_T'$ and $P_S'$ are deduced. Table 6.1 shows a summary of the properties calculated from the experimental variables α′, β′, $P_T'$ and $P_S'$ derived from the 5S probe calibration.

| Property | Equation |
|---|---|
| **Mach number** | $\boldsymbol{Ma} = \sqrt{\frac{2}{\gamma - 1}\left[\left(\frac{P_T'}{P_S'}\right)^{\frac{\gamma-1}{\gamma}} - 1\right]}$ |
| **Absolute velocity** | $\bar{\boldsymbol{V}} = Ma * a$ |
| **Axial velocity component** | $\boldsymbol{V_x} = \bar{V}\cos(\alpha')\cos(\beta')$ |
| **Radial velocity component** | $\boldsymbol{V_R} = \bar{V}\cos(\alpha')\sin(\beta')$ |
| **Circumferential Velocity component** | $\boldsymbol{V_\theta} = \bar{V}\sin(\alpha')$ |

**Table 6.1: Summary of flow quantities calculated from the 5S probe data**

The deduction of the velocity components is related to the way in which the calibration is carried out. Reichert and Wendt (1994) outline the methods of reducing the absolute velocity into its constituent components based on the angle definition system. The unit vector table for deducing angles from the 5S probe, which is calibrated in the Pitch-Yaw mode, is given in Appendix 6.

## 6.6 Data reduction from calibration data

When using the fully calibrated 5S probe in a test rig application, all five pressure signals are again recorded at each experimental condition and the yaw and pitch coefficients are calculated as in the calibration procedure. The pressure coefficients $K_T$ and $K_s$ are calculated from the calibration data once the experimental yaw and pitch angles are deduced. Two methods of interpolation were investigated; a linear interpolation of the angular calibration graph in Figure 6.7, and a polynomial interpolation of the polynomial surfaces shown in Figures 6.8 – 6.11. The latter method, as recognised by the author as the most commonly used technique in literature, was found to be computationally intensive. The reason for this is that the method requires the simultaneous solving of two polynomial equations, which represent the yaw and pitch angles. The function used in the MATLAB software, vpasolve, searched for a numerical solution which solved both of the angular polynomials. During the initial data analysis, it was found that, in order to analyse all of the data obtained, it would take longer than the scope of the project. An investigation was therefore carried out to determine the applicability of a novel linear interpolation method to the 5S calibration data to allow the test data to be analysed within the time frame of the project.

### 6.6.1 Polynomial interpolation method

The polynomial interpolation method mirrors that used by Lenherr (2010) and Behr (2007) which involves the calculation of experimental yaw and pitch angles by the equations shown in Equation 6.6 and eq 6.7.

$$\alpha' = \sum_{i=0}^{n}\sum_{j=0}^{m} k_{ij\alpha} K_{\alpha}^{i} K_{\beta}^{j}$$

**Equation 6.6: Polynomial regression model equation for the experimental pitch angle**

$$\beta' = \sum_{i=0}^{n}\sum_{j=0}^{m} k_{ij\beta} K_{\alpha}^{i} K_{\beta}^{j}$$

**Equation 6.7: Polynomial regression model equation for the experimental yaw angle**

Equations 6.6 and 6.7 represent polynomial regression models which are then used to evaluate values of α′ and β′, where $k_{ija}$ and $k_{ijb}$ are polynomial coefficients, found using a linear least squares method during the surface fit of each of the pressure coefficients. The aim is to minimise the difference in the polynomial estimated values and their corresponding real dataset values. α′ and β′ are found by solving the two regression models above as a pair of simultaneous equations. The polynomial surface fits in Figures 6.12 -6.15 show each calibration coefficient as functions of pitch and yaw angle measured during calibration. The deduction of the experimental angles must be carried out through simultaneous solving of Equations 6.6 and 6.7 because α and β are the dependent variables of $K_{\alpha}$ and $K_{\beta}$. The deduction of the pressure coefficients $K_T$′ and $K_S$′ can however be carried out independently of each other because, at this point, both of the independent variables, α′ and β′, have been solved for.

$K_T$′ and $K_S$′ are therefore calculated using the polynomial Equations 6.8 and 6.9.

$$K_T{}' = \sum_{i=0}^{n}\sum_{j=0}^{m} k_{ijT}\, \alpha'^{i}\, \beta'^{j}$$

**Equation 6.8: Polynomial regression model for the experimental total pressure**

$$K_S{}' = \sum_{i=0}^{n}\sum_{j=0}^{m} k_{ijS}\,\alpha'^{i}\;\beta'^{j}$$

**Equation 6.9: Polynomial regression model for the experimental static pressure**

Having found experimental pressure coefficients, values of $P_T'$ and $P_S'$ are then found by rearranging the initial calibration calculations in Equations 6.3 and 6.4.

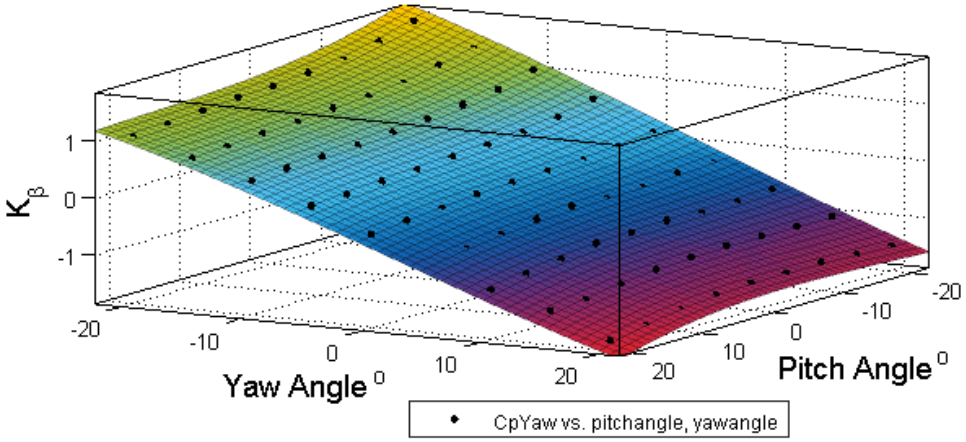



**Figure 6.12: 4th Order polynomial surface fit of yaw coefficient calibration data**

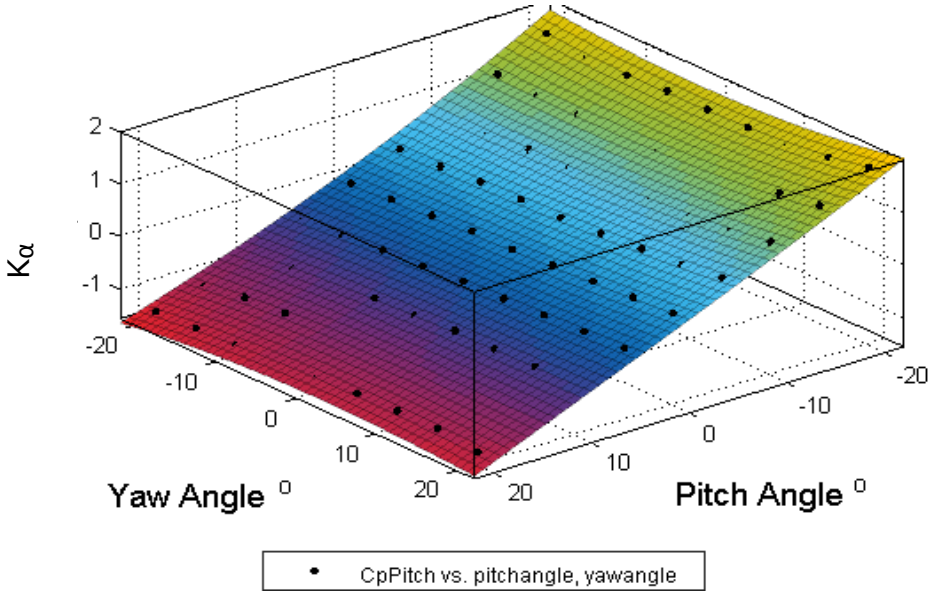



**Figure 6.13: 4th Order polynomial surface fit of pitch coefficient calibration data**

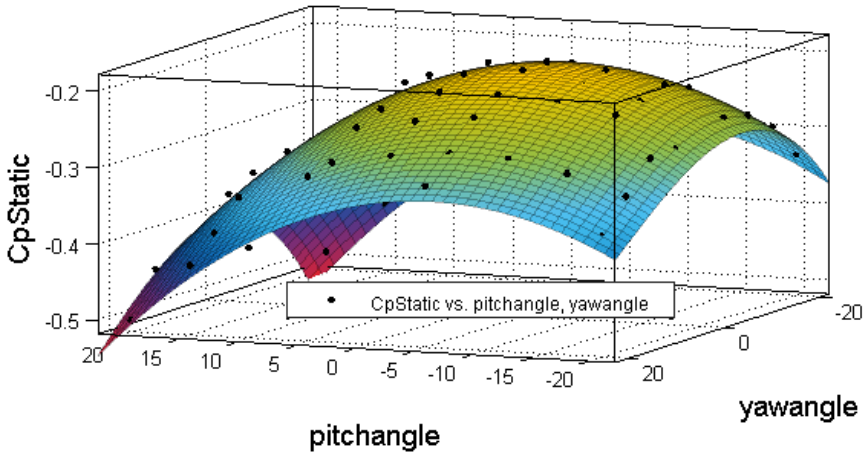



**Figure 6.15: 4th Order polynomial surface fit of static pressure coefficient calibration data**

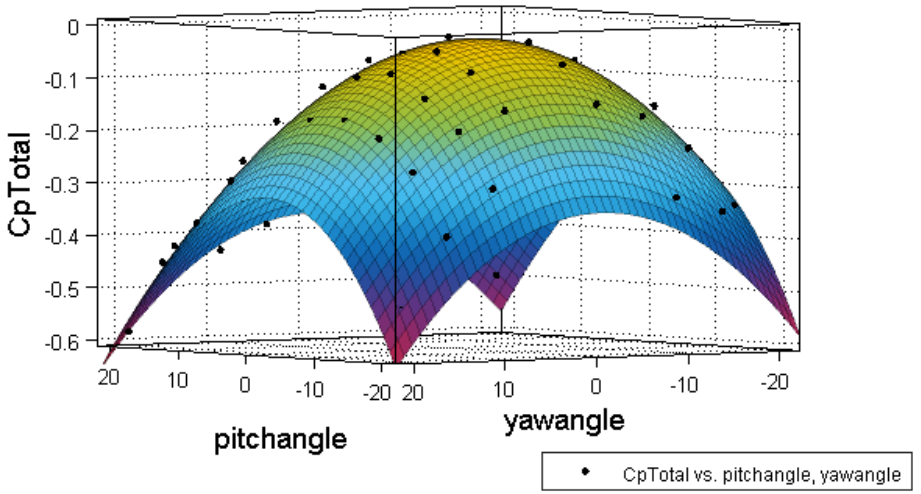



**Figure 6.14: 4th Order polynomial surface fit of total pressure coefficient calibration data**

### 6.6.1.1 Polynomial fit equation order investigation

A sensitivity study was carried out to investigate the effect of polynomial order on the quality of the surface fit.

Polynomial surface fits with increasing equation orders were generated for each of the calibration coefficients. Fits with orders n,m, where n represents the fit degree in the yaw direction and m in the pitch direction are displayed in Figure 6.16 as a single integer between 1 and 5. The number of yaw – pitch interaction terms increases as the polynomial fits increase in order from 1,1, which includes no level of interaction between the variables, up to the degree of 5,5.

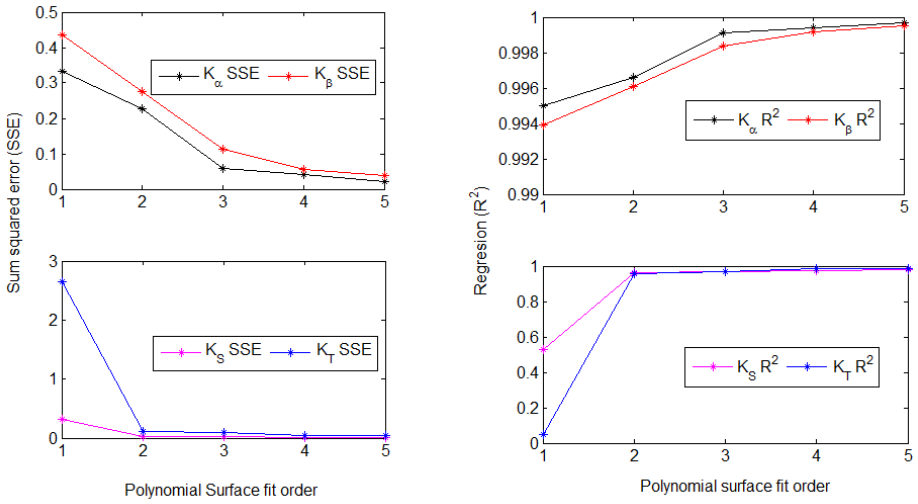



**Figure 6.16: Goodness of fit statistics for calibration data fitted to polynomial surface fits of increasing orders**

The sum squared error (SSE) statistic was used to measure the deviation in the resulting surface fit from the input calibration data. Values of SSE approaching zero are favoured as they indicate that the errors in the fit are low and that the model can be used confidently

for further prediction. The regression ($R^2$) value was also plotted as a measure of the success of the fit to the actual calibration data. Values of $R^2$ can lie between 0 and 1, with values closer to 1 indicating a better fit to the calibration data.

#### 6.6.1.2 Effect of increasing equation orders on $K_\alpha$ and $K_\beta$ surface fits

It can be seen from Figure 6.17 that the effect of increasing the surface fit order on the directional calibration coefficients, $K_\alpha$ and $K_\beta$ is that the statistics gradually improve until the 3rd order fit, thereafter they become much more stable. By increasing the fit order from 1 to 3 in both directions, an improvement of 0.45% and 0.41% in the $R^2$ values of $K_\alpha$ and $K_\beta$ respectively. The SSE is improved by 39% and 31% in the yaw and pitch surfaces when the order is increased from 1 to 3. It can be seen that increasing the fit order from 3 to 5 gives only a small improvement in quality of fit when looking at both statistics. The fit statistics show that polynomial orders of 1, for both $K_\alpha$ and $K_\beta$, give an appropriate fit for the data, although it can be improved by increasing the order.

#### 6.6.1.3 Effect of increasing equation orders on $K_T$ and $K_S$ surface fits

Unlike the fit statistics for $K_\alpha$ and $K_\beta$, those of $K_T$ and $K_S$ improve dramatically between first and second order polynomial fit orders. The first order surface fits for $K_T$ have particularly poor fit statistics of 2.6 and 0.04 in the SSE and $R^2$ values respectively. These are greatly improved when the interaction term between the yaw and pitch angles is introduced into the polynomial surface fit equations when they are increased to second order. Between orders 2 and 5, the SSE and $R^2$ values improve by 8% and 2.5% for $K_T$, and 1% and 1.5%

respectively for $K_S$. The large improvement in the fit between the first and second order models indicates that the total and static pressure coefficients must be represented by a surface fit as the data is grossly misrepresented when the yaw and pitch angle interaction terms are disregarded.

It is the author's suggestion that, due to the independent nature of the yaw-pitch calibration grid values shown in Figure 6.8, the $K_\alpha$ and $K_\beta$ matrices can be interpolated using a linear method as opposed to the simultaneous solving of high order surface polynomials. The proposed linear interpolation method is presented and discussed in Section 6.6.2. A comparison is then given between the polynomial and linear interpolation methods when applied to a calibration test point, whereby the error in the calculated value as well as the computation time are evaluated.

As stated above however, it is necessary to represent the $K_T$ and $K_S$ matrices with surface fits of polynomial orders of 2 or higher.

## 6.6.2 Linear interpolation method

This method utilises a double interpolation of the calibration grid shown in Figure 6.7; one at fixed yaw angle and one at fixed pitch angle. The aim of this method is to identify a local square around the query point within which a local interpolation can be carried out.

The first pass method averages down the lines of constant pitch to arrive at a 9 component row vector, containing the average pitch coefficient at each pitch angle. This is then compared with the $K_{\alpha'}$ value measured and the next largest component in the row vector is identified. Matlab's Find function was then used to identify the corresponding index within the averaged vector, which is used as an input to the interpolation in the yaw direction.

The yaw coefficient $K_{\beta'}$ is then used as a query point along the chosen constant pitch line and the interpolation is repeated. An overview of

how the local square, also referred to interchangeably as the local calibration cell, around the query point is found is shown in Figure 6.17.

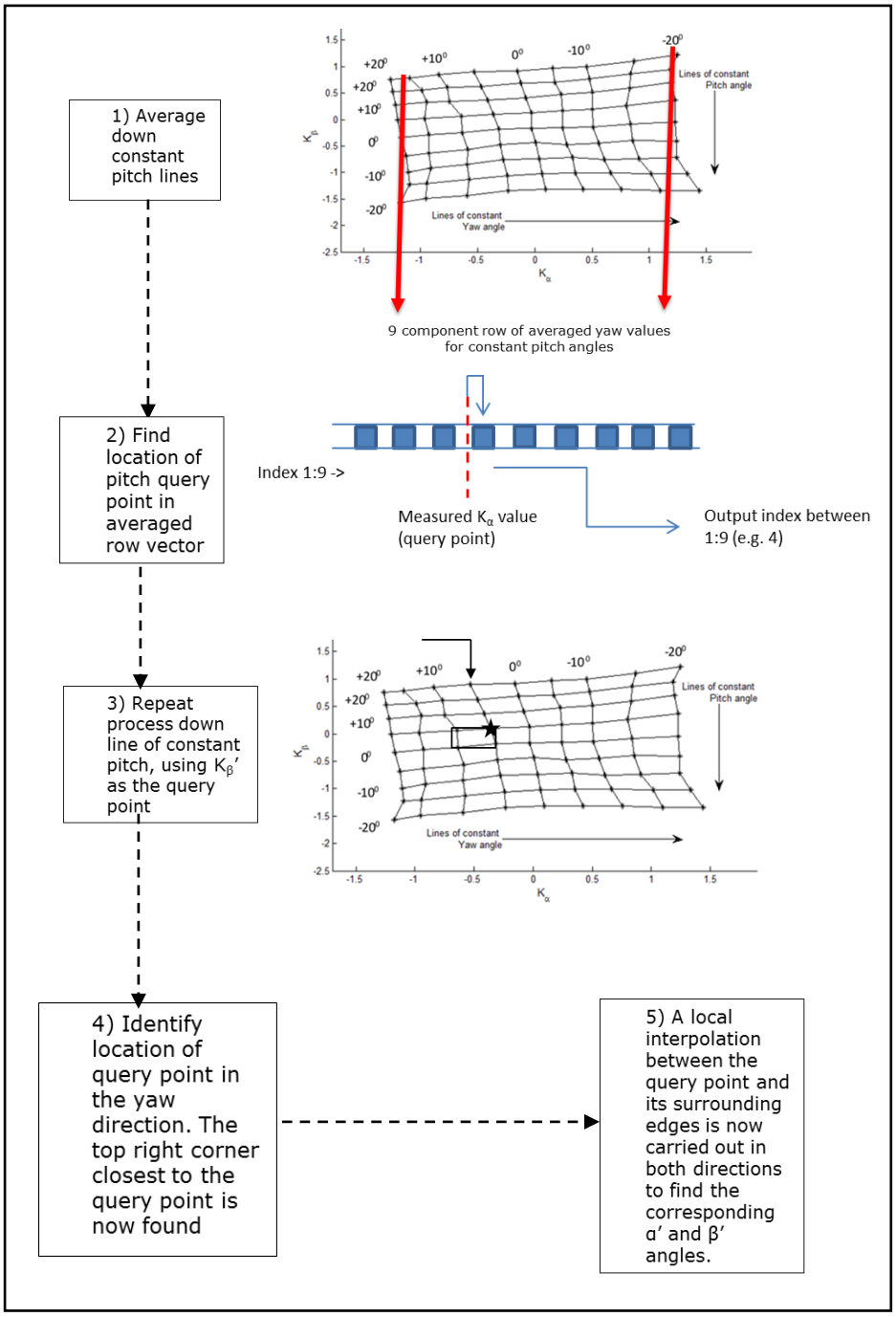



**Figure 6.17: Flow chart depicting the first pass linear interpolation process**

With the local cell around the query point identified, the double interpolation was then carried out. The calibration grid consists of the range of angles over which the probe was calibrated. Each node in the grid has a corresponding calibration coefficient for the angle in each direction, deduced through the calibration of the 5S probe. The experimental query point is a calibration coefficient, $K_\alpha$ or $K_\beta$. The difference between the coefficient query point and that of the next edge of the surrounding square in the calibration grid was identified and equated to a difference in angle, measured during the calibration process. This allowed the angle measured during the experimentation to be calculated from the calibration grid via linear interpolation. Equations 6.10 – 6.13 were used during the interpolation with the coordinates of the local square around the query point being given in Figure 6.18.

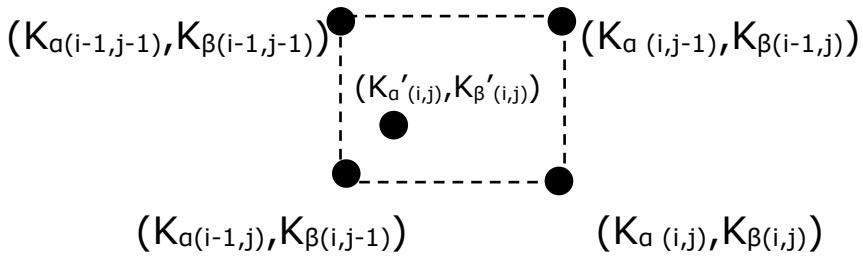



**Figure 6.18: Local Square around query point in first pass calibration data interpolation**

$$fraction_\alpha = \frac{K'_{\alpha(i,j)} - K_{\alpha(i,j)}}{K_{\alpha(i-1,j)} - K_{\alpha(i,j)}}$$

**Equation 6.10: Linear interpolation first pass method – fraction in pitch direction**

$$fraction_{\beta} = \frac{K'_{\beta(i,j)} - K_{\beta(i,j)}}{K_{\beta(i,j-1)} - K_{\beta(i,j)}}$$

**Equation 6.11: Linear interpolation first pass method – fraction in yaw direction**

$$\alpha' = \alpha_{(i,j)} - fraction_{\alpha}\left[\alpha_{(i,j-1)} - \alpha_{(i,j)}\right]$$

**Equation 6.12: Linear interpolation first pass method - experimental pitch angle**

$$\beta' = \beta_{(i,j)} - fraction_{\beta}\left[\beta_{(i-1,j)} - \beta_{(i,j)}\right]$$

**Equation 6.13: Linear interpolation first pass method - experimental pitch angle**

This method had its drawbacks due to the initial assumption of a completely regular grid which, as can be seen in the calibration data in figure 6.8, is not the case. This lead to errors near the edges of the imposed regular squares during the method trial. For this reason, a second pass method was implemented which assesses the local geometry around the query point more thoroughly. This allowed the irregular nature of the grid to be considered during interpolation. As shown in Figure 6.19, the local structure around the query point in the second pass method was represented as a series of non-parallel lines, where each is defined by its own straight line equation. This allowed the interpolation to cope with irregular query edges.

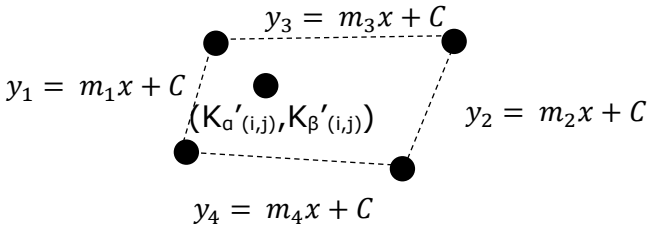



**Figure 6.19: Second pass method representation of the local structure around the query point**

In this way, the local structure around the query point is much improved in the second pass method. Although the general procedure is still followed as in Figure 6.18, the second pass method expands the local search area to neighbouring cells to ensure that the query point truly lies in the highlighted structure. The second pass methodology is as follows:

- The query point is compared to every data point in the grid and the closest data point is identified
- Use the closest data point as the centre of a 3x3 local grid to ensure that the query point is included
- Calculate the equations for each of the lines created by the points in the local grid (y = mx+c)
- Assess the relationship between the query point and each of the local grid lines to see where the point lies in relation to each lines (above, below, left or right)
- Isolate the four lines around the query point
- Carry out the interpolation in both directions as in the first pass method

The second pass method detailed above could solve for query points at the edges of the local cell. This was a great improvement over the first pass method which gave values out of the calibration range when

faced with irregular geometries in the local square formed around the query point. Although the improved method allows for irregular local structure cells to be interpolated, it does still assume perfectly straight lines between cell corners. A comparison between the newly created linear interpolation method and the tried and tested polynomial interpolation method was therefore carried out.

### 6.6.3 Interpolation method comparison: Software validation testing

A series of simulated test points were generated and superimposed onto the calibration grid, as shown in Figure 6.21. The test points were generated at set intervals of pitch and yaw coefficient, and used as a query test grid to validate the Linear Interpolation method script. The test points were then also passed through the Surface Fit method to assess the consistency of the two methods in their deduction of the yaw and pitch angles.

The aim of this software validation was to test the Matlab script written to run the Linear Interpolation method to ensure that:

- The calibration grid had been prepared correctly upon input to the script
- The method could handle angle boundaries at the edges of the grid squares
- The resulting interpolation outputs are consistent with observed values on the input calibration grid

This level of validation test was implemented with the sole purpose of meeting the aims outlined above; the accuracy of the generated angles was not able to be deduced as the test point were expressed as simulated calibration constants.

The simulated grid is symbolised in Figure 6.20 with a red 'plus' at each test point and the observed corner values have been estimated, with the pitch angle being displayed first followed by the yaw angle.

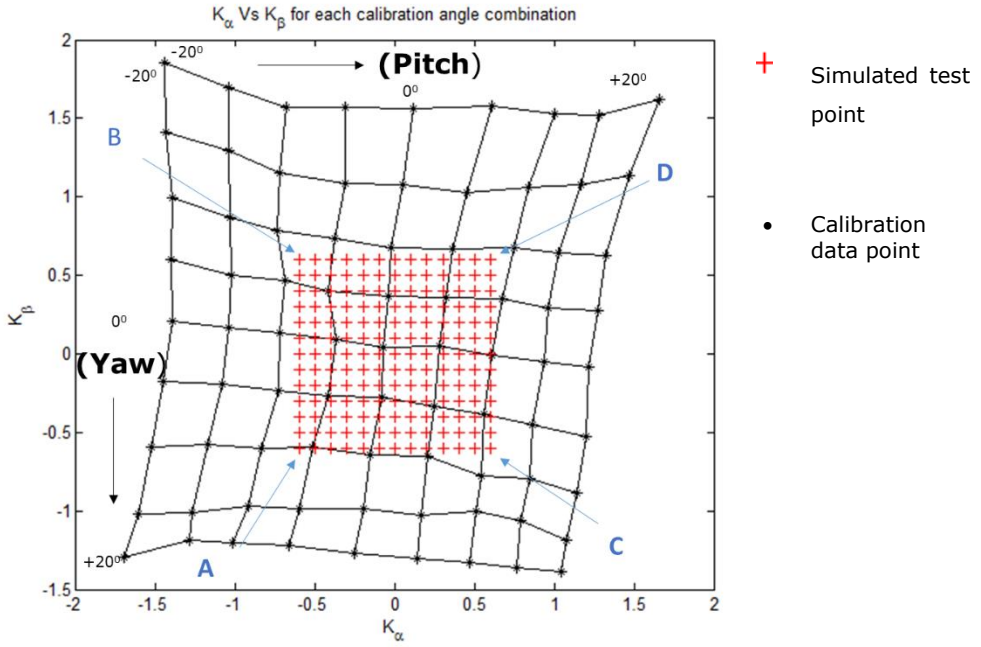



**Figure 6.20: Calibration grid showing variations in Kα and Kβ values with changing α and β angles. A grid of simulted test points has been plotted over the calibration data.**

Table 6.2 gives the estimated angles represented by the corners of the test grid, as observed at each of the test points A – D in Figure 6.21 above.

| Corner | Input test value ($K_\alpha$, $K_\beta$) | Observed output angles (α,β) |
|---|---|---|
| A | (-0.6,-0.6) | (-6,10) |
| B | (-0.6,0.6) | (-8,-6) |
| C | (0.6,-0.6) | (10,7) |
| D | (0.6,0.6) | (8,-9) |

**Table 6.2: Observed corner values from simulated test grid**

The simulated test grid was passed through both the Linear Interpolation method and the Surface Fit method for comparison.

Corners A and B represents test point 1 and 13 of the 13x13 simulated grid, indicating that that the grid columns are traversed in turn from bottom to top. Following this, the 14$^{th}$ data input point is at the bottom of the second grid column, adjacent to point A. This should then result in a stepped output in the pitch direction, where the pitch angle is constant throughout the upwards traverse of each simulated test point column. A step in pitch angle should then be observed at each column in the test grid. Figure 6.21 gives the pitch angle results of running the test grid through scripts for both interpolation methods.

Although the predicted step in pitch angle is observed, there is a distinct change in the pitch angle through each column of the test grid. This indicates how skewed the calibration data is in comparison to a regular-grid. When the pitch angle results from each method are compared, excellent correlation between the two can be seen.

Unlike the pitch angle, the yaw angle results should change as the test points are traversed and return to constant values at the top and bottom of each column. These observations do however, assume a very regular calibration grid structure which, as observed in Figure 6.8 and in the pitch angle results in Figure 6.21, is not the case. Figure 6.22 gives the yaw angle results of running the test grid through scripts for both interpolation methods.

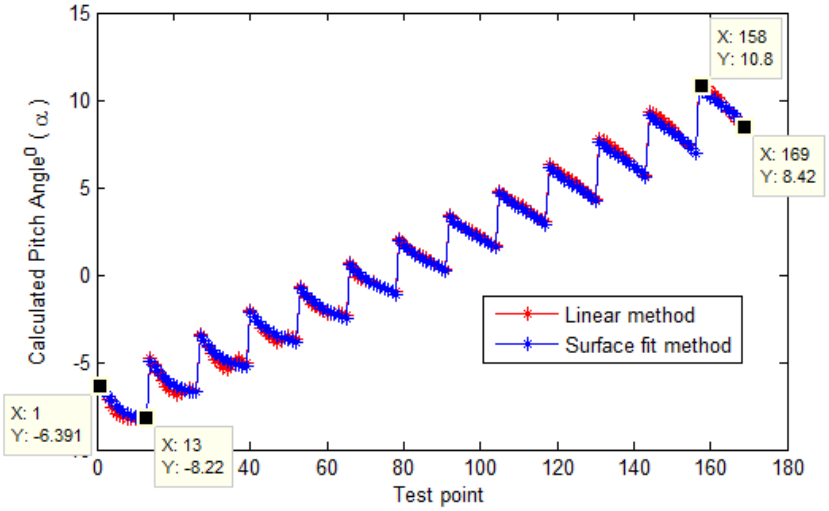



**Figure 6.21: Pitch angles resulting from simulated data points test**

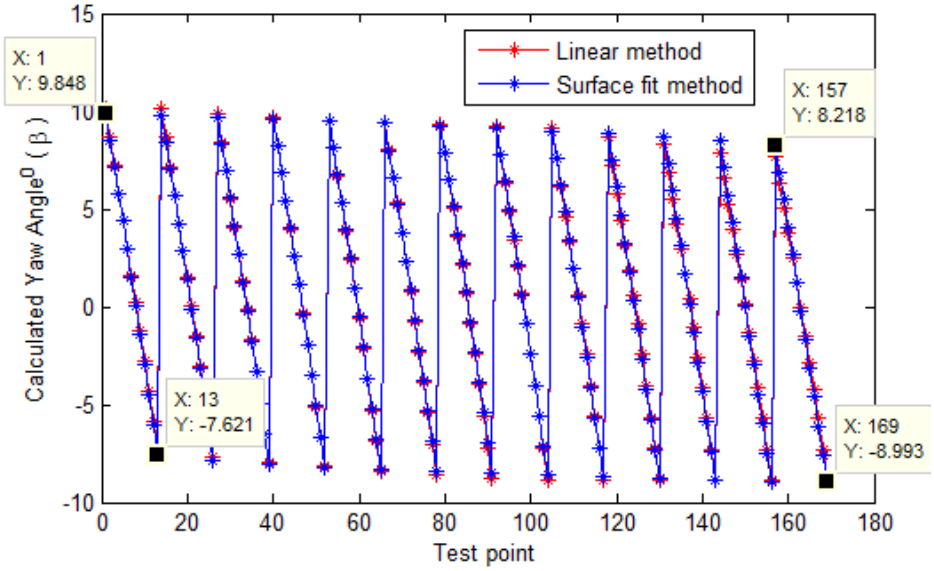



**Figure 6.22: Yaw angles resulting from simulated data points test**

The top and bottom edges of the test grid represent, for a regular calibration grid, $10^0$ and $-10^0$ respectively for the yaw angle. The actual results varied between $9.8^0$ and $8.2^o$ at the top edge and $-7.6^0$ and $-8.9^0$ at the bottom edge. This again highlights the skewness in the obtained calibration matrix. The ability of the Linear Interpolation method to give results which are correlated with the more tried and tested Surface Fit method is again proven in Figure 6.22.

Figs 6.21 and 6.22 show calculated angles which are consistent with those observed from the calibration grid, this indicates that the linear method has been set up correctly to give results which correlate with the surface fit method. It can be seen, for both angles, that the script is also able to handle the cross overs between internal grid cells in the Linear method. This is proven by the smooth output graphs for both methods throughout the full test grid.

### 6.6.4 Interpolation method comparison for real test case

The interpolation methods were also compared using a real test point in which the 5S probe was set to a pitch angle of $-5^0$ and a yaw angle of $13^0$. The aim of this test was to assess the ability of both methods when exposed to real data sets. The resulting pitch and yaw angles are given in Figures 6.23 and 6.24 respectively for both interpolation methods.

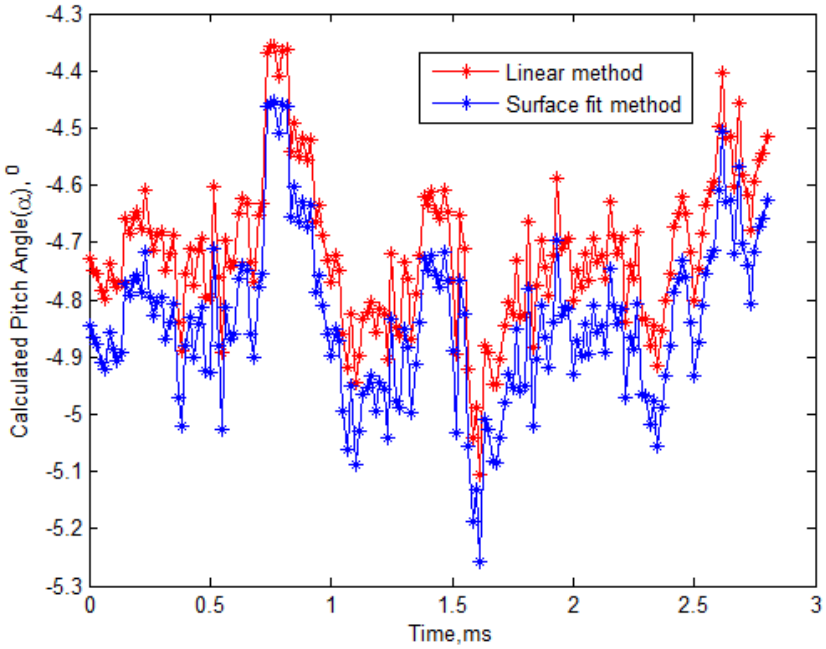



**Figure 6.23: Pitch angle results for both interpolation methods. Set pitch angle:-50**

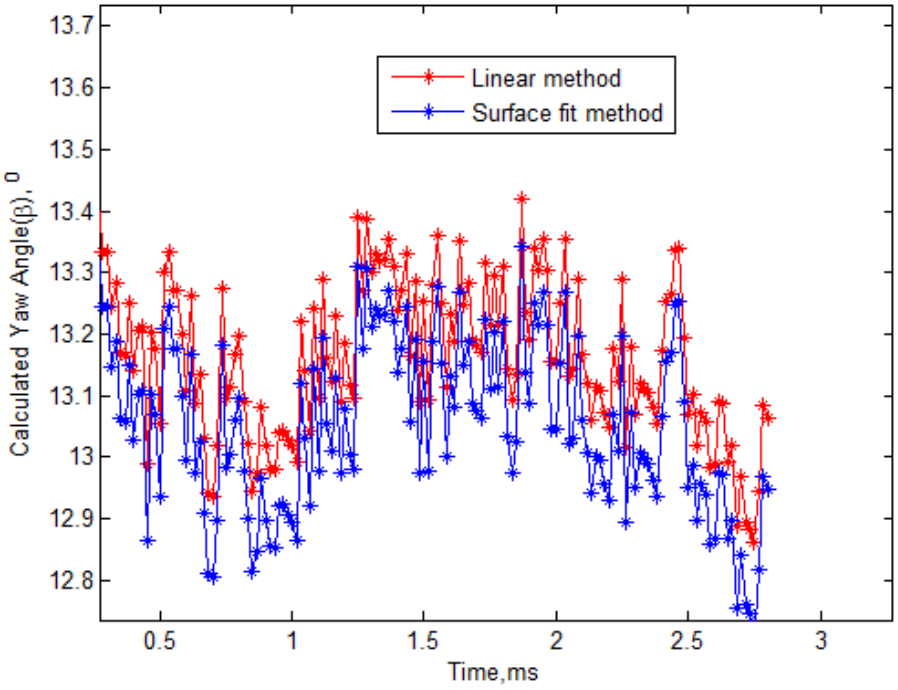



**Figure 6.24: Yaw angle results for both interpolation methods. Set yaw angle: 130**

The real test case results show a distinct correlation between the linear method and surface fit method outputs, not only in their time averaged values but in their fluctuations. Such averages for each of the time series' were calculated using the standard arithmetic mean and are shown in Table 6.3. The standard deviation was also calculated and shown in table 6.3. The square of the variation of each data point from the calculated mean was taken and the average of these deviations was calculated. This is the variance of the data and the square root of the variance was calculated as the standard deviation.

| **Interpolation method** | **Resulting angle** | **Mean** | **Standard deviation** |
|---|---|---|---|
| Liner | Pitch (α) | $-4.72^0$ | 0.133 |
| Surface fit | Pitch (α) | $-4.84^0$ | 0.142 |
| Linear | Yaw (β) | 13.17 | 0.132 |
| Surface fit | Yaw (β) | 13.07 | 0.146 |

**Table 6.3: Summary of first and second statistical modes of each of the time series' resulting from the test case**

Table 6.3 shows that the difference in the mean values between the two interpolation methods for the pitch and yaw angles is 0.12 and 0.1 respectively. It can be observed that, in all cases, the difference in the mean value is found to be within the standard deviation of the data itself showing the statistical similarity between the two interpolation methods.

The software validation results presented in this section give confidence that the novel linear interpolation method described in this chapter can deduce the yaw and pitch angles as well as the more commonly used polynomial fit method. The computation time for each of the results shown in the software validation testing has been investigated to assess the advantage of using the linear method over

the simultaneous solving of polynomial regression models when interpolating for α' and β'.

The elapsed time during interpolation of the calibration data to obtain both angles using both methods was obtained for the validation tests. The computation time for each method was compared in Figure 6.25 using a semilog scale as the difference between the two methods was of the order $10^4$ on average.

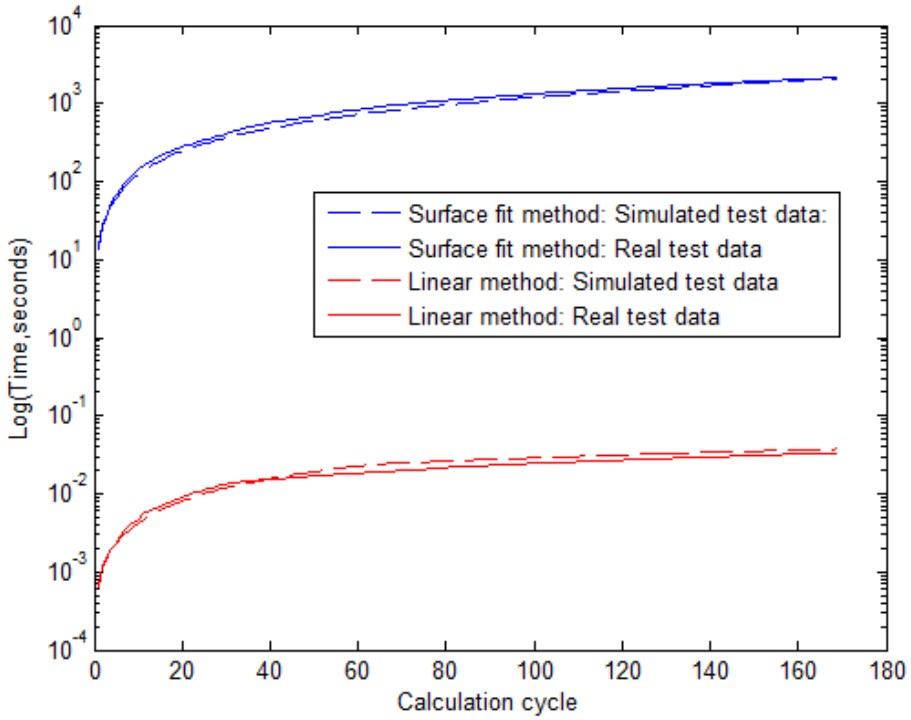



**Figure 6.25: Elapsed computation time comparison for each of the interpolation methods**

It can be observed that the surface fit method takes approximately 4 orders of magnitude longer than the linear interpolation method in all test cases. The test case results themselves show that the linear method can interpolate the calibration data to give angle values consistent with those deduced using the polynomial surface fit method. It was therefore concluded that the linear interpolation would be used for the deduction of the experimental angles α' and β' from the compressor data presented in Chapter 7.

## 6.7 Uncertainty analysis

As with any experimental project, the true values of measured quantities cannot always be stated explicitly due to inherent errors within various stages of the investigation. As differences in the true and measured value can be due to a range of sources such as instrumentation uncertainty, environmental drifts, data acquisition and the experimental facility itself, an overall quantitative analysis of the system uncertainty is made. This combines a range of different errors into an uncertainty value which can be quoted with readings of desired flow quantities. The specific methodology for this analysis can alter between professional bodies and international organisations (Lenerr, 2010) such as ASME (1985) and JCGM (2008).

### 6.7.1 Uncertainty methodology

The methodology used here is an adaptation of the Guide to the Expression of Uncertainty in Measurement (GUM) method (JCDM, 2008). The first step is to map the main sources of error and ambiguity in the processes which the 5S probe goes through to arrive at its measured and derived quantities. As the overall process of taking a measurement with the 5S probe is given in Figure 6.4, only those practices with a significant contribution to the overall error were mapped for this analysis, as opposed to the whole measurement chain. The ambiguity in other stages of the system are discussed in this section to give an appreciation of their contribution; however they are not included in the uncertainty calculations. The reason for this is that many of these errors were mitigated for by experimental design, as discussed in Chapter 5. Each error is then expressed in terms of a Gaussian probability distribution, with all uncertainties quoted to one standard deviation from the mean, representing a 67% confidence level. This condition allows all of the values to be given as standard

uncertainties, making comparisons easier to carry out. The uncertainty sources in the 5S probe measurements, along with a discussion of their standard uncertainty calculations, are given in this section.

Figure 6.26 gives an overview of the processes with the main errors which were either quantified or mitigated for. In the figure, the dashed red boxes signify errors within the system and the blue boxes represent steps in the measurement process. It can be seen that the errors are categorised into three main stages; those found during pressure acquisition, aerodynamic calibration and rig experiments.

Following the identification of the core errors found throughout the measurement system, the propagation and addition of such uncertainties was calculated using the rules outlined by the National Physics Laboratory (Bell, 2001). The combination of errors was carried out by combining fractional errors in quadrature, as shown in Appendix 8. There is also a summary of the main equations used and a worked example in this Appendix.

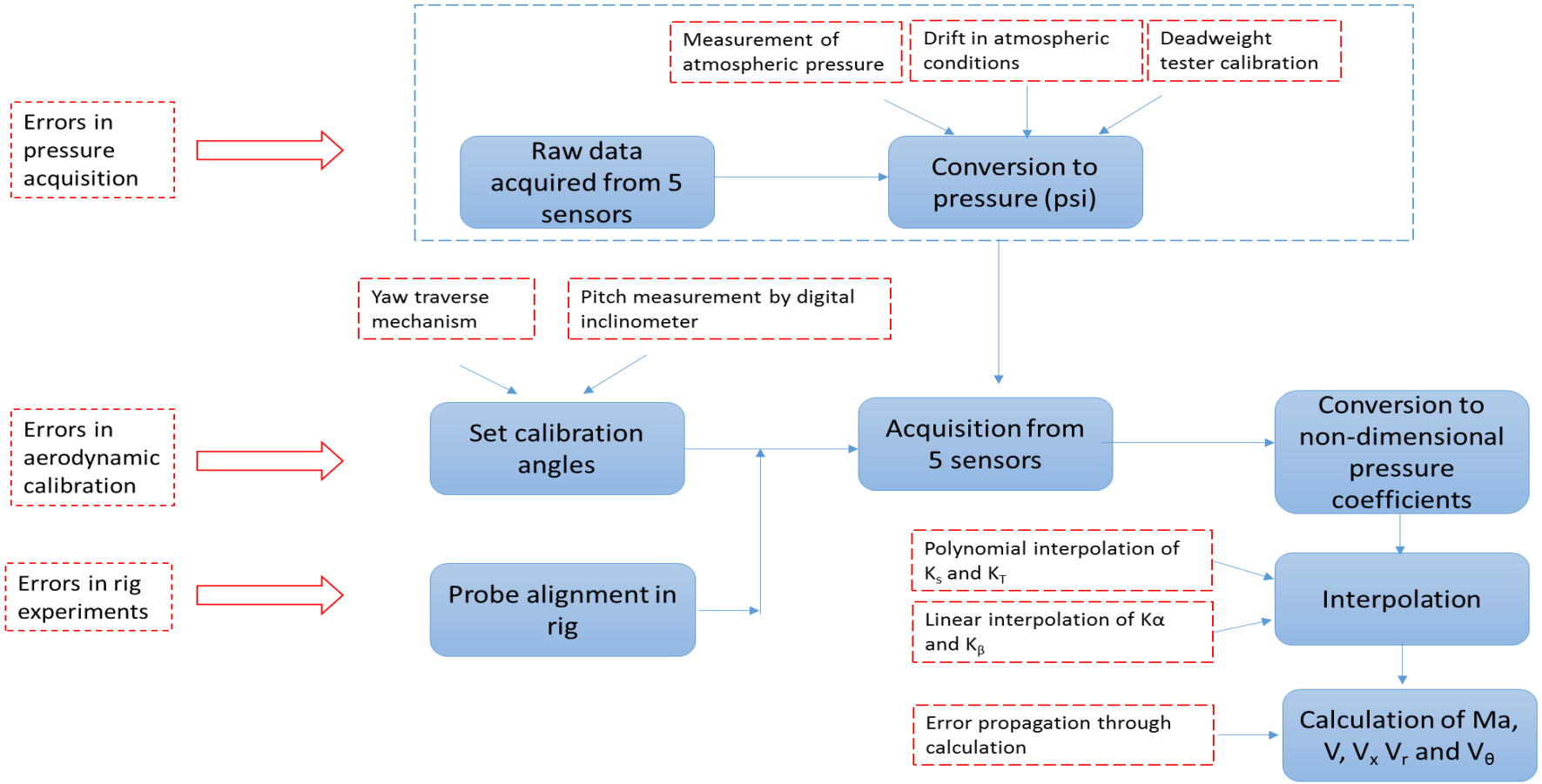



**Figure 6.26: Overview of the errors found within the processes of calibration and measurement using the 5P probe**

### 6.7.2 Errors in pressure acquisition

The ambiguity in the pressure readings from each sensor is an essential quantity as the data is used to align the probe properly into the highest flow vector. As stated in Chapter 5, the error related to the drift in atmospheric conditions is mitigated for by taking measurements with reference to a zero condition, utilising the assumption that no significant drift in atmospheric conditions occurs during the test.

The error imposed by the deadweight tester is quoted by its calibration certificate to be 0.04%. The certificate is found in Appendix 9. The quoted value was given as a tolerance, meaning that it has a 95% confidence level and represents 2σ. The relationship between tolerances and standard uncertainties is given in Equation 6.14.

$$U_e = k_f \times \sigma_f$$

**Equation 6.14: Expanded uncertainty relationship**

Where $U_e$ is the expanded uncertainty and represents the instrumentation tolerance value in this case. The constant $k_f$ is known as the convergence factor and is used to convert between the expanded uncertainty, $U_e$ and the standard uncertainty, $\sigma_f$. A convergence factor of 2 is usually applied to give a confidence level of 95% (Lenherr, 2010). The tolerance value of 0.04% was therefore halved to 0.02% to give the standard value. This uncertainty, along with other properties calculated from the sensor pressure readings, is given in Table 6.5.

The error in the measurement of atmospheric pressure was 0.02% also, as it was taken using a DRUCK pressure indicator. The value was

sensible as the tolerance value of the DRUCK measurement controller used by the ETH was found to be 0.05%, making the standard uncertainty 0.025% (Lenherr, 2010). These two pressure uncertainties propagate through the calculations of the calibration constants and the uncertainty for each is given in Table 6.4.

| **Flow property** | **Standard Uncertainty, %** |
|---|---|
| Sensor pressure, $P_1 - P_5$ | 0.02 |
| $\bar{P}$ | 0.04 |
| $K_\alpha$ | 0.035 |
| $K_\beta$ | 0.035 |
| $K_T$ | 0.035 |
| $K_S$ | 0.063 |

**Table 6.4: Uncertainties calculated for pressure readings and calculated calibration coefficients**

### 6.7.3 Errors in the aerodynamic calibration and interpolation processes

The errors in the calibration process are, for the most part, the ambiguity in the angles at which the 5S probe was set and the calculation of non-dimensional calibration coefficients. The former being the standard uncertainty in the equipment used to set the probe. The uncertainty in the yaw placement is therefore characterised by the accuracy of the traverse mechanism introduced in Section 6.3, which was found to be ± $0.018^0$. The accuracy of the

digital inclinometer used to set the pitch angle was quoted as $\pm 0.005^0$.

The uncertainty in the linear calibration process designed and implemented in this thesis was calculated by using the final definitions used for the deduced quantities. This gave two errors, one in the calculation of the calibration constants to be interpolated and one in the definition of the angle. These were then added in quadrature. The uncertainty in the polynomial interpolation method used to deduce the experimental values of $P_s'$ and $P_T'$ was calculated from the goodness of fit for the $4^{th}$ order polynomials shown in Figures 6.13 – 6.16. A summary of the uncertainties calculated for each of the parameters deduced during interpolation of the calibration data is given in Table 6.5

| .**Flow property** | **Standard Uncertainty, %** |
|---|---|
| α′ | 0.33 |
| β′ | 1.09 |
| $P_t'$ | 1.38 |
| $P_{s'}$ | 2.03 |

**Table 6.5: Uncertainties calculated for experimental parameters found through the calibration and interpolation process**

The remaining uncertainties are those which propagate through via calculation from calibrated quantities such as the Mach number and velocities. The standard uncertainties for these were calculated using the rules outlined by the National Physics Laboratory. The results are given in Table 6.6.

| Flow property | Standard Uncertainty, % |
|---|---|
| Ma and $\bar{V}$ | 0.38 |
| $V_x$ | 2.30 |
| $V_r$ | 1.32 |
| $V_\theta$ | 0.48 |

**Table 6.6: Uncertainties calculated through the propagation of errors through calculated quantities**

As the method used to derive the quantities given in Tables 6.4 – 6.6 was specific to the 5S probe measurement chain, the results were compared to those of other multi sensor fast response probes. The uncertainty values in the HT-FRAP (Lenherr, 2010) and the 2-sensor FRAP (Behr, 2007) have been used to compare the standard uncertainties found in the 5S probe. These comparisons are given in Table 6.7.

| Flow property | Expanded uncertainty, % | | |
|---|---|---|---|
| | 5S probe | HT-FRAP | 2-sensor FRAP |
| α′ | 0.66 | 0.8 | 1.3 |
| β′ | 2.18 | 1.8 | 1.6 |
| $P_t'$ | 2.76 | 2.6 | 2.8 |
| $P_{s'}$ | 4.06 | 2.9 | 3.7 |

**Table 6.7: Comparison of uncertainty values from the 5S probe and two probes from the ETH lab**

The values for the 5S probe have been converted to expanded uncertainties using a convergence factor of 2 and Equation 6.14. The pitch angle uncertainty is found to be slightly lower than the value found for the HT-FRAP, whereas the yaw angle value was almost 0.4%

higher. These differences can be attributed to the differences in yaw-pitch traverse facilities available for each probe. The uncertainty in the total pressure value lies between the values set by the two FRAP probes, whereas the static pressure value is slightly higher than the 2-sensor FRAP. This ambiguity between readings can be attributed to the difference in the interpolating polynomials used throughout the investigations. The comparisons for all four results do however, give confidence in the values calculated in this analysis for the 5S probe.

## 6.8 Conclusions

The calibration procedure along with the setup of the measurement system were presented in this chapter. The adaptation of the air jet rig to include a pitch manipulation device, which allowed the probe to be calibrated in both angular planes was described. The calibration results were presented in the form of non-dimensional pressure coefficients, $K_\alpha$, $K_\beta$, $K_T$ and $K_s$, which are then interpolated to give experimental parameters when the probe is exposed to an unknown flow. A linear interpolation method was compared with the more widely used surface fit method and it was decided that although the latter gave more accurate results, the linear method was to be used for the remaining analysis due its computational speed.

# Chapter 7: Application of 5S probe to Compressor rig

## 7.1 Introduction

Having verified the calibration and data reduction process for the 5S probe, testing in an industrial scale rig was carried out and the results are given in this chapter. It outlines the steps taken to prepare the compressor rig for use as well as the results obtained from the testing of the measurement system in the adapted rig. The characteristics of the turbomachinery flow were first investigated using both fast response and pneumatic pressure probes to gain experience of the flow conditions before using the fully calibrated 5S probe in the rig.

Firstly, the verification of the blade passing frequency of the last stage rotor was carried out at a range of compressor operating conditions using an FFT analysis technique. The 5S probe was then used to obtain time resolved data, which is presented in this chapter and it shows the effect of a single blade passing, turbulence intensity statistics and vector trajectories across a single blade cycle. This chapter really encapsulates the ability of the 5S probe to acquire data that cannot be obtained through traditional techniques such as 5-hole pitot probes. Fast response velocity data is obtained in a simultaneous manner, allowing time-resolved periodic flow changes were obtained in all 3 dimensions from the compressor rig.

## 7.2 Compressor rig description

The compressor rig in which the 5S probe was tested was first introduced in chapter 4. It is operated via a control panel in which the motor drive speed is set and diagnostic information is relayed. For each set speed, the corresponding compressor motor speed is measured using a digital tachometer. A bypass valve, located

downstream of the final compressor stage, was opened during the investigation to ensure that the Mach number range was kept to subsonic speeds. This was essential as the aerodynamic calibration method assumes that the probe is used in an incompressible flow.

The overall compressor loop components are shown in figure 7.1.

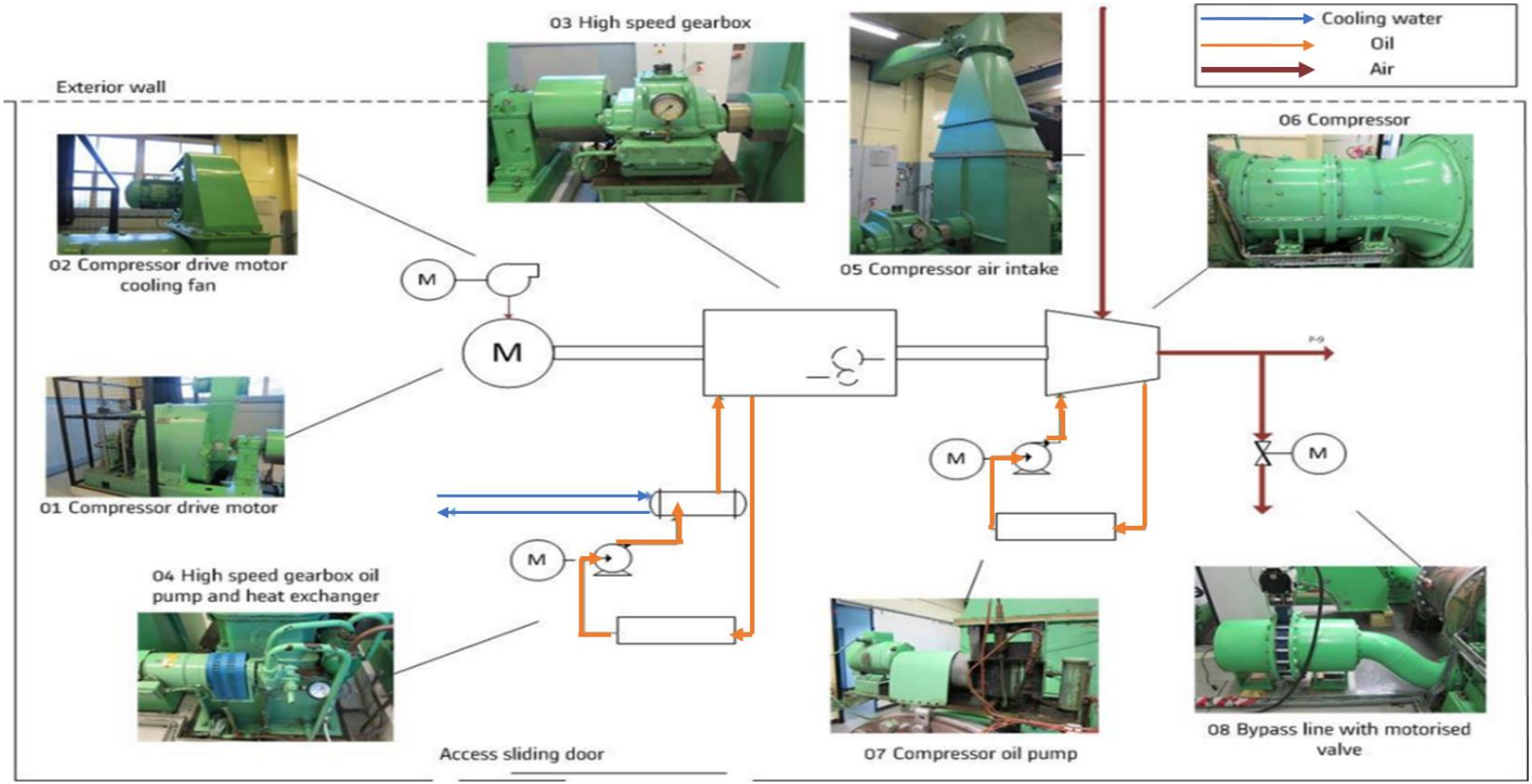



**Figure 7.1: Rig circuit overview**

Figure 7.1 shows the main air flow circuit. The intake is located by the ceiling of the rig room and draws in atmospheric air through a meshed opening in the wall. The intake channel, as shown in figure 7.1 as image 5, also contains a meshed surface to filter any debris incoming from the outside air. These air filters were essential due to the high sensitivity of the 5S probe sensors.

Pneumatic probes had been used in the rig previously but fast response probes had not been used in the compressor rig prior to this investigation. Part of the following investigation was therefore to assess the robustness of the 5S probe when faced with the real conditions faced in industrial style test rigs. Additional mesh grids were not added to the rig upstream of the compressor to avoid further pressure drops at the inlet due to flow restrictions. It was therefore decided that the FAP-250(1) sensor head, which was used for the investigations described in chapter 5, would be used initially to characterise the flow field and ensure that the conditions were safe for the fully calibrated 5S probe.

The compressor itself is made up of 6 blade stages and final blade set is a stationary nozzle which the incoming flow passes through before reaching the measurement probe. The dimensions of the last stage stator vanes are given below in figure 7.2.

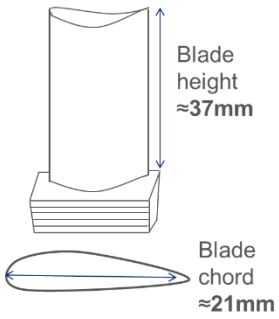



**Figure 7.2: Final stator stage blade dimensions**

Figure 7.3 gives the size of the probe head in relation to the last stage dimensions. It is approximately 6 times smaller than the chord of the last stage rotor blade and stator vane.

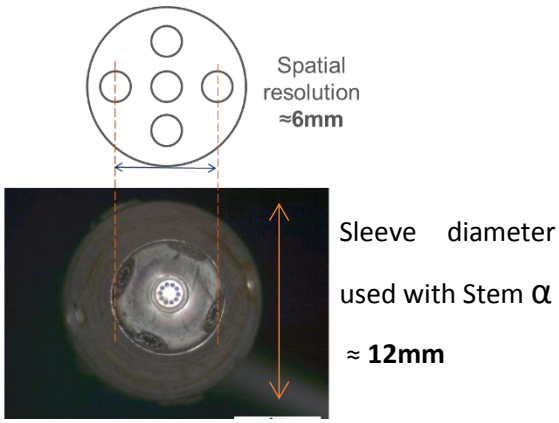



**Figure 7.3: Dimensions of the 5S probe tip used in the compressor rig**

Figure 7.3 shows the spatial resolution of the 5S probe as the maximum distance between opposing side sensors. All of the measurements in this investigation were taken from the middle of the blade as data recorded closer to the blade tip or hub were too close to the rig casing for the measurements to be viable.

The diameter of the sleeve used to couple the FAP-250 probe to Stem α was too large for the compressor rig experiments. A bespoke coupling sleeve was used when assembling the probe as Stem γ, which decreased the overall probe diameter from 12mm to 9mm, to reduce the blockage effect on the compressor flow imposed by the probe.

## 7.3 Rig adaptations to allow access to measurement area

The only entry points to the rig initially were via the flow exhausts. Access to the flow from the main and bypass exhausts was not feasible due to the length of the cavity between the last stage blades and the access points. Figure 7.4 shows a horizontal slice through the centre of figure 4.17 in chapter 4 where the rig was first introduced.

The length of the 5S probe between the $90^0$ bend in the stem and the tip of the sensor head was 50mm, meaning that the probe tip could only be placed as close as 310mm from the final nozzle, based on the cavity length. At the proposed distance of 310mm from the blade, the probe tip would be measuring in the region of 1 blade chords away and it was assumed that any unsteady interactions within the flow would be washed away by the merging of blade wakes at this distance downstream.

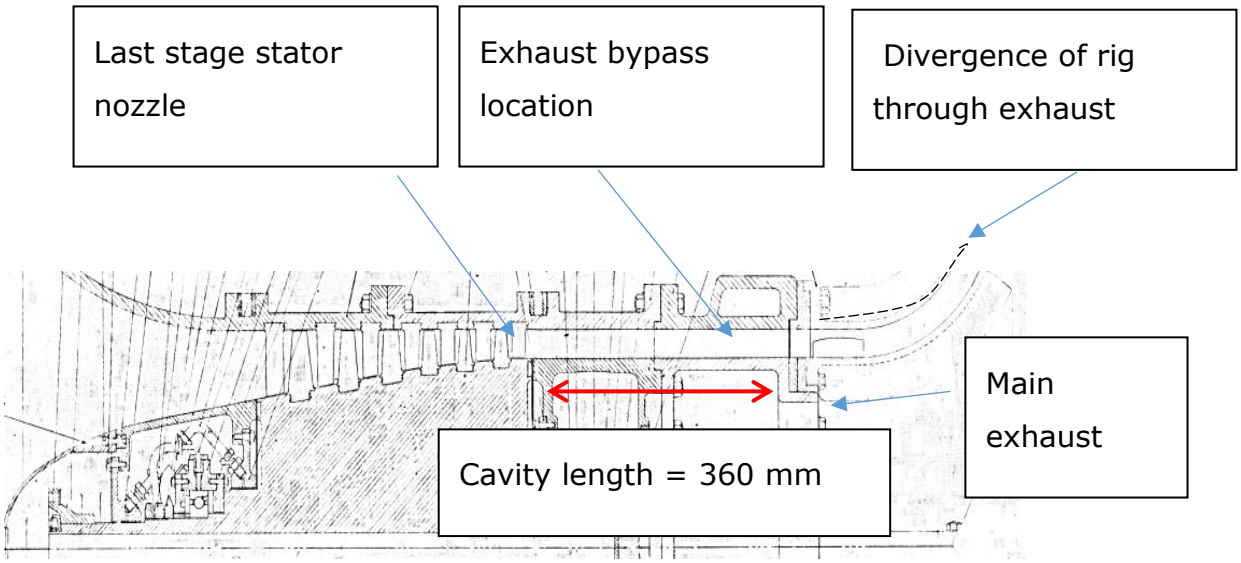



**Figure 7.4: Horizontal slice through rig diagram, showing cavity length between final blade row and the rig exhausts**

It was decided that the compressor rig casing upstream of the main exhaust was to be removed and altered to create entry points for the measurement probes, allowing the 5S probe to take data as close to the last stage as possible. Images of the removed rig casing and the internal rotor blades are shown in figure 7.5.





Top side casing removed from rig

Compressor rig intact



Exposed rotor blades inside rig

**Figure 7.5: Removal of compressor rig outer casing**

The rig casing was removed to allow the blades to be counted and measured to verify the CAD drawing of the rig. An advantage of adapting the casing on the bench was that it allowed the probe

insertion method to be tested before re-attaching the casing to the rig. A 10mm hole, already present in the rig casing, was used to carry out a trial run of inserting the probe from the outside surface of the casing. Although the test hole was too close to the blades to be used for measurement with the 5S probe, it allowed the $90^0$ bend in Stem γ to be trialled in the rig to assess if it could turn freely in the space provided. It can be seen in figure 7.6 that the stem was easily inserted from the opposite side to the blades, turned towards the blades and then yawed into the blade passage centre. This method of probe insertion was used throughout the compressor test campaign.



**Figure 7.6: LHS: Probe stem inserted though 10mm dimeter hole in compressor casing. Middle: Stem $90^0$ bend manoeuvred through access hole. RHS: Stem turned to align with blade passage**

A series of access holes were drilled and threaded to allow a 10mm diameter compression fitting to be used to secure the 5S probe in place. The measurement points were designed to allow the axial traverse from the blade exit to 1 blade chord downstream. This was designed with the aim of tracking the flow properties at increasing distances from the final blade stage. The proposed measurement points in relation to the final stator stage is given in figure 7.7. A 50mm distance was left between the nozzle row exit and the first access point, which allowed the probe tip to be placed at the centre of the blade passage.

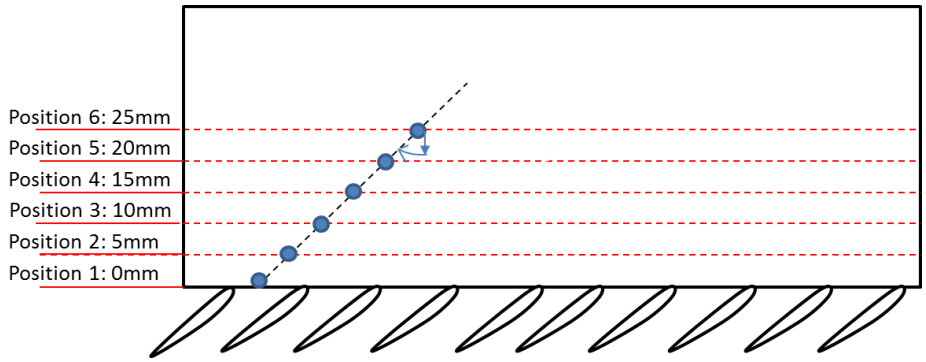



**Figure 7.7: Design of measurement access points**

Physically, the pattern of access holes could not be arranged exactly as depicted in figure 7.7. The diameter of the access hole required for the 5S probe would not allow for all 6 measurement points to be placed adjacent to each other in the trajectory of the same stator passage.

Also, existing features in the rig casing such as lifting eyes and holes for pressure tappings were obstructing the designed trajectory, making it necessary to scatter the measurement points through a range of blade passages. It was, at this point, assumed that the flow around the circumference of the compressor was equal at each stator passage.

The last stage vane exit angle, as show in figure 7.8, was measured during the benchtop investigation of the rig casing and was found to be $22^0$. This exit angle was confirmed during initial testing of the 5S probe in the running compressor rig, as shown in figure 7.15.

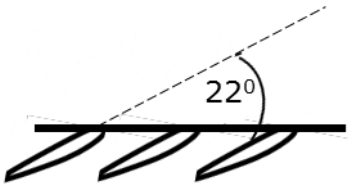



**Figure 7.8: Last stage stator exit angle, as measured from exposed compressor casing**

At each of the measurement points shown in figure 7.7, the test probe was inserted and turned through the bend in the stem so that the sensors were facing the direction of the incoming air flow. The probe was then rotated about the stem axis so that the measurement tip was aligned with the $22^0$ vane exit angle. This ensured that the data was taken from the centre of each vane passage used during the investigation. The securing of the 5S probe to the rig is shown in figure 7.9.



**Figure 7.9: 5S probe secured through the compressor rig casing**

## 7.4 Probes used in compressor rig application

As well as the 5S probe coupled with Stem γ, other measurement probes were used for flow measurement in the axial compressor.

The application of the 5S probe to the compressor flow had the aim of assessing the durability of the sensitive instrumentation in an industrial style rig as well as the deduction of turbomachinery flow unsteadiness. Factors such as high Mach numbers, contamination from uncontrolled inlet air flows and sudden shock waves can lead to probe damage during testing. The FAP-250(1) probe tip was therefore exposed to the compressor flow field initially to gain confidence in the capability of the probe to withstand the conditions found within the rig.

A pneumatic total pressure probe was also applied to the compressor using the same access holes as designed for the 5S probe.

### 7.4.1 Fast response probes

Following the aerodynamic calibration of the 5S probe using the air jet rig flow, the probe tip was decoupled from stem α and successfully re-assembled into the stem γ design described in chapter 5. The final probe design used in the compressor rig is pictured in figure 7.10.

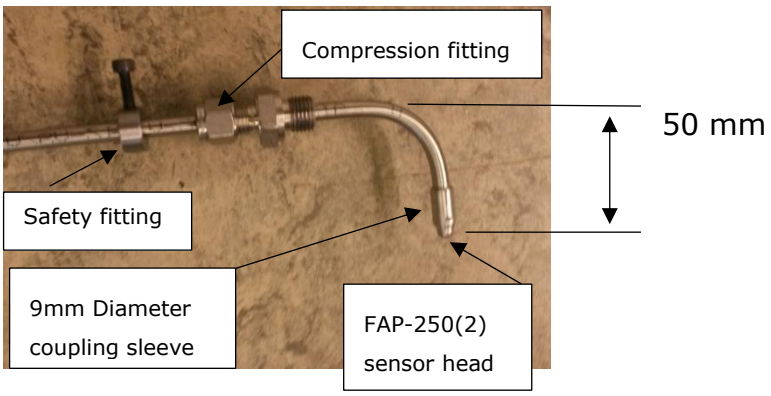



**Figure 7.10: Stem γ probe with main features designed for use with compressor rig**

The compression fitting depicted in fig 7.10 consists of a 10mm OD threaded end, to be screwed into the access holes in the compressor rig casing, and an adapter which altered the opposite end to a diameter of 9mm. This end was used to secure the probe stem when the probe was screwed into the rig and consisted of a bespoke nylon olive to allow the same fitting to be used throughout the experimental investigation. The safety fitting was also implemented to protect the probe in the unlikely event of a compression fitting failure. The fitting, which is clamped to the probe above the compression fitting using a tightened grub screw, was used to stop the probe from falling into the rig and becoming damaged. Its purpose doubled as a way of fixing the height of the probe in relation to the last stage vane to ensure that the measurements were taken at the same distance from the casing in each of the access holes.

The success of the initial measurement trial with the FAP-250(1) tip was determined by the ability of the probe to measure the flow pressure and the survival of the instrumentation. Following the successful pressure characterisation of the flow filed, the first sensor head was carefully removed from the stem and replaced with the fully calibrated Fap-250(2) head.

### 7.4.2 Pneumatic probes

A Pitot total pressure probe, as shown in figure 7.11 was used for measurements at the designed access points discussed in section 7.2.1. A Kiel tip was used to improve the accuracy of the measurement by increasing the acceptance angle of the pressure tapping at the probe tip.

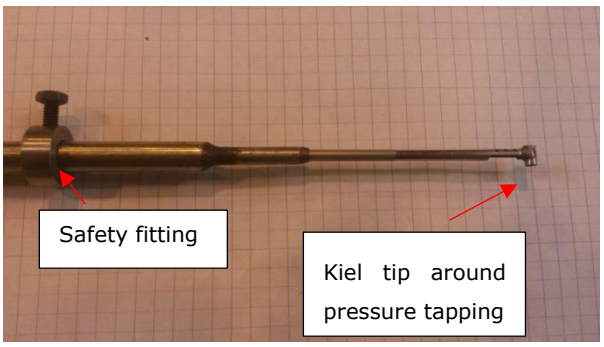



**Figure 7.11:Pitot total pressure probe used to characterise the flow field found within the compressor rig**

It should be noted that the distance from the access points to the probe tip is much smaller when using the Pitot probe than the 5S probe. This means that measurements were not completely comparable as the Pitot probe measurements were taken 50mm downstream of those taken using the 5S probe. The measurements were however used to assess the change in pressure in the first chord after the last stage and the flow field after the nozzle wakes were completely mixed out.

## 7.5 Experimental set-up and design

The experimental test points were discussed in section 7.2.1. As well as the 6 designed axial positions, there was also the capability to carry out a radial traverse at points between the last stage vane hub and tip. The bulk of the results discussed in this chapter are from the centre of the vane passage in the radial position, as the probe was deemed too large to take measurement in the tip jet region.

## 7.5.1 Measurement and analysis chain

During the experimental work, the measurement chain was set up as described in chapter 6, with the probe outputs being amplified and then acquired through the NI PXI system before being digitised and recorded using LabVIEW software. Each experimental run was saved as a series of Technical Data Management Streaming (TDMS) files due to their ability to retain data integrity whilst having the small disk footprint of a standard binary file system (NI, 2015). The full measurement and analysis software chain is described in figure 7.12 below.

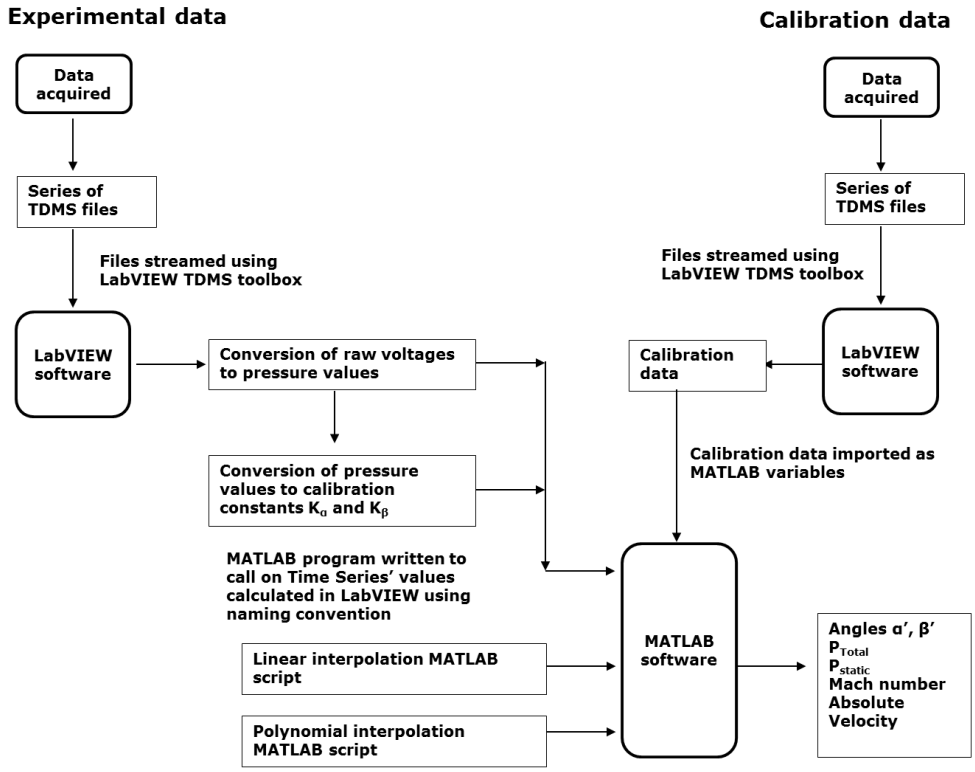



**Figure 7.12: Flowchart showing software data analysis chain**

## 7.5.2 Measurement of nozzle exit angle

The verification of the exit angle of the last stage was essential as the probe needed to be yawed into the centre of the nozzle passage between vanes. Although the value was measured on the bench top during the adaptation of the outer casing, its verification was carried out by taking measurements at a range of angles. The set-up of this test was as shown in figure 7.13.

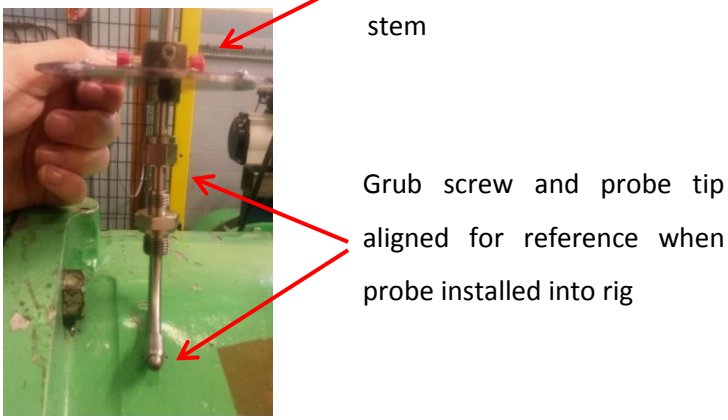



**Figure 7.13: 5S probe stem angular measurement system, set-up to assess the last stage exit angle**

A reference system was created on the probe stem so that the centreline of the sensor head was aligned with the positional datum on the protractor, which was secured to the stem. This meant that the direction in which the probe was pointing could be tracked using the protractor. The probe tip was then aligned to the centre point of the measurement hole with the rig running and data was taken at $2^0$ increments between $10^0$ and $30^0$ with the proposed exit angle resting somewhere in the middle of the range. The results of the angular measurements are given in figure 7.14. Each data point represents an average of 4 separate runs.

1

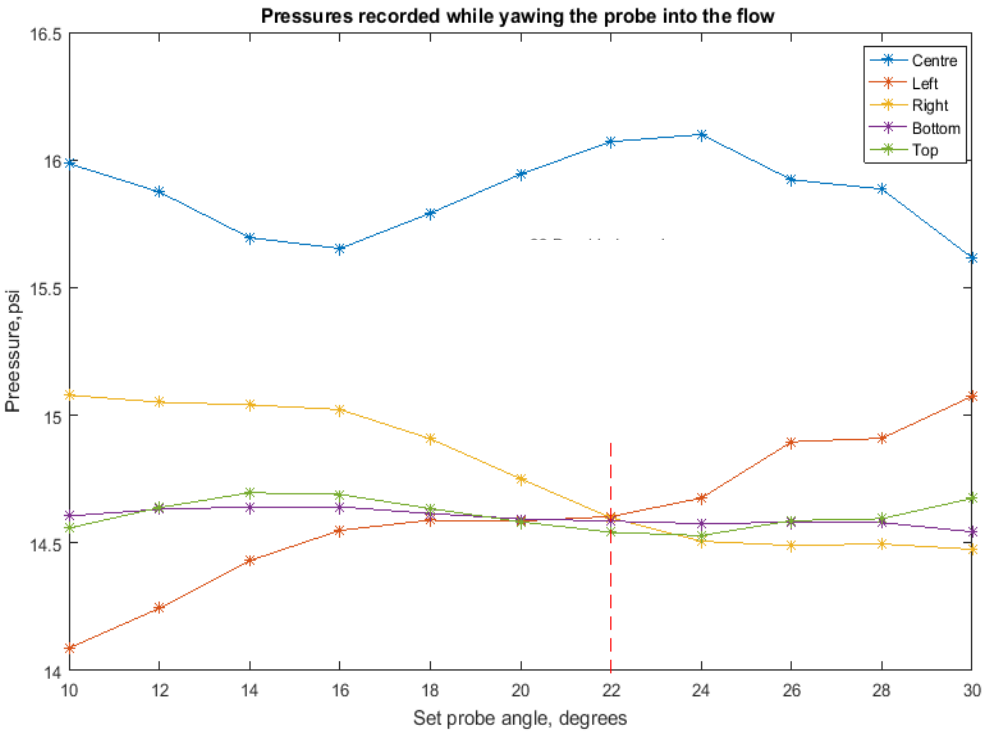



**Figure 7.14: Pressure data from each sensor during angular sensitivity test. Sensors aligned at an angle of $22^0$**

It is shown in the yaw sensitivity graph that the side sensors P2 to P5 (Left, Right, Bottom and Top) are best aligned and the centre sensor, P1 is at a maximum at an angle of $22^0$, as measured during the bench top investigation.

## 7.6 Compressor flow characterisation

The initial characterisation of the flow was carried out using a combination of the Pitot total pressure probe and a single sensor on the FAP-250(1) probe tip, both of which were introduced in section 7.3. The single sensor was used to represent a fast response pressure probe therefore care was taken to ensure that the sensor was properly

yawed into the flow before the data was captured. The total pressure and subsequent Mach number was calculated at each of the access points at a range of compressor speeds. To put the speeds set by the drive motor into context, table 7.1 shows the corresponding compressor motor speeds for each controlled driver rotational speed. The fast response sensor that was used to obtain the proposed blade passing frequency of the last stage rotor row.

| **Drive motor speed/rpm** | **Measured compressor speed/rpm (±25rpm)** | **Mach number at vane exit** |
|---|---|---|
| 300 | 1190 | 0.198 |
| 400 | 1590 | 0.23 |
| 500 | 1990 | 0.265 |
| 600 | 2383 | 0.302 |
| 700 | 2781 | 0.342 |
| 800 | 3181 | 0.383 |
| 900 | 3581 | 0.425 |

**Table 7.1: Summary of compressor operating conditions as measured during initial investigation of the flow field**

The Mach number values given in table 7.1 were calculated by the fap-250(1) sensor, at the exit to the last stage nozzle exit. Table 7.2 shows the number of aerofoils per stage; the values were used to calculate the blade passing frequency.

| **Compressor stage** | **Number of aerofoils** | |
|---|---|---|
| | Rotor | Stator |
| 6th Stage | 102 | 112 |
| 5th Stage | 102 | 112 |
| 4th Stage | 99 | 108 |
| 3rd Stage | *88* | *96* |
| 2nd Stage | *64* | *76* |
| 1st Stage | 37 | 52 |
| Pre-stator | - | 52 |

**Table 7.2: Number of aerofoils present in each compressor stage**

## 7.7 Time-averaged results

The pressure field was characterised by both the single sensor of the damaged fast response probe and the Kiel head probe. A true comparison between the two probes at the same spatial position as not possible due to the difference in the length of their stems which, when inserted into the rig meant a difference of 50mm in their measurement positions. The difference in the stem lengths allowed the compressor region, after the final stage, to be assessed in terms of time-averaged pressure, both directly after the vane exit as well over two blade chords downstream. The latter measurement area was assumed to be in a region of mixed out flow, where the turbulent

kinetic energy had already dissipated. Figures 7.15 and 7.16 show the measured Mach number results from both probes.

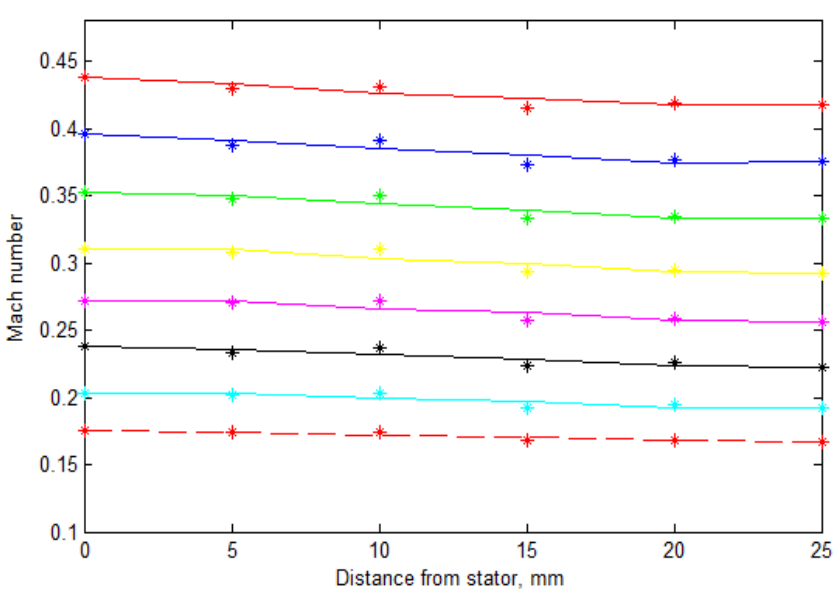



**Figure 7.16: Mach number deduced from a single sensor on the FAP-250(1) probe tip**

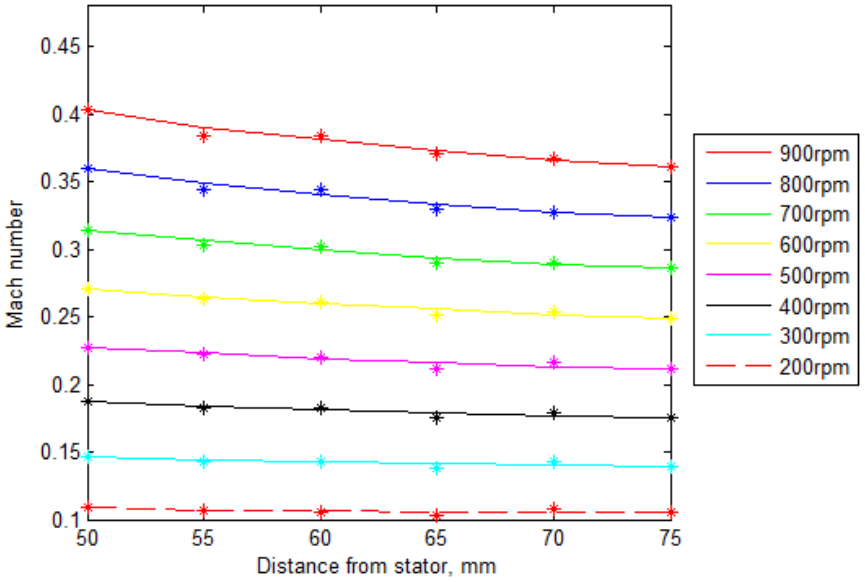



**Figure 7.15: Mach number deduced from the Kiel probe**

## 7.8 Time-resolved measurements

The blade passing frequency for each blade row was calculated to allow a comparison to be made between the predicted and measured frequencies found in the compressor wake.

The calculation was carried out using the number of aerofoils in each stage and measured compressor rotational speed for each set motor speed, as shown in figure using equation 7.1.

$$BPF, Hz = \frac{V_r \; x \; n_b}{60}$$

**Equation 7.1: Blade passing frequency equation**

Where $V_r$ is the rotational velocity, quoted in revolutions per minute (rpm), the data for which is given in table 7.1, and $n_b$ is the number of blades in each stage, as stated in table 7.2.

Due to the fluctuation in the measured compressor drive speeds, the input motor speeds have been used hereafter as a naming convention for the speed conditions. The corresponding compressor motor speeds are given in table 7.1.

Figure 7.17 shows the frequencies measured at position 1, closest to the exit vane, using the Right sensor of the fap-250(1) probe tip. The aim of this preliminary test was to assess the ability of the probe sensors to pick up the required frequency without exposing the fully working and calibrated 5S(2) probe to the unsteady flow. The investigation was deemed successful as the first probe tip was able to capture the required physical frequency from the compressor wake, as well as surviving the impact of the higher Mach number, pulsating flow field. In all cases, the frequencies measured by the fap-250(1) sensor were within 1% of those calculated using equation 7.1, with the largest difference being 0.8% for the 800rpm case.

It was therefore decided that the fully calibrated 5S probe would be implemented into the compressor rig with the aim of replicating the frequency data shown in figure 7.17, viewing the blade passing in the raw time trace of Mach number and analysing the statistical elements of the turbulent flow field data. The following section, 7.6, gives a representation of the capabilities of the calibrated 5S probe, starting with statistical quantities which time-averaged pneumatic probes are unable to provide. The raw Mach number time series results are shown as they truly highlight the unsteady nature of the flow as well as the ability of the probe to capture the blade passing amongst the turbulent flow field. A qualitative presentation of the wake flow at the last stage vane exit is also shown as filtered time series data. The final FFT graph, representing the 900rpm speed case, contains a second peak at a lower frequency than the blade passing frequency. A similar second peak can be seen in two other cases, the 400 rpm and the 800 rpm cases, although in these graphs the magnitude of the peak is around 1/5 of the blade passing frequency, where in the highest speed case the magnitude of the peak matched that of the fundamental flow frequency. The reason for this second frequency is at present unknown and further testing will need to be carried out to investigate it further. It can be deduced that the reason for the second peak must be of an aerodynamic nature and not purely mechanical. If it were mechanical the peak would most likely appear in all of the FFT results. A more likely explanation would be an extra resonance within the rig which only manifests itself at higher rotational speeds.

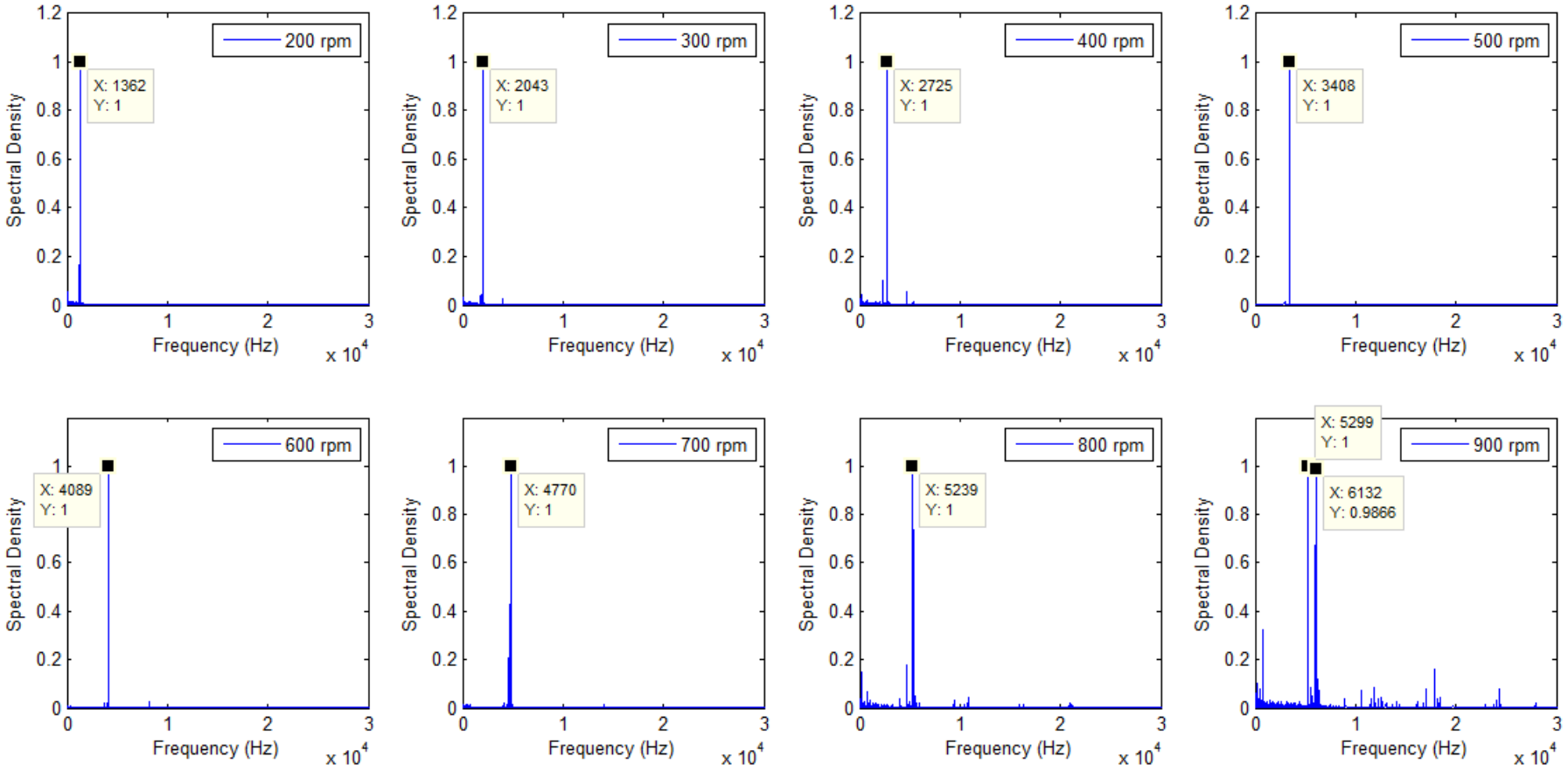



**Figure 7.17: Blade passing frequencies deduced from a single sensor on the fap-250(1) probe. Results are given for each compressor speed**

## 7.9 Statistical averaging of the results

One of the aims of this investigation was to assess how the time resolved results compare with traditional, averaged data from pneumatic probes. Of particular interest was the time over which measurements should be acquired to ensure that a steady average can be accomplished. In the compressor rig experiment, it was beneficial to see the time interval over which the 5S probe needed to be averaged to achieve a statistically steady result.

Figure 7.18 shows the arithmetic mean, normalised by the average reading at each motor speed, when divided over increasing time intervals. It shows the areas in which both fast response and pneumatic probes can take measurements. Figure 7.18 highlights the amount of unsteady information which is lost when taking time averaged measurements in unsteady flows fluctuating with time.

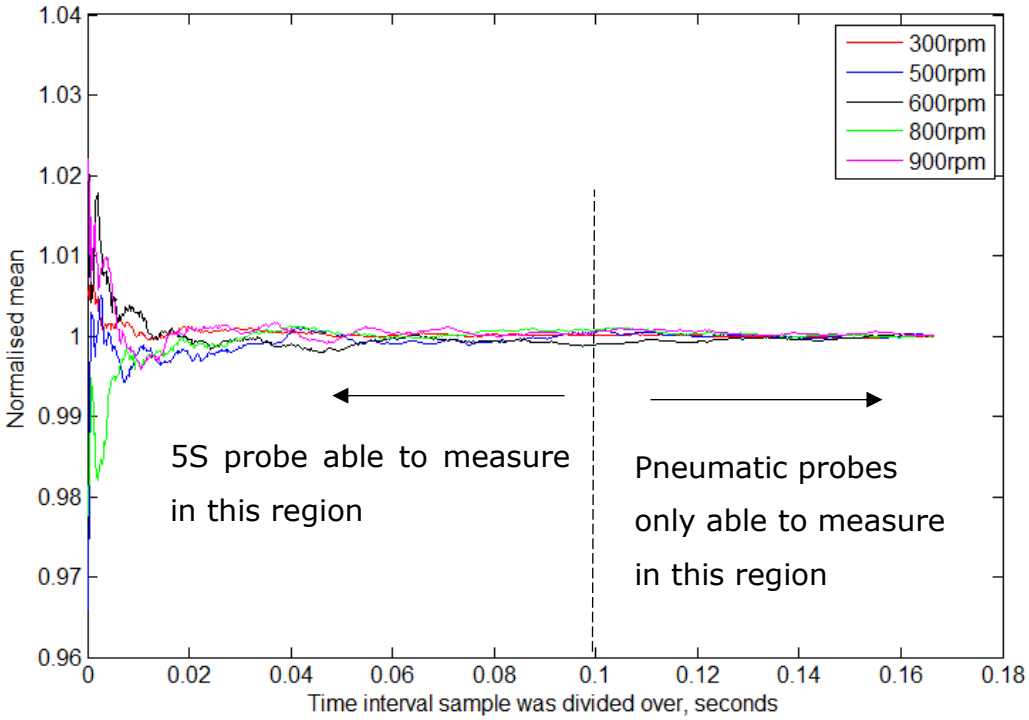



**Figure 7.18: Mach number statistical convergence**

The graph in figure 7.18 shows a running average for the time series data. The data has been normalised by the average taken over the full data set therefore the average on the graph lies at a normalised mean of 1. The data was averaged over a range of time intervals from 0.002 to 0.16 seconds. The x-axis shows these time intervals. Data on the left-hand side of the graph therefore shows the averages which can be obtained from sampling at a faster rate and the right-hand side of the graph shows the stabilised average which can be achieved using time-averaging probes. The graph shows the information, such as fluctuating averages, which is missed by using time-averaging Pitot style probes in unsteady flows. It can be seen that at the time interval of 0.1 seconds, the average results start to converge. Table 7.3 shows, for each motor speed shown in figure 7.18, the number of blade passages required until the statistics begin to converge.

| Speed, rpm | Blade passages until statistical convergence |
|---|---|
| **300** | 204 |
| **500** | 344 |
| **600** | 417 |
| **800** | 526 |
| **900** | 625 |

**Table 7.3: Calculation of blade passaging cycles until statistical convergence of the data**

The results in this section highlight how much data is missed when using a pneumatic probe in complex turbomachinery applications. The fluctuations in the first statistical mode shown in figure 7.18 at time intervals below 0.1 seconds contain the unsteady data of interest when deducing the frequencies present in the flow as well as the small scale temporal changes essential for deducing the turbulence intensity. Both of these quantities are essential for carrying out unsteady CFD predictions (Tucker, 2011).

## 7.10 Time resolved 5S probe measurements

Having seen the effect of time averaging on the Mach number data obtained from the FAP-250(1) sensor in section 7.6, examples of time resolved data are given in this section to highlight the capabilities of the fully calibrated 5S probe. The frequency analysis of the wake measurements, acquired over the range of experimental conditions, is given initially and the unprocessed Mach number traces are shown for a number of cases. Following this presentation of raw, unsteady data, visualisations of the blade passing in the time series data are

given along with the turbulence intensity found throughout the measurement area. The ability of the 5S probe to capture the dynamics present between blade passages is highlighted by plots of directional velocity components' trajectories as measured at the stator exit.

## 7.11 Blade passing cycle results

Fernández Oro *et al*. (2014) discuss the importance of carrying out a frequency analysis as an initial investigation step to ensure that measurement instrument is able to perform correctly under the unsteady conditions found in turbomachinery rigs. The frequency analysis carried out on the pressure trace obtained from a single sensor on the FAP-250(1) probe tip was therefore repeated on the Mach number traces acquired using the fully calibrated 5S probe. The results of which are shown in figure 7.19. This was carried out initially with multiple aims. It initially allowed for an understanding of the physical phenomena found within the flow on a high level before further analysis was carried out. It also highlights that the data integrity of the individual pressure traces was preserved when they were processed using the calibration and data reduction methodology described in chapter 6.

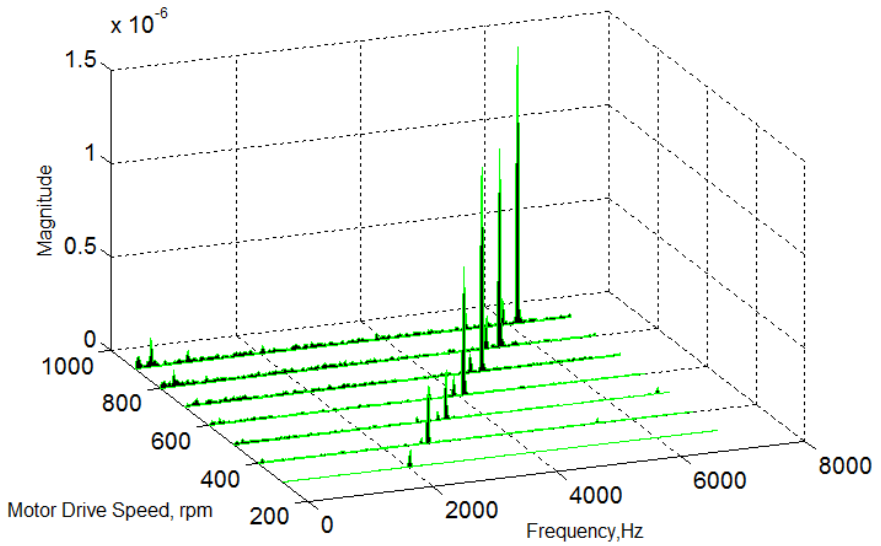



**Figure 7.19: BPFs calculated from the calibrated Mach numbers obtained from the 5S probe**

The results are shown in figure 7.19 are matching the frequencies measured using only the pressure trace. These measured BPFs are also compared to those calculated using equation 7.2, as shown in table 7.4.

| Motor Drive Speed, rpm | Measured last stage rotor blade passing frequency, Hz | % difference in predicted and measured BPF | Number of samples per blade passing | Time interval per blade passing, ms |
|---|---|---|---|---|
| **300** | 2043 | 0.99 | 29.37 | 0.49 |
| **400** | 2725 | 0.18 | 22.02 | 0.37 |
| **500** | 3408 | 0.03 | 17.61 | 0.29 |
| **600** | 4089 | 0.42 | 14.67 | 0.24 |
| **700** | 4770 | 0.21 | 12.58 | 0.21 |
| **800** | 5239 | 0.84 | 11.45 | 0.19 |
| **900** | 6132 | 0.03 | 9.78 | 0.16 |

**Table 7.4: Blade passing frequencies and subsequent time data for the blade passing cycles for each set motor speed**

It can be seen that in all cases, the percentage difference in the measured and calculated blade passing frequencies was less than 1%.

The number of samples captured per blade passing at each motor drive speed was calculated as in equation 7.2.

$$Samples\ per\ period = \frac{Sample\ rate\ (Hz)}{Frequency\ of\ interest\ (Hz)}$$

**Equation 7.2: Calculation of samples per period**

The resulting number of samples per blade passing is given above in table 7.4. These results were used to not only identify distinct Mach

number drops in the time traces highlighting blade passing, but also as a general measure of the probe's resolution at each set motor speed.

## 7.12 Presentation of unsteady data

The unsteady data acquired from the stator wake using the 5S probe is shown in this section as time series samples at various conditions. The aim of this presentation of raw data is to emphasise the level of randomness observed in the data and the irregular nature of the resulting Mach number traces. A selection of conditions are shown in figures 7.20 to 7.23. It can be seen in all examples given that distinctive blade passages are present in among unsteady data. These dips in Mach number are highlighted on each figure with the times in ms at the edges of each blade passage. In each figure, two blade passages have been identified with the first occurrence in the time series being named 'A' and the second being named 'B'.

Figure 7.24 has been included to show the results from each individual sensor as well as the constructed Mach number graph. The results represent the flow at a motor drive speed of 600rpm. Characteristic blade passing dips in the data have been highlighted through all 3 of the graphs shown; the Mach number trace at the top, the trace of the central sensor, P1 in the middle and the peripheral sensors, P2 – P5 at the bottom. It is shown that the characteristic dip representing the blade passing can be clearly seen in the Mach number and central sensor traces, but the P2-P5 sensors show varying attributes across the highlighted blade passages. Although the data from the individual sensors does not give any relatable information in terms of flow direction or velocity, it is interesting to see the difference in periodicity shown in each of the sensors.

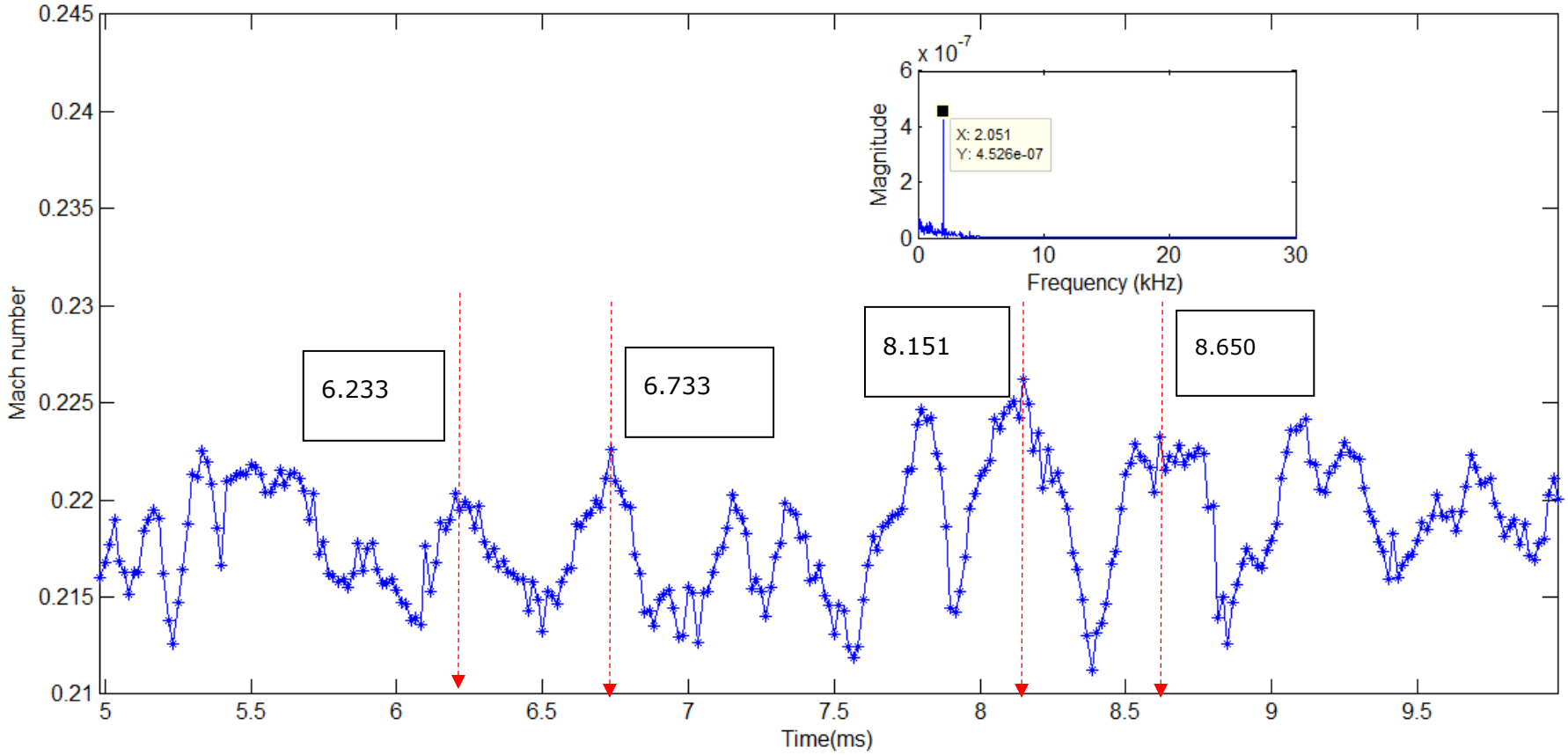



**Figure 7.20: 300rpm at position 1 at vane exit, time interval: 0.499 ms**

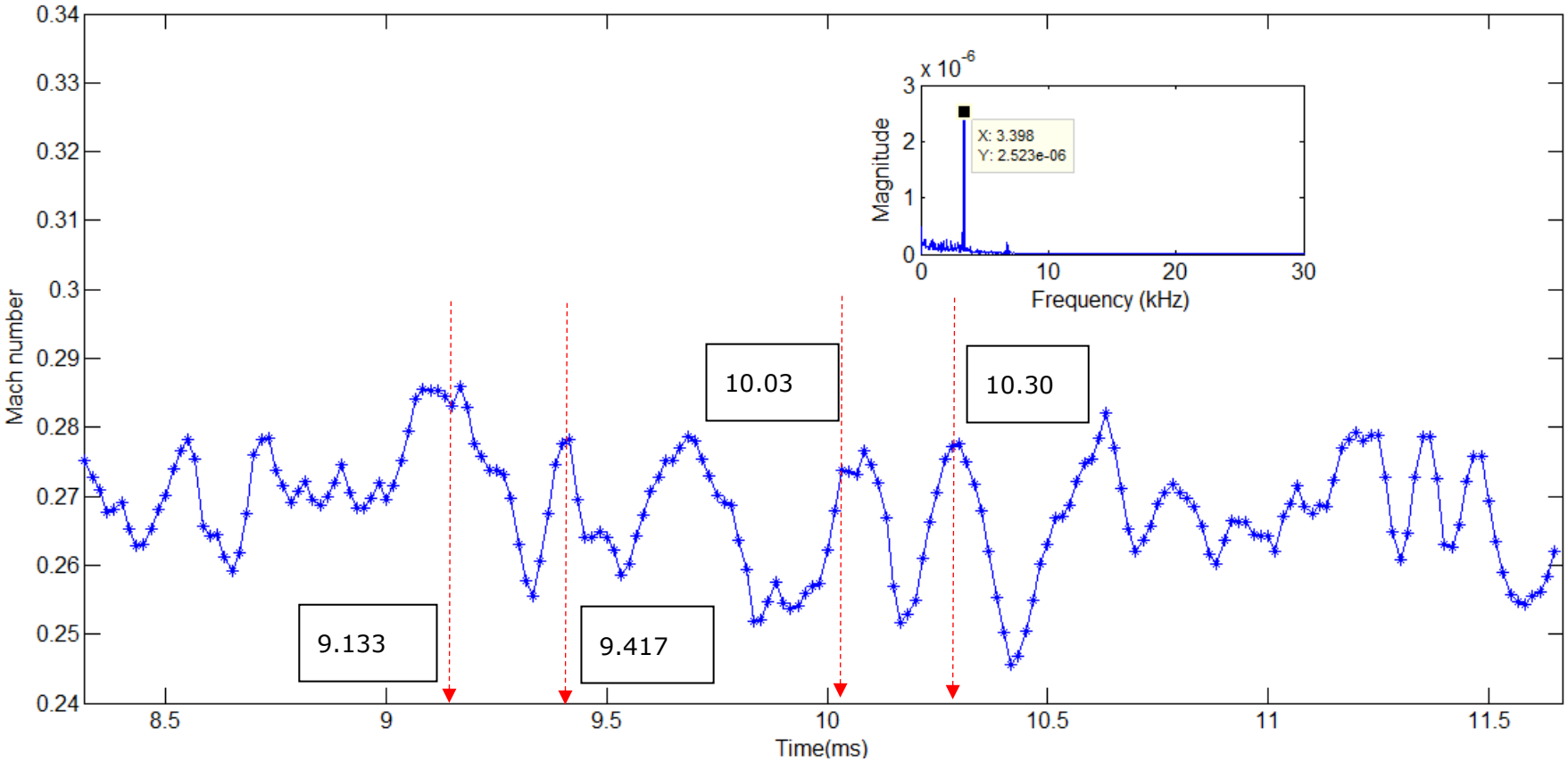



**Figure 7.21:500rpm at position 1 at vane exit, time interval: 0.29 ms**

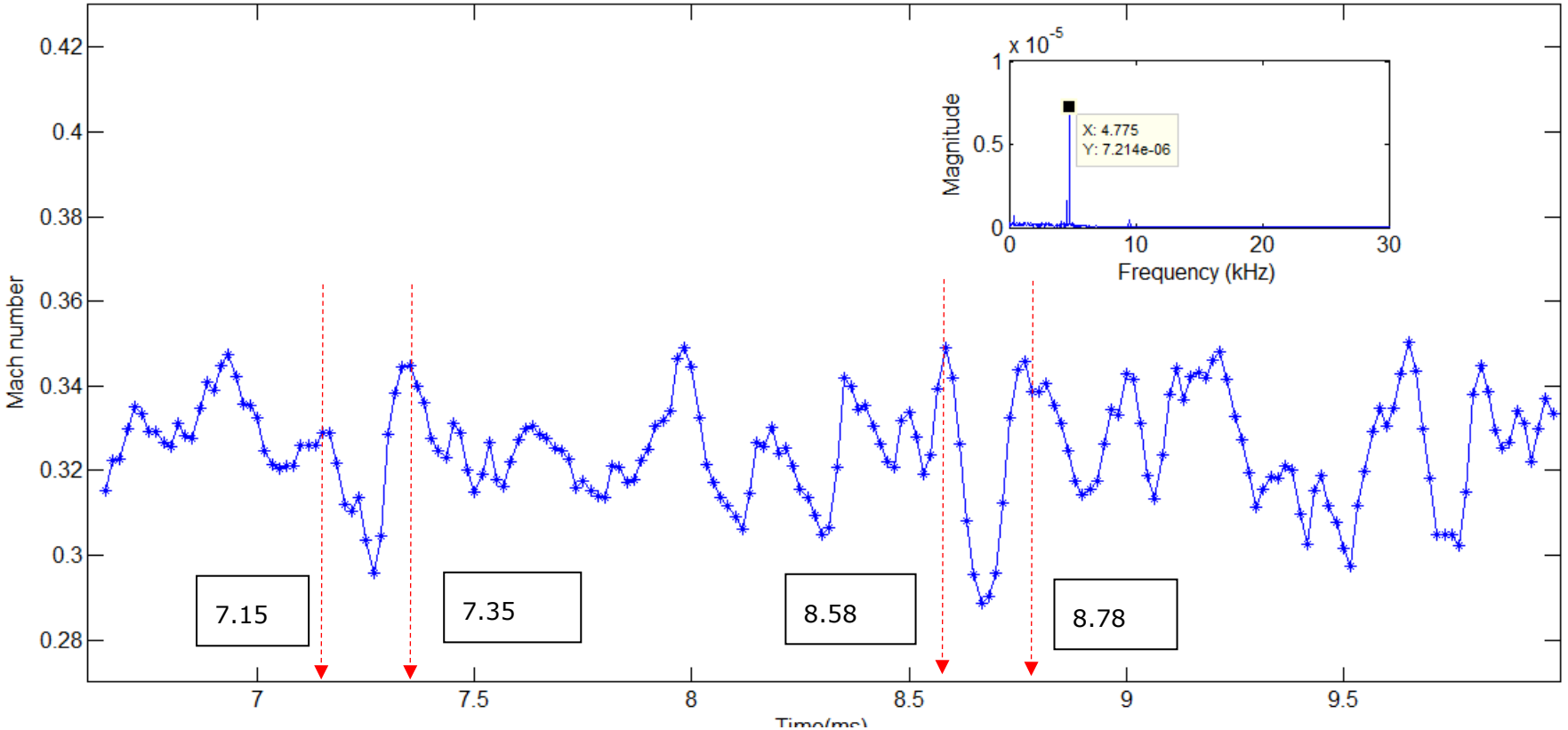



**Figure 7.22: 700rpm at position 1 at vane exit, time interval: 0.21 ms**

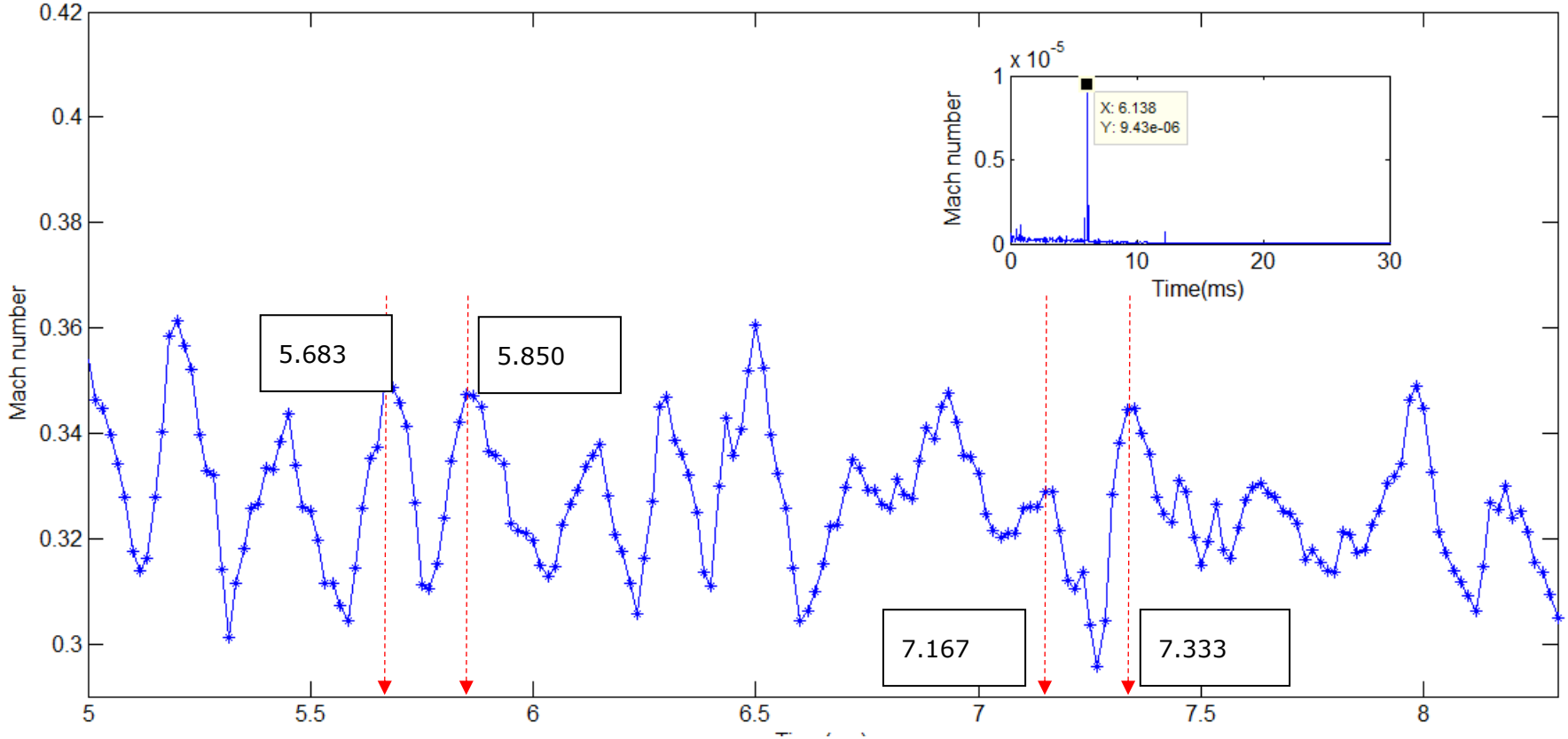



**Figure 7.23: 900rpm at position 1 at vane exit, time interval: 0.166 ms**

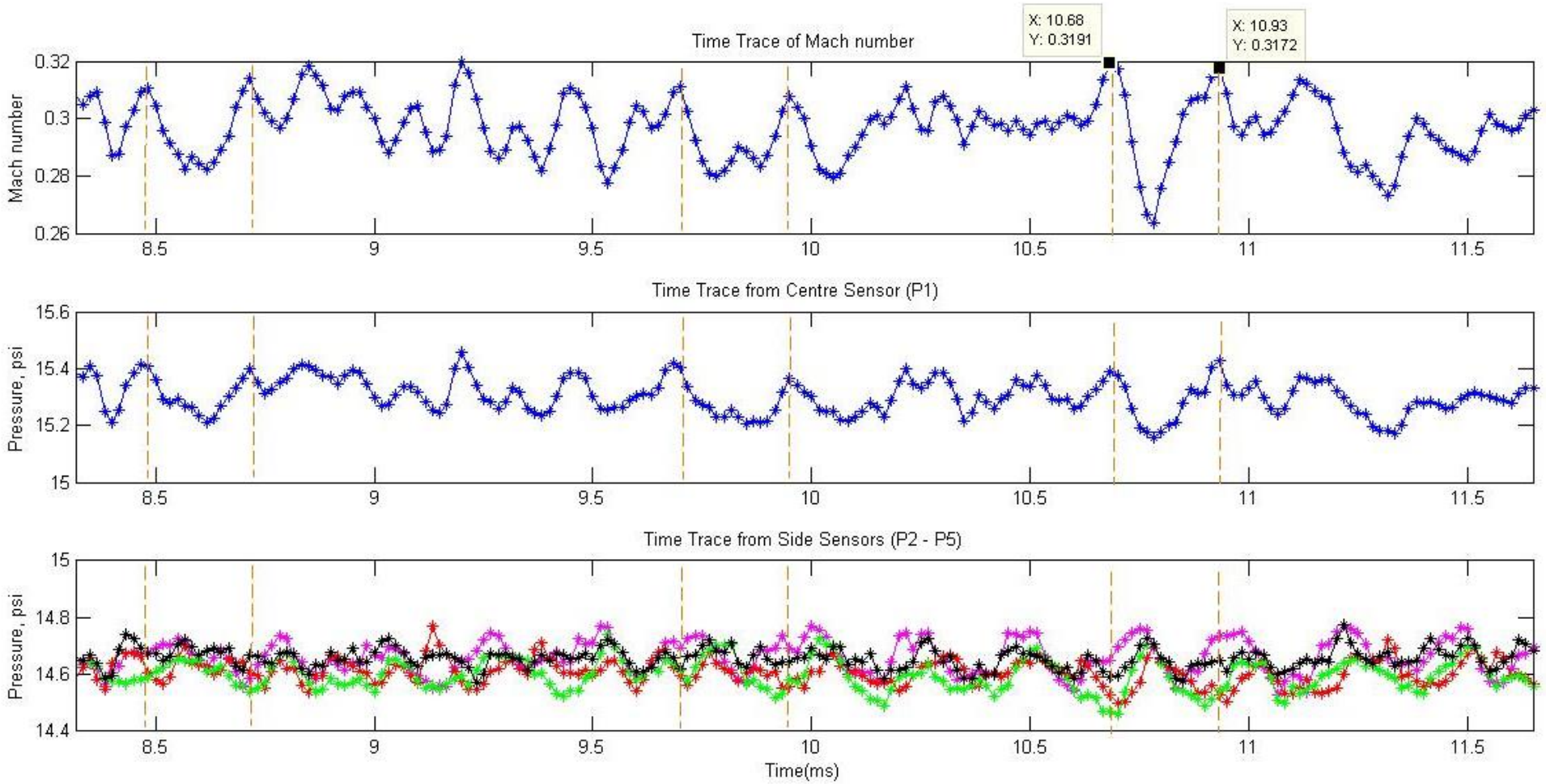



**Figure 7.24: Mach number trace with corresponding individual pressure traces from each of the sensors in the 5S probe**

The irregular nature of the Mach number traces is clearly shown in figures 7.20 to 7.23. In figure 7.22 for example, the blade passing trough B is quite regular, with the Mach number dip being well pronounced. Blade passing cycle A is less coherent than B with the Mach number fluctuating through the dip itself. This can be seen in figure 7.23 also, at the top motor speed of 900rpm. In this case, blade passing cycle A is more regular than B. The irregular dips in the time traces could be attributed to a combination of interactions with previous blade passages, unsteadiness caused by the compressor working beyond its design conditions, and random turbulence produced throughout the blade rows.

There is a need to deduce the general trend in the Mach number caused by the blade passing. Although this takes out the unsteadiness of the flow, if enough measurements are taken between blade passages, a visual representation of the blade passing in time can be construed. This allows the turbulence present in the flow to be analysed separately from the blade passing effect. The root causes of the flow unsteadiness mentioned previously can then be deduced independently. There are many possible reasons for the irregular time traces relating to aerodynamic changes inside the rig. It could be due to mixing within the flow, defects inside the rig or other small scale dynamics which can't be measured with an invasive method. These can lead to small pressure changes over time which interact with the bulk flow from the blade passing and lead to irregular time traces.

As a result of the irregular time traces, standard analysis techniques used throughout the industry to do this, such as ensemble and phase averaging, were unable to be used in this case. An analysis of the raw 5S probe data was carried out to view this averaged blade passing effect, which is discussed in the next section.

## 7.13 Wake analysis

This section gives some insight into the levels of analysis which can be applied to the 5S probe data. The aim is to highlight the type of results which can be deduced from the new measurement system which, to the author's knowledge, have not been reported in the industry before.

The analysis of the wake was carried out not only to determine the general trend in the Mach number based on the blade passing, but also to assess if any interactions with previous blade rows could be detected. The results of this method are intended to give a visual representation of the blade passing effect on the flow. The data was put through a reverse FFT filtering process which was used to highlight the effect of significant flow interactions on the time series data. The results were obtained by carrying out a Fourier Transform of the time series and identifying the main blade passing frequency along with up to 5 other fundamental frequencies, representing flow interactions, present in the FFT data. These were then used to reconstruct a wake time profile of Mach number by creating a superposition of measured frequencies. This resulted in a filtering effect where only the most prominent frequency components were taken into account and the smaller scale interactions are disregarded.

The results given in figures 7.25 to 7.27 show the wake analysis results for the motor speeds 900 rpm, 700 rpm and 500 rpm. Each figure also shows three measurement positions; position 1 at the stator exit, position 3 and position 6. Looking initially at the high speed case in figure 7.25, a peak in the middle of the Mach number dip, called A in the figure, is visible in position 1. This then reduces in magnitude moving away from the stator at position 3. It then completely disappears from the time trace at position 6, as highlighted in position C, one chord length away from the exit nozzle.

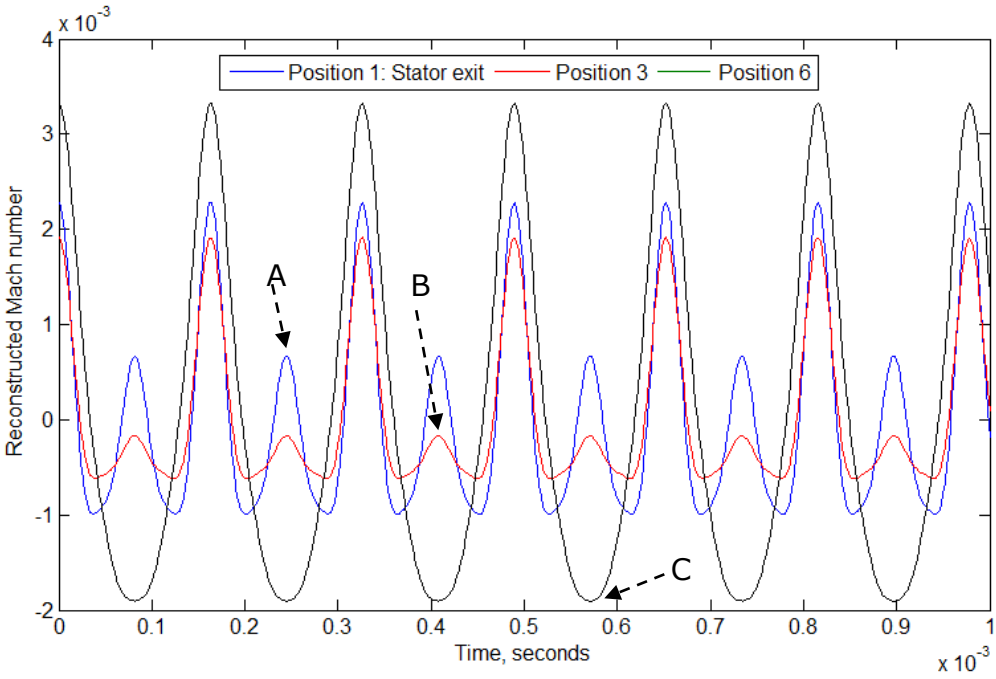



**Figure 7.25: Reconstructed Mach number time trace at a motor speed of 900rpm**

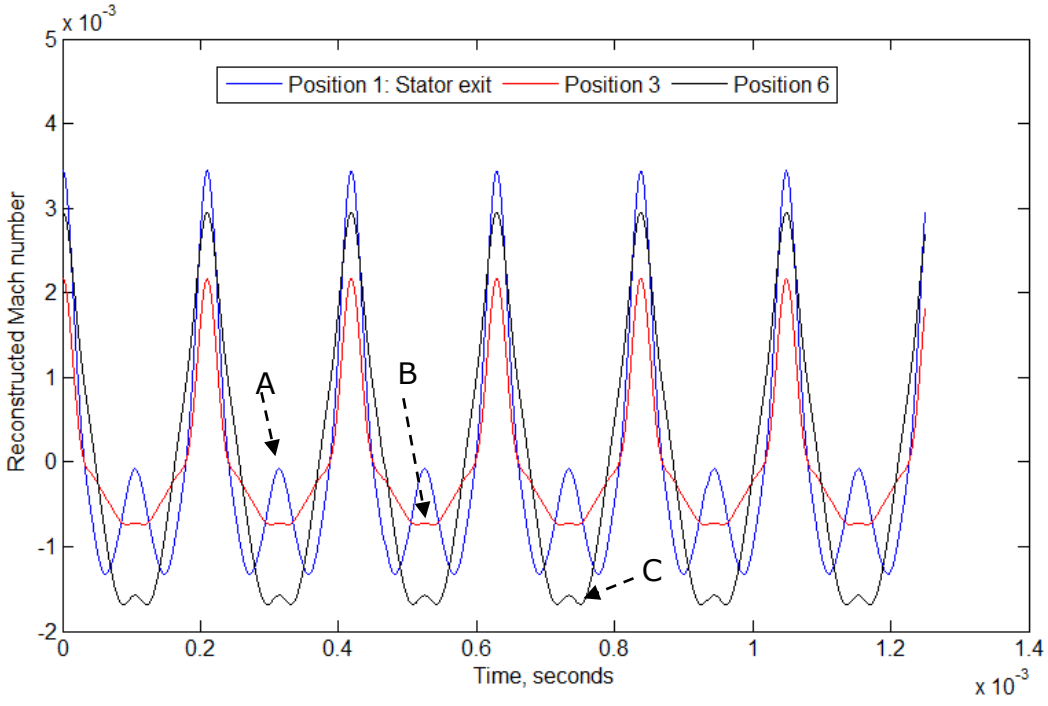



**Figure 7.26: Reconstructed Mach number time trace at a motor speed of 700rpm**

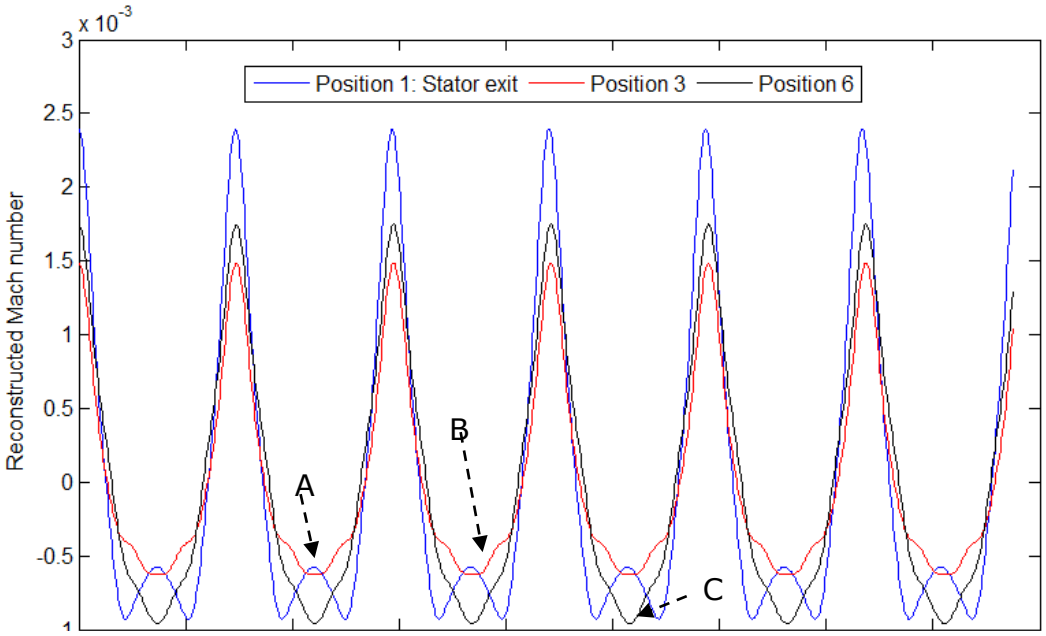



**Figure 7.27 Reconstructed Mach number time trace at a motor speed of 500rpm**

This trend is clearly visible in the lower speed cases. Figure 7.26 gives the results of the 700 rpm case. In this case, the peak A is similar in shape to the same peak observed in figure 7.25. Peak B shows a more flat bottomed profile than in the previous case and the final characteristic shape, C shows a small peak in the centre of the trough. Finally in figure 7.27, a similar trend between the results for the 900rpm case can be observed for each measurement position. The peaks and troughs in the centre of each blade passing cycle, denoted by A, B and C are narrower than the other results, potentially highlighting another interaction at the lower speed affecting the Mach number. Overall, these results show that although the general trend in the averaged Mach number over the blade passing is similar for a range of speeds, subtle differences can be seen at specific conditions.

The most likely reason for the peaks A and B shown in the results is an interaction with the previous blade passage. This is possible as the number of blades in rotor stage 5 and 6 is the same, so the frequency for both sets of blades passing the probe would be the same. The peaks observed in the centre of the troughs could indicate a phased

offset between the passing of each blade row, which would be highlighted in the time series trace but not in the frequency analysis.

These results show the level of detail which can be obtained using the 5S probe. They highlight the ability of the probe to pick up changes in the periodic nature of the flow at a range of speeds and axial positions.

Following the deduction of the trend in Mach number over time, an ideal analysis would allow for the averaged blade passing cycle to be subtracted from the raw data to leave periodic flow data and the fluctuating turbulent component. This is known as the Triple Reynolds Decomposition of the data, as shown in equation 7.3 as the decomposition of the raw data into mean, periodic and fluctuating components (Reynolds and Hussain, 1971), (Cantwell and Coates, 1983).

$$P(x,t) = \bar{P}(x) + \tilde{P}(x,t) + P'(x,t)$$

**Equation 7.3: General Reynolds Decomposition equation**

Where $P$ represents the fluid pressure in question. Equation 7.3 shows the property, in this case Mach number, which is a function of both space and time, being decomposed into its spatially averaged component, a periodically varying component and a fluctuating component which is changing more rapidly with time.

The big question, when applying this style of analysis to turbomachinery flow with the aim of deducing the fluctuating component, lies with which average to use when deducting it from the raw signal. In their research, McDonough (2007) states the general transitions which a flow can go through with increasing Reynolds number. This is shown in figure 7.28.

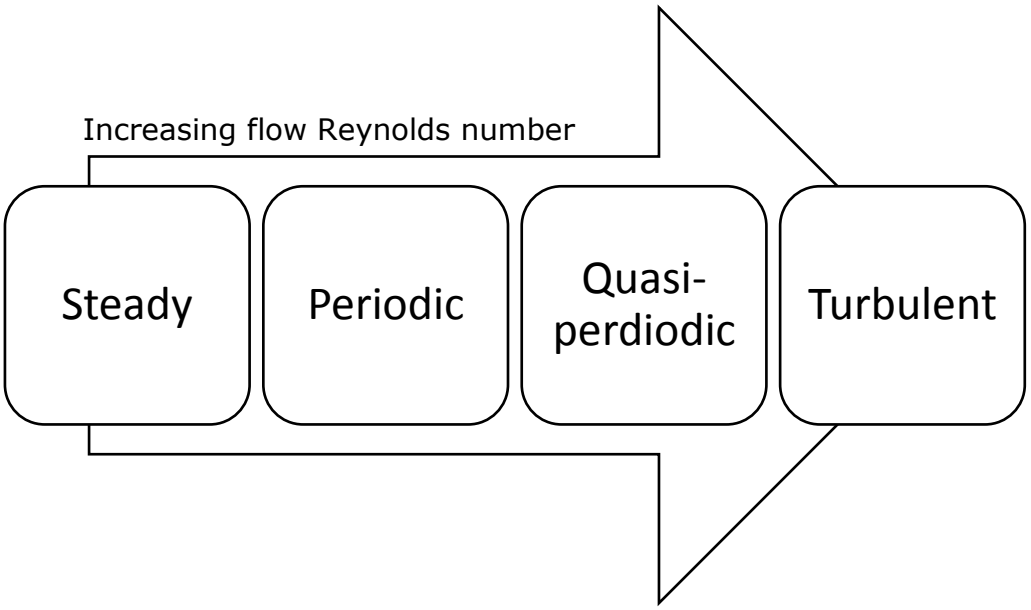



**Figure 7.28: Flow transitions with increasing Reynolds number**

Clearly the arithmetic mean calculated from the time series would not be applicable as the effect of the blade passing would be discounted. This type of averaging is only applicable to steady flows. In a low Reynolds number periodic flow, the averaged blade passing cycle could be taken as the mean component in the flow. The problem then lies with the final two transitions shown in figure 7.28. As the compressor flow is more unsteady than a purely periodic flow, something more physical than the blade passing cycle is needed to deduce the fluctuating component. For this reason, a moving average was applied to the raw data so that the mean component could be calculated.

## 7.14 Vector component trace results

As the data from the 5S probe was acquired simultaneously across all five sensors, the time resolved data contained within blade passing cycles can be analysed. This data would otherwise be lost during

phase or ensemble averaging techniques which are used when the data is acquired at different times and then reconstructed. The ability of the 5S probe to provide such data is highlighted in this section by the presentation of the time-resolved trajectory of the directional components of Mach number at the last stage stator exit.

The components were calculated from the interpolated Yaw and Pitch angles as well as the magnitude of Mach number. They have been denoted here as $Ma_u$, $Ma_v$ and $Ma_w$. Figure 7.29 shows the crosswise components plotted as a smoothed scatter plot against each other. The figure represents data from the highest motor speed of 900rpm. The trajectory direction has been labelled alphabetically with the start and end point being at A. The most noticeable attribute of the vectors captured during the blade passing cycle is that it forms a 'figure of eight' shape which suggests that the flow within the wake is oscillating equally in both crosswise directions. There are also clear points, labelled A – E whereby the vector components change direction.

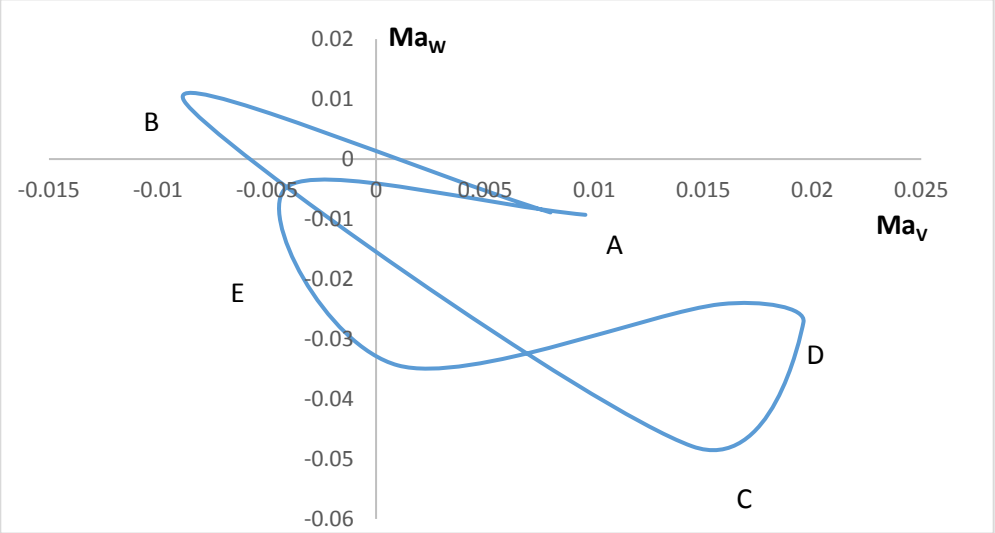



**Figure 7.29: Trajectory formed between the crosswise Mach number components at the last stage exit, as measured by the 5S probe**

This type of time-resolved data is essential for CFD inputs. When considering multiple time traces, statistical analysis can be performed over the entire data set. This is important because it highlights areas with high velocity gradients, such as the turning points shown in figure 7.29, where finer meshing is necessary in CFD simulations. This will help to make dynamic meshing techniques more efficient in the future. As well as its validation as the cost of simulating such a small scale temporal change in the flow properties would be too costly to consider in an industrial setting.

## 7.15 Conclusions

The ability of the 5S probe to be applied to an industrial scale compressor rig have been presented in this chapter. Following the initial characterisation of the rig flow using the pneumatic Kiel probe and a single sensor on the FAP-250(1) probe tip, the fully calibrated 5S probe, using the FAP-250(2) sensor, was used to take 3D, time-resolved measurements in the wake of the compressor stages.

The data integrity was preserved through the calibration and data reduction process outlined in chapter 6. This was shown through the conservation of the dominant blade passing frequency at each speed between the pressure trace acquired using a single sensor and the Mach number trace acquired using the 5S probe. Raw time series data was presented in this chapter which highlighted the unsteady and irregular nature of the flow, which the probe was able to resolve. The root causes of the unsteadiness in the compressor wake were then looked at in order to showcase the ability of the measurement system to deduce flow quantities which no other technique is capable of doing in such a high powered rig at present. As an initial step, the averaged blade passing cycle was calculated which emphasised the interactions occurring between previous stages as potential causes of the flow unsteadiness.

The results in this section obtained from the 5S probe truly show the new information available to the turbomachinery design and CFD engineering disciplines; data which is lost when taking measurements using a pneumatic probe or a time-resolved probe combined with a phase averaged approach to data acquisition.

# Chapter 8: Conclusions and future outlook

## 8.1 Research overview

The advancement of measurement techniques used by the sponsor company, GE power, to characterise the flow in their turbomachinery rigs was the main objective of this thesis. A commercially available 5 sensor piezoresistive probe has been incorporated into a novel system which was calibrated and then implemented into a 6-stage compressor rig. Fluctuating pressure data was acquired after the final stage stator nozzle of this industrial scale rig. This pioneering system made it possible to take three dimensional measurements of unsteady flow in turbulent conditions within an industrial scale turbomachine.

The pressure probe itself consists of a Kulite FAP-250 sensor head imbedded into a bespoke stem and integrated via a tailored coupling mechanism. This allows the head to be easily assembled into many different stems, providing the sponsor company with the flexibility of using the fully calibrated 3D probe for a range of applications with different geometries. The acquisition system, as described in chapter 4, allowed the simultaneous measurement of pressure from all 5 sensors, which allowed for instantaneous velocity measurements through the interpolation of the calibration data. The results obtained from compressor rig were analysed to highlight additional information about the flow which can be obtained with this novel system.

### 8.1.1 Probe design summary

The FAP-250 probe tip was acquired as a standalone piece of instrumentation, as shown in chapter 4. It was delivered as a

hemispherical tip with flush mounted pressure sensors. The back of the tip was packed with silicone sealant which allowed the sensors to be protected whilst keeping the 20 thin wires leading out from the head safely in place. This presented the major challenge of deciding how to connect the tip to a supporting stem without causing damage to the fragile sensors mounted into the probe head. Attachment using heat or chemical adhesives was too harsh for use with the probe. These solutions were also too permanent for the 5S probe, as the calibrated tip was to be used for multiple applications which required different stem geometries. A bespoke coupling mechanism was therefore designed and manufactured to give the sponsor company flexibility in the use of the finalised probe. The coupling piece allows the probe stem to be changed for a range of applications without risking damage to the sensors.

Three probe stem designs were presented in chapter 4; one swan neck stem to be used with an air jet rig, one straight stem with an angled tip to be used with a low pressure turbine rig and one $90^0$ angled stem for use with a compressor rig. The stems were named $\alpha$, $\beta$ and $\gamma$ respectively. The reason for the variety in stem geometries was due to the differences in access requirements between the applications.

### 8.1.2 5S probe characterisation summary

The initial characterisation of the fast response probe was performed using the sensor head coupled with Stem $\alpha$. The sensor calibration was carried out to determine the sensitivities of each probe transducer . They were all between 4 and 5 mV/psi. This process was carried out using a Deadweight tester (DWT), a closed system whereby the sensors are exposed to a range of steady pressures to

view the output voltages. The results highlighted the drift in the baseline values of the sensors between different atmospheric conditions. The resulting gradient for each sensor was found to be steady between calibration runs. All experimental probe data was therefore taken with respect to a datum value to negate the effect of the zero drift.

The effect of thermal drift was also investigated by calibrating the sensors in an oven at temperatures ranging from $25^0$C to $50^0$C. This investigation was carried out with temperature compensation networks supplied by the manufacturer as well as those manufactured in-house. Tests were also performed without any resistors attached. It was found that the effect of thermal drift was reduced with the attachment of the resistor networks into the sensor circuitry.

The 5S probe was characterised further using the air jet rig as a vortex shedding experiment using a copper rod as a bluff body. This allowed the ability of the sensors to measure the frequency content of the flow. It was shown in this section that all five sensors were able to measure the vortex shedding frequency clearly. This was shown in an FFT trace of the acquired data as well as time series data from opposing sensors on the probe tip. The latter result highlighted the alternative vortices being shed at either side of the rod. At this point, the abilities of the probe hardware, as standalone pieces of instrumentation, were proven to be suitable to undertake novel measurements in the industrial scale compressor rig.

### 8.1.3 Aerodynamic calibration and validation summary

The probe was then calibrated aerodynamically to map the effect of a range of flow angles to the response of the tip sensors. A yaw-pitch manipulator was designed to position the probe tip at a range of angles relative to the core of an axisymmetric jet. The probe was then exposed to angle pairs of $\pm 20^0$ in both the yaw and pitch directions

and the resulting pressures recorded from the sensors were converted into four non-dimensional calibration coefficients, $K_\alpha$ and $K_\beta$ to represent the angular coefficients and $K_s$ and $K_T$ to represent the static and total coefficients. The results were plotted as pressure surfaces and the method of data interpolation was investigated. A new method of interpolation was proposed for the angular coefficients, whereby the local grid points around a query point are found by linear interpolation. This method was proven to give results which were in agreement with the more tried and tested surface fit method for the angular coefficients. It was also found to be 4 orders of magnitude faster than the traditional $4^{th}$ order polynomial method. The time improvement is due to the reduction in the equation order as well as the fact that the linear method negates the need to simultaneously solve the equations. This interpolation method gives way to the possibility of in-situ data reduction to assess rapid angle changes in the flow whilst testing, saving a lot of time and cost associated with setting the experiment up to repeat test runs. It was also shown in chapter 6 why this method was suitable for the angular coefficients and not for the pressure coefficients. Researchers have previously used the simultaneous solving of high order surface polynomials for all 4 calibration coefficients. It has been proven in this thesis that this is only necessary for two of them, and a much faster and simpler approach has been provided and used throughout this investigation. Prior to testing the fully calibrated 5S probe in the compressor rig, an uncertainty analysis was carried out on the measured and inferred quantities. The main sources of ambiguity were highlighted and expanded uncertainties of the main flow properties $\alpha'$, $\beta'$, $P_t'$ and $P_s'$ were calculated as 0.66%, 2.18%, 2.76% and 4.06% respectively. These results are comparable with those calculated by researches working on fast response pressure probes, as shown in chapter 6.

### 8.1.4 Compressor rig testing summary

The 6-stage compressor rig was adapted to allow the 5S probe to be inserted through the outer casing and be angled into the flow field beyond the final stage stator. Time averaged statistics were presented to highlight the area of unsteadiness which can be measured using the fast response probe. The Mach number variation across the measurement section was also presented. The novel, time resolved measurements were first shown as a plot of the blade passing frequency measured at varying speeds at the exit of the last stage. A clear frequency peak can be seen in each case, which is comparable with those calculated using the engine speed and number of blades per stage. The raw, unsteady data was then shown for a number of cases to highlight how chaotic and irregular the flow field was found to be. Clear blade passages are picked out in these raw time series results, however little repetition was found between each blade passing cycle. As a result, an analysis of the wake was carried out to filter out much of the data noise. This aim of this analysis was to view the effect of the blade passing the 5S probe over time. The time series was transformed into the frequency domain and the dominant peaks were identified and used to re-construct the Mach number time traces. It was found that the dominant shape of the wake, as represented as Mach number time series', altered depending on the position of the probe as well as the speed. Interestingly, the effect of previous blade passages can clearly be seen in the reconstructed Mach number traces shown in chapter 7. This result emphasises the capabilities of the 5S probe as an unsteady measurement system.

## 8.2 Limitations

This section outlines the main limitations of the 5S probe instrumentation and the overall study which need to be considered for its future use. The study limitations are focused on the way in

which the probe was calibrated as restrictions on its potential application are related to the calibration methodology. The limitations relating to the probe itself are associated with the instrumentation used within its head as well as its overall geometry.

The pressure rating of the instrumentation was a key limitation of the 5S probe. Although the range at which it could work with confidence in its calibration was up to twice its rated pressure, in order to move to highly pressurised systems a probe with a higher pressure rating would need to be acquired and calibrated as per this thesis.

A main feature of the study is that the probe was built with the aim of being tested in scaled turbine models which represented realistic site turbomachines. The study did not include any testing in a full sale turbine such as those used for energy generation, meaning that further testing will need to be carried out to ensure that the probe is robust enough for harsher conditions. Similarly, limitations exist for testing in smaller turbomachines, designated for research purposes, due to the size of the probe head.

One of the main limitations of the study is the Mach number at which the 5S probe was calibrated. The probe was calibrated and tested at subsonic Mach numbers, meaning that it could not be applied to flows with transonic or supersonic characteristics such as shock waves. Theoretically the probe is able to work at supersonic Mach numbers as long as the environment pressure does not exceed the rating of the probe, however a higher Mach number calibration would need to be carried out.

It was also proven that the 5S probe was able to measure fast response transient data, but turbulent flow fluctuations were not acquired from the air jet rig or the compressor rig. Further testing and comparisons with tried and tested turbulence measurement techniques such as hot wires would need to be carried out to determine the potential for the 5S probe to measure true turbulent fluctuations.

## 8.3 Future work

This section discusses potential adaptions to the measurement system for use in future applications. Recommendations are made for improving the accuracy of the system as well as some considerations for taking measurements in a gas rig, such as the LP turbine rig introduced in chapter 4.

### 8.3.1 Improving calibration accuracy

In order to improve the accuracy of the system, an improvement in the calibration matrix will give the biggest benefit, in the reader's opinion. The accuracy of the interpolation methodology has been discussed in chapter 6, however further improvements can be made by increasing the order of the surface polynomials. This does however lead to an increase in computation time and cost, reducing the benefit of the increased accuracy.

The calibration procedure can be improved by automating the setting of the calibration angle of the probe tip. It was shown in the uncertainty analysis that the pitch angle uncertainty was 1.5% less than the yaw angle. The reason for this is that the yaw angle was set using a motorised traverse mechanism and the pitch angle was set manually, and checked with the digital inclinometer. An improvement in the setting of the calibration angle would also have the aim of making the 2D calibration grid more regular, which would in turn improve the linear interpolation accuracy.

### 8.3.2 Taking measurements in the turbine rig

To take measurements in the LP turbine rig, the 5S probe will have to be calibrated in the working gas R134a due to the difference in

density between that and the air calibration. If the calibration were to be repeated using the gas with the aim of implementing the probe into the LP rig, it would save a lot of time and reduce the risk of damage if the probe were calibrated and tested in one stem. Although changing the stem did not have a significant impact on the probe calibration, there were problems during assembly of the probe to the stem which resulted in the temperature compensation circuit becoming damaged.

An adapter piece would have to be designed to allow the angled stem β, as introduced in chapter 4, to be used in a straight flow as well as the angled flow found within the rig. This will allow the probe to be easily moved between calibrations and testing without timely changes to the probe geometry.

# References

Adrian, R. J. 1991. PARTICLE-IMAGING TECHNIQUES FOR EXPERIMENTAL FLUID MECHANICS. *Annu. Rev. Fluid Mech,* 23, pp.261 - 304.

Adrian, R. J. 2005. Twenty years of particle image velocimetry. *Experiments in Fluids,* 39, pp.159-169.

ANSI/ASME PTC 19.1, (1985), Supplement to Performance Test Coded, Instruments and Apparatus. Part 1-Measurement Uncertainty, *The American Society of Mechanical Engineers,* New York.

Ainsworth, R., W , Miller, R., J, Moss, R., W & Thorpe, S., J 2000. Unsteady pressure measurement. *Meas. Sci. Technol,* 11, pp.1055–1076.

Ansys. 2006. *Modeling Turbulent Flows* [Online]. Available: http://www.southampton.ac.uk/~nwb/lectures/GoodPracticeCFD/Articles/Turbulence_Notes_Fluent-v6.3.06.pdf [Accessed July, 2017.

Antonia, R., A 2003. On estimating mean and instantaneous turbulent energy dissipation rates with hot wires. *Experimental Thermal and Fluid Science,* 27, pp.151–157.

Babinsky, H., Kuschel, U., Hodson, H. P., Moore, D. F. & Welland, M. E. The Aerodynamic Design and Use of Multi-Sensor Pressure Probes for MEMS Applications. XVth Bi-Annual Symposium on Measuring

Techniques in Transonic and Supersonic Flows in Cascades and Turbomachines, 2002 Florence, Italy.

Bendant, J., S & Pierson, A., G 2010. *Random Data: Analysis and Measurement Procedures, 4th edition*

USA, Wiley.

Behr, T. 2007. *Control of rotor tip leakage and secondary flow by casing air injection in unshrouded axial turbines.* SWISS FEDERAL INSTITUTE OF TECHNOLOGY ZURICH. (ETH Zürich).

Bell, S., A 2001. A beginner's guide to uncertainty of measurement. *Measurement Good Practice Guide - NPL,* 11.

Bhattacharyaa, R., Kumarb, N., Kumarc, N., Bandyopadhyay, A. 2018. A Study On The Effect Of Process Parameters On Weld Width And Heat Affected Zone Of Pulsed Laser Welding Of Dissimilar Transparent Thermoplastics Without Filler Materials In Lap Joint Configuration. *Materials Today: Proceedings.* 4. pp 3674–3681

Blevins R. D. 1990. Flow Induced Vibrations, Van Nostrand Reinhold Co.

Bradbury, L, J, S 1965. The structure of a self-preserving turbulent plane jet. *J. Fluid Mech.,* 23, pp.31-64.

Browne, B., L, W, Antonia, R., A & Shah, D., A 1986. Turbulent energy dissipation in a wake. *J. Fluid Mech,* 179, pp.307-326.

Burton, Z., Ingram, G., Hogg, S. 2013. A literature review of low pressure steam turbine exhaust hood and diffuser studies. *Journal of engineering gas turbines power*

Cantwell,B., and Coles, D. An experimental study of entrainment and transport in the turbulent near wake of a circular cylinder. *Journal of fluid mechanics,* 136, pp. 321-374

Crawford, J., D. 2011. *DESIGN AND CALIBRATION OF SEVEN HOLE PROBES FOR FLOW MEASUREMENT.* Queen's University.

Dynamics, D. 2017. *Fluid Mechanics* [Online]. Available: https://www.dantecdynamics.com/fluid-mechanics [Accessed June, 2017.

Davidson, P. A. 2004. *turbulence, An introduction For Scientists And Engineers,* USA, Oxford University Press.

Denton, J. D. 1993. Loss Mechanisms in Turbomachines. *IGTI Scholar Lecture*.

Dudzinski, T. J. & Krause, L. N. Flow direction measurement with fixe-position probes.

Ecke, R. 2005. The Turbulence Problem An Experimentalist's Perspective. *Los Alamos Science* 29.

Elsner, J. W. & Elsner, W. 1996. On the measurement of turbulence energy dissipation. *Meas. Sci. Technol,* 7, pp.1334–1348.

Fernández Oro, J. M., Argüelles Díaz, K. M., Rodríguez Lastra, M., Galdo Vega, M. & Pereiras García, B. 2014. Converged statistics for time-resolved measurements in low-speed axial fans using high-frequency response probes. *Experimental Thermal and Fluid Science,* 54, pp.71–84.

George, W. & Hussein, H., J 1991. Locally axisymmetric turbulence. *J. Fluid Mech.,* 233, pp.1-23.

Gerner, A., A, Maurer, C., L & Gallington, R., W 1984. Non-nulling seven-hole probes for high angle flow measurement. *Experiments in Fluids* 2, pp.95 - 103.

Gonsalez, J., C & Arrington, A., E 1996. Five-Hole Flow Angle Probe Calibration For the NASA Glenn Icing Research Tunnel. *19th Advanced Measurement and Ground Testing Technology Conference* New Orleans.

Guenette, G., R & Castner, R., S 2011. FULLY INTEGRATED MINIATURE, HIGH FREQUENCY FLOW PROBE UTILIZING LEADLESS, SOI TECHNOLOGY SUITABLE FOR GAS TURBINES. *ASME Turbo Expo*

He. (ed.) 2003. *Handbook of Turbomachinery,* USA: Marcell Dekker, Inc.

Husted, B. P., Petersson, P., Lund, I. & Holmstedt, G. 2009. Comparison of PIV and PDA droplet velocity measurement techniques on two high-pressure water mist nozzles. *Fire Safety Journal,* 44, pp.1030-1045.

IEA. 2008. *Energy Efficiency Indicators For Public Electricity Production From Fossil Fuels.* [Online]. Available: https://www.iea.org/publications/freepublications/publication/En_Efficiency_Indicators.pdf. [Accessed May 2017].

Jahanmiri, M. 2011. *Particle Image Velocimetry: Fundamentals and Its Applications,* Sweden

JCDM 2008. Evaluation of measurement data — Guide to the expression of uncertainty in measurements. *GUM 1995*

Jensen, K. D. 2004. Flow Measurements. *J. of the Braz. Soc. of Mech. Sci. & Eng*.

Johansen, E., S & Rediniotis, O., K. 2005. Unsteady Calibration of Fast-Response Pressure Probes, Part 1: Theoretical Studies. *AAIA,* 43.

Johansen, E., Rediniotis, O, K & Jones, G. 2001. The Compressible calibration of miniature multi-hole probe. *Journal of fluids engineering*., 123. pp 123 – 138.

Jørgensen, F. 2002. How to measure turbulence with hot-wire anemometers - a practical guide. *Dantec Dynamics*.

Kovacs, T. 2017. Laser welding process specification base on welding theories. *Procedia Manufacturing.* 22 pp.147-153

Kutlie. 2017. *Sensor Description* [Online]. Available: https://www.kulite.com/technology/sensor-description/ [Accessed June, 2017]

Kulite, 2004. *Transducer Handbook* [Online]. Available: https://www.kulite.com/technology/reference-library/ [Accesed June,2017]

Kupferschmied, P., Koppel, P., Gizzi, W., Roduner, C. & G, G. 2000. Time-resolved flow measurements with fast-response aerodynamic probes in turbomachines. *Meas. Sci. Technol.,* 11, pp.1036–1054.

Kurosakat, M. & Gertzs, J., B 1987. Energy separation in a vortex street. *J. Fluid Mech,* 178, pp.1-29.

Lenherr, C. 2010. *High Temperature Fast Response Aerodynamic Probe.* PhD.

Liberzon, A., Gurka, R., Sarathi, P. & Kopp, G. A. 2012. Estimate of turbulent dissipation in a decaying grid turbulent flow. *Experimental Thermal and Fluid Science,* 39, pp.71-78.

Ligrani, P. M., Singer, B. A. & Baun, L. R. 1989. Miniature five-hole pressure probe for measurement of three mean velocity components in low-speed flows. *J. Phys. E: Sci. Instrum,* 22, pp.868-876.

Logan, E. (ed.) 2003. *Handbook of Turbomachinery,* USA: Marcell Dekker, Inc.

Mansour, M., Chokani, N., Kalfas, A. I. & Abhari, R. S. 2008. Unsteady Entropy Measurements in a High-Speed Radial Compressor. *Journal of Engineering for Gas Turbines and Power,* 130, pp.021603.

McDonough, J.M. 2007. *INTRODUCTORY LECTURES on TURBULENCE. Physics, Mathematics and Modelling.* University of Kentucky.

Mersinligil, M., Brouckaert, J.-F., Courtiade, N. & Ottavy, X. 2013. On Using Fast Response Pressure Sensors in Aerodynamic Probes to Measure Total Temperature and Entropy Generation in Turbomachinery Blade Rows. *Journal of Engineering for Gas Turbines and Power,* 135, pp.101601.

Mersinligil, M., Brouckaert, J.-F. O., Courtiade, N. & Ottavy, X. 2012. A High Temperature High Bandwidth Fast Response Total Pressure Probe for Measurements in a Multistage Axial Compressor. *Journal of Engineering for Gas Turbines and Power,* 134, pp.061601.

Mohammed, M. & Larue, J., C 1990. The decay power law in grid-generated turbulence. *Journal of Fluid Mechanics,* 219, pp.195-214.

NI, 2015. *The NI TDMS File Format* [Online]. National Instruments. Available: http://www.ni.com/white-paper/3727/en/ [Accessed June. 2017.

Pope, S. B. 2000. *Turbulent Flows,* UK, Cambridge University Press.

Reichert, B. A. & Wendt, B. J. 1994. A New Algorithm for Five-Hole Probe Calibration, Data Reduction, and Uncertainty Analysis. *NASA Technical Memorandum*.

REYNOLDS, W. C. & HUSSAIN, A. K. M. F. 1972. The mechanics of an organized wave in turbulent shear flow. Part 3. Theoretical models and comparisons with experiments. *Journal of fluid mechanics*. 54, pp. 263-288

Rose, M., G 1966. Results of an attempt to generate a homogeneous turbulent shear flow. *J. Fluid Mech.,* 35, pp.97-120

Saarenrinne, P. & Piirto, M. 2000. Turbulent kinetic energy dissipation rate estimates from PIV velocity vector fields. *Experiments in Fluids,* 29, pp.300–307.

Saarenrinne, P., Piirto, M. & Eloranta, H. 2001. Experiences of turbulence measurement with PIV. *Meas. Sci. Technol.,* 12, pp.1904–1910.

Sakakibara, K., Yamada, M., Miyamoto, Y. & Saito, T. 2007. Measurement of the surrounding liquid motion of a single rising bubble using a Dual-Camera PIV system. *Flow Measurement and Instrumentation,* 18, pp.211-215.

Schlienger, J., Pfau, A., Kalfas, A. I. & Abhari, A. S. 2002. Single Pressure Transducer Probe for 3D Flow Measurements. *The 16th*

*Symposium on Measuring Techniques in Transonic and Supersonic Flow in Cascades and Turbomachines.*

Shapiro, A. S. 1953. *The Dynamics and Thermodynamics of Compressible Fluid Flow,* UK, Wiley

Sieverding, C., H, Arts, T., Denos, R. & Brouckaert, J.-F. 2000. Measurement techniques for unsteady flows in turbomachines. *Experiments in Fluids,* 28, pp.286-321.

Sieverding, C. H., Ottolia, D., Bagnera, C., Comadoro, A., Brouckaert, J. F. & Desse, J.-M. 2004. Unsteady Turbine Blade Wake Characteristics. *Journal of Turbomachinery,* 126, pp.551.

Sieverding, C. H., Richard, H. & Desse, J.-M. 2003. Turbine Blade Trailing Edge Flow Characteristics at High Subsonic Outlet Mach Number. *Journal of Turbomachinery,* 125, pp.298.

Tanaka, K., Kalfas, A. I. & Hodson, H. P. 2002. Development of Single Sensor Fast Response Pressure Probe. *Proceedings of the XVth Bi-Annual Symposium on Measuring Techniques in Transonic and Supersonic Flows in Cascades and Turbomachines, 21-22 September, Florence, Italy*

Taylor, G., I 1935. Statistical theory of turbulence *Royal Society of London. Series A, Mathematical and Physical Sciences,* 151, pp.421-444.

Telionis, D. & Yang, Y. Recent Developments in Multi-Hole Probe (MHP) Technology. 20th International Congress of Mechanical Engineering November 15-20, 2009 Gramado, RS, Brazil.

Tropea, C., Yarin, A. & Foss, J. F. 2007. *Springer Handbook of Experimental Fluid Mechanics,* UK, Springer.

Tsinober, A., Kit, E. & Dracos, T. 1992. Experimental investigation of the field of velocity gradients in turbulent flows. *J. Fluid Mech.,* 242, pp.160-192.

Tucker, P. G. 2011. Computation of unsteady turbomachinery flows: Part 1—Progress and challenges. *Progress in Aerospace Sciences,* 47, pp.522-545.

Tucker, P. G. 2013. Trends in turbomachinery turbulence treatments. *Progress in Aerospace Sciences,* 63, pp.1-32.

Uberoi, M. S. 1967. Effect of Grid Geometry on Turbulence Decay. *Physics of Fluids,* 10, pp.1216.

Westphal, R., V, Pauley, W., R & Eaton, J., K 1987. Interaction Between a Vortex anda Turbulent Boundary Layer Part I: Mean Flow Evolution and Turbulence Properties. *NASA Technical Memorandum*.

Windmanna, M., Röttger, A., Kügler, A., Theisen., W. 2017. Microstructure and mechanical properties of the heat-affected zone in laserwelded/brazed steel 22MnB5–AA6016 aluminum/AZ31 magnesium alloy. *Journal of Materials Processing Tech.* 247. pp11-18

Wulff, D. L. 2006. Unsteady Pressure and Velocity Measurements in Pumps. *In Design and Analysis of High Speed Pumps* pp.4-1 – 4-34.

Zilliac, G., G 1993. Modelling, calibration, and error analysis of seven-hole pressure probes. *Experiments in Fluids* 14, pp.104 - 120.

# Appendices

## Appendix 1: Resistor diagrams for temperature compensation modules

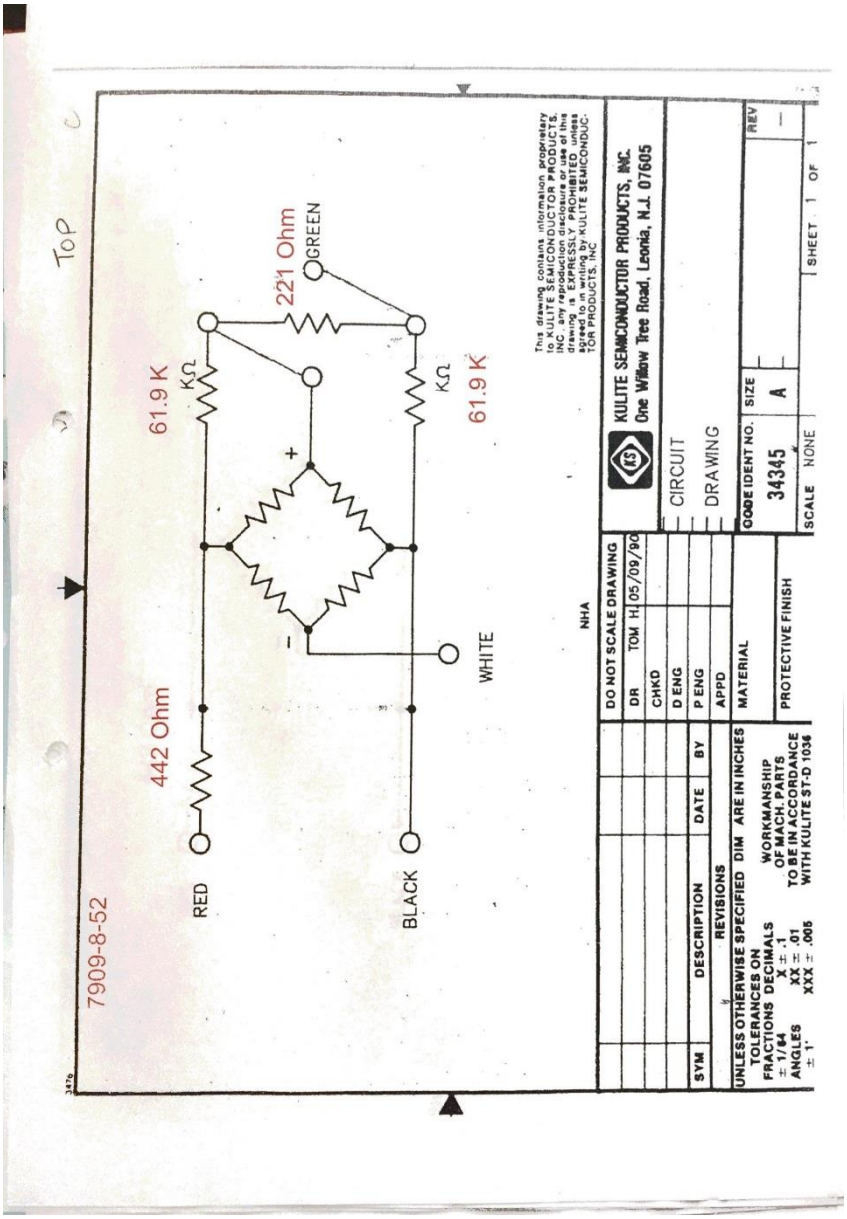



**Figure A1-1: Resistor diagram for temperature compensation module - Top sensor**

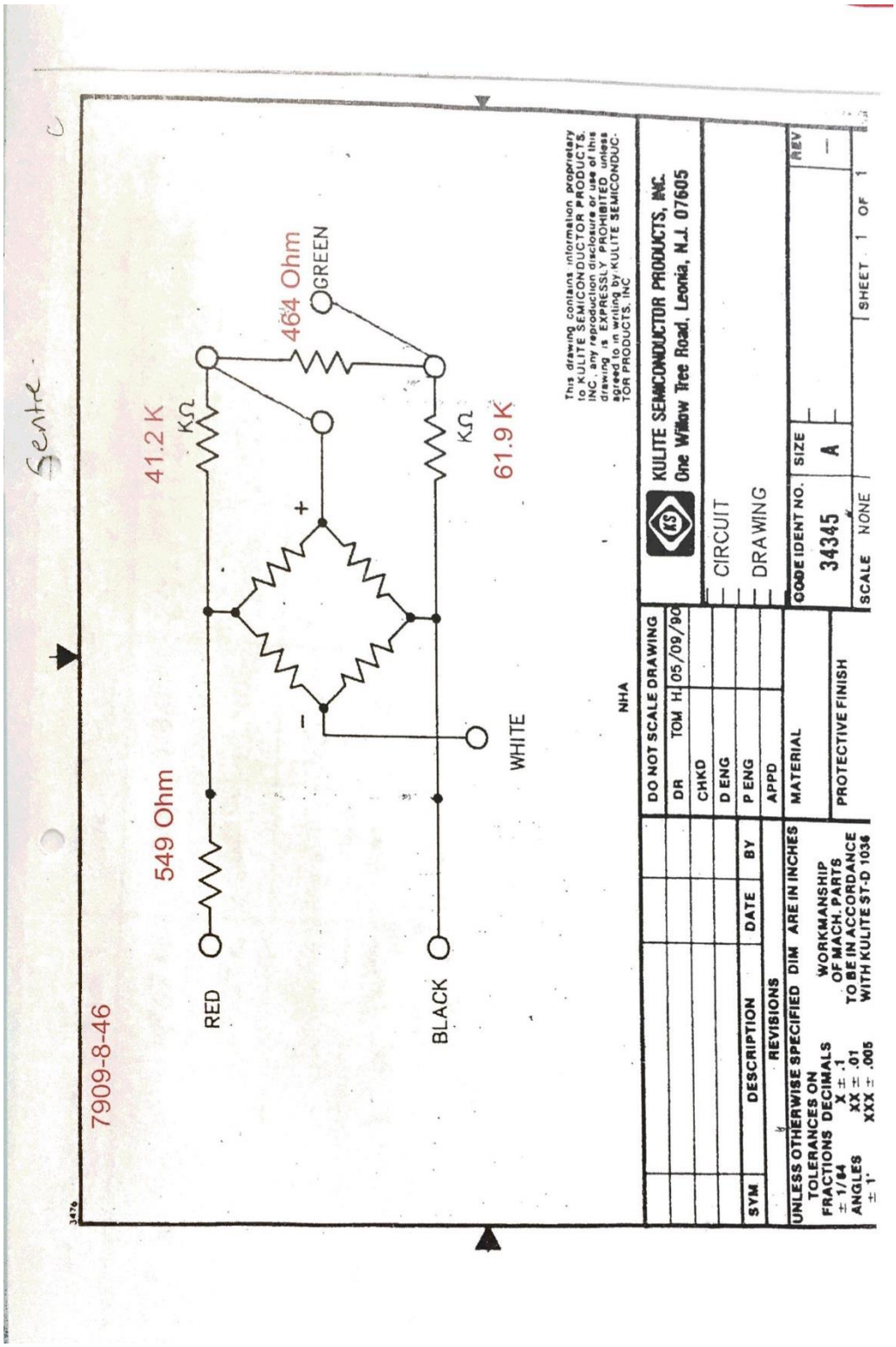



**Figure A1-2: Resistor diagram for temperature compensation module – Centre sensor**

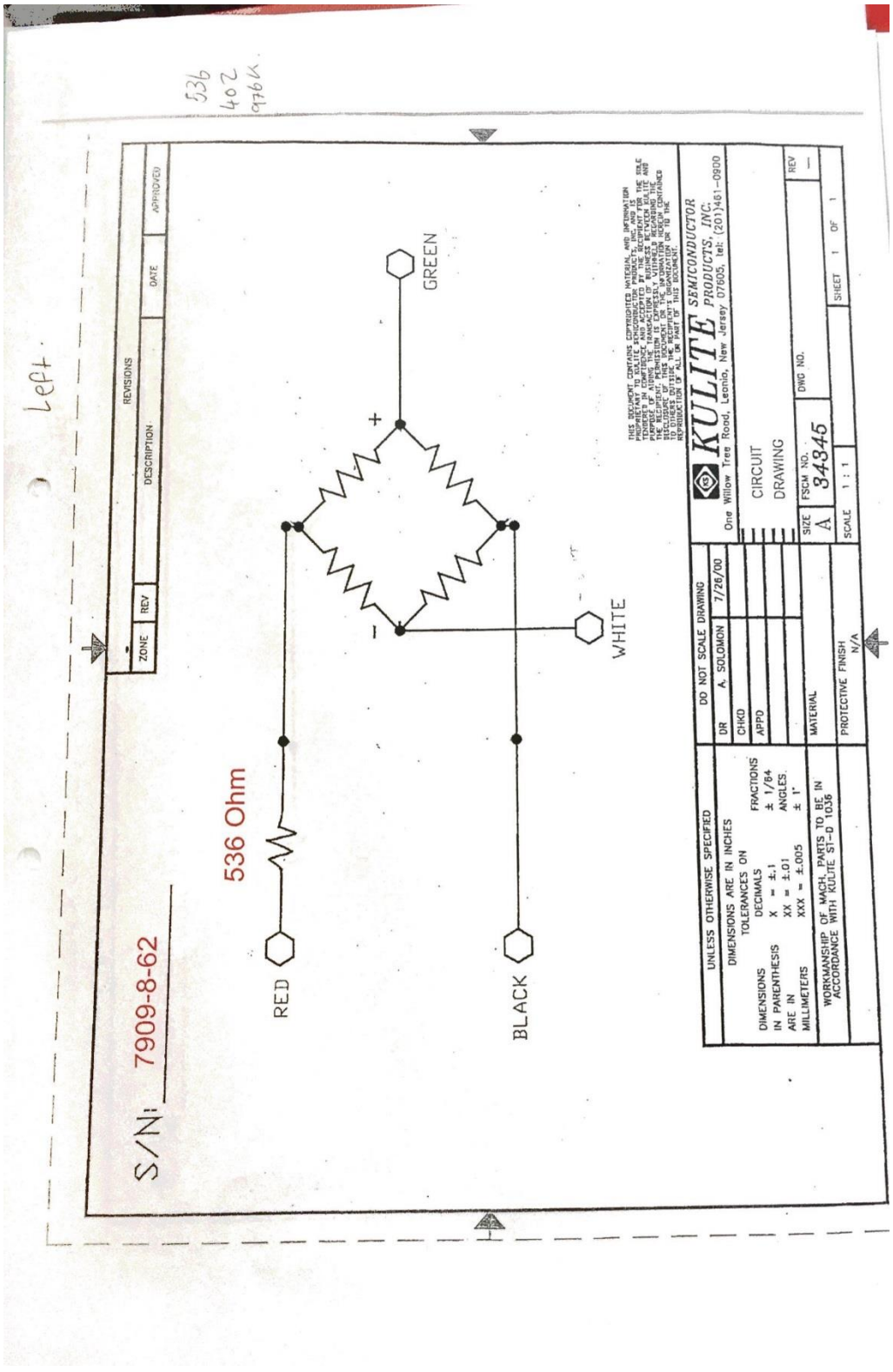



**Figure A1-3: Resistor diagram for temperature compensation module - Left sensor**

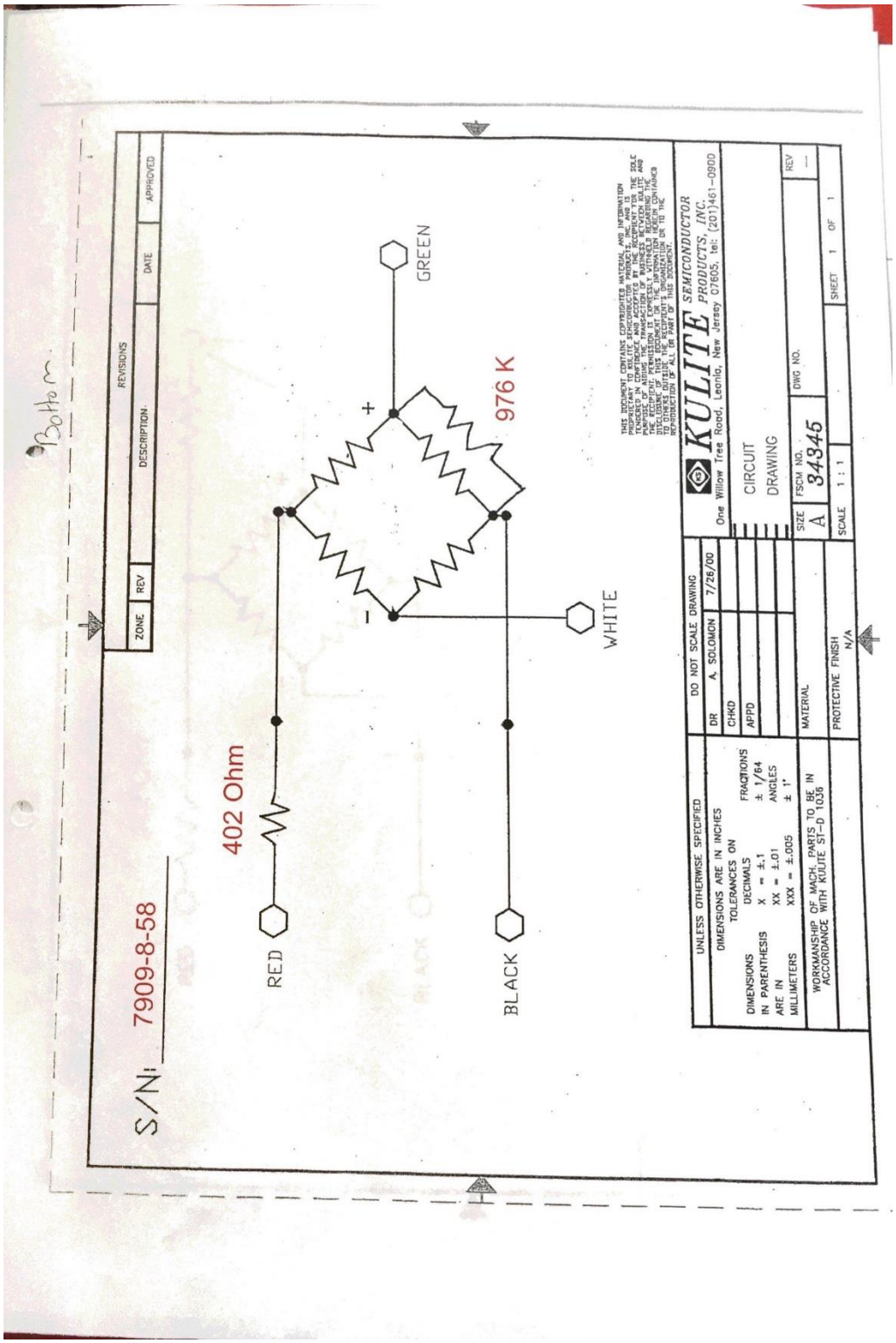



**Figure A1-4: Resistor diagram for temperature compensation module - Bottom sensor**

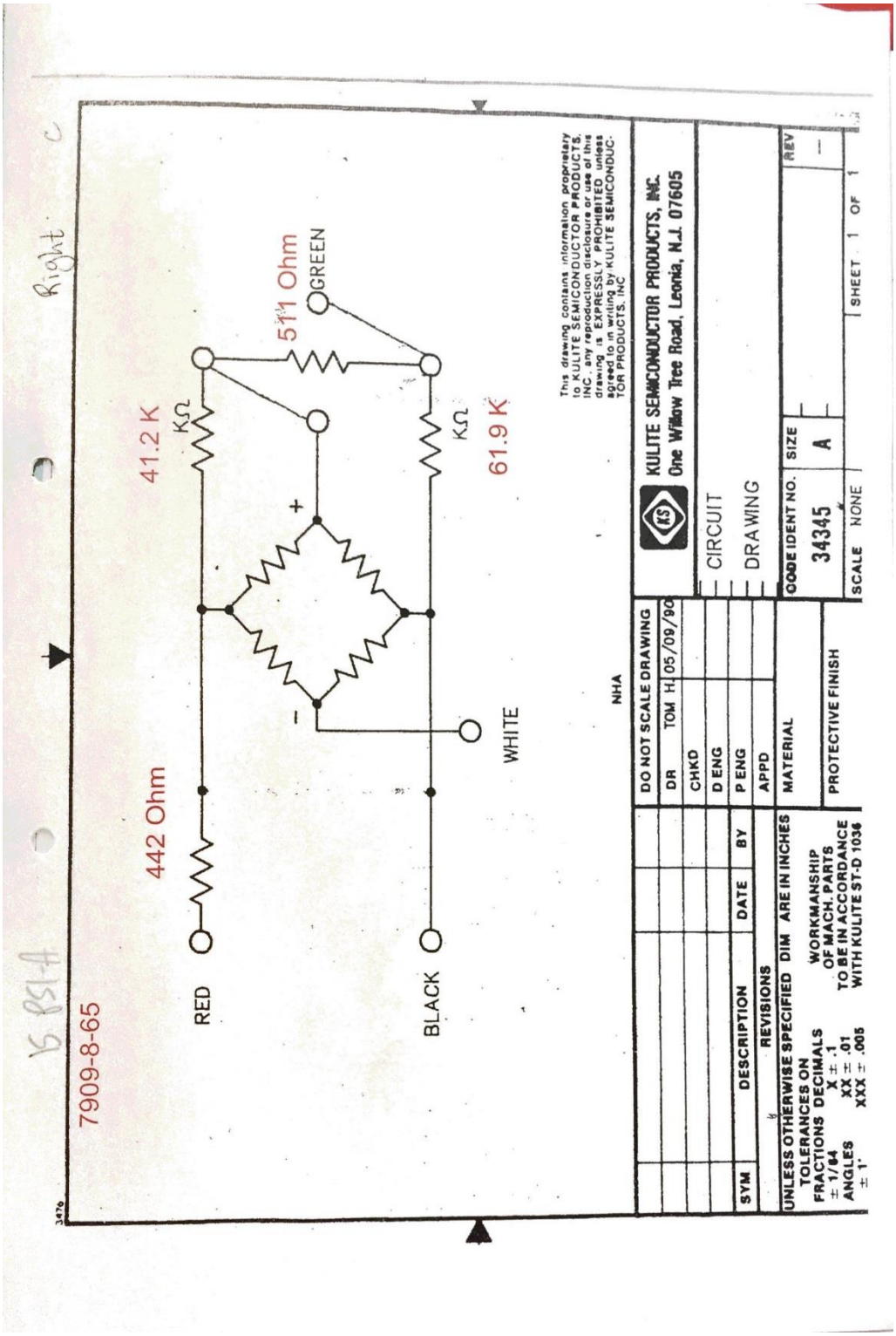



**Figure A1-5: Resistor diagram for temperature compensation module - Right sensor**

# Appendix 2: Intermediate drawings of Stem β

Intermediate drawings of Stem β are shown in figure A2 -1. They show the required probe neck bend for different probe tip angles. It can be seen that the $40^0$ protrudes out of the 9.6mm outer diameter constraint and that the other designs, for $20^0$ and $30^0$ are not physically possible by simply bending the probe stem.

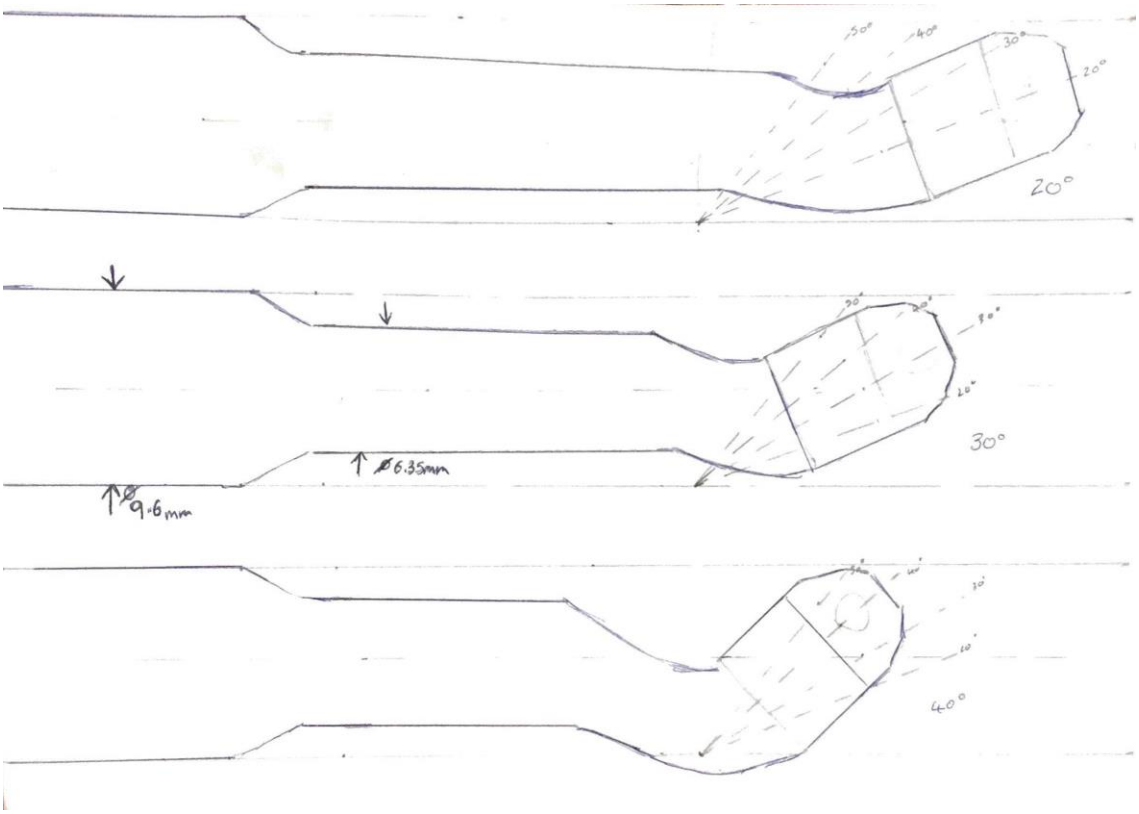



**Figure A2 - 1: Intermediate drawings of stem /Beta. Drawn to scale with FAP-250 probe tip schematic drawing**

# Appendix 3: Vortex shedding experimental measurement points

Proposed vortex shedding experiment measurement points are shown in figures A3 – 1 and 2.

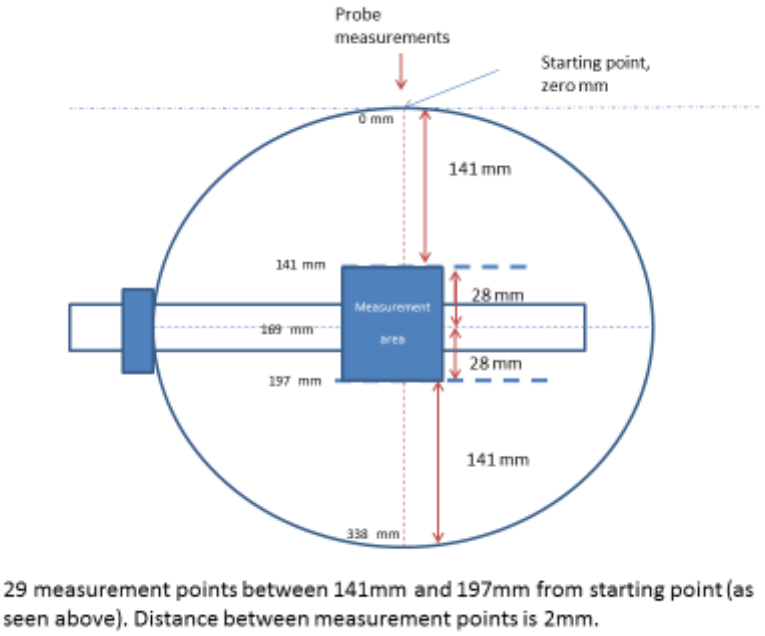



**Figure A3 - 1: Measurement area for vortex shedding experiment**

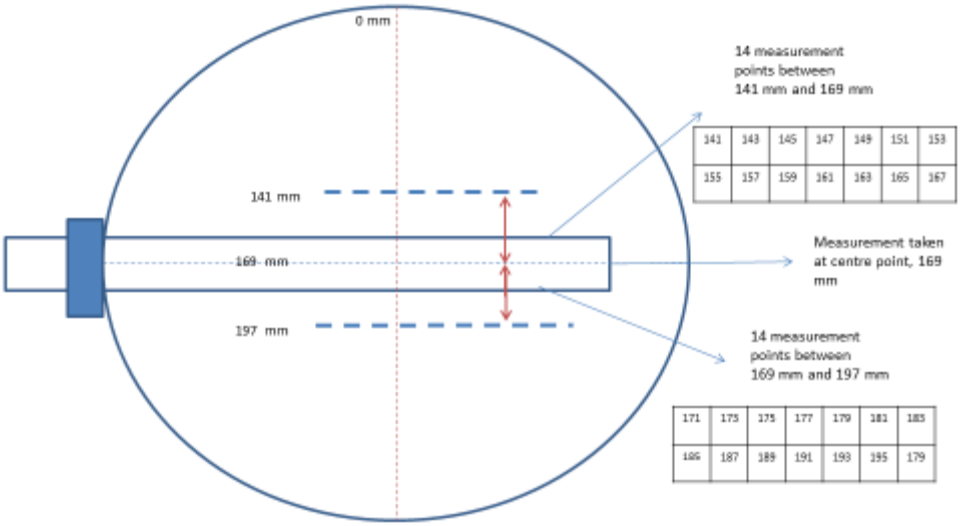



**Figure A3 - 2: Proposed measurement points for vortex shedding experiment**

# Appendix 4: CAD drawings of flow extension tube for Air Jet Rig

The CAD drawing of the flow extension tube is shown in figure A4-1.

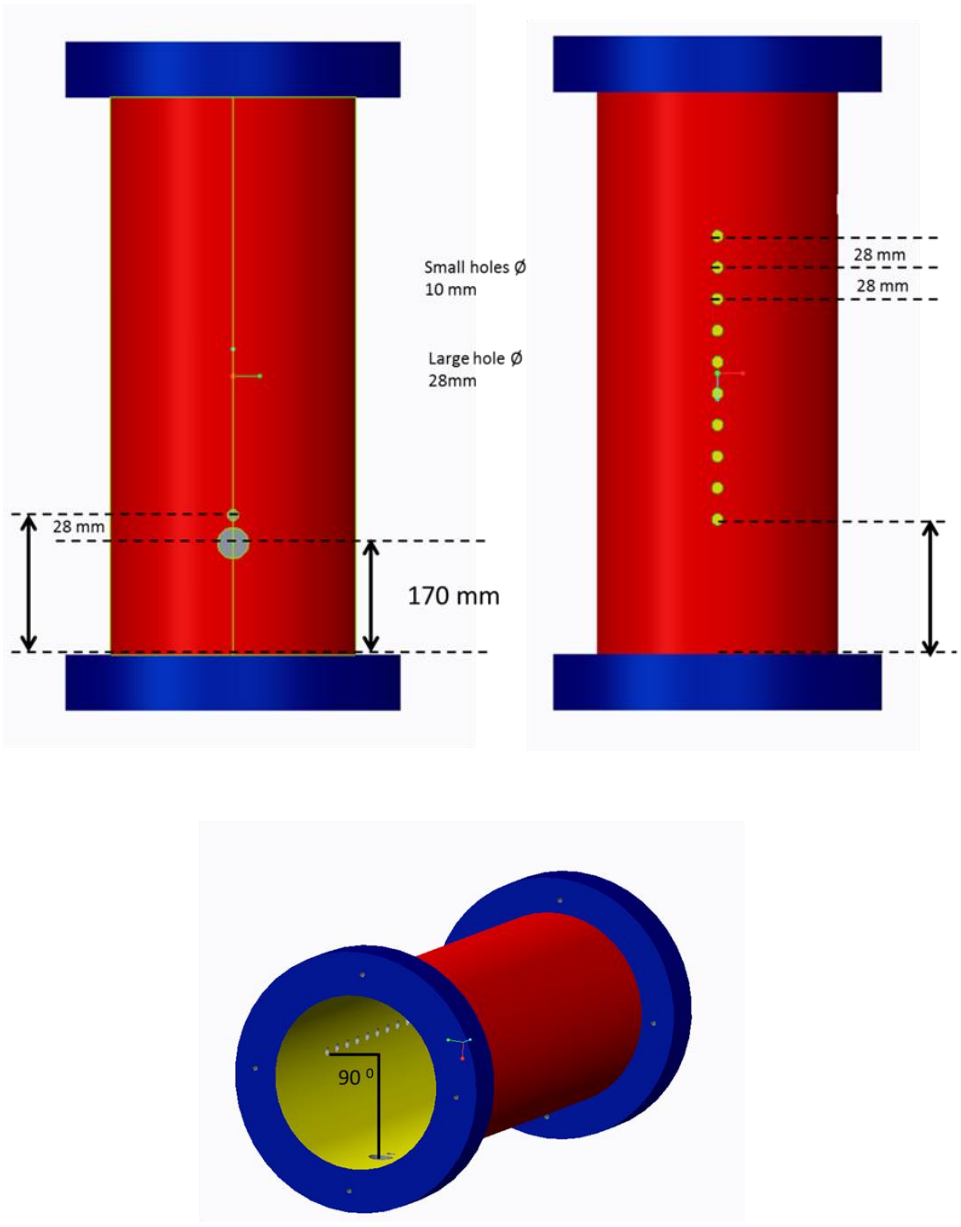



**Figure A4 - 1: CAD drawings of flow extension tube retrofitted to the Air Jet Rig.**

# Appendix 5: Yaw–Pitch manipulator design

The drawing of the pitch plate is shown in figure A5 – 1.

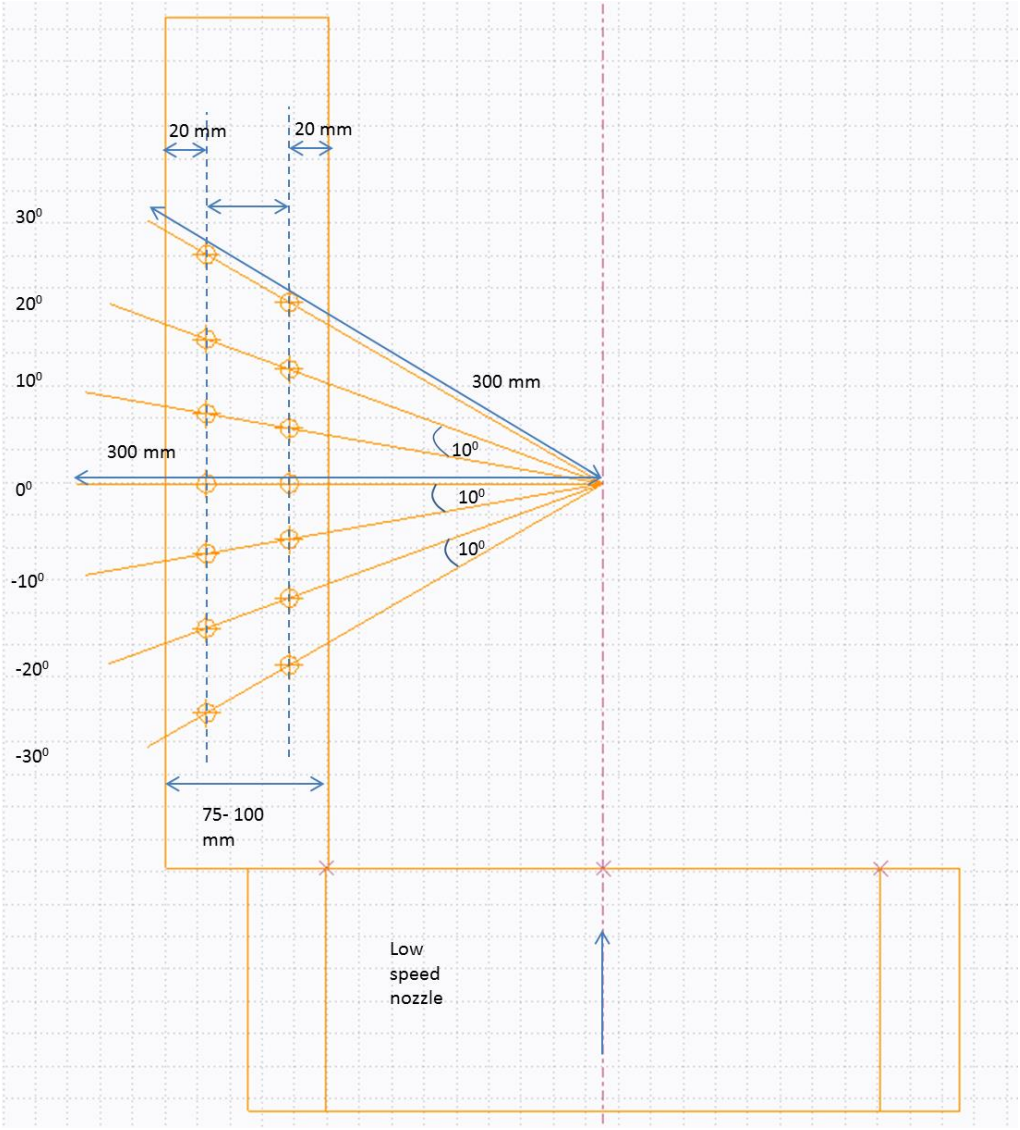



**Figure A5-1: Manual pitch plate designed to calibrate the 5S probe aerodynamically**

# Appendix 6: Unit vector relations for the aerodynamic calibration

Table A6 -1 shows the possible unit vector relations to deduce the velocity components from the 5S probe data. The Pitch-Yaw method was used in this investigation and the unit vectors were deduced using Table A6 – 1. They were multiplied by the absolute velocity to obtain the magnitudes in each direction.

| Unit Vector | Yaw-Pitch method | Pitch-Yaw method |
|---|---|---|
| $\boldsymbol{V_x}$ | cos(α)cos(β) | cos(α)cos(β) |
| $\boldsymbol{V_R}$ | cos(α)sin(β) | sin(α) |
| $\boldsymbol{V_\theta}$ | sin(α) | cos(α)sin(β) |

**Table A6 - 1: Table used to deduce unit vectors of velocity components. Adapted from Reichert and Wendt (1994).**

# Appendix 7: Data flow overview

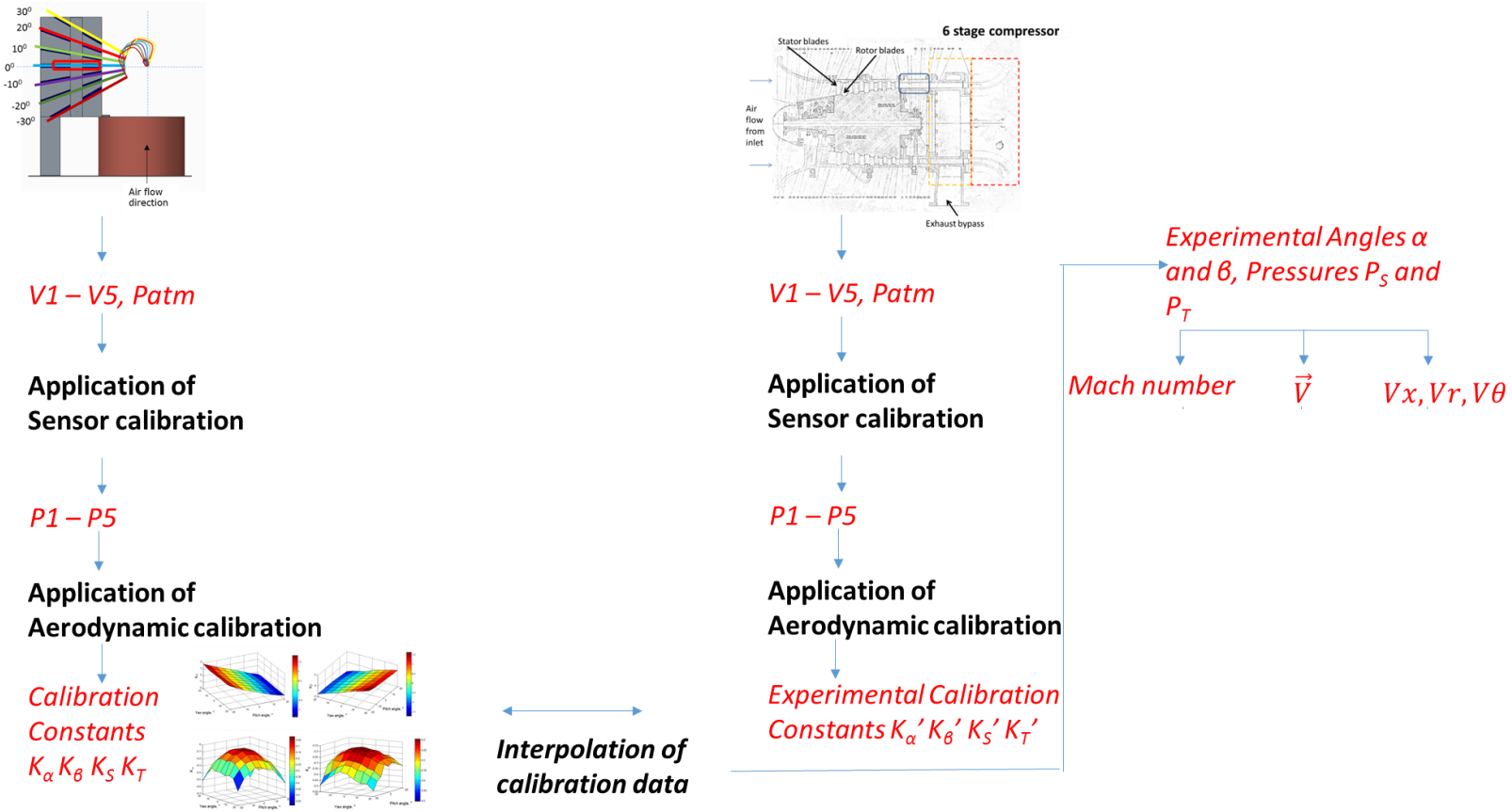



**Figure A7 - 1: Flowchart of the processes used on the data throughout the investigation**

# Appendix 8: Error propagation rules

The following rules (Bell, 1999) were used in chapter 6 to deduce the standard uncertainties in quantities deduced from the 5S probe.

For small changes in a function f(x,y,...), it is possible to use a Taylor expansion and arrive at the following relationship:

$$df = \frac{\partial f}{\partial x}dx + \frac{\partial f}{\partial y}dy + \cdots$$

This formulation can be used for addition of errors, rather than looking at small changes in variables. If errors are Gaussian (i.e. random) the best estimate of $\sigma_f$ is given by the relationship below:

$$\sigma_f^2 = \left(\frac{\partial f}{\partial x}\right)^2 \sigma_x^2 + \left(\frac{\partial f}{\partial y}\right)^2 \sigma_y^2 + \cdots$$

Therefore, errors add in quadrature, with the partial derivatives acting as a multiplicative scale factor. For instance, if f = x±y, then the resulting error would be given by:

$$\sigma_f^2 = \sigma_x^2 + \sigma_y^2$$

As a result of the partial derivative scaling factors, the power to which a variable is raised has an effect upon the error. As an example, take $f = x^n$. The error calculation runs as follows:

$$\sigma_f^2 = (nx^{n-1})^2\sigma_x^2$$

$$\sigma_f = \frac{nf}{x}\sigma_x$$

$$\frac{\sigma_f}{f} = n\frac{\sigma_x}{x}$$

Therefore, the contributing multiplier for these fractional errors is the power by which the variable is raised to within the original equation. These fractional errors can similarly be added in quadrature, as shown above, with the exponent squared substituting for the partial differentials.

Example:

Consider the Mach number equation:

$$Ma = \sqrt{\frac{2}{\gamma - 1}\left[\left(\frac{P_T'}{P_S'}\right)^{\frac{\gamma-1}{\gamma}} - 1\right]}$$

The two contributing factors to error in this calculation arise from $P_T$' and $P_S$', the errors for which are derived from goodness of fit values in MatLab. The equation can therefore be decomposed to show how Ma depends upon each of these variables, the relationships of which are shown below:

$$Ma \sim P_T'^{\frac{\gamma-1}{2\gamma}}$$

$$Ma \sim P_S'^{-\frac{\gamma-1}{2\gamma}}$$

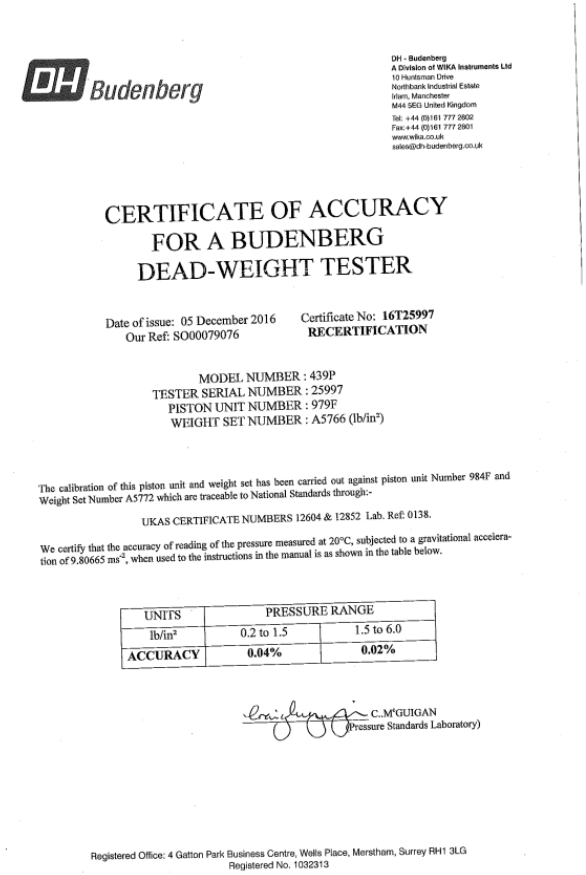
There is an inverse relationship between the two variables; this has no effect when considering error contributions, since in the final equation the partial derivatives are squared, thus removing the sign. Therefore, the multiplicative factor is identical for each variable.

Bearing this in mind, fractional errors can then be added in quadrature, using the relationships outlined above. Thus, where σ always represents a partial error:

$$\sigma_{Ma}^2 = \left(\frac{\gamma - 1}{2\gamma}\right)^2 \sigma_{P_T'}^2 + \left(\frac{\gamma - 1}{2\gamma}\right)^2 \sigma_{P_S'}^2$$

For values of γ = 1.4, $\sigma_{PT'}$ = 1.38% and $\sigma_{PS'}$ = 2.03%, this gives an error in Mach number of 0.35%. The lower error is due largely to the weak dependence of the variables i.e. the relatively small exponent value.

# Appendix 9: Deadweight tester calibration certificate



DH Budenberg

DH - Budenberg
A Division of WIKA Instruments Ltd
10 Huntsman Drive
Northbank Industrial Estate
Irlam, Manchester
M44 5EG United Kingdom
Tel: +44 (0)161 777 2802
Fax:+44 (0)161 777 2801
www.wika.co.uk
sales@dh-budenberg.co.uk

## CERTIFICATE OF ACCURACY FOR A BUDENBERG DEAD-WEIGHT TESTER

Date of issue: 05 December 2016
Our Ref: SO00079076

Certificate No: **16T25997**
**RECERTIFICATION**

MODEL NUMBER : 439P
TESTER SERIAL NUMBER : 25997
PISTON UNIT NUMBER : 979F
WEIGHT SET NUMBER : A5766 (lb/in²)

The calibration of this piston unit and weight set has been carried out against piston unit Number 984F and Weight Set Number A5772 which are traceable to National Standards through:-

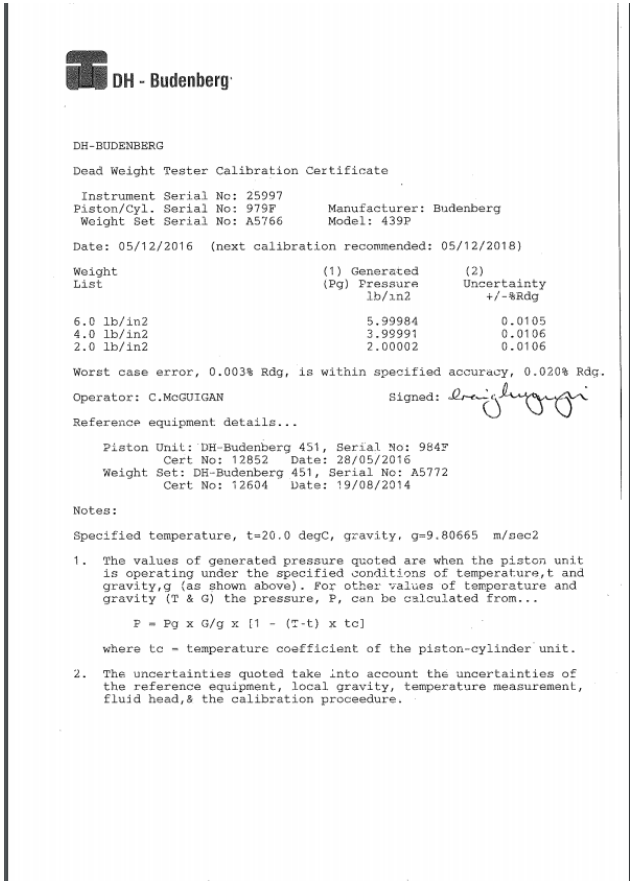
UKAS CERTIFICATE NUMBERS 12604 & 12852 Lab. Ref: 0138.

We certify that the accuracy of reading of the pressure measured at 20°C, subjected to a gravitational acceleration of 9.80665 $ms^{-2}$, when used to the instructions in the manual is as shown in the table below.

| UNITS | PRESSURE RANGE | |
|---|---|---|
| lb/in² | 0.2 to 1.5 | 1.5 to 6.0 |
| **ACCURACY** | **0.04%** | **0.02%** |

C.M'GUIGAN
(Pressure Standards Laboratory)





DH - Budenberg

DH-BUDENBERG

Dead Weight Tester Calibration Certificate

Instrument Serial No: 25997
Piston/Cyl. Serial No: 979F  Manufacturer: Budenberg
Weight Set Serial No: A5766  Model: 439P

Date: 05/12/2016 (next calibration recommended: 05/12/2018)

| Weight List | (1) Generated (Pg) Pressure lb/in2 | (2) Uncertainty +/-%Rdg |
|---|---|---|
| 6.0 lb/in2 | 5.99984 | 0.0105 |
| 4.0 lb/in2 | 3.99991 | 0.0106 |
| 2.0 lb/in2 | 2.00002 | 0.0106 |

Worst case error, 0.003% Rdg, is within specified accuracy, 0.020% Rdg.

Operator: C.McGUIGAN  Signed:

Reference equipment details...

Piston Unit: DH-Budenberg 451, Serial No: 984F
Cert No: 12852  Date: 28/05/2016
Weight Set: DH-Budenberg 451, Serial No: A5772
Cert No: 12604  Date: 19/08/2014

Notes:

Specified temperature, t=20.0 degC, gravity, g=9.80665 m/sec2

1. The values of generated pressure quoted are when the piston unit is operating under the specified conditions of temperature,t and gravity,g (as shown above). For other values of temperature and gravity (T & G) the pressure, P, can be calculated from...

   $P = Pg \times G/g \times [1 - (T-t) \times tc]$

   where tc = temperature coefficient of the piston-cylinder unit.

2. The uncertainties quoted take into account the uncertainties of the reference equipment, local gravity, temperature measurement, fluid head,& the calibration proceedure.

# Appendix 10: Kulite FAP-250 probe head specification

kulite

## FLOW ANGLE PROBE MINIATURE PRESSURE TRANSDUCER

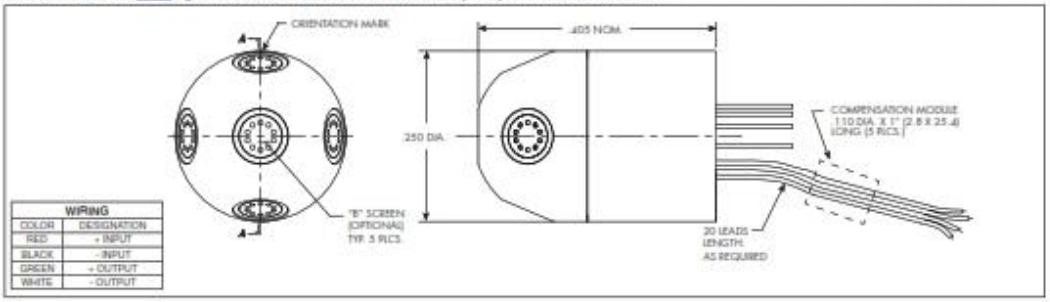
### FAP-250 SERIES

- High Frequency, High Accuracy Performance
- Patented Ultra Miniature Rugged Design
- Ideal For Aero Propulsion Measurements and Complex Flow Structures
- Patented Leadless Technology VIS®



The FAP-250 design features Kulite's patented SOI leadless technology with sensors positioned at the tip of the probe head. These fast response probes are ideal for aerodynamic measurements with complex flow structures, including turbomachinery flow distortions diffusers/mixers. The 5 position sensor construction allows concurrent measurements of 2 flow angles, total and static pressure, Mach number and flow speed.

**Kulite recommends the KSC-2 signal conditioner to maximize the measurement capability of the FAP-250 transducer.**




| WIRING | |
|---|---|
| COLOR | DESIGNATION |
| RED | + INPUT |
| BLACK | - INPUT |
| GREEN | + OUTPUT |
| WHITE | - OUTPUT |

| | | | | | |
|---|---|---|---|---|---|
| INPUT | Pressure Range | 3.5<br>50 | 7 BAR<br>100 PSI | | |
| | Operational Mode | Absolute | | | |
| | Over Pressure | 2 Times Rated Pressure With No Change in Calibration | | | |
| | Burst Pressure | 3 Times Rated Pressure | | | |
| | Pressure Media | Most Conductive Liquids and Gases - Please Consult Factory | | | |
| | Rated Electrical Excitation | 10 VDC | | | |
| | Maximum Electrical Excitation | 12 VDC | | | |
| | Input Impedance | 1000 Ohms (Min.) | | | |
| OUTPUT | Output Impedance | 1000 Ohms (Nom.) | | | |
| | Full Scale Output (FSO) | 100 mV (Nom.) | | | |
| | Residual Unbalance | ± 5 mV (Typ.) | | | |
| | Combined Non-Linearity, Hysteresis and Repeatability | ± 0.1% FSO BFSL (Typ.), ± 0.5% FSO (Max.) | | | |
| | Resolution | Infinitesimal | | | |
| | Natural Frequency of Sensor Without Screen (KHz) (Typ.) | 200 | 240 | 300 | 380 |
| | Acceleration Sensitivity % FS/g Perpendicular | $7.0x10^{-4}$ | $5.0x10^{-4}$ | $3.0x10^{-4}$ | $1.5x10^{-4}$ |
| | Insulation Resistance | 100 Megohm Min. @ 50 VDC | | | |
| ENVIRONMENTAL | Operating Temperature Range | -65°F to +250°F (-55°C to +120°C) | | | |
| | Compensated Temperature Range | +80°F to +180°F (+25°C to +80°C) Any 100°F Range Within The Operating Range on Request | | | |
| | Thermal Zero Shift | ± 1% FS/100°F (Typ.) | | | |
| | Thermal Sensitivity Shift | ± 1% /100°F (Typ.) | | | |
| | Steady Acceleration | 10,000 g. (Max.) | | | |
| | Linear Vibration | 10-2,000 Hz Sine, 100g. (Max.) | | | |
| PHYSICAL | Electrical Connection | 4 Leads 36 AWG (Length as Required) | | | |
| | Pressure Sensing Principle | Fully Active Four Arm Wheatstone Bridge Dielectrically Isolated Silicon on Silicon Patented Leadless Technology | | | |

*Note: Custom pressure ranges, accuracies and mechanical configurations available. Dimensions are in inches. Dimensions in parenthesis are in millimeters. All dimensions nominal. (F) Continuous development and refinement of our products may result in specification changes without notice.* *Copyright © 2014 Kulite Semiconductor Products, Inc. All Rights Reserved.* *Kulite miniature pressure transducers are intended for use in test and research and development programs and are not necessarily designed to be used in production applications. For products designed to be used in production programs, please consult the factory.*

KULITE SEMICONDUCTOR PRODUCTS, INC. • One Willow Tree Road • Leonia, New Jersey 07605 • Tel: 201 461-0900 • Fax: 201 461-0990 • http://www.kulite.com